Structural and Magnetic Properties of the Insulating T'-RE$_2$CuO$_4$ Parent Compounds of Electron-Doped Superconductors

Dissertation

zur
Erlangung der naturwissenschaftlichen Doktorwürde
(Dr. sc. nat.)

vorgelegt der
Mathematisch-naturwissenschaftlichen Fakultät der
Universität Zürich

von

Gwendolyne Banasan Pascua
aus den Philippinen

Zürich, 2014

Promotionskomitee:

Prof. Dr. Elvezio Morenzoni (Vorsitz)
Dr. Hubertus Luetkens (Leitung der Dissertation)
Prof. Dr. Hugo Keller
Prof. Dr. Roberto de Renzi

Die vorliegende Arbeit wurde von der Mathematisch-naturwissenschaftlichen Fakultät der Universität Zürich auf Antrag von Prof. Dr. Elvezio Morenzoni als Dissertation angenommen.

dedicated to my Lolo William and Lola Catalina, my Mama, and Thibault

Abstract

The rare earth cuprates RE_2CuO_4 crystallizing in the T'-structure are the parent compounds for electron-doped superconductors. Various investigations illustrated that these systems turn superconducting upon electron-doping and/or fine-tuning of the oxygen reduction annealing conditions. These undoped parent compounds are characterized by a very strong antiferromagnetic coupling between the Cu moment within the CuO_2 planes and a very weak coupling between adjacent planes. The reason for this weak interlayer coupling lies in the body-centered tetragonal (BCT) structure of these compounds which cancels out the isotropic Heisenberg interaction between one and the next nearest layer. Therefore, the BCT cuprates can be regarded as quasi-2 dimensional (2D) magnetic systems. Even though the Mermin-Wagner theorem forbids the magnetic ordering of a 2D magnetic system, the BCT cuprates are known to order at temperatures around 280 K due to the weak interlayer coupling along the third spatial direction. The actual process how these quasi-2D systems approach the ultimate 3D magnetic order and which kinds of spin structures are realized, are anyhow still a matter of current debate. Moreover, the rare-earth cuprates exhibit underlying interactions involving both the copper and the magnetic rare-earth subsystems that demonstrated interesting phenomena such as spin reorientation transitions.

In this work, a systematic investigation of the 3D magnetic ordering process, the influence of a magnetic rare-earth ion and the effect of oxygen reduction on the magnetism of these undoped compounds, were focused upon. The rich magnetic behavior of the BCT cuprates T'-RE_2CuO_4 (RE= La, La/Sm, and Pr) is investigated primarily using the muon spin rotation and relaxation (μSR) technique. Complementary experimental studies were also carried out with nuclear magnetic resonance (NMR) and neutron scattering techniques. The structural properties, primarily the oxygen content and site occupation, are determined by neutron scattering and synchrotron x-ray diffraction.

All the studied T'-RE_2CuO_4 (RE= La, La/Sm, and Pr) compounds revealed series of magnetic transitions as a function of temperature. The sensitivity of the μSR technique to such transitions is well-evidenced here while neutron scattering measurements on some of the compounds did not detect these transitions.

μSR results on the novel T'-La_2CuO_4 (T'-LCO) are of outstanding importance in this work primarily due to the observation of distinct transitions even with a nonmagnetic La^{3+} ion. The three characteristic temperature regimes encompass a quasi-static order with slow magnetic fluctuations between 220 K and 115 K, a static regime with a broad asymmetric field distribution at the muon site between 115 K and 40 K, and a low temperature regime wherein an abrupt change to a narrow and symmetric field distribution had been manifested. These transitions had been affirmed by ^{139}La-NMR measurements. Plausible physical scenarios at each characteristic temperature regime had been verified via magnetic dipole field calculations at the La and muon site, respectively. For this purpose, the muon site has firstly been determined theoretically and then different magnetic structures have been checked for consistency with the measured data. Specifically, those structures were tested which belong to the two irreducible representations (IR) of the magnetic symmetry group.

The quasi-static behavior of T'-LCO, which is essentially a 2D system at high temperatures but finally orders in a 3D magnetic structure at low temperatures, is explained in two possible physical scenarios. Firstly, it is likely that below 220 K, there is an antiferromagnetic coupling between the Cu moments within the planes and the coupling to the next plane is weak due to frustration. This would allow that the relative orientation between the planes could be random and even fluctuates. There is then a coupling of every second plane which is ferromagnetic that gave rise to the 3D magnetic ordering transition at 220 K seen by NMR. Secondly, it could be possible that this quasi-static magnetism is a signature of the quasi-2D behavior and a dimensional crossover happening in cuprates. That is, these systems undergo a crossover from a 2D Heisenberg to 2D XY behavior and later order in 3D when lowering the temperature. A more provocative conjecture about this quasi-static regime might be that, it could be a result of a so-called Kosterlitz-Thouless transition.

For the static regime observed between 115 K and 40 K with a broad asymmetric field distribution, magnetic dipole field calculations indicate that there exists a distribution of relative angle of the spin alignment in neighboring planes across the sample. It turns out that all local spin configurations belong to the same IR. A physical scenario may be that the system is consisting of grains possessing all different spin structures which are allowed by symmetry. Another possible scenario is a spin density wave with a continuous modulation of the relative angle between neighboring planes along the c-direction from unit cell to unit cell.

The last transition at 40 K is characterized by an abrupt change of the field distribution to a single-symmetric Lorentzian line. Magnetic dipole field calculations prove that the best-suitable model for the low-temperature regime in T'-LCO is a noncollinear structure belonging to one of the possible IRs. Hence, the spin structure below 40 K *locks-in* to this magnetic structure which is this energetically preferred alignment of the system due to a small anisotropy in the CuO_2 plane.

Moreover, another remarkable finding is that the T'-La_2CuO_4 exhibited a strongly-reduced Néel temperature compared to the orthorhombic T-La_2CuO_4 and to other T'-RE_2CuO_4 cuprates such as T'-Nd_2CuO_4 and T'-Pr_2CuO_4. This reduction can be traced back to a ten times decrease in the interlayer coupling possibly due to the missing polarizable lanthanide ion in T'-La_2CuO_4. The results on T'-$La_{1.85}Sm_{0.15}CuO_4$ confirmed our notion that the magnetic coupling in the c-direction is enhanced with the substitution of a magnetically polarizable Sm ion in the T'-La_2CuO_4 that strengthened the so-called pseudo-dipolar interactions in the system. Thus, the magnetic rare-earth has influence on the interlayer magnetic coupling and dynamics in the system. The presence of a magnetic rare-earth can, e.g. directly raise the Néel temperature. Nevertheless, the results herein gave indications that the nature of the RE moments and the induced magnetic polarization in the RE magnetic system may not directly be at the core of the explanation for the observed reorientation transitions since they are similarly also observed in T'-La_2CuO_4. Although surely, the magnetic RE adds another degree of freedom to the complex magnetic interactions in the CuO_2 plane.

Another aspect that plays an important role in the magnetism of the BCT cuprates is the oxygen content and oxygen site occupation. The results on the T'-$La_{1.85}Sm_{0.15}CuO_4$ and T'-Pr_2CuO_4 revealed that the annealing conditions can impose structural modifications that have different effects on the static and dynamic properties of the Cu magnetism. That is, annealing conditions can influence which oxygen site is vacated or may even induce Cu vacancies leading to disorder in the system. A higher annealing temperature reduces the O(2) occupation and magnetically disorders the system while a slightly lower annealing temperature only affected the O(3) and has surprisingly no effect on the magnetism in contrast to the general belief that it is exactly this defect site which is responsible for the appearance of magnetism and suppression of superconductivity in the electron-doped compounds. However, moderately low annealing condition can repair Cu vacancies or redistribute oxygen and Cu, leading to a more-ordered system. In spite of that, series of magnetic transitions had been illustrated by both the as-grown and the reduced samples. This is yet another remarkable observation since no direct evidence for spin reorientation in the T'-Pr_2CuO_4 had been accounted before.

Zusammenfassung

Die Kuprate mit Seltenen Erd Ionen (RE) der Form RE$_2$CuO$_4$ die in der sogenannten T' Struktur kristallisieren sind die undotierten Ausgangsverbindungen der elektronendotierten Supraleiter. Diverse Untersuchungen zeigen, dass diese Systeme durch Elektronendotierung und/oder durch Feinabstimmung der Sauerstoff Reduktionsbedingungen supraleitend werden. Diese undotierten Ausgangsverbindungen zeichnen sich durch eine sehr starke antiferromagnetische Kopplung der Kupfermomente in den CuO$_2$ Ebenen und durch eine sehr schwachen Kopplung zwischen benachbarten Ebenen aus. Der Grund dieser schwachen Zwischenschichtkopplung liegt in der raumzentriert tetragonalen (BCT) Struktur dieser Verbindungen. In dieser Struktur hebt sich die isotrope Heisenberg Wechselwirkung zwischen einer und der nächsten Ebene auf, weshalb diese BCT Kuprate als quasi 2-dimensionale (2D) magnetische Systeme angesehen werden können. Obwohl das Mermin-Wagner Theorem eine magnetische Ordnung eines magnetischen 2D Systems verbietet, ist es bekannt, dass die BCT Kuprate bei Temperaturen um die 280 K auf Grund einer schwachen Kopplung entlang der dritten Raumdimension ordnen. Der tatsächliche Ablauf, wie diese quasi 2D Systeme sich der ultimativen magnetischen 3D Ordnung annähern und welche Spinstrukturen dabei realisiert werden, wird bis heute diskutiert. Zusätzlich zeigen die Kuprate mit Seltenen Erden Wechselwirkungen des Kupfer als auch des magnetischen Seltenen Erd Subsystems die interessante Phänomene wie beispielsweise Spinreorientierungsübergänge hervorbringen.

Diese Arbeit konzentriert sich auf eine systematische Untersuchung des magnetischen 3D Ordnungsprozesses als auch auf den Einfluss der magnetischen Seltenen Erd Ionen und des Sauerstoffreduktionsprozesses auf den Magnetismus dieser undotierten Verbindungen. Das vielfältige magnetische Verhalten der BCT Kuprate T'-RE$_2$CuO$_4$ (RE = La, La/Sm und Pr) wird hierbei hauptsächlich mit der Methode der Myonenspinrotation und Relaxation (μSR) untersucht. Mit Hilfe von Neutronenstreuungs- und Kernspinresonanz (NMR) Techniken wurden weitere komplementäre Untersuchungen durchgeführt. Die strukturellen Eigenschaften dieser Verbindungen, hauptsächlich deren Sauerstoffgehalt und Besetzungswahrscheinlichkeit der verschiedenen Kristallplätze, wurden mit Neutronen- und Synchrotron-

Röntgenstreuung bestimmt.

Alle untersuchten T'-RE$_2$CuO$_4$ (RE = La, La/Sm und Pr) Verbindungen zeigten eine Serie von magnetischen Übergängen als Funktion der Temperatur. Hierbei zeigte sich die besondere Empfindlichkeit der μSR Technik für diese Übergänge, während die Neutronenstreuung, an einigen dieser Verbindungen, die Übergänge nicht nachweisen konnte.

Die an dem neuartigen T'-La$_2$CuO$_4$ erhaltenen μSR Resultate sind von herausragender Bedeutung in dieser Arbeit, da eindeutige Übergängen in einem Material mit nichtmagnetischen La^{3+} Ionen beobachtet wurden. Die drei charakteristischen Temperaturintervalle beinhalten eine quasi-statische Ordnung mit langsam Fluktuationen zwischen 220 K und 115 K, einen statischen Bereich mit einer breiten und asymmetrischen Feldverteilung am Myonenort zwischen 115 K und 40 K, und einen Tieftemperaturbereich in dem ein abrupter Übergang zu einer schmalen und symmetrischen Feldverteilung beobachtet wird. Diese Übergänge wurden mit ^{139}La-NMR Untersuchungen bestätigt. Plausibele physikalische Szenarien für die entsprechenden Temperaturintervalle wurden mit Hilfe von magnetischen Dipolrechnungen am La als auch am Myonenort überprüft. Hierfür wurde zunächst der Myonenplatz theoretisch bestimmt und danach verschiedene magnetische Strukturen mit den Rechnungen auf Konsistenz mit den Messdaten getestet. Speziell wurden magnetische Modelle getestet, die zu einer der zwei irreduziblen Darstellungen (IR) der magnetischen Symmetriegruppe gehören.

T'-La$_2$CuO$_4$ ist im Wesentlichen ein 2D System bei hohen Temperaturen, das letztendlich als 3D magnetische Struktur bei tiefen Temperaturen ordnet. Das quasi-statische Verhalten im Übergangsbereich wird in zwei möglichen Szenarien erklärt. Erstens ist es wahrscheinlich, dass unterhalb von 220 K eine antiferromagnetische Kopplung zwischen den Kupfermomenten innerhalb der Ebene existiert und dass die Kopplung zwischen den Ebenen auf Grund von Frustrationseffekten schwach ist. Dies könnte ermöglichen, dass die relative Orientierung der Spins zwischen den Ebenen zufällig ist oder gar fluktuiert. Die ferromagnetische Kopplung zu der übernächsten Ebene erzeugt dann den magnetischen 3D Ordnungsübergang bei 220 K wie er von NMR Messungen gefunden wird. Zweitens wäre es möglich, dass der beobachtete quasi-statische Magnetismus eine Signatur des quasi-2D Verhaltens und des anschliessenden Dimensions-Übergangs in den Kupraten darstellt. Dies bedeutet, dass diese Systeme von einem 2D Heisenberg zu einem 2D XY Verhalten und später zu einer 3D Ordnung übergehen. Eine etwas provokative These wäre, dass dieses quasi-statische Regime eine Folge eines sogenannten Kosterlitz-Thouless Übergangs ist.

Im statischen Bereich zwischen 115 K und 40 K, in dem eine breite asymmetrische Feldverteilung beobachtet wird, zeigen die magnetischen Dipolrechnungen, dass eine Verteilung von relativen Spinorientierungen zwischen benachbarten Ebenen innerhalb der Probe existiert. Es zeigt sich, dass alle lokalen Spinkonfigurationen zu ein und derselben IR gehören. Ein physikalisches Szenario wäre, dass das System aus einzelnen Körnern besteht, die alle unterschiedliche magnetische Strukturen aufweisen die durch die Symmetrie erlaubt sind. Ein anderes mögliches Szenario wäre eine Spindichtewelle die eine kontinuierliche Modulation der relativen Winkel zwischen benachbarten Ebenen entlang der c-Richtung des Kristalls erzeugt.

Der letzte Übergang bei 40 K ist charakterisiert durch eine abrupte Veränderung der Feldverteilung zu einer einzigen symmetrischen Lorentzlinie. Magnetische Dipolfeldrechnungen beweisen, dass das beste Modell für diese Tieftemperaturphase von T'-La_2CuO_4 eine nichtkollineare Struktur ist, die zu einer der möglichen IR Darstellungen gehört. Dies zeigt, dass die magnetische Struktur unterhalb von 40 K in die Struktur einrastet, die aufgrund einer kleinen Anisotropie in der CuO_2 Ebene energetisch bevorzugt wird.

Ein weiterer bemerkenswerter Befund ist, dass T'-La_2CuO_4 im Vergleich zu dem orthorhombischen T-La_2CuO_4 und anderen T'-RE_2CuO_4 wie z. B. T'-Nd_2CuO_4 oder T'-Pr_2CuO_4 eine stark erniedrigte Néel Temperatur aufweist. Diese Erniedrigung kann auf eine 10-fache Verringerung der Zwischenschichtkopplung zurückgeführt werden, die möglicherweise durch das Fehlen eines polarisierbaren Lanthanoid Ions in T'-La_2CuO_4 reduziert ist. Messungen an T'-$La_{1.85}$ $Sm_{0.15}CuO_4$ bestätigten unsere Sichtweise, das die magnetische Kopplung entlang der c-Richtung mit dem polarisierbaren Sm Ion verstärkt wurde. Dies stärkte die sogenannte Pseudo-Dipolare-Wechselwirkung. Aus diesem Grund hat das magnetische Seltene Erd Ion Einfluss auf die magnetische Kopplung zwischen den Ebenen und auf die Dynamik des Systems. Die Präsenz eines magnetischen Seltene Erd Ions kann z. B. die Néel Temperatur erhöhen. Nichtsdestotrotz weisen die in dieser Arbeit erhaltenen Resultate darauf hin, dass die Art des Seltenen Erd Atoms und dessen Polarisierbarkeit nicht von zentraler Wichtigkeit für die Erklärung der Spinreorientierungsübergänge sind, da diese auch in T'-La_2CuO_4 beobachtet wurden. Dennoch steuert ein magnetisches Seltene Erd Ion natürlich einen weiteren Freiheitgrad zu den ohnehin schon komplexen Wechselwirkungen innerhalb der CuO_2 Ebene bei.

Ein weiterer Aspekt der eine wichtige Rolle für den Magnetismus der BCT Kuprate spielt ist der Sauerstoffgehalt und die Besetzungswahrscheinlichkeit der verschiedenen Sauerstoffplätze im Kristallgitter. Die an T'-$La_{1.85}$ $Sm_{0.15}CuO_4$ und T'-Pr_2CuO_4 erhaltenen Resultate zeigten, dass verschiedene Reduktionsbedingungen verschiedene strukturelle Veränderungen hervorrufen können, die wiederum unterschiedlichen Einfluss auf den statischen und dynamischen Magnetismus der Kupferatome haben. Insbesondere können die Temperbedingungen beeinflussen, welcher Sauerstoffplatz geleert wird. Es können sogar Cu Fehlstellen erzeugt werden die eine Unordnung des Systems erzeugen. Eine höhere Temperatur beim Tempern reduziert die O(2) Besetzung und erzeugt magnetische Unordnung während eine leicht niedrigere Temperatur nur die O(3) Besetzung beeinflusst und erstaunlicherweise keine Veränderung des Magnetismus hervorruft. Dies ist im Gegensatz zu der allgemeinen Auffassung, dass gerade dieser Sauerstoffdefektplatz verantwortlich für das Auftreten von Magnetismus und die Unterdrückung der Supraleitung in elektronendotierten Verbindungen ist. Andererseits können moderate Temperaturen bei der Reduktion Kupferfehlstellen ausheilen und Sauerstoff- und Kupferatome umverteilen und somit ein geordneteres System erzeugen. Davon unbeeinflusst zeigten sowohl die unbehandelten also auch die reduzierten Proben eine Serie von magnetischen Phasenübergängen. Dies ist noch eine weitere bemerkenswerte Beobachtung, da bisher keine direkten Beweise für Spinreorientierungsübergänge in T'-Pr_2CuO_4 berichtet wurden.

Contents

1 Introduction and Motivation

1.1 Magnetism

The word *magnetism* may not be a layman's term but its synonyms include *attraction*, *fascination*, *appeal*, *influence*, *pull*, *drawing power*, *captivatingness*, *magic*, *lure*, and the like. As a child, most of us had played with magnets and got amazed and fascinated with its power to attract iron objects. Its ability to exert forces at a distance, that is, it can move the iron objects without physical contact or material intervention, had intrigued one's young mind.

The early accounts of magnetism date back to the discovery of a naturally-occuring mineral called magnetite or lodestone around the 6th century BC by the ancient Greeks, who first observed magnetic phenomena through the attraction of lodestone to bits of iron ore and other lodestones. This then gave the first references to lodestone's magnetic properties. The etymological origin of the word *magnet* came from these lodestones found in Magnesia, a Greek town and province in Thessaly, northern Greece. Hence, magnet literally means *the stone from Magnesia* [1].

The first application of lodestone was first realized in the 12th century when the Chinese, who had also found this kind of rock, observed that if this rock is suspended on something that would let it spin freely, it would always rotate to point in the same direction, toward the magnetic poles. The part of the rock that pointed *North* was called the *North-seeking pole* or simply the *North Pole*. This was the first simple navigational compass.

Though various theoretical phenomena are yet to be further understood, known studies had already led to powerful pursuits, consequently unfolding technological developments that we are relishing today. Numerous magnetic materials are regarded as being indispensable in modern technology. One primary reason is that they are used as components in an enormous range of industrial, medical, and technological innovations. Added applications of magnetism and magnetic materials encompass those from micro- or nanoscale devices used for information or data storage in computers, to electrical devices such as transformers and motors utilized in electric power generation. Facilitating magnetic device architectures that cater to the increasing demand of storage and processing prototypes, sensors, permanent magnets, energy conversion and exploration, plus all the other advancements in research and development on this certain field, not only gave rise to relevant applications but had also revealed a wealth of new fundamental physics.

Over the past centuries, the research on magnetism was steadily progressing alongside the evolving ideas and enhancement of other fields like electricity and quantum mechanics. It had remained a great mystery in solids and had always been difficult to explain. One big reason is that its origin is quantum mechanical. Most magnetic effects are unexpected consequences of quantum-mechanical and collective interactions of assembly of electrons on vast scales with one another. Adding up to the challenge is the fact that magnetic ions interact with each other over given and sometimes, even large distances, and their response to external stimuli such as temperature, pressure, or applied field, tend to give more complexity in elucidating them.

Magnetic effects are enthralled by two relevant ingredients: first, atoms should have magnetic moments, and second, these moments should have interactions with one another [2]. Through a certain characteristic interaction, the collective behavior of the individual magnetic moments of the atoms can give rise to an ordered magnetic state. In solids, there are a number of different types of magnetic order such as those called as e.g. ferromagnetism, antiferromagnetism, and ferrimagnetism. Probably the ordering that one is most familiar with is the ferromagnetic type of ordering that is observed in iron and in rare earth elements such as gadolinium and dysprosium. Ferromagnetic ordering is manifested from the parallel alignment of the magnetic moments giving rise to a macroscopically observable magnetization. A rather different type is antiferromagnetic ordering in which the interaction between the magnetic moments tends to align the nearest-neighbor moments antiparallel to each other, such that the net spontaneous magnetization is zero. In addition, their response to applied external fields at a constant temperature is similar to that of paramagnetic materials, those that have randomly oriented moments. That is, the magnetization is linear in a small applied field and the susceptibility is small and positive [3].

The materials highlighted in this work are the parent compounds of the electron-doped cuprates. These are all antiferromagnetic insulators, materials that do not conduct electricity. However, these supposedly insulating materials surprisingly become metallic then turn into perfect conductors (came to be known as superconductors) when an adequate amount of electrons are added via chemical substitution, for example, substitution of Ce to Nd in Nd_2CuO_4. Hence, that is where the coined phrase 'parent compound of *electron*-doped superconductors' comes from.

As superconductivity is yet another phenomenon apart from magnetism that made a milestone to human exploits and curiosity, a brief introduction about it is a prerequisite into building up the relevance of investigating the antiferromagnetic parent compounds focused in this work. The succeeding paragraphs will briefly describe this.

1.2 Superconductivity

The quest for liquefaction of gases in the 19th century led to the development of methods to cool matter to extremely low temperatures. This feat prompted the discovery of superconductivity. The triumphant researcher to do this is H. Kamerlingh Onnes, a Dutch physicist who succeeded in liquefying helium in his laboratory in Leiden. This subsequently allowed him to do methodical measurements on materials such as mercury which can be made pure, and specifically observing how the resistance behaved when cooled to very low temperatures. His experiments in 1911 showed that when the mercury sample was gradually cooled below the boiling point of liquid helium which is at 4.2 K, the resistance of mercury precipitously disappeared [4, 5, 6, 7]. Hence, the remarkable discovery of superconductivity. Further explorations of this new phenomenon had been performed with samples of tin and lead which further confirmed that mercury was not unique.

As the phenomenon on superconductivity made a stir to the scientific research community, a number of experimental works had been performed that deliberately increased the number of superconducting elements that were unraveled. The two main factors for a material to be called a superconductor is firstly, it should exhibit a drop in resistivity to zero when cooled down below a temperature called the critical temperature [4, 5, 6, 7]. Above this critical temperature, the material is said to be in its normal state. Then secondly, another factor is that superconductors show perfect diamagnetism. This is also known as the Meissner-Ochsenfeld effect [8], the ability of the material to forcibly expel an applied magnetic field and is responsible for the incredible capability of superconductors to levitate above magnets (or for magnets to levitate above superconductors). This property had initiated deeper quest and theoretical efforts in understanding superconductivity.

The London brothers, Fritz and Heinz London, proposed a phenomenological theoretical advance in understanding superconductivity. They showed that a mathematical relationship can be used that is something like the phenomenon of electrical resistance by the well-known Ohm's law for ordinary metals. What they developed is a theory that was able to explain both the Meissner-Ochsenfeld experiment as well as the persistent current of Kamerlingh-Onnes [9]. Another important aspect of the theory of superconductivity had been phenomenologically achieved by the Ginzburg-Landau theory developed in 1950 by extending the London equations that was able to describe the thermodynamics of the fundamental properties of superconductors. This theory postulated the existence of a macroscopic wave function $\psi(\mathrm{r})$ which was equivalent to an order parameter, with solutions to ψ giving the London equations, and microscopic parameters called the penetration depth and the coherence length [10].

One of the most important experiment that directly paved the way to an explanation of superconductivity was observed on the isotope effect on the critical temperature of mercury. This was simultaneously and independently observed by the groups of E. Maxwell [11] and C. A. Reynolds *et al.* [12], both observed a decrease in T_c with an increase in isotopic mass. These experiments imply that the mass of a nuclei plays some role in the superconductivity phenomenon in a manner that it gives rise to what is known as lattice vibrations (phonons). The isotope effect observations allow for the assumption that the basis of superconductivity relies on electron-phonon interactions. A relevant assumption that later led to the development of the monumental theory by Bardeen, Cooper, and Schrieffer (BCS) [13, 14, 15]. The BCS theory provided a forthright explanation of superconductivity in terms of paired electrons known as Cooper pairs, that are formed resulting from the electron-phonon interaction in an energy shell $\hbar\omega_D$ (ω_D is the Debye frequency) around the Fermi energy ϵ_F.

As the periodic table provides an array of elements that may produce a yet undiscovered material to harness better application of superconductivity, a further breakthrough of elevating the critical transition temperature was needed. The then slowly stagnating confinement to low-temperatures phenomenon had gone to a reviving upheaval with the discovery of high-transition temperature (high-T_c) superconductivity in 1986 by Bednorz and Müller in the doped layered copper oxides La-Ba-Cu-O ceramics with a T_c of ~ 30 K [16]. Thereafter, similar materials which came to be commonly known as the cuprates were discovered to reveal superconductivity at high-T_c values, even reaching the highest critical temperature achieved so far at $T_\mathrm{c} = 133 - 140$ K, in Hg-based cuprates [17, 18, 19]. Interestingly, inducing high pressure in this compound could even augment the T_c to 164 K [20]. More recently, the cuprate monopoly in the high-T_c superconductivity pursuit was somehow interrupted when a new class of compounds known as the iron pnictides were discovered and unfolded new route for further research in the field [21]. These new class of systems share some common properties with the cuprates specifically for having layered crystal structures and exhibiting antiferromagnetic ordering in the mother compounds. Nonetheless, differences between the two classes are observed in their electronic and magnetic structures. Figure 1.1 shows the time evolution of the superconducting critical temperature of the different classes of compounds discovered since 1911.

The discovery of high-T_c superconductivity in the cuprates cannot be expounded by the

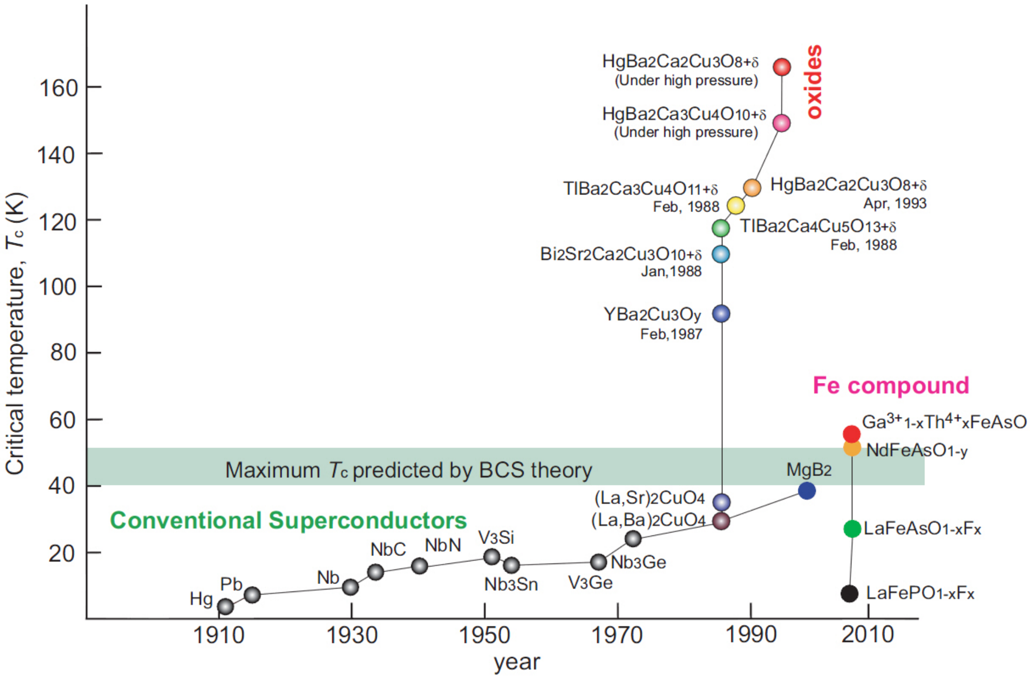

Figure 1.1: Time evolution of the superconducting critical temperature. The figure is adapted from Ref. [22].

BCS theory. In general, the underlying mechanism of high-T_c superconductivity is still under discussion. Hence, it is fundamentally indispensable to search for alternative theories, or perhaps a modified model of the BCS theory that can account for high-T_c superconductivity. Among these models are those that postulate polaronic mechanism that are reinforced by experimental findings, e.g. isotope effects and lattice effects in cuprates [23, 24, 25]. There is also a debatable viewpoint that magnetic spin fluctuations play a role in the emergence of superconductivity. Thus, one of the core topics in the research on high-T_c superconductivity is the relationship between magnetism and superconductivity. Corroborating evidence towards understanding the relationship between these two ground states is steadily ascending, primarily deliberating as to whether this relationship is cooperative or competitive.

In addition, there are structural requirements for superconductivity which influence their magnetic and transport properties. Looking closer into the crystal structure has initiated detailed understanding that could lead to the discovery of possible superconducting materials, giving a wider playground of several systems that could ultimately give answer and explain the true mechanism for superconductivity.

The engineering and design of these materials geared toward applications for energy primarily as a good current carrier, not only deals with the battle of increasing the critical temperature T_c, but of yet another important parameter called the critical current density J_c. Ultimately, scientists aim to have a material that superconducts at room temperature with superb current-carrying density. What isolates a superconductor from the usual conductors we normally have is that a wire made of superconducting coils does not heat up, hence, avoiding power loss. This would revolutionize and maximize energy and future technology. But presently, despite experimental progress, a satisfactory theoretical explanation remained elusive, keeping the need and high demand for thorough attention and research on these materials both theoretically and experimentally.

1.3 Motivation of the thesis

Understanding the mechanism of superconductivity may be a long-term coup but part of the momentary motivation is the challenge of investigating the interesting magnetic behavior of these complex systems. Various experiments and numerical calculations on different systems are aimed at exploring magnetic effects and its enigmatic role that affects and interplays with superconductivity. The copper oxides, or commonly known as the cuprates, are perpetual example. The common constituent within these certain ceramic oxide perovskites is the square planar copper-oxygen layers separated by charge reservoir layers which varies from material to material. By tuning the chemical composition of the charge reservoir layers, one can modify the density of charge carriers on the copper-oxygen sheet. These charge carriers may be holes or electrons. Thus, the cuprates can be classified as either hole- or electron-doped [26].

In these cuprate systems, interactions between electrons significantly lead to phenomena that has led researchers to wide-ranging quest to comprehend. Such phenomena include spin and charge (stripe) order, superconductivity fluctuations, proximity to a Mott insulator, a pseudogap phase and quantum criticality which is frequently an ardent topic for discussion, to name a few.

As previously described, it is a widespread knowledge that charge-carriers induced by doping the CuO_2 planes of the undoped antiferromagnetic Mott insulator enhance and lead to superconductivity. The so-called generic phase diagram of the cuprates is asymmetric with respect to electron- and hole- doping [27] as shown schematically in Figure 1.2. A remarkable theory of high-T_c superconductivity has to thoroughly explain the occurring similarities and differences when the copper-oxide plane is doped by holes or electrons. While for the hole-doped compounds there is already a stockpile of experimental data available, the electron-doped side of the phase diagram still needs experimental scrutiny. The diffi-

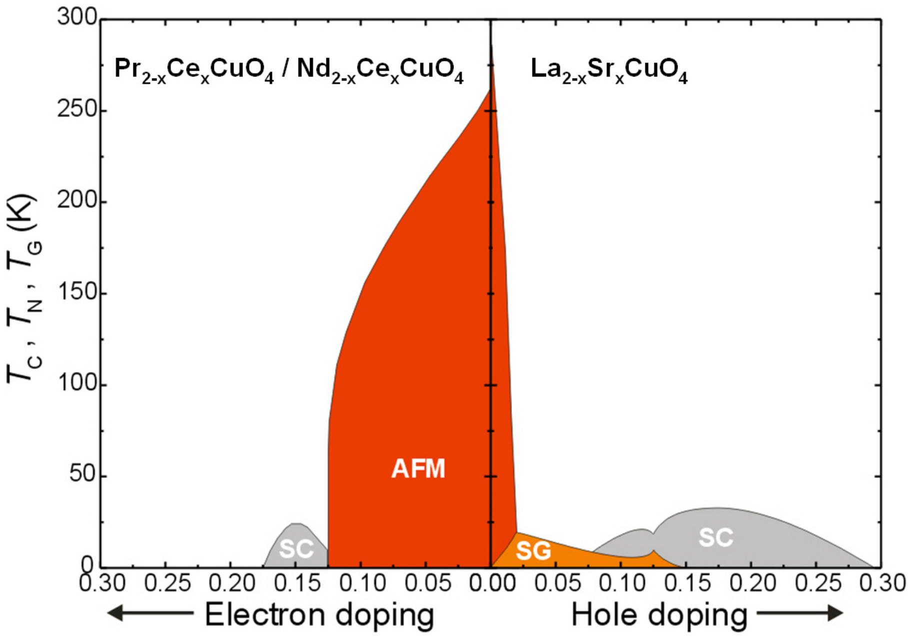

Figure 1.2: Generic phase diagram of the typically-studied cuprates.

culty in the sample synthesis accounts for this lack of database on these materials. Studies on electron-doped systems have been done and mainly identified on systems containing magnetic rare-earth ions like in $Nd_{2-x}Ce_xCuO_4$ [28, 29, 30, 31, 32] and $Pr_{2-x}Ce_xCuO_4$ [28, 32, 33]. In these systems, it was found that the Cu magnetism is much more robust against doping than e.g. the one of the prototype hole-doped superconductor $La_{2-x}Sr_xCuO_4$ and that superconductivity only sets in at higher doping levels accordingly. The symmetry or the lack thereof, between doping with electrons or holes has theoretical signification as simple models inherently assume symmetry. Figure 1.3 shows a more recently modified phase diagram with the thin film studies of $La_{2-x}Ce_xCuO_4$. This gave a larger window for the superconducting dome that eventually resulted to a more symmetric picture of the phase diagram [34]. However, there is still a lack of LCCO thin films in the low-doping range. This motivates the search for bulk samples which, in addition, has the advantage that one can perform, e.g. neutron scattering, to determine oxygen occupation which, as it will be discussed below, has a major effect on magnetic and superconducting properties of the specimens.

Another criterion that influences superconductivity in these RE_2CuO_4 systems is the oxygen content. In their as-grown state, the electron-doped materials display antiferromagnetic order ubiquitously in the accessible doping range. It had been established that not only adding charge carriers will drive superconductivity but rather an oxygen reduction treatment is equivalently necessary to induce superconductivity. It will be shown in this work that

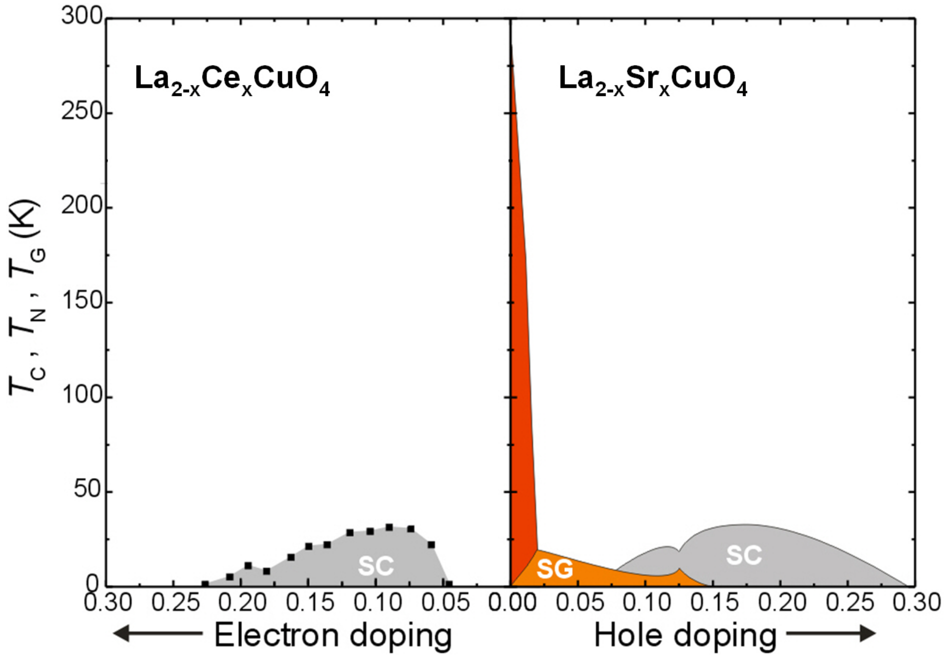

Figure 1.3: Phase diagram of La-based cuprates. The data points in the superconducting dome of the electron-doped side are obtained from resistivity measurements of Tsukada *et al.* [34] on thin films of LCCO.

the reduction process also has influence in the magnetic properties of the undoped mother compounds.

As a general overview in this thesis, the magnetism of the rare-earth cuprates mother compounds are studied primarily using the muon spin rotation and relaxation (μSR) technique. Complementary experimental studies were also done with NMR and neutron scattering techniques. One of the highlighted compounds is the novel T'-La_2CuO_4. As most T'-structures, this is a very suitable candidate compound for electron doping. This would be more straightforward primarily because the complexity due to a magnetic rare-earth ion is eradicated in this compound as La is non-magnetic. A step higher is a study of the effect of inclusion of a magnetic rare earth ion, e.g. $La_{1.85}Sm_{0.15}CuO_4$ which might modify the magnetic coupling in the c-direction. In addition, the influence of the oxygen removal was also investigated in the said compound. Moreover, in this work, interesting findings on the magnetic properties and structures on another rare-earth T'-cuprate, the Pr_2CuO_4, are presented and discussed. Specifically, the effect of oxygen annealing conditions were investigated on the Pr_2CuO_4 compounds. From the gathered experimental data from muon spin rotation, observations reveal their magnetic structures and indications for spin reorientation transitions.

2 Structural, Electronic, Magnetic, and Superconducting Properties of Rare-Earth Cuprates

This chapter is intended to introduce the needed theoretical backbone for the discussion of results in the succeeding chapters. Hence, it would be selective and topical. As one looks at a generic phase diagram of cuprates, one must follow a certain trend to systematically understand how the electronic structure changes with doping. This means, one has to carefully and precisely map the phase diagram by initially studying the undoped compound and progressively into the doped ones. Prior to that, the structural properties has to be well-described in order to have a physical picture to eventually infer how the magnetic and superconducting properties interrelate with it. Focus is also given to the CuO_2 plane as this is the primary playground in the interplay of different mechanisms within the system. Richer interactions are exhibited as these rare-earth cuprate systems are not simply two dimensional but are rather made of stacks of planes called perovskites, specifically, these are tetragonal systems. Additionally, rare-earth ions spice up the already complicated interpretation of the magnetic interactions involved. Albeit complexity, a number of possible mechanisms are suggested in which the quantum nature of the Cu spins and the underlying interactions with weak anisotropies and interplanar couplings bring about magnetic structures that define the magnetic properties of these systems. It is imperative to at least qualitatively understand to what could be attributed the magnetic ordering and the observed characteristics of each compound.

2.1 Structural Properties of T'-RE$_2$CuO$_4$ Cuprates (RE= La, Pr, Nd, Eu)

A particular interest on the comparison on the phase diagrams for hole- and electron- doping in cuprates conjointly aims to replenish the lacking database of the electron-doped materials and to understand the still unresolved mechanism of superconductivity. Since the discovery of electron-doped superconductors in 1989 [35], the parent compounds T'-RE$_2$CuO$_4$ (RE: rare-earth) of these systems were likewise intensively studied based upon the idea that understanding these compounds would shed light to knowing the mechanism as these systems turn superconducting as a function of doping. The magnetism and conductivity of lanthanum cuprates are incessantly the focus of interest in numerous theoretical and experimental scientific exploits. This section will elaborate the crystallographic properties of the parent compounds of the electron-doped superconductors.

The lanthanoid cuprates has customarily two different crystal modifications: the K_2NiF_4 structure (T-phase) and the Nd_2CuO_4 structure (T'-phase). The underlying feature that differentiate these two structural modifications is the absence of the apical oxygens below and above the Cu ions of the CuO_2-plane in the T'-phase. The T'-phase is determined to crystallographically have the Nd_2CuO_4 structure (space group I4/mmm, no.139). Here, the copper ions form CuO_4 squares and are not octahedrally-coordinated as in the T-structure. On the other hand, the structure of the T-La_2CuO_4 is congruous to the tetragonal K_2NiF_4-structure but known to be monoclinically (space group Bm11, no. 8) or orthorhombically(space group Bmab, no. 64) distorted [36, 37]. There is also another structure called the T^*-structure with CuO square pyramidal sheets, having an identical metal-atom positions as those in the K_2NiF_4 or Nd_2CuO_4, except for the order of the cations Nd(Ce) and Sr [38]. This would not however be elaborated here. Figure 2.1 shows the comparison of the two aforementioned structures. As already stated, the most obvious difference is the octahedral copper environment in the T-structure compared to the planar fourfold coordination in the T'-structure. Furthermore, due to the missing apical oxygen, the T'-structure has a clearly shrinked c-axis lattice parameter.

The determining criterion deciding which of the structures is formed is the ionic radius of the Ln^{3+} ion. The T-phase is formed by the La^{3+} ion, which has a large ionic radius, while the T'-phase is formed by the Ln^{3+} ions having smaller radius (Ln= Pr, Nd, Sm, Eu, and Gd) [40, 41, 42]. Though there is an added impediment on the synthesis of these T' systems since it has been observed that the ionic size of the rare-earth ions affects the stability of the T' phase, as evident from the distorted structure of Gd_2CuO_4 [43], a novel synthesis

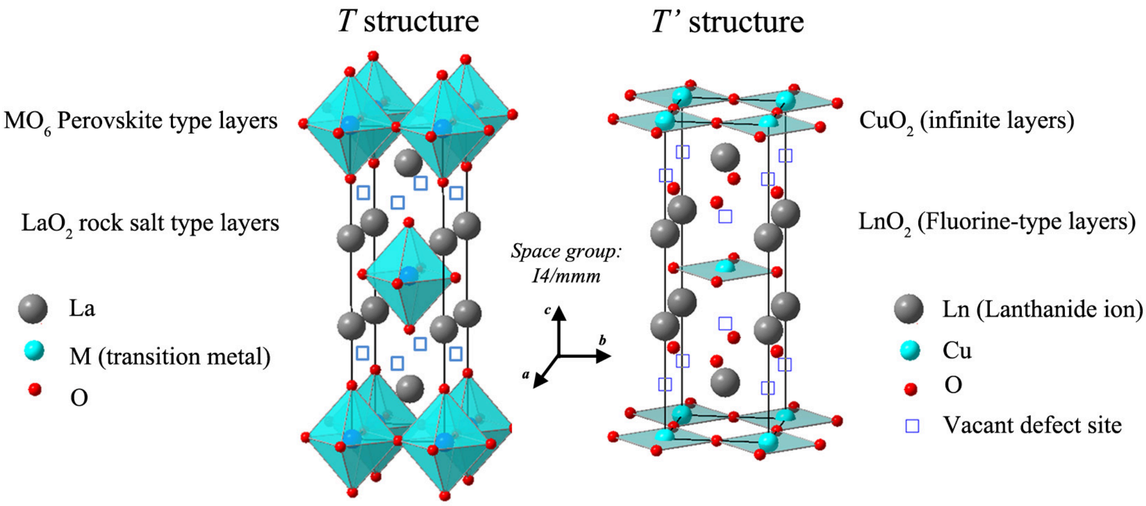

Figure 2.1: Comparison of the T- and T'-structure of La_2CuO_4. The figure is adapted from Ref. [39].

method has to be formulated and tested to aim for structural stability. So that even there is the boundary between La^{3+} and Pr^{3+}, and systematic synthesis for T'-Pr_2CuO_4 is already established, this might make it possible, nonetheless, to produce a metastable La_2CuO_4 in the T'-structure which rather requires a more complicated and unconventional synthesis route since the radius of La^{3+} is near to this boundary.

The profound interest in the different crystal structures of La_2CuO_4 from the perspective of high-T_c superconductivity lies in the foregoing knowledge that the T-phase can be hole-doped e.g. by Sr, and the T'-phase can be electron-doped e.g. by Ce. There is currently no single cuprate system that can be made superconducting by both electron- and hole-doping. $La_{2-x}M_xCuO_4$ with M= Sr in the T-phase for hole doping and M = Ce in the metastable T'-phase for electron doping, is a promising and an ideal compound that could satisfy this fundamental aim which could eventually give a clearer picture on the symmetry of the high-T_c cuprates generic phase diagram. Evidently, it would be the best option to have a direct comparison of T-La_2CuO_4 and T'-La_2CuO_4 to subsequently come up with a more suitable discernment of the intrinsic magnetic and superconducting properties of their hole- and electron-doped derivatives.

It was a challenge to synthesize the undoped T'-phase mother compound and low-doped $La_{2-x}Ce_xCuO_4$ with Ce-doping as low as about x= 0.05, due to the structural instability of the T'-phase as it deteriorates back into the T-structure even in epitaxially stabilized thin films [34]. Only recently, bulk T'-La_2CuO_4 has been synthesized at moderate temperatures from cesium hydroxide fluxes [44] and from sodium or potassium hydroxide fluxes [45, 46, 47, 48]. Having this compound is a step forward in the hope to better compare similar compounds on both sides of the phase diagram. The use of a nonmagnetic rare earth La-ion also simplifies the complexity in understanding the basic magnetic interactions that underlie within the CuO_2 layer. Moreover, the substitution of La^{3+} by smaller Ce^{4+} should sustain the stability of the T'-phase, henceforth, adding our database for the electron-doped cuprates.

2.2 Electronic Structure of the Cuprates

The cuprates parent compounds are essentially not standard band-theory insulators but rather what are called the Mott insulators [49]. The primary contributor to their magnetic and electronic properties is the CuO_2 layers, that results from the strong hybridization between the Cu and O orbitals. The Cu^{2+} ions has nine 3d-electrons out of a maximum number of ten. It implies that the orbital having the highest energy is *half-filled*. This is the $3d_{x^2-y^2}$ orbital because of tetragonal crystal field [50]. A simple band-theory prediction would point out that a half-filled electronic band at the Fermi level would be metallic. Yet, in a Mott insulator, the carriers are highly localized. Due to the strong Coulomb repulsion between two carriers, there is an energy cost U for them to stay on one site. This strong local Coulomb interaction prevents electron hopping from Cu to Cu (thus discourages double occupation), suppressing charge fluctuations, and the exchange correlation is antiferromagnetic in sign. Hence, the system is insulating because the carriers are immovable.

Now because of the presence of the O^{2-} ions and their valence orbitals, the case for the cuprates becomes a bit more sophisticated. According to Ref. [50], the $2p_\sigma$ are the relevant O^{2-} orbitals, that is, the in-plane orbitals that lie along the Cu-O-Cu directions, $\sigma = x, y$. Figure 2.2*a* illustrates this in a schematic diagram of the CuO_2 plane. In the cuprates parent compounds, the O $2p_\sigma$ orbitals are filled and the Cu $3d_{x^2-y^2}$ orbitals are half-filled [51].

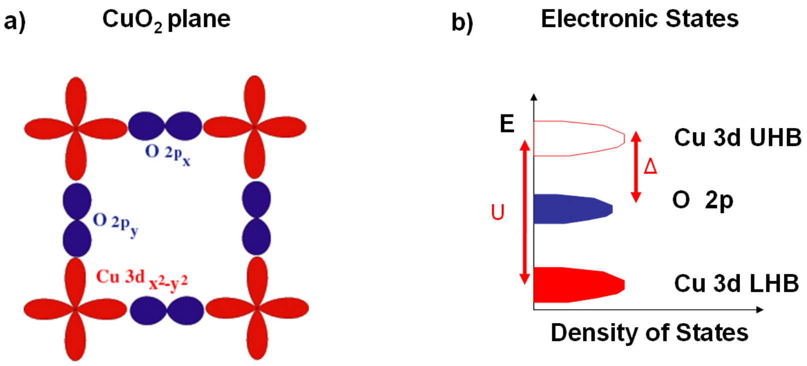

Figure 2.2: Schematic diagram for a) The CuO_2 plane, and b) the density of states in the three-band Hubbard model.

There is a model that is widely regarded to encompass the important low-energy electronic interactions in the CuO_2 plane and this is called the three-band Hubbard model [52]. Three band because it involves one copper orbital and two oxygen orbitals. Figure 2.2*b* displays the three-band Hubbard model. The half-filled Cu $3d_{x^2-y^2}$ band is split into a filled lower Hubbard band (LHB) and an unfilled upper Hubbard band (UHB). There is an energy gap between the two bands which is denoted as U, the on-site Coulomb repulsion. The O $2p_\sigma$ band lies in between the UHB and LHB Cu $3d_{x^2-y^2}$. This can imply that an electron from the filled oxygen orbital is easier to remove than one from the half-filled copper orbital. The Fermi energy is found between the oxygen 2p band and the UHB. The separation between the two bands is called the charge transfer gap, Δ, that is the energy it takes to transfer an electron from the oxygen to the copper. In other words, the energy to overcome for charge motion is the energy associated with the potential difference between Cu $3d_{x^2-y^2}$ and O $2p_{x,y}$ orbitals, and not the strong on-site Coulomb interaction on the Cu site. Hence, the cuprates are more appropriately referred to as charge-transfer band insulators. Since the Hubbard Hamiltonian is said to be the minimal model that includes the strong local interactions dominating these compounds, many theorists frequently and simply use the single-band Hubbard model. Here, one can consider the charge transfer gap Δ as the effective value for U:

$$H = \sum_{ij\sigma} t_{ij} c^\dagger_{i\sigma} c_{j\sigma} + U \sum_i n_{i\uparrow} n_{i\downarrow} \tag{2.1}$$

where $c^\dagger_{i\sigma}$, $c_{i\sigma}$, and $n_{i\sigma} = c^\dagger_{i\sigma}\ c_{i\sigma}$ are the creation, annihilation, and number operators, respectively, for an electron with spin (up or down) σ at site i. If $U \gg t_{ij}$ the single band is split into two, the so-called upper and lower Hubbard bands that are respectively unfilled and completely filled at half-filling.

The Cuprate Electronic Structure Upon Doping

Doping these insulating CuO_2 layers causes the emergence of new electronic ordered states including high-T_c superconductivity. The doped holes preferentially reside in what is called the *charge transfer band* composed primarily of oxygen orbitals, as illustrated in Figure 2.3. These holes have their own spin and frustrate the magnetic interaction between neighboring copper moments. This frustration significantly weakens the antiferromagnetic state.

On the other hand, doped electrons preferentially reside on the Cu $3d_{x^2-y^2}$ orbitals, as displayed in Figure 2.4. This only gradually weakens the antiferromagnetism since effectively electron-doping simply results to dilution of the spin system.

Since in this thesis, only the undoped magnetic mother compounds are investigated, I refer the interested reader to the review [53] for further reading. In the following, I will elaborate on the magnetism of the undoped cuprates.

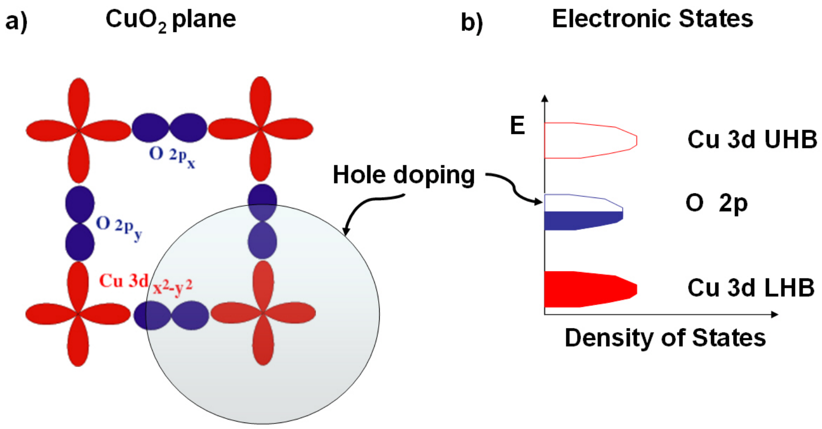

Figure 2.3: Holes are doped into oxygen 2p orbitals.

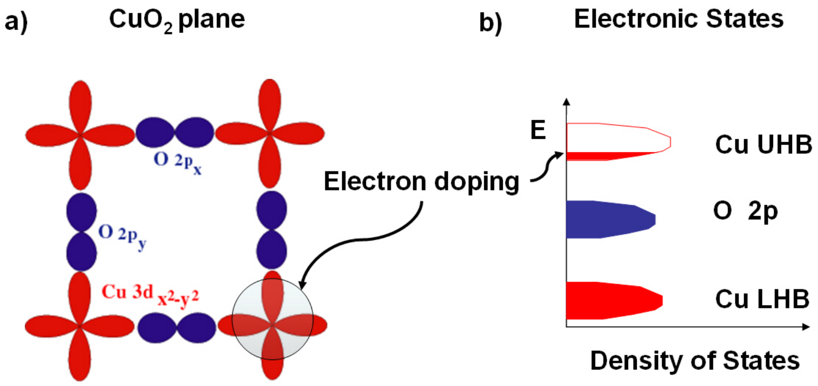

Figure 2.4: Electrons are doped into copper 3d orbitals.

2.3 Magnetism in Cuprates

A step towards coalescing the jigsaw-puzzle picture of the mechanism of superconductivity is to understand a piece of the puzzle, the simpler undoped lamellar copper oxide systems. As already established, T'-RE$_2$CuO$_4$ crystallizes in the tetragonal structure with CuO sheets that form a planar square lattice, in comparison to their hole-doped counterparts where the out-of-plane oxygens move to apical positions. The presence of the apical oxygen in the T-phase gives rise to an orthorhombic distortion that pave way to a weak Dzyaloshinskii-Moriya (DM) interaction, leading to weak ferromagnetism [54]. This makes the interactions in this phase a bit more complicated to decipher. On the other hand, this DM interaction is strongest after the direct in-plane exchange interaction and therefore governs the magnetic ordering of the T phase. As will be elaborated below, in the tetragonal T'-phase, where DM interaction is not present by symmetry, several weaker interaction compete and leave the system with a manifold of nearly degenerate ground states.

A combined field of interest of superconductivity and of lower dimensional quantum magnetism emerge. The latter was linked owing to the fact that the parent compounds of the cuprate superconductors like La$_2$CuO$_4$ are essentially antiferromagnetic Mott insulators with a system of interacting localized Cu^{2+} spins that conform to the rather good approximations to the simpler S= 1/2 two-dimensional (2D) square lattice Heisenberg antiferromagnet [55, 52]. In addition, they exhibit weak anisotropies and a relatively small coupling between the CuO$_2$ layers that result to the formation of a three-dimensional (3D) Néel-ordered state [56, 57, 58]. To date, a number of the best experimentally-studied systems in this category are the tetragonal systems such as the oxychloride Sr$_2$CuO$_2$Cl$_2$, Nd$_2$CuO$_4$ and Pr$_2$CuO$_4$. All of these CuO$_2$ systems are marked by a strong, nearly isotropic, nearest-neighbor exchange coupling *within* the sheets, that is, a fairly strong Cu-Cu exchange in the CuO plane. Then a much weaker exchange coupling *between* the sheets, i.e. a very small Cu-Cu interplane exchange interaction. Moreover, in the I4/mmm structure, the interplanar coupling is effectively reduced because the exchange interaction between the nearest-neighbor planes is frustrated [59, 60, 53], as will be shown in chapter 2.3.3.

The succeeding subsections will introduce plausible explanations governing the magnetic mechanisms in cuprates through published theoretical and experimental results. In order to have a clear understanding on the magnetism in cuprates, it would be best to firstly have a look at the intrinsic fundamental nature of the CuO$_2$ planes on a microscopic scale. Afterwards, the discussion will move a step forward by dealing with the magnetic interactions in the investigated body-centered tetragonal (BCT) systems. Then, there will be a discussion about resolving a question as to what happens when the system has magnetic rare-earth ions in it? What magnetic interactions and mechanisms govern such systems? What causes the spins to orient themselves in a certain magnetic structure? The last subsection would introduce some proposed magnetic structures and spin reorientation transitions in rare-earth cuprates.

2.3.1 The CuO_2 Plane

The most interesting features of the cuprates concerns the magnetism associated with the Cu ions, since superconductivity occurs in the 2-dimensional CuO_2 planes when doped with charge carriers. Generally, the cuprates are characterized by small ratios of J'/J, where J' is the exchange coupling between neighboring CuO_2 planes and J is the in-plane coupling constant. That is, the in-plane Cu exchange interactions are much stronger than along the c-axis, thus the magnetism is quasi- two-dimensional. The Cu^{2+} has a spin 1/2 magnetic moment and lowering the temperature can make the system order in a way that the neighboring Cu moments align antiparallel with each other which happens at astonishingly small temperatures compared to J. In this regard, the Cu spins provide one of the forthright physical realizations of a 2D quantum Heisenberg antiferromagnet.

Thus, the discussions herein about the magnetic properties of the studied undoped cuprate systems, will be generally derived and be frequently elucidated in the context of the Heisenberg model of antiferromagnetism on a square lattice for which the leading term of the Hamiltonian is:

$$\mathcal{H} = J_{ij} \sum_{<ij>} S_i \cdot S_j \tag{2.2}$$

where $< ij >$ indicates a sum over pairs of nearest neighbors, J_{ij} is the antiferromagnetic exchange constant between the i^{th} and j^{th} spins.

2.3.2 The Quantum Nonlinear Sigma Model

Motivated by the neutron scattering experiments by Endoh and coworkers in single-crystal La_2CuO_4 [56], Chakravarty, Halperin, and Nelson pioneered a theoretical model that predicts and describes the temperature dependence of the correlation length ξ and also the static structure factor peak intensity S(0) of the two-dimensional square-lattice quantum Heisenberg antiferromagnet for a general spin S [61, 62]. They exhibited that the 2D Heisenberg model can be mapped onto a quantum nonlinear sigma model (QNLσM) [62]. This is the simplest continuum model that can be solved in the low-energy, long wavelength limit. It uses finite temperature analysis consistent with the Hohenberg-Mermin-Wagner theorem

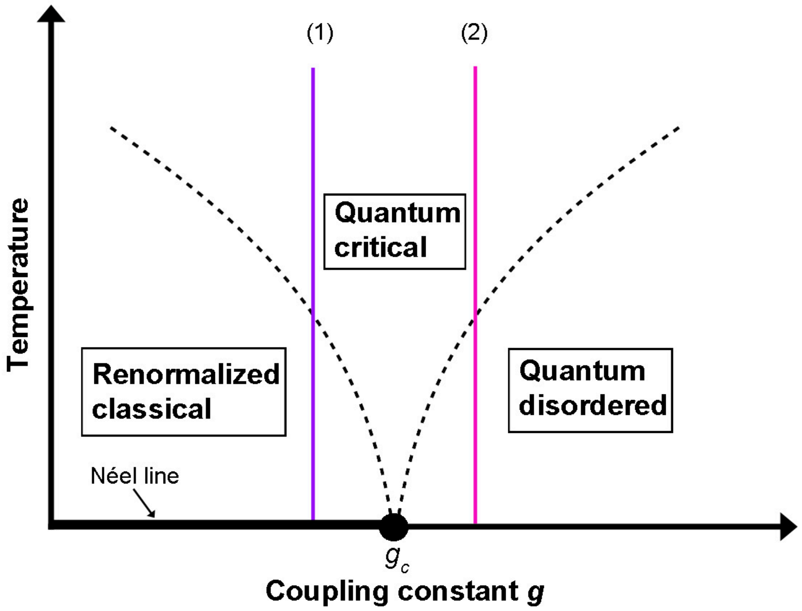

Figure 2.5: Phase diagram of the quantum nonlinear sigma model as a function of temperature and coupling parameter g. The thick line indicates antiferromagnetic order at $T = 0$. The figure was adapted from Ref. [51] and modified from Ref. [62].

[63, 64] in a hypothetical sense that rigorously shows that there is no true long-range order in a 2D Heisenberg system at any finite temperature T. However, the QNLσM predicts a long range order at $T = 0$ and with this assumption, the static and dynamic properties of the spin-$\frac{1}{2}$ Heisenberg antiferromagnet were derived [62].

The QNLσM describes the long-wavelength dynamics of a lattice Heisenberg model [62]. The two parameters involved are the spin stiffness, ρ_s and the spin-wave velocity c_s. The spin stiffness is the energy cost of putting in a small rotation angle θ between adjacent or neighboring rows in the ground state. This is defined as [65]:

$$\rho_s = \frac{1}{N}\frac{d^2E_0(\theta)}{d\theta^2}\bigg|_{\theta=0} \tag{2.3}$$

where E_0 is the ground state energy and N is the number of spins. For a classical Heisenberg in 2D or in the limit of large S, $\rho_s = JS^2$ [66, 62]. For a long-range ordered system, the spin stiffness has a positive value. Otherwise, it is zero in the absence of long-range order.

Figure 2.5 shows the phase diagram of the QNLσM as a function of temperature and the coupling parameter g$\sim \hbar c_s/a\rho_s$. The correlation length ξ functions differently in the different regimes. For the case when a long-range order at $T = 0$ is assumed, renormalization-group analysis results to an exponentially diverging correlation length as a function of temperature in the $T \rightarrow 0$ limit. Hence, the correlation length in the renormalized classical regime is [62]:

$$\xi = C_{\xi} a \exp(2\pi\rho_s / k_B T) \tag{2.4}$$

where a is the lattice constant, ρ_s is the actual spin stiffness at $T = 0$, that is, with the quantum fluctuations taken into account, and C_{ξ} is a dimensionless constant that depends on the choice of the system [62].

Taking large values of the dimensionless coupling constant g, there is a quantum disordered regime. At this regime, quantum fluctuations keep order from happening or arising even at $T = 0$. The result in such a case is that the correlation length ξ approaches a finite value as $T \rightarrow 0$ [62, 51].

The two regimes are separated by a quantum critical point, at $T = 0$. A power-law dependence of the correlation length is anticipated at the critical coupling g_c, $\xi \propto T^{-1}$. At a region close to g_c, the correlation length crosses over between different behaviors as a function of temperature. As the temperature is lowered, along path (2), see pink line in the phase diagram in Figure 2.5-within the quantum disordered regime close to g_c- the correlation length will become essentially temperature independent as it crosses the crossover line. Along the path (1), see purple line- within the renormalized classical regime close to g_c- the correlation length will diverge exponentially once it crosses the crossover line [62].

The mother compounds for the electron-doped cuprates have distinguishable properties from other antiferromagnetic cuprates. Having a tetragonal structure where Cu^{2+} ions form a body-centered lattice, the Cu^{2+} ions in the adjacent CuO_2 planes do not interact in the mean field approximation with the assumption of a conventional isotropic exchange coupling. Thus, there are some weak interactions that are manifested which may be masked in other cuprate systems. Although comparisons with theoretical predictions [62] point out that the Heisenberg model well-describes the magnetic properties of the cuprates, some of the observed magnetic features depend on more subtle interactions, e.g. bond-dependent anisotropic exchange interactions, that require more explanation and thorough understanding. This will be further discussed in the succeeding sections.

2.3.3 Frustrated Body-Centered Tetragonal Systems

A familiar feature in many magnetic systems proves that microscopic interactions can give rise to phenomenal emergent behavior such as frustration. This happens when competition between different interactions of competing strength with the influence of certain lattice symmetries, lead to a scenario where the energy of the spin bonds in the system cannot be minimized simultaneously. This means that the resulting configurations minimize the energy of the entire system, but not all the energies of interaction between one spin and its neighbors. Consequently, this frustration results to degenerate ground states. It is customary idea that order cannot arise from disorder. However, the lifting of degeneracy in these frustrated magnetic systems make the system more ordered and this can remarkably be achieved by disorder (thermal or quantum fluctuations), a phenomenon referred to as *order by disorder* [67]. This theme recurs in varied condensed matter systems, from a simple nearest-neighbor Ising antiferromagnet on a triangular or a face-centered-cubic (fcc) lattice [68, 69, 70], to layered systems i.e. quintessential examples include the cuprates, with several competing orders including high-T_c superconductivity and magnetism.

A large number of frustrated magnetic systems show that *order by disorder mechanism* should exist in many quantum systems with a classically degenerate ground state. In a body-centered cubic lattice (BCC) in which spins exhibit a strong second neighbor interactions and weaker neighbor interactions, such a geometrical arrangement ensures that the classical exchange field at any site on one sublattice due to the spins in the other sublattice is zero. Hence, effectively now having two simple cubic antiferromagnetic sublattices that are decoupled in the mean field sense. The energy is independent of the value of the angle θ between the two sublattices. [71]. This is exhibited in Figure 2.6.

Henley provided a simple physical explanation to the tendency of the system toward collinear ordering by quantum fluctuations [73, 74]. Specifically, his arguments include what happens when external fields $\mathbf{h}_i$ are applied to an antiferromagnet. Figure 2.7 schematically illustrates that with uniform $\mathbf{h}_i$, the fixed-length spins in each sublattice will prefer to be transverse to the field since they can gain energy by relaxing towards it. This occurs since there is no net coupling of the field to the ground state in first order [72];

$$\sum_{i}^{N} \mathbf{h}_i \cdot \mathbf{S}_i = 0 \tag{2.5}$$

Because of quantum disorder (fluctuations), the exchange field acting on (for example) the even sublattice has a random fluctuating odd component from the odd sublattice as illustrated in Figure 2.7 [72].

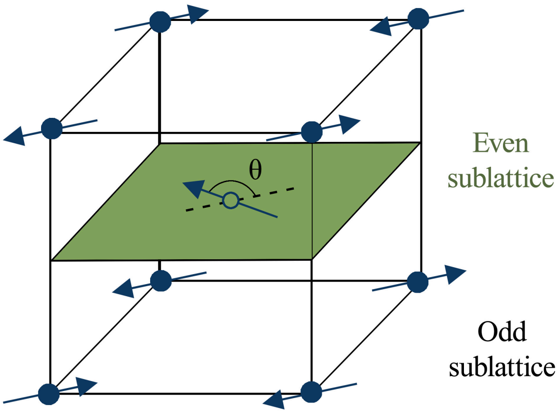

Figure 2.6: Two antiferromagnetic sublattices on a BCC lattice. Note that the mean field due to spins in one sublattice (i.e. spins at the corners shown by filled circles) on the spins in other sublattice (i.e. spin at the center shown by open circle) is zero. Therefore in the classical limit, the energy of the system is independent of θ, resulting an infinite degenerate ground state manifold. Reproduced from Ref. [72].

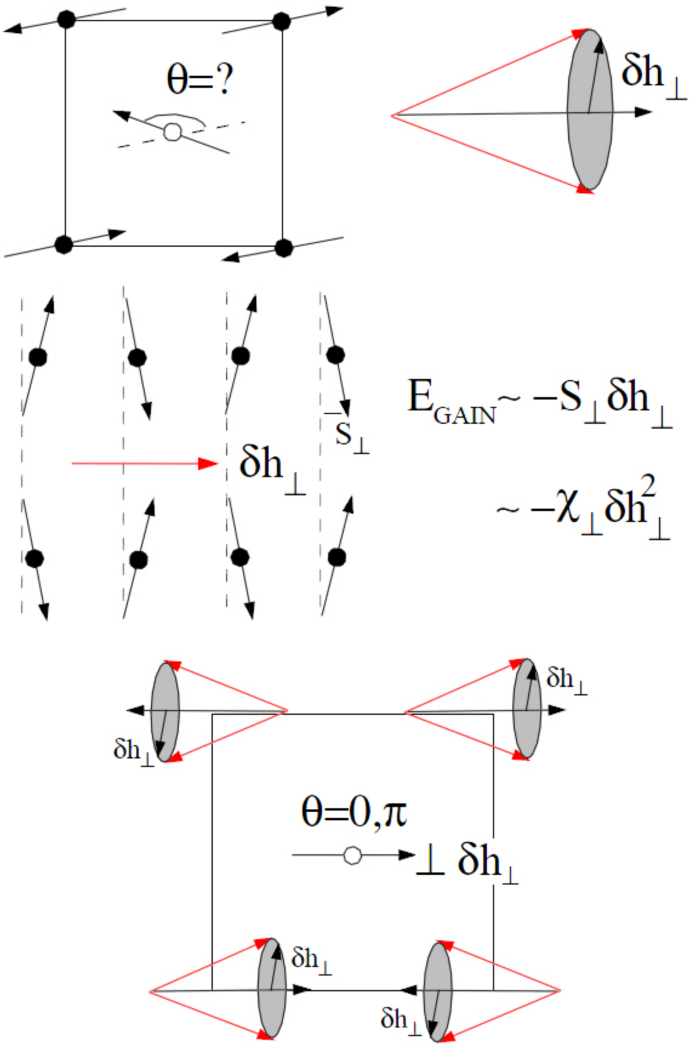

Figure 2.7: A schematic illustration of *ordering by disorder*. Top right figure shows the quantum zero point fluctuations which give rise to a random field $\delta h_\perp$ perpendicular to the direction of the ordered moment. On the middle we show how an antiferromagnet orients itself to an external field. On the bottom, we consider the fluctuating component of the spins in one sublattice as an external field acting on the spins in other sublattice. This leads to collinear ordering by zero-point fluctuations of the spins. Reproduced from Ref. [72].

2.3.4 3D Ordering in (BCT) Rare-Earth Cuprates

The magnetism in a body-centered tetragonal (BCT) structure is dominated by a strong antiferromagnetic inplane Cu-Cu exchange interaction with a coupling constant J. The magnetic interaction perpendicular to the planes (J') is very much reduced. This is because the isotropic exchange between nearest-neighbor CuO_2 sheets in these systems is fully frustrated as discussed in the previous chapter. That means, in a tetragonal symmetry, the mean field exerted by one CuO_2 layer on an adjacent layer vanishes. Therefore, this system can be considered as a very good approximation of the S= 1/2 two-dimensional (2D) square lattice Heisenberg model which does not possess a magnetic phase transition at finite temperature. According to the Mermin-Wagner theorem [64], it is forbidden for a 2D system with a continuous order parameter to have a symmetry-breaking transition (e.g. to antiferromagnetic order) at a non-zero temperature. The undoped cuprates, however, exhibit 3D magnetic order. The three-dimensional magnetic ordering in body-centered tetragonal (BCT) structures, which happens at a rather low temperature compared to J and the actually realized magnetic structure is therefore governed by subtle interactions like bond-dependent anisotropic exchange, in-plane anisotropy arising from quantum zero point energy, easy-plane anisotropy due to a combination of spin-orbit and Coulomb interactions, biquadratic exchange, and direct Cu-Cu magnetic dipole interactions [71]. Due to the tetragonal symmetry at the Cu sites, the dominant spin-spin anisotropy is the XY symmetry [71]. The combination and competition of these small interactions determines the relative ordering of the spins in neighboring planes and the orientation of the Cu spins within the easy plane. The breaking of the XY rotational invariance is especially noteworthy since the S= 1/2 Cu does not allow for a single ion anisotropy.

In the commonly-studied orthorhombic T-La_2CuO_4 (T-LCO), an orthorhombic distortion of the lattice breaks the tetragonal symmetry, partially lifting the interplanar frustration, and the transition was accounted for by the finite coupling between planes and by the antisymmetric spin exchange anisotropy [54]. The latter anisotropy is absent in tetragonal lamellar systems but rather contain several novel anisotropies. For the body-centered tetragonal (BCT) cuprates, there exists frustration of the interplanar coupling. In a lot of cases such as for the Nd_2CuO_4 [59], the exchange interaction between adjacent CuO_2 planes is as low as $J' \sim 10^{-8}\, J$ which is rather too small to drive the observed transition to three-dimensional order [51]. The ordering is rather fostered by the XY anisotropy that arise in the systems due to spin-orbit coupling. As the temperature is lowered, this anisotropy causes a crossover from 2D Heisenberg to 2D XY correlations [51]. In a magnetic system with XY anisotropy, the inplane spin fluctuations behave differently from out of plane spin fluctuations. This paves way to what is referred as a Kosterlitz-Thouless transition [75], a non-symmetry-breaking order, in which the correlation length in the planes starts to diverge [59, 76, 51]. Thus, in a case when this correlation length is sufficiently large, the otherwise weak interplanar coupling causes three-dimensional order.

Since it was assumed that the CuO_2 planes are not very different in the T'-RE_2CuO_4 rare-earth cuprates and in the tetragonal compound oxychloride $Sr_2CuCl_2O_2$ (SCCO), it is as well essential to point out some experimental investigations on this analogue compound that are also believed to be candidate electron-doped compound. The similarities lie on the fact that the anisotropy of the Cu-Cu exchange is the same in the T'-RE_2CuO_4 as in SCCO [77, 55]. Single-crystal X-ray diffraction studies confirm the body-centered-tetragonal (I4/mmm) K_2NiF_4-type structure of this compound [78, 79]. It has CuO_2 planes similar to the orthorhombic T-La_2CuO_4 but has the difference of having the out-of-plane oxygens replaced by Cl and the La by Sr. It does not then exhibit the out-of-plane canting seen in T-La_2CuO_4 related to the tetragonal to orthorhombic transition. The Cu^{2+} S=1/2 magnetic moments order in 3D below $T_N \simeq 260$ K- along the [110] crystal direction [80] in a collinear structure. Good thing about $Sr_2CuO_2Cl_2$ is that it remains tetragonal even at low temperatures and has larger interplanar lattice spacing compared to T-La_2CuO_4 making it an ideal prototype material of a two-dimensional spin-1/2 Heisenberg system.

As a recapitulation, the underlying features of the Cu subsystem of the BCT cuprates remain the same as the other cuprates without magnetic ions such as the orthorhombic T-La_2CuO_4 (LCO)[81] and $Sr_2CuO_2Cl_2$ (SCCO) [82], (i.e. there is strong intraplane coupling and weak interplane exchange interactions resulting to a low-temperature antiferromagnetic long-range ordering of Cu spins that is characteristic of quasi- 2D Heisenberg antiferromagnet).

In contrast, the cuprates which include a magnetic (NCO) or nearly magnetic (PCO) rare earth element in their structure possess qualitatively very different magnetic structures from the above mentioned compounds. This suggests that the interaction of the Cu and the rare earth (RE) subsystems greatly modifies their magnetic properties. Further quantification of the role of the RE-RE interaction has to be done in these systems although it is understood that the RE ions exhibit magnetic moments that are primarily induced by the exchange field of the Cu ions [59]. Thus, the weak pseudo-dipolar interaction which derives from this slight polarization of the magnetic RE angular momenta by the antiferromagnetic ordered Cu spins plays an important role for the actually realized spin structure [83]. Unlike in the orthorhombic T-LCO and SCCO, the rare-earth cuprates prefer a noncollinear arrangement of Cu spins which seems to be attributed to the presence of the magnetic rare-earth ions [84].

2.3.5 Rare-Earth Magnetism in Cuprates

The magnetic interactions in rare-earth (RE) cuprates T'-RE$_2$CuO$_4$ (RE= Pr, Nd, Eu) crystallizing in the tetragonal structure, have been the subject of various studies. Specifically because, rare-earth (RE) cuprates demonstrate atypical but riveting magnetic behavior involving both the copper and rare-earth spin subsystems which exhibits a large single-ion anisotropy. Electron-doped cuprates parent compounds are consisting of a rare-earth sublattice and a copper sublattice. Typically, compounds with rare-earth and a transition metal (e.g. Cu) are distinguished by intrinsic properties governed by exchange interactions and magnetocrystalline anisotropies. The exchange interactions occur between all unpaired RE-4f and Cu-3d electrons. In rare-earth cuprates, there are three types of interactions, namely, the RE-RE, the Cu-Cu, and the RE-Cu interactions. The large magnetic moments that can exist at the rare-earth sites and their response to the local crystal field determines the magnetism of the RE system. Significantly, the different magnitudes of the magnetic moments of the rare-earth ions lead to different magnetic structures.

Table 2.1: The magnetic properties arising from RE moments. The RE effective moment is from a fit of the high-temperature susceptibility to the Curie-Weiss law while the ordered moment is estimated at low temperature from 0.4 to 10 K mostly from neutron-scattering experiments. The Néel temperature corresponding to the magnetic ordering of the RE moments was determined using specific heat. Compiled by Armitage *et al.* [53] from the works of [85, 59, 86, 87] and references therein.

	PCO	NCO	SCO	ECO	GCO	PLCO
J	4	9/2	5/2	0	7/2	-
Effective moment Curie-Weiss	$3.65\mu_B$	$3.56\mu_B$	$0.5\mu_B$	$0\mu_B$	$7.8\mu_B$	-
Ordered moment measured	$0.08\mu_B$	$1.23\mu_B$	$0.37\mu_B$	$0\mu_B$	$6.5\mu_B$	$0.08\mu_B$
RE Néel temperature (K)	-	1.7	5.95	-	6.7	-

Table 2.1 presents the estimated magnetic moment of the commonly used rare-earth ions in the electron-doped cuprates. It could be that the strong coupling of the rare-earth ion to the Cu spin sublattice results to successive spin reorientation transitions. A typical example is the Nd magnetic moments which is known to enlarge in decreasing temperature because it is a Kramers doublet [88]. This temperature-dependent complex interaction of the Nd ions with the Cu sublattice has a striking implication to the low-temperature properties that

characterize pairing symmetry [53]. In addition, the strong anisotropy of the structure and the presence of some defects complicate the interpretation of experimental results. Consequently, it is of fundamental importance to thoroughly look into the nature of magnetic interactions which determine the three-dimensional (3D) magnetic structure.

2.3.6 Cu Spin Reorientations in Nd_2CuO_4 and Pr_2CuO_4

As already pointed out, for most of the case of the electron-doped cuprates having rare-earth ions, it was observed that additional magnetism originates from the large magnetic moments that can exist at the rare-earth sites. This can also imply that for different rare-earth ions, it will exhibit different spin magnitudes that lead to different magnetic structures, some of which with well-defined order [53]. The reader is referred to the review of Lynn and Skanthakumar [87] for more details on the magnetism of the rare-earth ions on these compounds.

For the case of Nd_2CuO_4, it was known early on that the moderately large magnetic moment of the Nd ion couples to the Cu spins sublattice [89, 90]. It is believed that this effective RE-Cu interaction is responsible for the two spin reorientation transitions between noncollinear magnetic structures that have been observed as a function of temperature for Nd_2CuO_4 [91, 92, 59, 93, 94, 60, 95] with the Nd ion possessing a magnetic ground state. In fact, the reordering and the low temperature interaction of the Nd and Cu were first observed by muon spin rotation and relaxation by Luke and coworkers [31] that were later confirmed by other techniques such as crystal field spectroscopy [96] and ultrasound propagation experiments [97]. These transitions are observed in neutron scattering as sharp changes of intensity for specific Bragg reflections, as shown in Figure 2.8.

As temperature decreases, these reflections reveal a growing interaction between the Cu and the Nd spins [53]. A so-called phase I noncollinear magnetic structure is first exhibited as Cu spins order below $T_{\mathrm{N1}} \approx 276$ K. At lower temperatures, there are two other successive spin reorientation transitions which are at $T_{\mathrm{N2}} = 75$ K and $T_{\mathrm{N3}} = 30$ K. At T_{N2}, the so-called phase II come about wherein the Cu spins rotate by 90° about the c-axis and the rotation direction is opposite for two successive Cu planes. Then at T_{N3}, phase III occurs wherein they realign back to their initial direction. Thus, making phase I and III identical with the difference that the Nd magnetic moment had grown larger at low temperatures because it is a Kramers doublet. Figure 2.9 illustrates these phases of NCO spin configurations at the characteristic reorientation temperatures. Lastly, an additional Bragg intensity is observed below 1.7 K originating from the antiferromagnetic ordering of the in-plane oriented Nd moments. This characteristics at low temperature indicates the presence of substantial Nd-

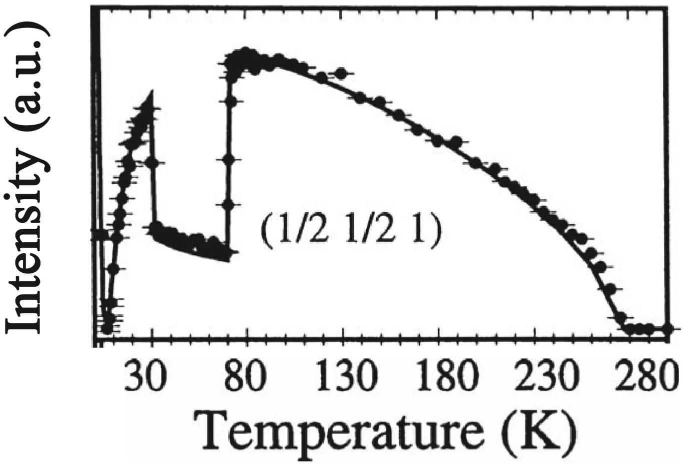

Figure 2.8: Elastic neutron-scattering intensity as a function of temperature at the (1/2 1/2 0) reciprocal space position for as-grown Nd_2CuO_4.The figure is reproduced from Reference [87].

Nd interaction on top of the Nd-Cu interactions that define the transitions at T_{N2} and T_{N3}. Thus, the sequence of spin reorientations in NCO is inferred by competing Nd-Nd, Nd-Cu, and Cu-Cu interactions.

Sachidanandam and coworkers [60] have shown that the dominant interactions is the Cu-Nd interactions that are between nearest neighbors. These interactions cannot be the usual isotropic exchange interactions because in such a case, the exchange field on a Nd ion would vanish when summed over the neighboring plaquette of Cu ions [60]. Consequently, anisotropic interactions, such as dipolar interactions, are instead considered [98]. However, the dipolar interaction has the wrong algebraic sign that it cannot elucidate the low temperature phase of NCO. Moreover, the magnitude of the dipolar interaction is rather small to be relevant in this context [60]. Thus, it is inevitable to introduce a pseudodipolar interaction that results from the anisotropic component of the Nd-Cu exchange interaction [71]. The dominance of this interaction then reveals that there is a tight coupling between a Cu plane together with the nearest-neighboring Nd planes [60].

On the one hand, no such reorientation transitions have been observed with neutron scattering for Pr_2CuO_4 [33] since Pr has a non-magnetic ground state, but has a polarizable low lying crystal field level. Only when a very small hydrostatic pressure of 0.25 GPa is applied to Pr_2CuO_4 [99] a very discontinuous behavior of the magnetic peaks is observed which has been interpreted as spin reorientation transitions analogous to the case of Nd_2CuO_4.

Figure 2.10 shows the proposed magnetic models for the Pr_2CuO_4 [33], which are not distinguishable in a simple neutron scattering experiment. But as with all the other known

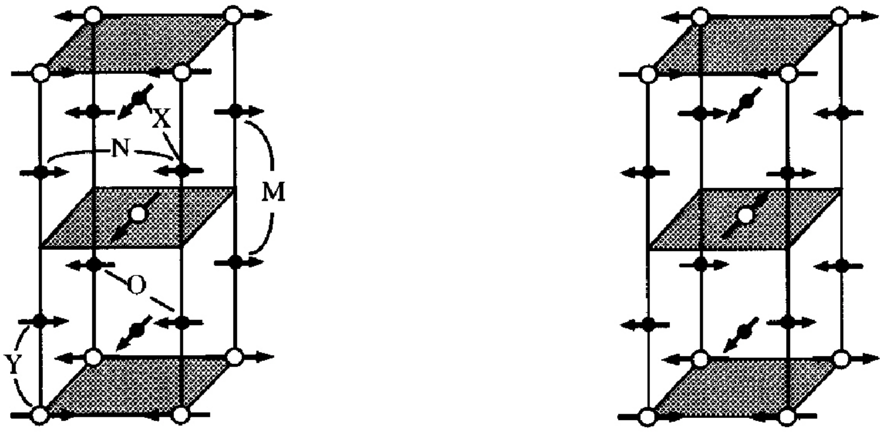

(a) Noncollinear Phase I&III

(b) Noncollinear Phase II

Figure 2.9: Possible relative orientations of spins in the chemical unit cell of Nd_2CuO_4. Here the open circles are Cu ions and the filled ones RE ions.The figure is reproduced from Ref. [60].

rare-earth cuprates and as cited in the review paper [53], experimental investigations on $Pr_{2-x}Ce_xCuO_4$ (PCCO) and $Pr_{1-y-x}La_yCe_xCuO_{4\pm\delta}$ (PLCCO) similarly give evidence of the same noncollinear c-axis Cu spin order as phase I NCO. In addition, the μSR experiments on single crystal $(Pr_{2-x}Ce_x)CuO_{4-\delta}$ support a noncollinear cross-like structure with a hidden canting arrangement of the spins [100]. At low doping, the magnetic moments at the Pr site have been observed to be small but nonzero due to exchange mixing with a value of approximately 0.08 μ_B/Pr [33, 101]. Matsuda and coworkers [59] claim that due to the small moment, the magnetic transitions linked with the RE-Cu and RE-RE interactions in NCO do not seem to occur in PCO [59]. Nonetheless, there is indication for Pr-Pr interactions in both the in-plane and out-of-plane directions mediated by Cu spins [33].

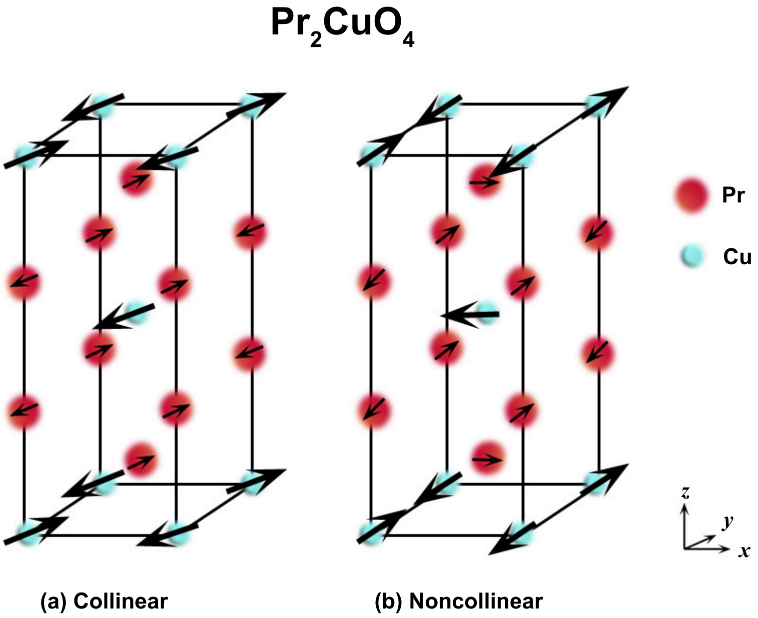

Figure 2.10: Proposed spin structure configurations for the Cu and Pr ions in Pr_2CuO_4. a) Domain of the collinear model, b) Noncollinear model. The figure is adapted from Ref. [33].

2.3.7 Definition of Magnetic Structure Models for the T'-cuprates

As discussed in the previous sections, various magnetic structures are realized in the different cuprates with no consistent naming convention used by the different authors. Therefore, in this section, I will define the naming convention for the different structures that I will later use to discuss the experimental data obtained in this thesis work.

In electron-doped cuprates, it was already previously mentioned that the resulting isotropic exchange between planes cancels out due to an in-plane alignment and crystal symmetry, and the three-dimensional (3D) magnetic order is governed by a delicate balance of the RE-Cu coupling, superexchange, spin-orbit, and Coulomb exchange interactions [53, 71, 60, 83, 87]. However, in all cases, the resulting spin configuration favors the one where the in-plane nearest neighbor spins are coupled antiferromagnetically due to the strong superexchange coupling J along the Cu-O-Cu bonds. In the BCT cuprates it is experimentally found that different spin structures are actually adopted [33, 60, 87, 102, 84, 101]. From elastic neutron scattering experimental findings, the cuprates are generally proposed to possess either a collinear or a noncollinear spin configuration. In the noncollinear structure, the spins are pointing along the Cu-O bonds, while in the collinear structures, which is for example adopted in the orthorhombic T-LCO [26], the spins point at roughly 45° to the Cu-O bond directions (i.e. along the diagonal of the *ab*-plane). To understand the proposed magnetic models, the following will further illustrate these spin geometries or configurations and it will focus on the geometries achieved by body-centered tetragonal structures such as the T'-cuprates.

In the case of T'-RE_2CuO_4 cuprates with the I4/mmm structure, there is one magnetic ion in the primitive cell. Typically for the tetragonal structures, the two antiferromagnetic propagation vectors K_1=($\frac{1}{2}$,$\frac{1}{2}$,0) and K_2=(-$\frac{1}{2}$,$\frac{1}{2}$,0) are found experimentally. The magnetic representation of the symmetry group of these propagation vectors can be decomposed into irreducible representations (IR). These are τ_3, τ_5, and τ_7 in the Kovalev notation [103]. τ_3 and τ_5 possess magnetic order parameters with the Cu moments within the plane while τ_7 has moments in c-direction. Due to the strong easy-plane anisotropy of the cuprates [104, 101, 105, 53], I will consider only τ_3 and τ_5 in the following.

Landau's theory of second order phase transition states that the low symmetry phase (or the low-temperature phase) can be described by the order parameter belonging to only one of the irreducible representations (IR).

The Cu spin geometry of T'-RE_2CuO_4 cuprates is shown in Figure 2.11, along with its 2D projections. The Cu spins in neighboring planes are distinguished by color such that the Cu spins within the plane are in blue and the spins in the center of the unit cell are drawn in red. This results in alternating blue and red layers of spins which I will also sometimes call even and odd layers. Additionally, the rotation angles of spins in the different planes are also defined in the figure. α is the angle of rotation of the in-plane spins (blue spin in the figure), β is the angle of rotation of the spin in the neighboring plane (red spin in the figure). The angle between the two spins at the origin of the unit cell and in the center, i.e. on neighboring planes, is given by $\gamma = \beta - \alpha$.

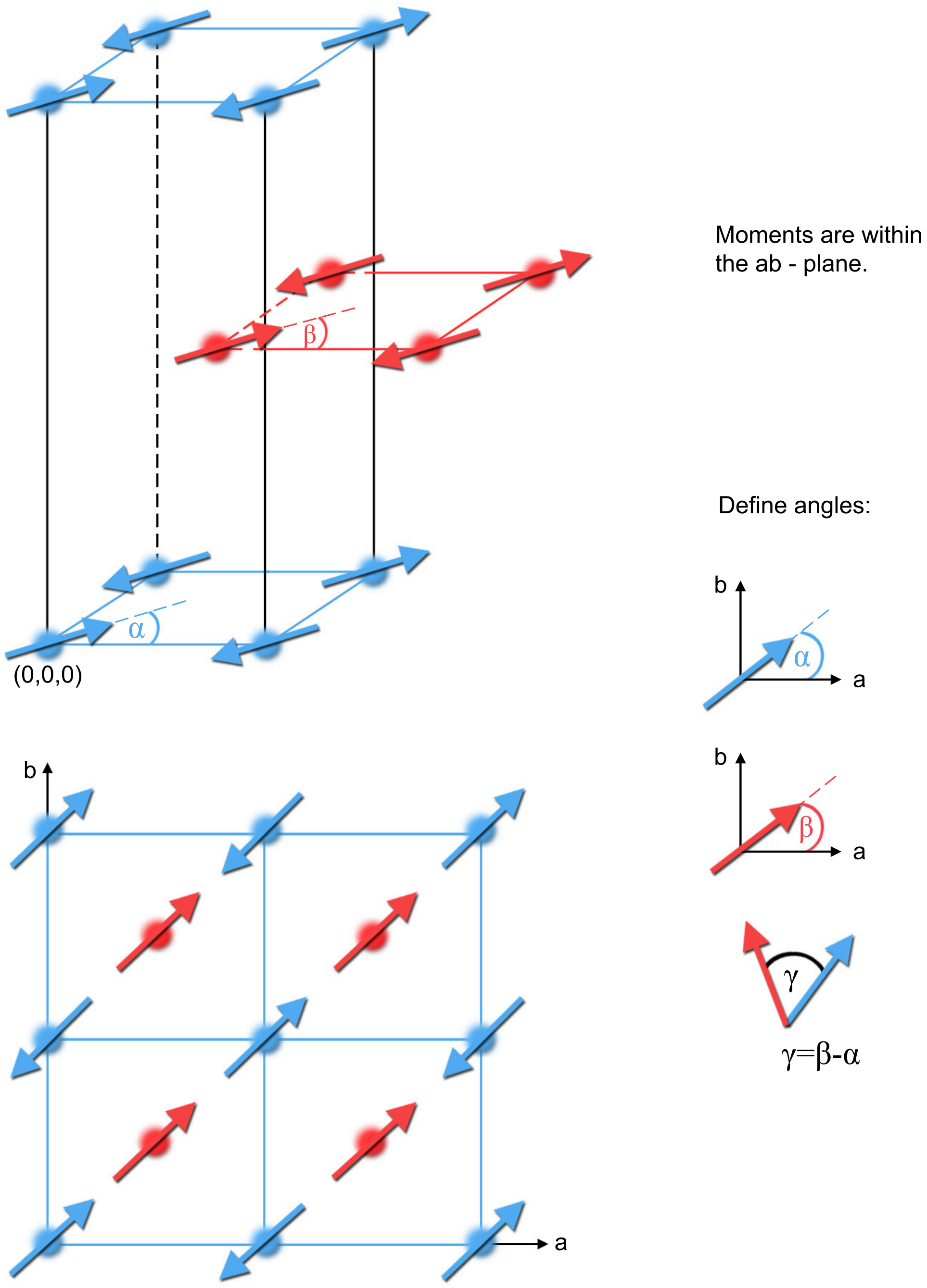

Figure 2.11: Definition of the unit cell and angles of the spin structure of T'-cuprates used in this thesis. As an example the Col I(K_2) structure is shown.

In Figure 2.12 and Figure 2.13, magnetic structures which belong to the τ_3 and τ_5 IR, respectively, are depicted. The most simple magnetic structures which are allowed by symmetry are collinear AFM structures which are generated from a single propagation vector and therefore possess a one-component order parameter. In Fig. 2.12, these are the two structures Col I(K_1) and Col I(K_2). In these structures the blue and red spins are either parallel ($\gamma = 0°$) or antiparallel ($\gamma = \pm 180°$), i.e. a collinear spin arrangement is obtained. The two collinear structures originating from K_1 and K_2 propagation vectors, are energetically degenerate domains in the tetragonal system. Also, if one domain from K_1 propagation vector is rotated as a whole by 90°, the corresponding structure originating from the K_2 propagation vector is obtained. Therefore, these kinds of structures are sometimes called 90°-domains. Here, I would like to introduce a simplified nomenclature of the magnetic structures as shown in the figures. Collinear structures will be referred as Col and noncollinear structures will be referred as NCol. The Roman numeral (I) will describe the structures belonging to τ_3 IR while the (II) are those structures belonging to τ_5 IR.

The lower two structures shown in Fig. 2.12 are special cases of non-collinear structures with $\gamma = -90°$ or $\gamma = -270°$. Please note that the non-collinear structures are linear combinations of the two collinear structures from the same IR, i.e. in a non-formal notation NCol $I^{(+)}$ = Col I(K_1) + Col I(K_2) and NCol $I^{(-)}$ = Col I(K_1) - Col I(K_2). For a more rigorous mathematical formulation, the interested reader is referred to the group theoretical treatment given in [103, 106]. In the same way, non-collinear structures can be composed from the collinear structures for the IR τ_5, see lower two structures in Fig. 2.13. It is evident that again, also the two non-collinear structures from the same IR are 90°-domains with respect to each other and are therefore energetically degenerate in the tetragonal system.

It is also interesting to compare the structures that are derived from the IR τ_3 (Fig. 2.12) with the ones obtained from IR τ_5 (Fig. 2.13). All four structures have a corresponding structure in the other figure with the only difference that the red spins are rotated by 180° in the IR τ_5 structures compared to the ones from the IR τ_3 structures. This leads to the situation that e.g. the the NCol I possesses a 2-in-2-out magnetic structures while NCol II exhibits a 4-in-4-out structure. As it is evident by this simple argument, these two structures therefore are different in anisotropy energy and one may be favored above the other.

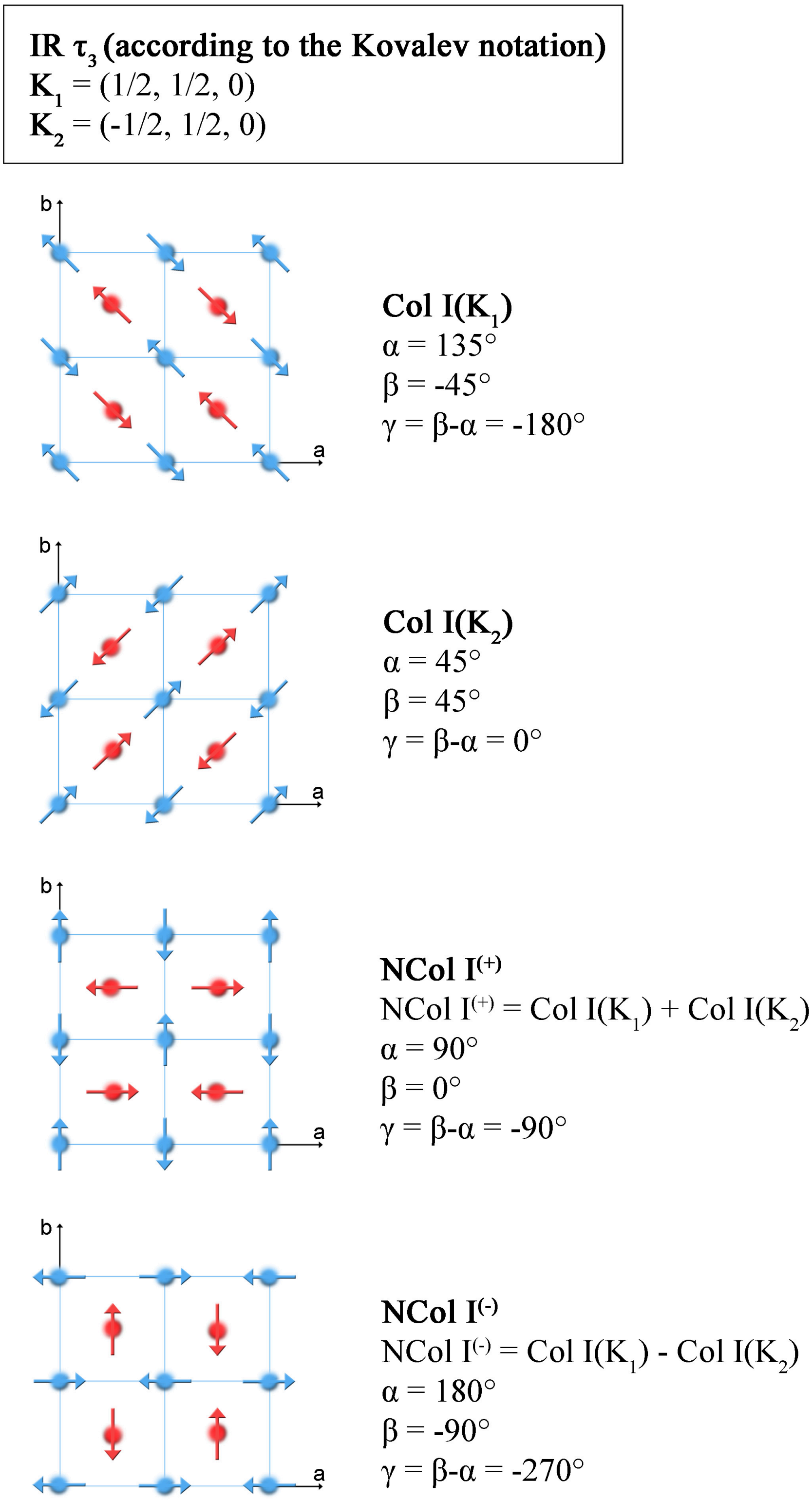

Figure 2.12: Special spin structures belonging to the τ_3 IR. The Col I(K_1) and Col I(K_2) structures are energetically degenerate 90° domains in a tetragonal system. The NCol I structures can be obtained by a linear combination of the upper structures with equal contribution of the two collinear domains.

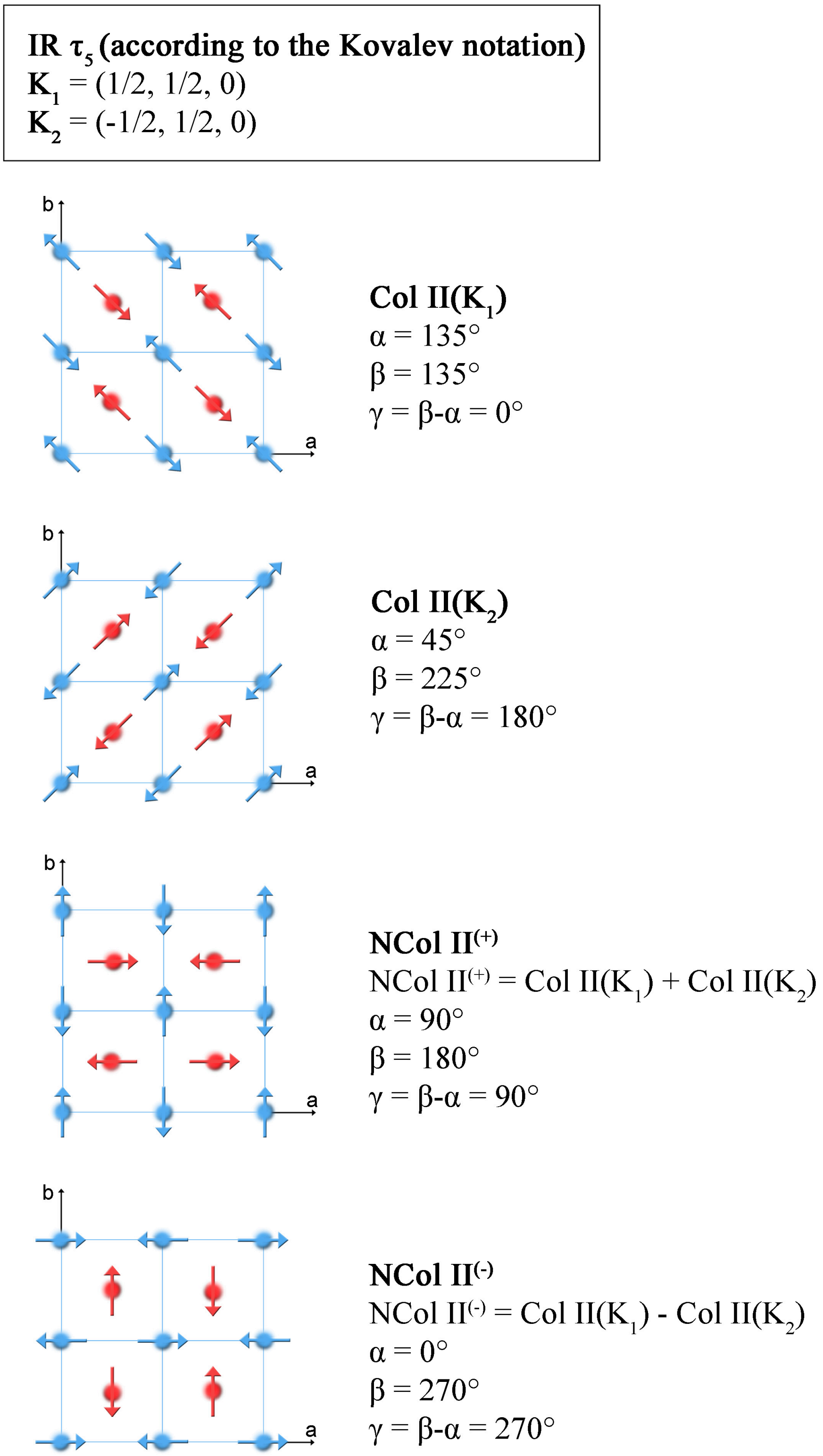

Figure 2.13: Special spin structures belonging to the τ_5 IR. The Col II(K_1) and Col II(K_2) structures are energetically degenerate 90° domains in a tetragonal system. The NCol II structures can be obtained by a linear combination of the upper structures with equal contribution of the two collinear domains.

As shortly summarized in the previous sections of this thesis, the four structures Col I and NCol I (Fig. 2.12) and Col II and NCol II (Fig. 2.13) have been used in the literature to describe the magnetism of the various rare-earth cuprates. Anyhow, these are only special cases of a larger group of magnetic structures with K_1 and K_2 propagation vectors that are allowed by symmetry. In general, any coherent superposition (linear combination) of the two collinear structures within one IR is symmetrically allowed. This leads to the general structures for the IR τ_3

$$c \cdot \mathrm{Col\,I}(\mathrm{K}_1) + d \cdot \mathrm{Col\,I}(\mathrm{K}_2) \tag{2.6}$$

and for the IR τ_5

$$c \cdot \mathrm{Col\,II}(\mathrm{K}_1) + d \cdot \mathrm{Col\,II}(\mathrm{K}_2) \tag{2.7}$$

with c and d being arbitrary real constants.

Some examples of these *general* case structures are given in Figure 2.14 and Figure 2.15 for τ_3 and τ_5, respectively. As one can verify in the given figures, an arbitrary linear combination of the collinear structures does not produce spin structures with an arbitrary alignment of the individual spins but rather still reflects the symmetry of the system. This results e.g. in the fact that only 90° NCol structures are produced with the spins pointing along the Cu-O bonds and Col structures with the spins pointing along the diagonal of the $ab-plane$. Also, the angles α and β in the even (blue) and odd (red) planes can not be chosen independently. It follows that if a blue spin is rotated by an angle Δ the corresponding red spin is forced by symmetry to be rotated by $-\Delta$. Since all rotation angles Δ are allowed, one can arbitrary choose an origin for this rotation as given in the corresponding figures. One can easily verify that for the IR τ_3 (Fig. 2.14) the relative angle between the even and odd plane spins is given by $\gamma = -2\Delta$ while the for the IR τ_5 (Fig. 2.15) the relation $\gamma = 180° - 2\Delta$ holds.

As said before, in a mean field sense and in the absence of any XY anisotropy in the plane, all these symmetry-allowed magnetic structures are energetically equivalent. Since all anisotropies which exist in the real system are small and several interactions might compete, it is not *per se* obvious which structures can and cannot be realized. Therefore, the most general models described in this section should be compared against the experimentally obtained data. This will be done in the later chapters of this thesis.

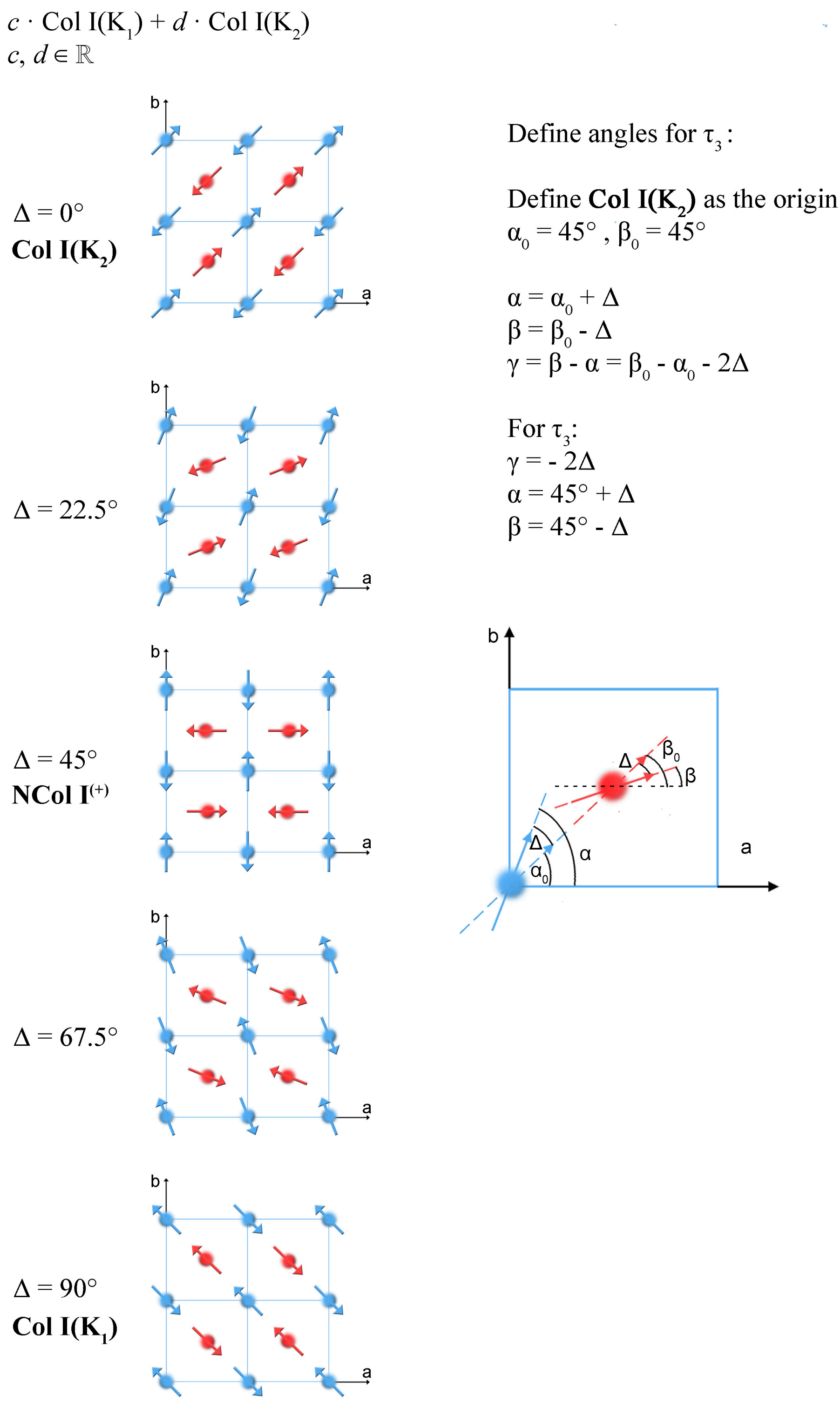

Figure 2.14: Symmetry allowed general spin structures belonging to the τ_3 IR. All structures can be obtained by a linear combination of the two collinear domains Col I(K_1) and Col I(K_2). Note that the relative angle between the spins in neighboring planes is given by $\gamma = -2\Delta$.

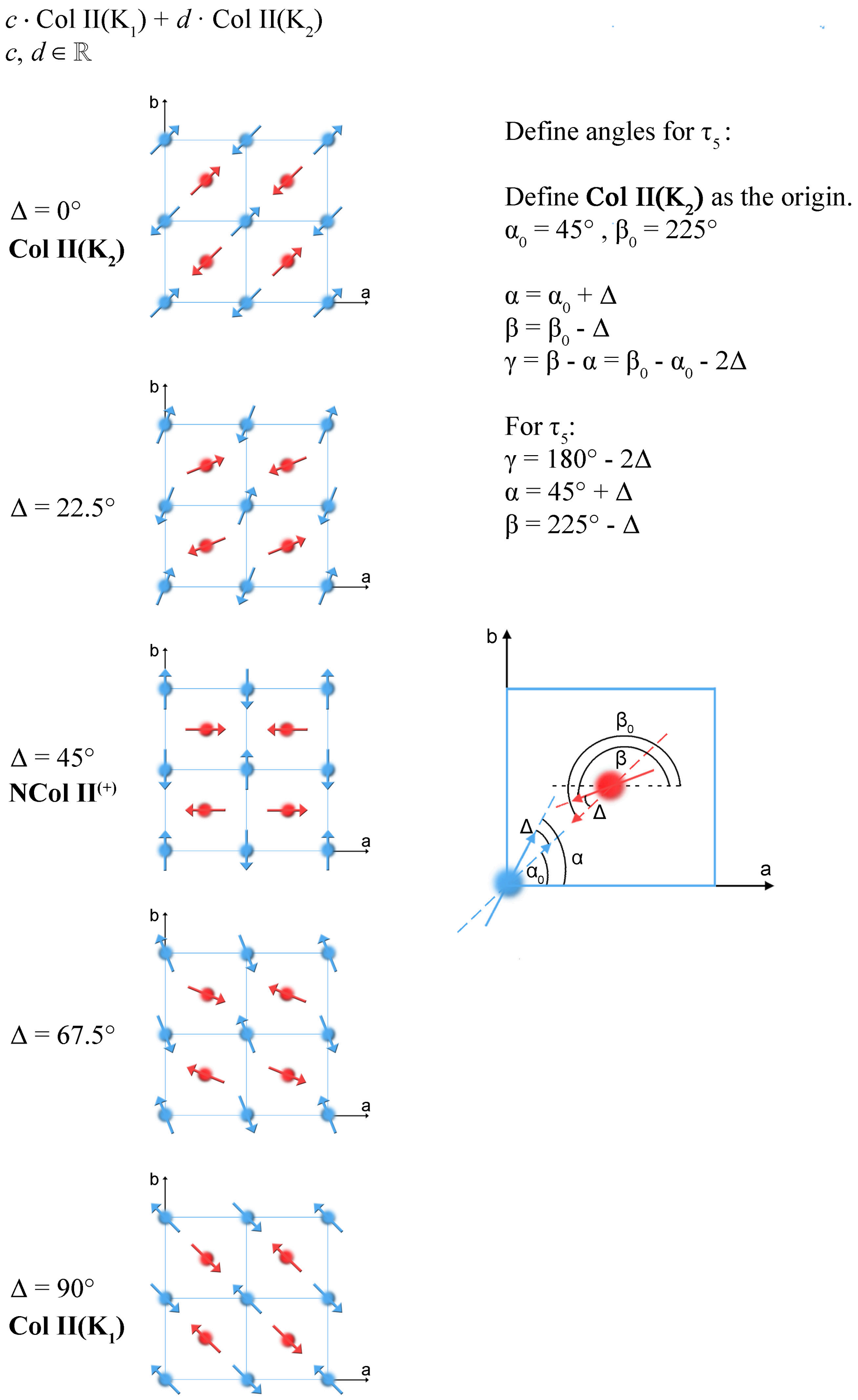

Figure 2.15: Symmetry allowed general spin structures belonging to the τ_5 IR. All structures can be obtained by a linear combination of the two collinear domains Col II(K_1) and Col II(K_2). Note that the relative angle between the spins in neighboring planes is given by $\gamma = 180° - 2\Delta$.

2.4 Superconductivity in the Rare-earth Cuprates

Previously, the phase diagram of hole-doped materials has vaster superconducting dome and a smaller antiferromagnetic region as compared to their electron-doped counterparts. However, this picture had changed when a study on a series of doped rare-earth cuprates $\mathrm{Ln}_{2-x}\mathrm{Ce}_x\mathrm{CuO}_{4+y}$ (Ln = La, Pr, Nd, Sm, Eu) thin films summarized in Figure 2.16, exhibit an increasingly larger superconducting dome with increasing ionic radius of the Ln-ion [34]. The largest lanthanide ion which is La, gave the maximal T_c of around 30 K that occurs at a doping level around 0.1 [34, 107, 108]. Another interesting note in the phase diagram is the abrupt disappearance of superconductivity towards lower doping [31, 109]. Yet, one factor plays an important role here. That is, by improving the oxygen removal process i.e. in the compound $\mathrm{Pr}_{2-x}\mathrm{RE}_x\mathrm{CuO}_{4+y}$, the superconducting region can be extended even with a slightly increased critical temperature down to a doping level of around x=0.04 [110]. As discussed in the introduction of this thesis, this leads to a more symmetric phase diagram with respect to the hole-doped cuprates. In the subsequent chapter, I will elaborate on the important role of the oxygen reduction and high temperature annealing on the actually-adopted electronic ground state.

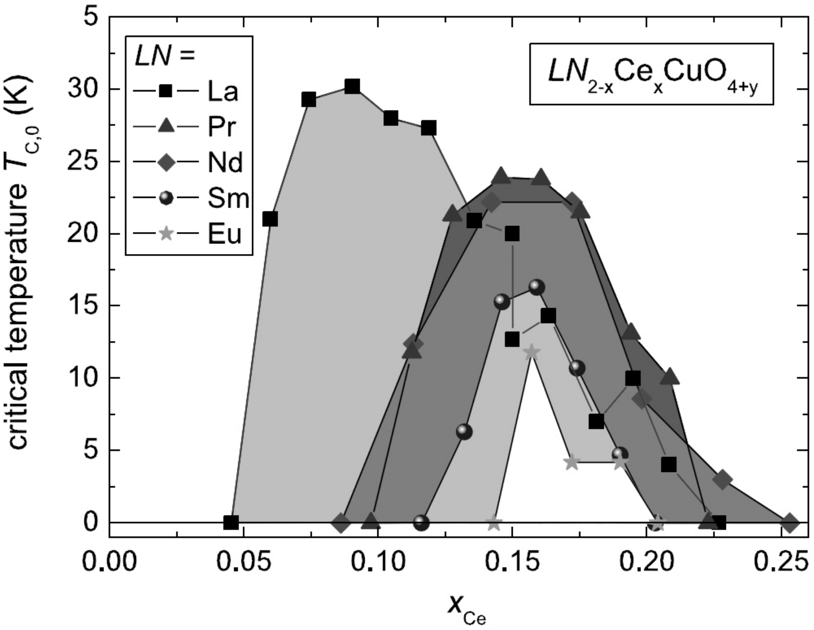

Figure 2.16: Phase diagram of electron-doped high-T_C superconductors $\mathrm{LN}_{2-x}\mathrm{Ce}_x\mathrm{CuO}_4$ (LN= La, Pr, Nd, Sm, and Eu). The figure is adapted from Ref. [34].

2.5 Oxygen Occupation in T'-RE$_2$CuO$_4$ and the Reduction Process

Intrinsic differences between hole- and electron-doped superconductity in the cuprates phase diagram have been partly blurred by an enduring materials issue encompassing the annealing process in the electron-doped materials. This is first demonstrated through the studies on single crystals of $Pr_{2-x}Ce_xCuO_4$ that extended the superconducting region down to x= 0.04 via a novel reduction route [110]. These observations of superconductivity in the underdoped regime, evidently, are not greatly accounted in terms of carrier doping into a parent compound of a Mott insulator as is the case for the hole-doped cuprates. There has to be a better and deeper understanding and explanation as to how superconductivity arises after reduction annealing in the electron-doped systems.

In this connection, a fundamental question also concerns the origin of the antiferromagnetic order in the phase diagram of these materials. It is widely known that as-grown crystals having the T'-structure tend to contain excess oxygen. Since reduction annealing causes the destruction of this antiferromagnetic order in the doped compounds, and subsequently the emergence of superconductivity, this then leads to the notion that the antiferromagnetic order originates from the remaining excess oxygen in the system. Altering the oxygen stoichiometry indicates changing the carrier doping. Although various citations provide sometimes contrasting but lucid explanations about the effect of reduction annealing, the difference in viewpoints arise from the fact that in oxygen reduction, there is a degree of freedom as to which among the oxygen sites is vacated during the process. Consequently, distinctive electronic properties evolve bringing about particular phenomena or mechanism.

Several plausible scenarios had been proposed to verify the effect of the annealing process that enhances the material towards superconductivity.

There are two primary sites that oxygens occupy in electron-doped cuprates: O(1) in the CuO_2 planes and O(2) in the rare-earth oxide layers. Ideally, the T'-structure should not contain the apical oxygen O(3). There are, however, experimental accounts from Mössbauer spectroscopy [111], Raman and far-infrared crystal-field spectroscopy [112, 113], neutron scattering [114, 115], and extended X-ray absorption fine structure (EXAFS) spectroscopy [116, 117], depicting the presence of O(3). Thus optimally, reduction annealing should solely remove apical oxygen atoms while maintaining intact the oxygen sites at O(1) and O(2) occupied. A common viewpoint is that the presence of even a minute amount of randomly-doped apical oxygen in the as-grown materials instigates localization of doped electrons and thus obstructing superconductivity to emerge. The apical oxygen empirically plays the role of a very strong scatterer as well as a pair-breaker due to magnetic (Kondo) scattering by Cu spins induced by residual apical oxygen [118]. Accordingly, in the metallic doped compounds, the Néel temperature depends dramatically on the oxygen reduction as shown in as-grown non-superconducting $Pr_{1.85}Ce_{0.15}CuO_{4+\delta}$ and $Nd_{1.85}Ce_{0.15}CuO_4$ where antiferromagnetic correlations develop below $T_N \sim 150$ K but essentially disappear in reduced superconducting samples [119]. This statement does not only hold for x$\sim$ 0.15 but also over a whole range of x. Hence, in this case, it is suggested by Matsumoto and coworkers [120] that the role of the oxygen-reduction process is to primarily remove the excess apical oxygen in the system. This then substantially increase the mobility of doped electrons to permit metallic behavior, decreasing impurity scatterers, and allowing superconductivity to flourish. However, details about this speculation have not yet been verified.

Tokura and coworkers [35] had originally suggested that an as-grown material had stoichiometric oxygen and the reduction process eliminates oxygen from the CuO_2 plane. This makes the oxygen content less than four and hence introduces mobile electrons into the system. In addition, some other experimental works like Raman scattering and infrared transmission measurements on PCCO [112] and NCCO [113] demonstrate that reduction did not affect the apical oxygens. In the Raman scattering results, O(3) was unaffected by reduction but the feature related with O(3) is observed to increase with Ce concentration. It was then concluded that O(3) is bound strongly to the Ce^{4+} ion that is in the proximity. Measurements of the rare-earth crystal field excitations with the use of infrared transmission spectroscopy displayed that the effect of reduction changes at x= 0.08 Ce concentration. Madelung potential considerations found that below this concentration, it was the out-of-plane O(2) that is removed, while it is the O(1) that is taken out when the Ce concentration is above this concentration [113, 112]. Contrary to expected results, the astonishing conclusion turned out that for superconductivity to emerge, oxygen must be taken out from the very CuO_2 planes thought to be of critical importance to superconductivity. To account for this apparent contradiction, Mang and coworkers [27] proposed that this can be understood and explained by the partial decomposition of NCCO and the appearance of an epitaxial secondary phase $(Nd,Ce)_2O_3$ as a decomposition by-product of reduction. This phase, representing approximately 1% of the entire volume, remarkably disappear with oxygenation. It was proposed that since this secondary phase does not contain Cu ions, these might be because these zones act as Cu reservoirs for the Cu that migrate into the CuO_2 planes during the reduction process and are said to repair the defects intrinsic in the as-grown materials, resulting in Cu deficient region with the epitaxial $(Nd,Ce)_2O_3$ intercalation [121]. Hence, the decrease in the density of the Cu vacancies in the CuO_2 planes eliminates pair-breaking sites allowing superconductivity to emerge. Figure 2.17 illustrates the structures of the materials investigated by Kang and coworkers [121], depicting an intrinsic presence of Cu deficiencies in the as-grown material and the *repair* of these deficiencies after oxygen reduction along with the appearance of the impurity phase.

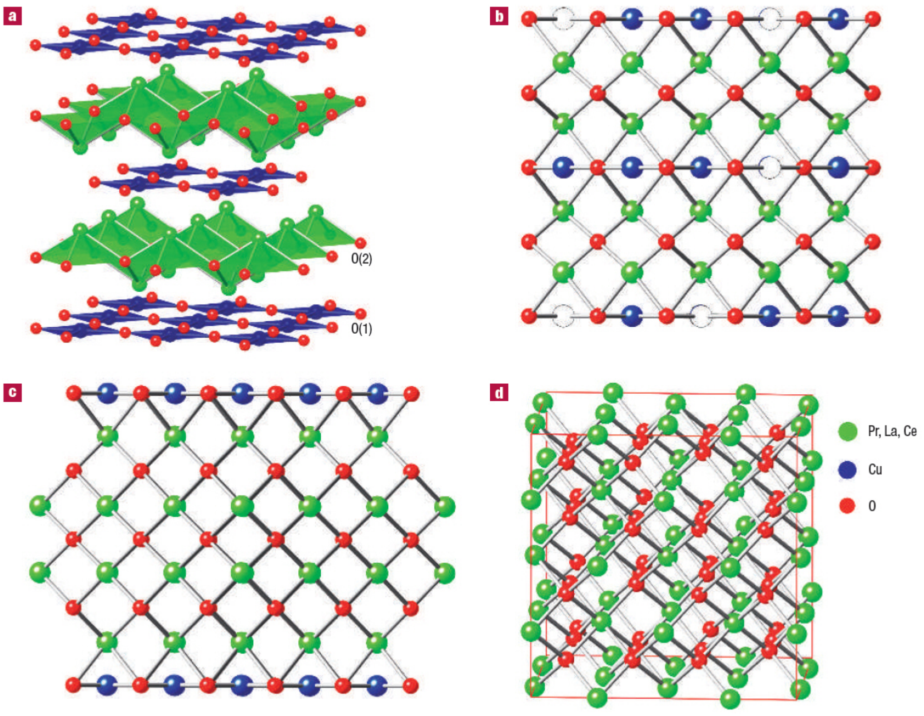

Figure 2.17: a) Typical T'-structure of PLCCO, b) as-grown PLCCO with random Cu vacancies in the CuO$_2$ planes, c) Structure of an oxygen-reduced PLCCO with a Cu-free secondary phase and a repaired Cu vacancies in the CuO$_2$ plane, the Cu atoms have been removed from one layer leaving behind a thin slab of the anion-deficient fluorite impurity phase: R$_2$O$_3$ = (Pr,La,Ce)$_2$O$_3$, d) The vacancy-ordered C-type sesquioxide structure of the R$_2$O$_3$ impurity phase (space group Ia3). The figure was taken from Ref. [121].

In addition to speculative notion to the role it plays in enabling superconductivity, the oxygen reduction process is said to also add charge carriers. Experiments to tune superconductivity were carried out with varying doping concentrations and annealing conditions. Mang and coworkers [27] confirmed earlier works of Luke and coworkers [31] with their neutron scattering studies on NCCO. They provided a phase diagram showing the Néel temperature as a function of cerium content resulting to a T_N(x) line going to zero at x~0.17. With these results, they claim that reduction lowers T_N and the corresponding staggered in-plane magnetization, while enhancing superconductivity. This change in T_N(x) with oxygen content was then interpreted as a direct consequence of carrier doping. That is, oxygen reduction acts exactly like cerium substitution [27]. However, these results had been refuted by Motoyama and coworkers who asserted that the antiferromagnetic state terminates at x ≈ 0.134 [122]. These results may then point out that this shifting of T_N(x) by an amount corresponding to the added electron contribution from reduction is only applicable for low dopings. Different mechanisms may be occurring near superconducting compositions.

The old school knowledge about the complete removal of the apical oxygen atoms extends the generic phase diagram of the superconducting T'-cuprates is also confronted with the report on the discovery of superconductivity in undoped T'-(La,RE)$_2$CuO$_4$ with T_c of over 30 K. This has made a stir in the high-T_c superconductivity community as this had contested previous knowledge about these compounds to be generally insulating and not superconducting without doping [123, 124]. In addition and very astonishingly, thin films of Nd$_{2-x}$Ce$_x$CuO$_4$ (NCCO) show superconductivity in a wide range even at x= 0 when the films are properly reduced [120]. Moreover, clarifying the question whether these are undoped superconductors or oxygen-doped Mott-Hubbard superconductors substantially points at optimizing reduction conditions to be the main driving force for superconductivity. This is further proven by the undoped Gd$_2$CuO$_4$ that has a $T_c{}^{onset}$ as high as 20 K and up-to-now, there has been no citations that electron-doped Gd$_{2-x}$Ce$_x$CuO$_4$ gets superconducting. A very recent intensive work of Krockenberger and coworkers [125] on T'-Pr$_2$CuO$_4$ illustrates the influence of the annealing conditions. More specifically, they investigated and compared the influence of doping to the influence of annealing and they speculated that a hidden, hole-like Fermi surface may be present. This was checked by implementing a new systematic two-step annealing scheme revealing certain annealing conditions that suitably preserve the T'-structure and induce superconductivity into Pr$_2$CuO$_4$ [125]. In this two-step scheme, they illustrated that the as-grown compound contains more than the stoichiometric amount of oxygen which are randomly distributed at apical sites. As said above, this presence of additional oxygen has already been previously known [114, 115]. The first annealing step did not cause any change in the lattice parameters in comparison to the as-grown sample. However, an increase in the resistivity value is observed. Such behavior was explained by the introduction of oxygen vacancies in the CuO$_2$ plane. The presence of such defects would sharply disturb the electronic conduction. After the sample is annealed for the second time, the in-plane defects are repaired by relocating apical oxygen atoms to the planes that significantly lowered the observed resistivity. This final step provides electronic properties similarly observed for the cerium doped superconductors [126], especially it induces superconductivity in the undoped compound.

3 Muon Spin Rotation and Relaxation (μSR)

3.1 Overview

Muon spin rotation and relaxation, denoted here as μSR, is an experimental technique distinctively used to explore magnetic order, magnetic fluctuations, and superconductivity in various condensed matter systems. It utilizes a short-lived subatomic particle called a muon, whose spin and charge are sensitive local magnetic and electronic probes of matter.

μSR is a good complementary technique as it closes the gap with the relatively faster neutron scattering and the slower nuclear magnetic resonance (NMR). It is, in fact, similar to NMR and electron spin resonance (ESR) on the basis of the probe's magnetic moment (in this case, the muon's spin) response in the local magnetic field. Moreover, in comparison to the nuclei and electrons used for NMR and ESR, respectively, the muon is an unstable particle having a mean lifetime of 2.2 μs that it has to be intermittently or constantly implanted into a sample by a pulsed or a continuous muon beam. However, as it is nearly 100% spin polarized, it has the edge of conducting measurements without having to necessarily apply a magnetic field in the course of the experiment, contrary to NMR or ESR. Consequently, magnetic and nonmagnetic materials can be probed with great accuracy at a wide range of accessible temperature. One strength of μSR is its capability to investigate magnetically inhomogeneous materials. These are materials with chemical inhomogeneity or more interestingly, those with competing interactions in a chemically inhomogeneous system which lead to interesting phenomena such as phase separation or competition or coexistence of different ground states.

Muons are particularly very sensitive to small internal magnetic fields making them very usable to measurements where magnetism is weak or dilute. In a magnetically-ordered material, μSR is a great tool to measure the magnetic order parameter, magnetic fluctuations, or changes in magnetic structure. It is notably useful for antiferromagnetic systems with small ordered magnetic moments, short-range order, disordered systems, such as spin glasses (randomness), or systems with dilute magnetic impurities. We can investigate many different systems having different magnetic structures in which we have nuclear moments, electronic moments, static moments, or fluctuating moments. All these different situations will give a distinguishable μSR signal that has a theoretically predicted, given relaxation function.

μSR is an important technique also used in the investigation of the structure of vortices within the bulk of superconductors. It is used to measure the absolute value of the magnetic penetration depth in the vortex state of type-II superconductors. Essentially, with the state-of-the-art facility with ultra-low energy muons, an absolute value of the penetration depth can be determined near the surface of a sample in either the Meissner phase or in the vortex phase.

Specifically, for systems with phase separation between different electronic phases like magnetically-ordered, paramagnetic, and superconducting phases, μSR can determine the volume fraction of each electronic phase. Hence, because of its high sensitivity to weak internal magnetic fields and its capability to determine the volume fraction of magnetic phases, μSR is ideally suited to address the forefront issues on the relationship between magnetism and superconductivity on a microscopic scale.

There are two general techniques for acquiring the muon polarization as a function of time, one applicable for a facility which produces a pulsed beam of protons from which the muons are eventually derived, and one applicable for a continuous beam facility. The Laboratory for Muon Spin Spectroscopy of the Paul Scherrer Institute uses a continuous beam of protons wherein all μSR data given in this dissertation were obtained. Moreover, the discussion is also limited to the use of positive muons.

Most positive muon beams are produced from pions decaying at rest in the surface layer of the primary production target. Hence, the common name, surface muons. The surface muon beam is only one of the possible but most convenient scheme for most of the μSR experiments. Fully polarized muons of relatively low energies are provided by these surface muon beams, which are then stopped in condensed matter systems within few hundred micrometers from the surface. In this manner, muons are bulk probes, thus requiring moderate amounts of material.

In the following, I will discuss the essential properties of the muon that makes it useful for the μSR technique. In addition, the principles in doing a μSR experiment will also be presented. For further reference, a detailed description about the technique can be found in textbooks [127, 128, 129, 130] and in some review articles [131, 132, 133, 134].

3.2 Muon Discovery, Production, and Implantation

The muon was discovered as a secondary radiation from cosmic rays. It has a mass that is 200 times that of an electron or 9 times less than that of a proton. It has a positive or negative electric charge (±1) and a spin of 1/2 [135]. From a fundamental viewpoint, it is a lepton and its properties are listed in Table 3.1. Although either positive or negative muons can be used to perform μSR, their very different behavior in matter makes μ^+ more suitable for most condensed matter physics or chemistry applications. Having a negative charge in matter, μ^- behaves as a heavy electron and is easily captured into the atomic orbitals and are also strongly attracted by nuclei giving more information about the nuclear interactions rather than about its solid state properties. In contrast, μ^+ avoids the positively charged nuclei in the host material. For our purpose, we made use of the positive muon to probe the magnetic properties of our sample.

Table 3.1: Muon Properties

Mass	m_μ= 0.1126 m$_p$ = 206.7684(6) m$_e$ = 105.65849(4) MeV/c^2
Charge	+ or -
Spin	1/2
Magnetic moment	3.18 μ_p
Gyromagnetic ratio	$2\pi \cdot 135.53875$ (6) MHz/T
Unstable particle	mean lifetime : 2.19703 (4) μs

The discovery of the violation of parity (the principle of invariance under space reflection) in decays regulated by weak interaction had instigated the application of the μSR technique to condensed matter research. Notable scientists, Lee and Yang, were awarded the Nobel Prize in 1957 for their investigation of the so-called parity laws [136]. Parallel experiments of C.S. Wu *et al.* [137] on their experimental test on the β-decay of ^{60}Co , and the muon decay experiments of R.L. Garwin *et al.* [138], had directly illustrated violation of parity.

Thence, owing to parity violation, a muon beam may be produced starting from an accelerated proton beam with nearly 100% spin polarization. The muon is implanted into the sample and generally ends up in few equivalent, most energetically favored interstitial lattice sites, keeping its initial spin polarization. The phenomenon of not conserving parity also leads to the detection of the muon spin coherent behavior from the direction of emission of its decay-positron (electron). That is, the emitted positron emerges predominantly along the direction of the muon spin at the time of its decay. The distribution of decay directions varies with positron energy. By averaging over an ensemble of muons which are implanted one by one, or in bunches at intermittent times, and granting that we detect on which direction the positron is emitted and at which time, we can reconstruct the time evolution of the muon spin. These muon characteristics that make μSR technique possible will be elaborated in the succeeding paragraphs.

3.3 Essential Muon Properties

There are three muon characteristics which are essential for the application of the μSR technique. These are the following:

1) The muon spin ensemble is 100% polarized.

The muon originates from the pion which decays very quickly (26ns) into two particles, a muon and a muon neutrino. This is a two-body decay. But for a start, in order to obtain the pions, a proton beam of high energy (>500MeV) is directed onto a beryllium or a pyrolytic graphite target.

The decay of charged pions gives the following decay processes for both positive and negative pions $\pi^{\pm}$ into muons and neutrinos:

$$\pi^{+} \rightarrow \mu^{+} + \nu_{\mu}$$
$$\pi^{-} \rightarrow \mu^{-} + \bar{\nu}_{\mu}$$

Figure 3.1 briefly illustrates pion decay. For the pion decay process, the mirror image does not exist in nature. This is because the concept of parity is not followed. Parity means simply that in the macroscopic world, one expects that the mirror image of any possible event is also a possible event, this *parity* symmetry is however incredibly broken in the microscopic realm of elementary particles.

Due to parity violation of the weak interaction in pion decay, there exist only left-handed neutrinos in nature. This means that the neutrino has its spin aligned antiparallel to its momentum. Conversely, the muon can have its spin antiparallel to its momentum because the conservation of the total spin and total momentum has to be fulfilled.

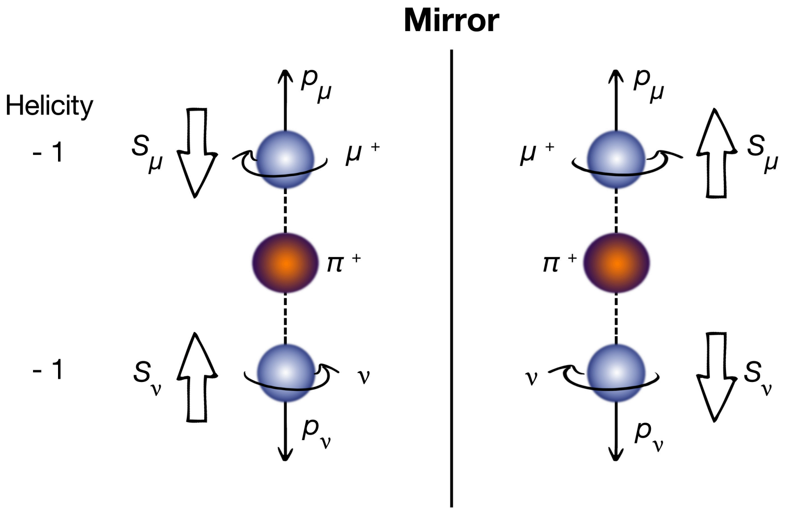

Figure 3.1: Parity-violating collinear decay of a pion π^+ at rest into a muon μ^+ and a muon neutrino ν_μ. The right mirror image does not occur in nature in the parity-violating decay.

2) The decay positron is preferentially emitted along the muon spin direction.

The muon decay is anisotropic. It is a three-body decay, a muon decaying into a positron and two neutrinos:

$$\mu^+ \to e^+ + \nu_e + \overline{\nu}_\mu$$

This is schematically shown in Figure 3.2.

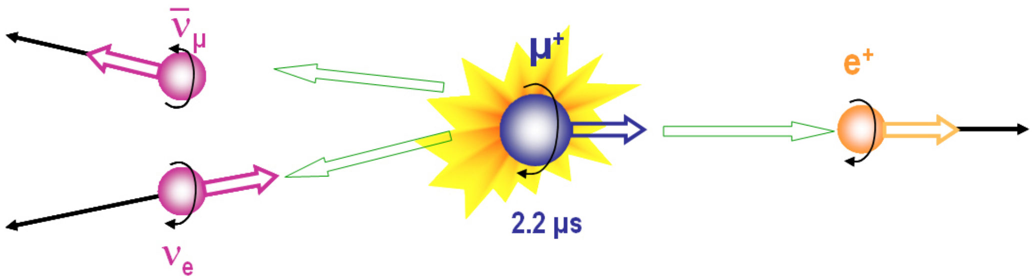

Figure 3.2: Illustration of a muon decay, conservation of linear (long green arrows) and angular (short arrows) momentum together with parity violation. This shows a correlation between the muon spin direction and the positron linear momentum.

The phenomenon of parity violation due to weak interactions is also involved in the decay of muons. Like in the case for muon production, conservation of angular momentum plays a significant role in muon decay, with the constraint that the neutrinos must have well defined helicities. That is, negative for the particle ν_e and positive for the antiparticle $\overline{\nu}_\mu$. At maximum positron energy, corresponding to two neutrinos emitted opposite to the positron, the correlation imposed on the directions of the muon spin and of the positron momentum is rather simple. In this given collinear situation, the two neutrinos do not contribute to angular momentum since they are collinear and of opposite helicity. On the one hand, the positron must nearly have positive helicity since it is highly relativistic. So, it must emerge in the direction of the muon spin to satisfy conservation of angular momentum. Thus, positrons are preferentially emitted along the direction of the muon spin at decay time. This is illustrated in Figure 3.2.

For energy and momentum conservation, the energy of the positron is distributed from a minimum to a maximum. There is a continuum of possible geometries and a corresponding range of energies for the emitted positron (E ≤52.83 MeV) which can be mapped out as shown in Figure 3.3. In this figure, the radial distance represents the relative probability that a positron is emitted in a given direction.

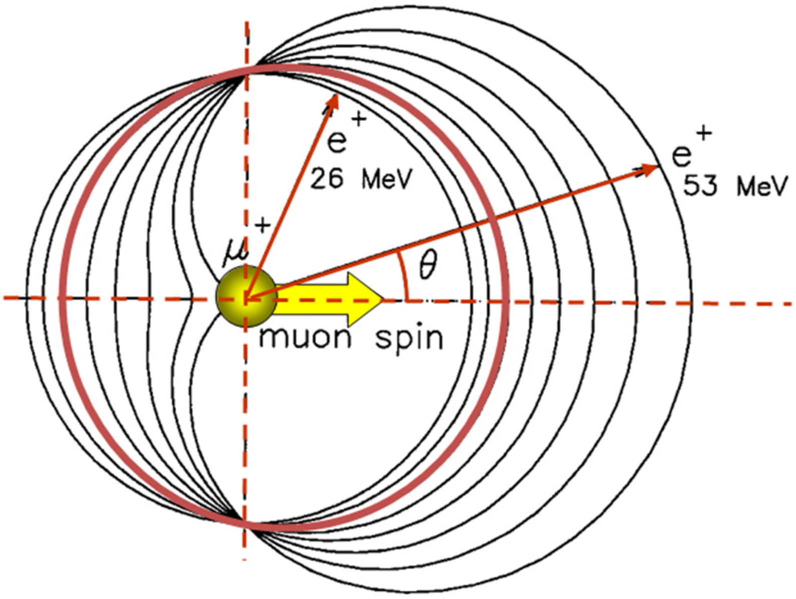

Figure 3.3: Angular distribution of positrons from the parity-violating anisotropic muon decay. The outer-rightmost curve is for the highest-energy emitted positron. When all positron energies E are sampled with equal probability, the integrated asymmetry parameter has the value A= 1/3 (red curve).

The probability distribution function for the positron emission is correlated to the instantaneous direction of the muon spin by:

$$P(\theta) \propto 1 + A(E)cos\theta$$

where A(E) is an asymmetry factor which depends on the energy of the emitted positron, which is equal to 1 for E= E_{max}.

3) The muon spin precesses in a magnetic field.

To illustrate, the muon can be considered here either as a classical or a quantum-mechanical particle. The quantum-mechanical description is shown in Figure 3.4. Here, you have a spin-1/2 particle in a magnetic field applied along the spin direction, giving two energy states of the system. Then, if the magnetic field is obliquely applied, that is, it is no longer parallel to the initial muon spin direction, the two states are no longer eigenstates. Therefore, the spin components <S_x> and <S_y> are mixed and start to precess with the Larmor frequency ω_L. These are the so-called Rabi oscillations.

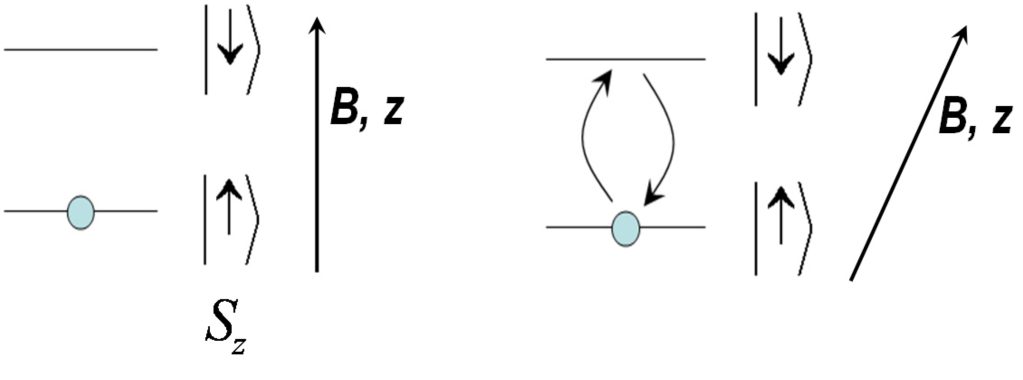

Figure 3.4: Quantum-mechanical description of the muon spin response to a magnetic field.

For simplicity, a classical picture can also be considered using the Ehrenfest theorem. An analog system is shown in Figure 3.5 wherein you have a magnetic moment in an oblique magnetic field.

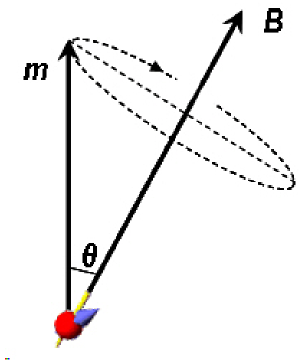

Figure 3.5: Classical description of the muon spin response to a magnetic field.

The muon spin precesses around this magnetic field and its motion is described by the Bloch equations:

$$\frac{d\vec{m}}{dt} = \gamma\vec{m} \times \vec{B}$$

$$\frac{d\vec{m}}{dt} = \gamma\vec{m} \times \vec{B} - \Gamma\vec{m}$$

where the oscillation frequency is given by the Larmor frequency $\omega_L = \gamma\vec{B}$. In addition, the relaxation of the system, $\Gamma\vec{m}$ is given by the coupling to a heat bath.

In summary, there are three main muon characteristics that make μSR spectroscopy possible:

1. The muon spin ensemble is 100% polarized.
2. The decay positron is preferentially emitted along the muon spin direction.
3. The muon spin precesses in a magnetic field.

As the muons are implanted, they decelerate mainly by inelastic collisions with electrons. In other words, they lose their kinetic energy by ionizing outershell electrons, then finally stops at an interstitial site. There, the muon spin is subject to interactions with other spins, i.e. the electronic and nuclear spins close by. This is similar to the well known NMR technique. However, a more simplified situation holds for the muon, being spin one-half, it does not have an electric quadrupole moment. Thus, it does not couple to the electric field gradient. This means that the muon is less sensitive to structural distortions or changes than NMR or Mössbauer spectroscopy. On the other hand, this very often is of advantage, since the observed muon spin relaxation always has magnetic origin and can not be misinterpreted.

3.4 Principles of a μSR Experiment

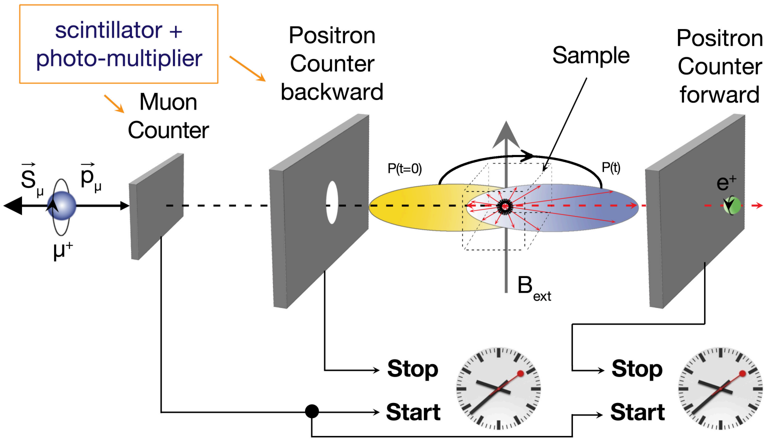

Figure 3.6: Schematic of the μSR experiment principle, top view.

The μSR technique is based on the observation of the time evolution of the muon spin polarization $\vec{P}(t)$ of an ensemble of muons. A schematic layout of a μSR experiment is shown in Figure 3.6 with an applied field perpendicular (transverse) to the initial muon spin polarization.

The basic principle for a μSR experiment is initiated by the implantation of positively charged muons (μ^+) in a sample one at a time. This is called a time-differential measurement where an electronic clock is started instantly when a muon is implanted into the sample. The μ^+ come to rest at interstitial lattice sites where they act as magnetic microprobes. The muon spin interacts with its magnetic environment until it decays weakly after a mean lifetime of τ_μ = 2.2 μs into two neutrinos and a positron, the latter being preferentially emitted along the direction of the muon spin at the moment of the decay. The clock is stopped when the positron emitted from the decayed muon is detected. Again, one muon at a time is allowed into the sample. This means that if a second muon arrives typically within five muon lifetimes, that is ~ 10 μs, then the event is discarded. An electronic trigger logic ensures that during the observation period, only those events accepted are those from where one muon was inside the sample, so that the start and stop signals come from the same muon event. A histogram is thus built from the positron counts versus the time after implantation. One obtains histograms for the forward N_F and the backward N_B detectors, which have the forms:

$$N_F(t) = N_0^F e^{-t/\tau_\mu}(1 + A_0\vec{P}(t)\hat{n}_F) + N_{Bgr}^F \tag{3.1}$$

$$\begin{aligned} N_B(t) = N_0^B e^{-t/\tau_\mu}(1 + A_0\vec{P}(t)\hat{n}_B) + N_{Bgr}^B \\ = N_0^B e^{-t/\tau_\mu}(1 - A_0\vec{P}(t)\hat{n}_F) + N_{Bgr}^B \end{aligned} \tag{3.2}$$

Equation 3.1 and 3.2 are applicable for the ideal case when the two detectors (F and B) are identical so that the N_0, N_{Bgr}, and A_0 are the same in both detectors. Here, $\vec{P}$(t) is the muon spin polarization function with the unit vector $\hat{n}_F$, $\hat{n}_B$ with respect to the muon spin polarization. The exponential factor $N_0 e^{-t/\tau_\mu}$ accounts for the radioactive decay of the muon. N_{Bgr} is a background contribution coming from uncorrelated starts and stops. A_0 is the initial asymmetry, a parameter to be determined experimentally. It depends on factors such as detector solid angle, efficiency, absorption and scattering of positrons in the material. Generally, $A_0 < 1/3$ (decay asymmetry). Typical values lie between 0.25 and 0.3. In such idealistic case, the positron histograms recorded by the two detectors differ only by the phase. The difference between the phases of the histograms is 180° if the detectors are precisely aligned opposite each other.

As the positrons are predominantly emitted in the direction of the muon spin which precesses with the frequency ω_μ, the forward and backward detectors will detect an oscillating signal having the same frequency. In order to remove the exponential decay due to the finite muon lifetime, what is referred as the asymmetry signal *A(t)* is calculated:

$$A(t) = A_0 P(t) = \frac{N_B(t) - N_F(t)}{N_B(t) + N_F(t)} \tag{3.3}$$

where $N_F(t)$ and $N_B(t)$ are the number of positrons detected in the forward and backward detectors, respectively. *A(t)* and *P(t)* are quantities that depend on the spatial distribution and dynamical fluctuations of the muon magnetic environment. Thus, these obtained functions would yield us physical information about our sample of interest. The μSR polarization functions are elaborated in the next chapter.

3.5 Experiment Configurations in μSR

The flexibility of choosing from a number of different experimental configurations is a prevalent advantage of μSR spectroscopy in studying matter on a local scale.

3.5.1 Longitudinal and Zero-Field μSR

The longitudinal field μSR (LF-μSR) configuration is the simplest possible experimental setup that involves the application of an external magnetic field parallel to the initial direction of the muon spin polarization, $\mathbf{B}_{ext} \parallel \vec{P}(0)$. This is illustrated in Figure 3.7. Applying such a field does not bring about precession of the muon spins and overcomes any smaller static field brought about by magnetic order that would otherwise cause precession.

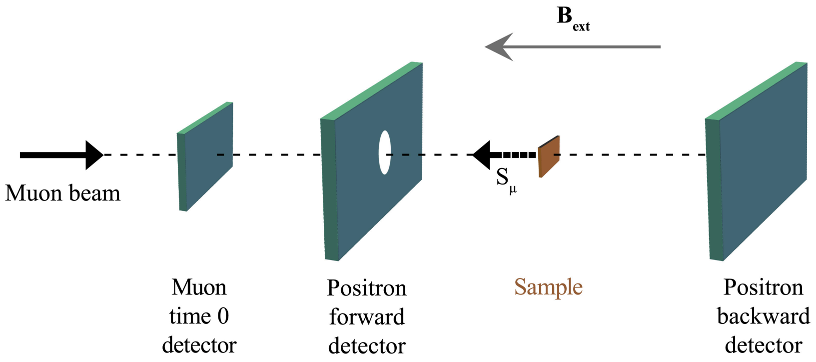

Figure 3.7: Longitudinal field μSR configuration.

With this configuration, one can also do experiments in the absence of magnetic field, $\mathbf{B}_{ext} = 0$. This is the **Zero-Field (ZF) μSR**. The size of the ordered moment and thus the magnetic order parameter can be derived from zero-field measurements. This is because the frequency of a μSR signal is directly proportional to the internal magnetic fields at the spot where it comes to rest, the muon site.

3.5.2 Transverse-Field μSR

This experimental setup involves the application of an external magnetic field perpendicular to the initial direction of the muon spin polarization, $\mathbf{B}_{ext} \perp \vec{P}(0)$. This is shown in Figure 3.8.

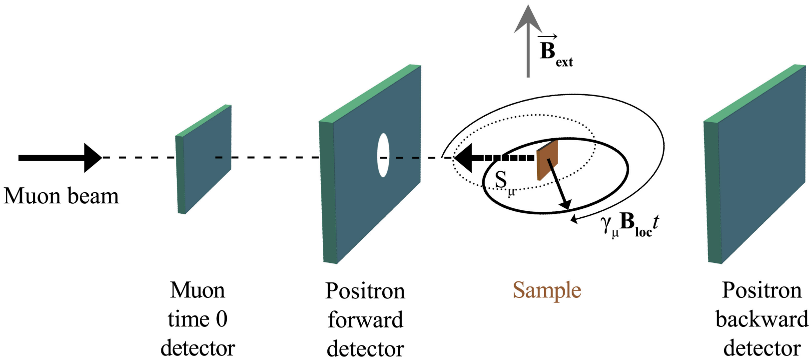

Figure 3.8: Transverse field μSR configuration.

4 Muon Polarization Functions

4.1 Overview

With the μSR technique, the ensemble average muon polarization projected onto an axis as a function of time, $P_z(t)$, provides the muon polarization function. This polarization function monitors the properties of the local field. It contains the enthralling physics that awaits interpretation, yielding us information about magnetic fields in the studied material. The local magnetic field at a muon site is generally originating from a combination of dipolar interaction with surrounding nuclear and electronic spins, and contact hyperfine fields from the spin density at the muon site.

The sensitivity of the μ^+ as a magnetic probe can be well-suited to extremely small magnetic moments (down to 10^{-3} - 10^{-4} μ_B) since it has a very large magnetic moment. As a local probe, one can determine the distribution of static internal fields and also fields which are fluctuating. Generally, the presence of magnetic fields in the sample can be determined within the range of 0.00002 Tesla to a few Tesla which are static on the timescale of the muon lifetime of 2.2 μs. In addition, fluctuating magnetic fields can also be detected with a fluctuation rate $\nu \lesssim 10^{11}$ Hz since the μSR technique has a broad time window of 10^{-4} s to 10^{-11} s.

A variety of magnetic systems can be investigated and for a given magnetic structure, a distinct μSR signal is obtained and there exists a predetermined theoretical relaxation function that describes the distribution of magnetic moments giving the distribution of fields and also their fluctuations [130].

As in NMR, the established basic concepts on spin relaxations and models are also adapted to μSR. There are mainly two distinguished types of relaxation processes. One is the transverse relaxation that is due to dephasing of precessions which occur without energy dissipation. The other is the longitudinal relaxation that is due to the recovery of thermodynamic equilibrium which requires contact with a thermal reservoir (e.g. the lattice) in order to dissipate the excess spin energy stored in the non-equilibrium state of the initial muon polarization (this is called T_1 in NMR, or spin-lattice processes). The experimental parameter that allows us to independently measure the two relaxation terms is the geometry or configuration of the experimental setup. That is to say, either the initial muon spin polarization is longitudinal (in parallel) or transverse (perpendicular) to an external magnetic field. These were already described in the previous chapter. In the following, the muon polarization functions typically describing magnetic systems are discussed. Further reading about the theoretical concepts and detailed explanations about the technique and polarization functions can be found e.g. in Ref. [130].

4.2 Polarization and Relaxation Functions for Static Fields

In a case when there are no spin fluctuations in the studied spin system, the spin of a muon implanted into the sample will undergo Larmor precession around the static local field at the muon site, $\vec{B}_{loc}$. Static means B$_{loc}$ is constant over time, t $\gtrsim$ 5-10 τ_μ, where τ_μ is the muon lifetime. Hence, the precession frequency being directly proportional to the local field gives $\omega = \gamma_\mu |B_{loc}|$, and the proportionality constant γ_μ= $2\pi \times 135.5$ MHz T^{-1}, is the gyromagnetic ratio of the muon spin. This ratio is related to the muon magnetic moment m_μ via the relation, $m_\mu = \gamma_\mu S_\mu$, with $S_\mu = \frac{1}{2}$.

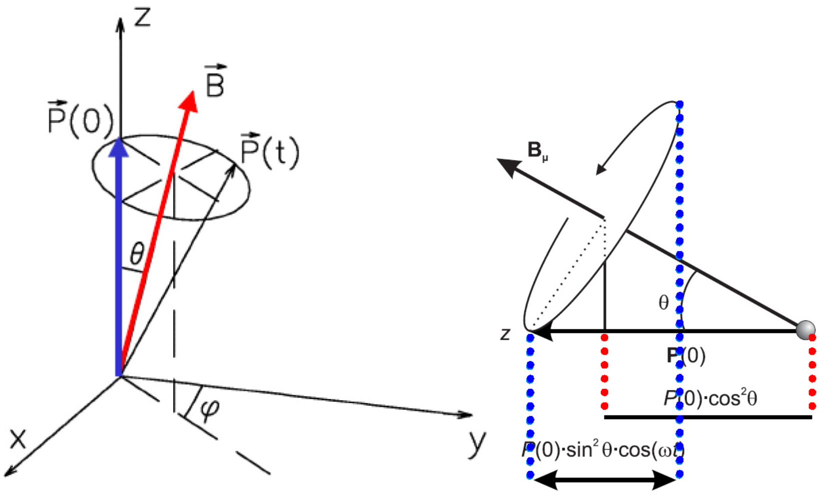

Figure 4.1: Muon spin precession in a constant field. The initial polarization is along the z-axis, which is also the observation direction, $\hat{n}$.

For a muon stopping in a sample at t= 0 and its spin is pointing in the z-direction as schematically shown in Figure 4.1, the time evolution of the z-component of the muon spin is given by

$$P(t) = P_{\vec{B}}(t) = \cos^2\theta + \sin^2\theta\cos(\omega_L t) \tag{4.1}$$

where θ is the angle between $\vec{B}$ and the initial muon spin which is assumed to lie along z.

The muons will sample a distribution of magnetic field magnitudes and directions. A particular field distribution, $\rho(\vec{B})$, is then assumed. If this field distribution $\rho(\vec{B})$ is known, the corresponding polarization function can thereupon be calculated:

$$P(t) = \frac{\int P_{\vec{B}}(t)\rho(\vec{B})\mathrm{d}^3B}{\int \rho(\vec{B})\mathrm{d}^3B} \tag{4.2}$$

This means that the muon polarization function can be obtained in a general way by calculating the muon spin precession around $\vec{B}$, finding its projection onto the z-axis, weighting it by $\rho(\vec{B})$, then integrating over all possible $\vec{B}$.

The above expression can be used to calculate the muon polarization function in some very special useful cases like those illustrated in Figure 4.2.

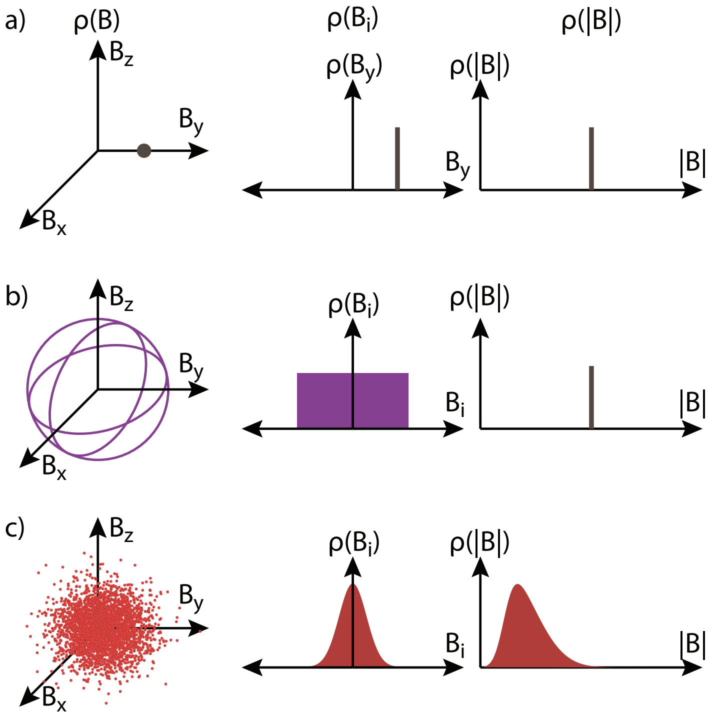

Figure 4.2: (a) $\vec{B} = B_0\hat{y}$, with no distribution of magnitude or direction, (b) a single field magnitude having random directions ($\rho(\vec{B})$ is a spherical shell of radius B_0), and (c) $\rho(\vec{B})$ has some distribution of field magnitudes and directions. The figure was adapted from Ref. [139].

In Figure 4.2(a), this case is exhibited by ideal single crystal samples where each muon senses a unique field of $\vec{B} = B_0\hat{y}$ while Figure 4.2(b) is exhibited in powder samples, wherein the field magnitude is unique but points in random directions, resulting to a $\rho(\vec{B})$ which is a spherical shell and $\rho(|B|) = \delta(|B| - B_0)$. The third one, case (c) is common for magnetic specimens possessing a certain degree of disorder or spin glass systems.

Since the samples investigated in this work are magnetic polycrystalline samples, then in the following I will elaborate on the muon polarization functions that describe the distribution of magnetic moments and their fluctuations in such a system.

$|\vec{B}|$ constant, random direction isotropically distributed

Again, in a simple case when we consider $|\vec{B}|$ is constant, it has random direction and isotropically distributed (e.g. in domain structures of magnetic materials or in ferromagnetic or antiferromagnetic powder samples), the field distribution is $p(\vec{B})d^3B = \delta(B - B_{loc})dBd\Omega$. We therefore obtain the powder average by integrating over θ and ϕ and we get the polarization function as:

$$P(t) = \frac{\int(\cos^2\theta + \sin^2\theta\cos(\omega_L t)\mathrm{d}(\cos\theta)d\phi}{\int\mathrm{d}(\cos\theta)d\phi} = \frac{1}{3} + \frac{2}{3}\cos(\gamma_\mu B_{loc}t) \tag{4.3}$$

The μSR spectrum illustrating this is shown in Figure 4.3. The presence of only one type of muon localization site is assumed, characterized by a single spontaneous local field. The $1/3$ term, which typically referred in the μSR jargon as the "1/3 tail", originates from the average projection of each muon spin onto the direction of the local field. This can be easily understood by considering that since the magnetic fields can have all the orientations, on the average one third of the muons will see fields parallel to their initial polarization and will not precess. This non-precessing component is always present for an isotropic field distribution. On the one hand, the 2/3 precessing component, are on the average, two thirds of the muons that see fields perpendicular to their initial polarization and will precess around them with the Larmor precession frequency, $\omega = \gamma_\mu B_{loc}$. This oscillating part indicates the magnetic long-range order in the compound.

In the case when the correlation length of a magnet is relatively small, or if the magnet is not perfectly ordered, the local field can take a large number of values close to each other. Consequently, one observes the oscillation to be strongly damped and can even vanish. If the muon spins precess too rapidly relative to the time resolution of the spectrometer, the oscillation or wiggles will be averaged out to zero. In addition, the obtained muon polarization will be constant at a level of $\frac{1}{3}$. Therefore, at a magnetic phase transition, if no wiggles are observed in the muon signal, one anticipates a drop in the effective initial asymmetry, A_{eff}.

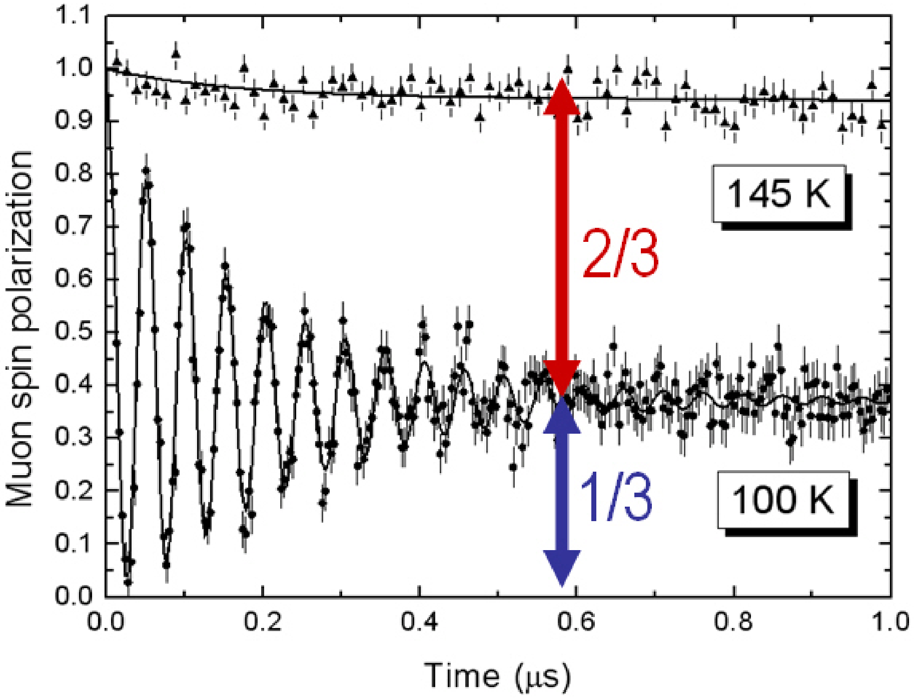

Figure 4.3: Example of a powder average of the μSR signal from a single muon site in a magnetically-ordered material.

That is, from $A_{eff} = A_0$ in the paramagnetic state to $A_0/3$ in the ordered state.

Although a similar signal can be obtained from a perfectly aligned single crystal with a unique field direction at the muon site as that of a powder of the same material, there are certain information that we can only obtain using a perfectly aligned single crystal such as that concerning the crystallographic direction of the internal fields. This, we cannot extract from a powder sample. In any case, the μSR technique can readily have access with the magnitude and the distribution of the magnitude of the internal fields with a powder sample, allowing experiments on systems that are not available to other techniques that specifically require single crystals.

μSR experiments are particularly straightforward since the muon ensemble is 100% polarized due to the parity violating beta decay of the pion. For instance, to learn the physics within a system, for example the case of nuclear dipolar fields when only relatively weak, random magnetic fields are present in the system, can simply be described by theoretical functions. The polarization functions adapted for this case were obtained by Kubo and colleagues [140]. This is further discussed in the following subsection.

4.2.1 Kubo-Toyabe Functions

Dense, randomly oriented magnetic moments

The magnetic field distribution sensed by muons in a system composed of dense randomly oriented magnetic moments, i.e. nuclear dipolar fields, is a Gaussian function. The corresponding relaxation function is given by the so-called Kubo-Toyabe function [140], derived from the names of the authors who first calculated it.

As illustrated in the left figure of Figure 4.4, randomly oriented spins with equal moments occupy each lattice site. In such a dense arrangement of spin system, the average spin-spin distance is of the same magnitude as the muon distance, and the magnetic fields arising from randomly pointing neighboring spins tend to cancel each other in the muon site.

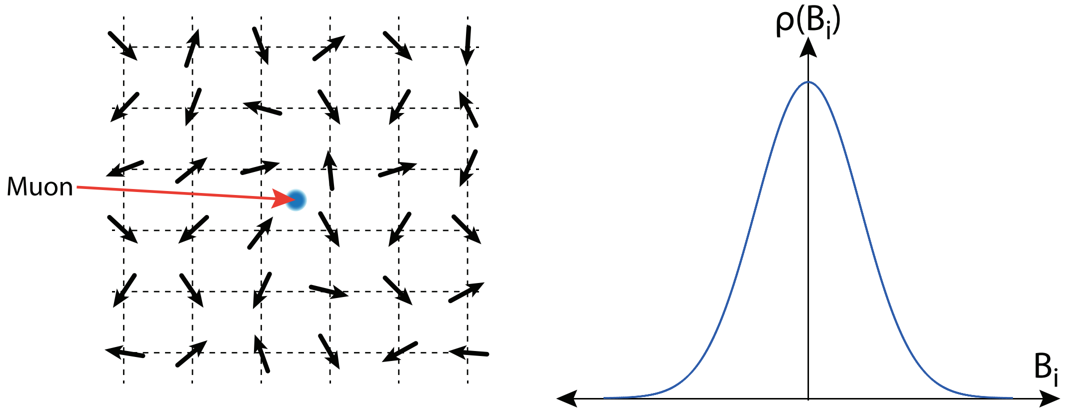

Figure 4.4: (left) Randomly oriented dense moments and (right) the resulting distribution of fields projected onto an axis. The projection is a Gaussian distribution.

Hence, for Gaussian distribution of $\vec{B}$ in x, y, and z direction with $\langle B\rangle = 0$ and $\left\langle \triangle B^2\right\rangle = \left\langle (B-\langle B\rangle)^2\right\rangle = \left\langle B^2\right\rangle - \langle B\rangle^2 = \frac{\sigma^2}{\gamma_\mu^2}$, this results in a field distribution with components that are well-approximated by independent Gaussian distribution, illustrated in the right figure of Figure 4.4 and written as:

$$\rho^G(B_i) = \frac{\gamma_\mu}{\sqrt{2\pi}\sigma}\exp\frac{-\gamma_\mu^2 B_i^2}{2\sigma^2}, \quad \text{for i = x, y, z} \tag{4.4}$$

where σ is the Gaussian field width.

Since the total distribution is isotropic, $\rho(|B|) = 4\pi B^2\rho(B_x)\rho(B_y)\rho(B_z)$, thus we obtain the distribution function for the absolute value $|\vec{B}|$ to be:

$$\rho^G(|\vec{B}|)\mathrm{d}(|B|) = \left(\frac{\gamma_\mu}{\sqrt{2\pi}\sigma}\right)^3 \exp-\frac{\gamma_\mu^2|B^2|}{2\sigma^2}\cdot 4\pi|B^2|\mathrm{d}|B| \tag{4.5}$$

The individual components are Maxwell-distributed with maximum at $|B| = \sqrt{2}\frac{\sigma}{\gamma_\mu}$ and $\left\langle |\vec{B}| \right\rangle \approx \sqrt{\frac{8}{\pi}}\frac{\sigma}{\gamma_\mu}$. The relaxation function is obtained in this case from:

$$P^{G-KT}(t) = \int \rho^G(B_x)\rho^G(B_y)\rho^G(B_z)P_{\vec{B}}(t)\mathrm{d}B_x\mathrm{d}B_y\mathrm{d}B_z \tag{4.6}$$

where $P_{\vec{B}}(t)$ is given in Equation 4.1.

The integration in Equation 4.6 can be explicitly performed. By doing so, the well known Kubo-Toyabe function can be obtained:

$$P^{G-KT}(t) = \frac{1}{3} + \frac{2}{3}(1 - \sigma^2 t^2)\exp[-\frac{\sigma^2 t^2}{2}] \tag{4.7}$$

Dilute, random moments

There also exists a case when the local fields are Lorentz instead of Gauss-distributed which is typically for dilute random spin systems, e.g spin glasses or dilute ferromagnetic impurities in a non-magnetic matrix. In such systems, the muon may sit very close to or very far from a magnetic moment, and the average spin-spin distance is much longer than the closest probable spin-muon distance. This is illustrated in the left figure of Figure 4.5.

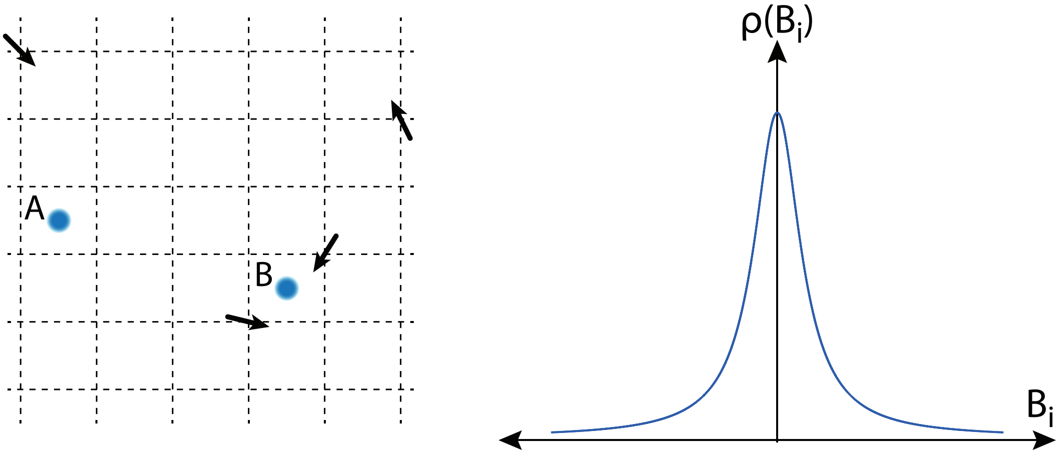

Figure 4.5: (left) Randomly oriented dilute moments. Muons at site A feel weak fields, while those at B feel stronger fields. (right) the resulting distribution of fields projected onto an axis. The projection is a Lorentzian distribution.

Muons positioned far from moments like in site A, experience weak fields with Gaussian distribution. On the other hand, muons which are close to moments experience stronger fields, though still with a Gaussian distribution but with a larger field width.

$$\rho^L(|B|)\mathrm{d}|B| = (\frac{\gamma_\mu^3}{\pi^2})\frac{a}{(a^2+\gamma_\mu^2 B^2)^2}\cdot 4\pi|B^2|\mathrm{d}|B| \tag{4.8}$$

It holds:

$$\begin{aligned}\rho^L(B_x) = \iint \mathrm{P}(|B|)\mathrm{dB_y dB_z} \\ = (\frac{\gamma_\mu}{\pi})\frac{a}{(a^2+\gamma_\mu^2 B_x^2)}\end{aligned} \tag{4.9}$$

where ($\frac{a}{\gamma_\mu}$ = half width at half maximum).

In this case the integration yields what is referred as the static Lorentz Kubo-Toyabe function (in ZF):

$$P^{L-KT}(t) = \frac{1}{3}+\frac{2}{3}(1-\mathrm{at})\mathrm{e}^{-\mathrm{at}} \tag{4.10}$$

4.2.2 LF-μSR for Static Fields

Further confirmation of the distribution of internal fields may be obtained by applying an external magnetic field along the initial direction of the muon spin. This is what is known as longitudinal field (LF) μSR. This technique is not only good in elucidating the distribution of static fields but also gives information about fluctuating fields. Thus, LF- μSR measurements are primarily used to distinguish between static and dynamic contributions to the relaxation.

Taking the abovementioned Gaussian Kubo-Toyabe example but in addition an external field $\vec{B}_{ext}\|\hat{z}$ is applied, the total distribution is displaced along the z-axis, as illustrated in Figure 4.6. In this case, the distribution modifies to:

$$\rho^G(B_z) = \frac{\gamma_\mu}{\sqrt{2\pi}\sigma}\exp[-\frac{\gamma_\mu^2(B_{ext}-B_z)^2}{2\sigma^2}] \tag{4.11}$$

The distributions $\rho(B_x)$ and $\rho(B_y)$ remain unchanged, while $\rho(B_z)$ becomes $\rho(B_z+B_{ext})$. Integrating Equation 4.6 with the new distribution, we get the so-called Gauss-Kubo-Toyabe relaxation in longitudinal field:

$$P^{G-KT}(t,B_{ext}) = 1-\frac{2\sigma^2}{(\gamma_\mu B_{ext})^2}[1-\mathrm{e}^{-\frac{\sigma^2 t^2}{2}}\cos(\gamma_\mu B_{ext}t)]+\frac{2\sigma^4}{(\gamma_\mu B_{ext})^3}+\int_0^t \mathrm{e}^{-\frac{\sigma^2 t^2}{2}}\sin(\gamma_\mu B_{ext}t')\mathrm{d}t' \tag{4.12}$$

If B_{ext} is large with respect to the local fields, the polarization of the muon is kept and the spin will be aligned along the z-direction. That is, the spectra obtained in LF-μSR will

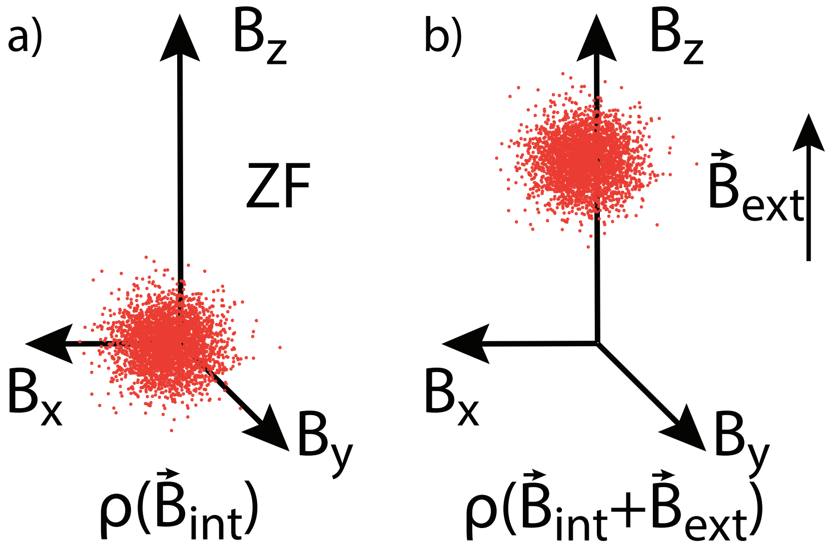

Figure 4.6: Distribution of static internal fields (a) without and (b) with a longitudinal applied field $LF = B_{ext}\hat{z}$.

no longer have an asymptote at 1/3, but rather goes closer to 1 as LF increases. This is the so-called *decoupling* of static fields, shown in Figure 4.7.

4.3 Fluctuating Moments

Previously, internal magnetic fields which are static on the timescale of the muon lifetime were considered in deriving the muon polarization functions. In this section, the polarization functions of the muon ensemble for the case of fluctuating spin systems is qualitatively discussed. There are models that introduce and elucidate the effects of time dependent fields in μSR polarization functions: the simple model that depicts the Brownian motion of the phase of the muon spin precession, and the stochastic strong collision model. For further reading about these models, see the review on μSR relaxation functions in magnetic materials [141].

There are two possible reasons why a magnetic system could appear dynamic in a μSR measurement. Either the magnetism itself is dynamic or the muon is dynamic, i.e. diffusing in a static spin system [142]. The latter depends on the binding potential of the muon on the crystal. Usually in oxides, the muon is strongly bound to the oxygen atom. Muon diffusion will be ruled out in the discussions as this was not observed in this work.

For dynamical cases, the muon polarization function is quite different. Using the technique established by Kubo and Toyabe [140], the dynamic polarization functions were also derived. It assumes a strong collision Markovian process wherein the muon feels a sudden change of

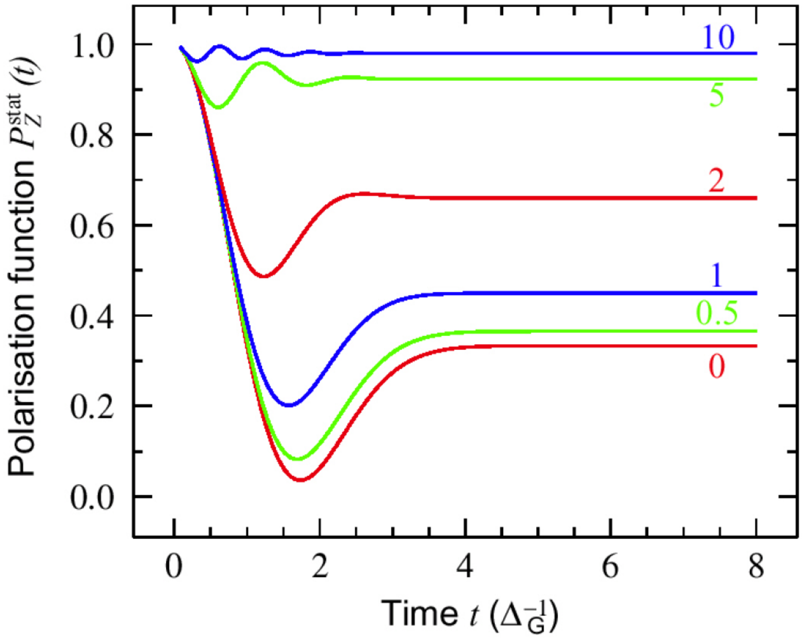

Figure 4.7: Field dependence of the polarization function for isotropic Gauss-distributed fields. Time scale in units of $1/\sigma$. B_{ext} in units of σ/γ_μ. The zero field curve corresponds to the Kubo-Toyabe function.

field and that is uncorrelated to the previous field direction. In the fast fluctuation limit, the dynamical Gaussian Kubo-Toyabe function is given by:

$$G_{DynamicGKT}(t, \nu \gg \sigma) = \exp(-\lambda t) \tag{4.13}$$

One of the signatures of a dynamic relaxation process is the loss of the 1/3 tail, i.e. in the case of dynamic fields there is no longer an asymptote at 1/3 but instead at 0. In the fast fluctuation limit, $\nu \gg \sigma$, the relaxation is well-described by an exponential function. Here, ν is the fluctuation rate.

In contrast to static field distributions where the partial decoupling happens when the magnitude of the external field is similar to that of the static internal fields, the decoupling in the case of fluctuating fields happens only when the external field is of the same scale as the fluctuation rate, as γ_μ $\mathrm{B}_{LF} \sim \nu$ which is in the fast fluctuation limit much larger than the static field width. Thus, the decoupling of the muon polarization function in an applied LF makes it possible to isolate the origin of the muon relaxation either as static or dynamic. Figure 4.8 illustrates the dynamic Gauss-Kubo Toyabe in ZF case.

One can also perform an LF-μSR experiment as a function of temperature. What one can observe from plotting the relaxation rate λ from this measurement is that it gives a peak at

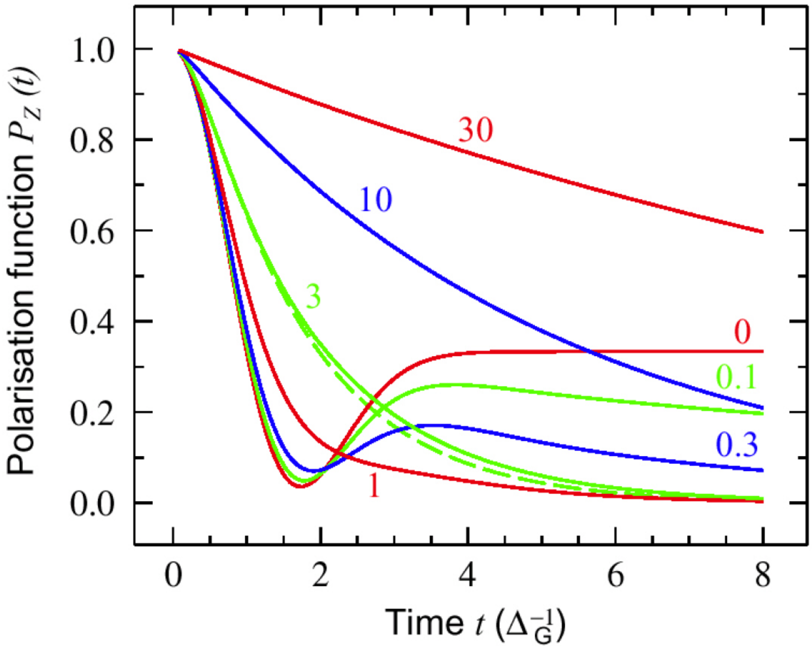

Figure 4.8: Dynamic Gauss Kubo-Toyabe: Strong Collision Model for an isotropic Gauss distribution of fields (with variance σ), B$_{ext}$ = 0. The fluctuation rate ν is given in units of σ. The dashed curve is the motional narrowing limit (exponential) for $\frac{\nu}{\sigma} = 3$.

the transition temperature. This peak indicates that at low temperatures the relaxation rate is low because the magnetic system is ordered, while at high temperatures the relaxation rate is low because the magnetic system fluctuates very rapidly. This is the μSR version of the famous $1/T1$ peak, where T_1 is the spin-lattice relaxation time in the NMR jargon.

In the slow fluctuation limit ($\nu \ll \sigma$), it is possible to multiply the static relaxation function with a dynamic relaxation function. In the case of a random Gaussian field distribution this results in: G$_{dynamicGKT}$(t, $\nu \ll \sigma$) = P^{G-KT}(t) exp(-λ_L t), where λ_L is the dynamic relaxation rate and P^{G-KT}(t) is Equation 4.7.

In the case of a Lorentzian field distribution with a non-zero first moment (average field) in the slow fluctuation limit, the ideal relaxation function given in Equation 4.3 changes to:

$$P(t) = \frac{1}{3}\exp(-\lambda_L t) + \frac{2}{3}\cos(\gamma_\mu B_{loc} t)\exp(-\lambda_T t) \tag{4.14}$$

with λ_L being the dynamic longitudinal relaxation rate, and λ_T the transverse relaxation rate being a measure for the width of the field distribution and dynamic effects.

4.4 The Cosine and Bessel Functions

Magnetic materials with an isotropic distribution of well-defined local field B at the muon site gives a coherent muon spin precession, which for powder averaged samples yield the functional form known as the Cosine function, given in Equation 4.3 and Equation 4.14. Corresponding examples arising from the said distribution are the commensurate spin density wave systems.

The Bessel function is commonly used to describe depolarization of the muons in a polycrystalline sample that has a field distribution that resembles the Overhauser distribution:

$$\rho(B) = \frac{2}{\pi} \frac{1}{\sqrt{\mathrm{B}_{\mathrm{max}}^2 - \mathrm{B}^2}} \tag{4.15}$$

with the polarization function derived as

$$P(t) = \frac{1}{3} \exp(-\lambda_L t) + \frac{2}{3} J_0(\gamma_\mu B_{loc} t) \exp(-\lambda_T t) \tag{4.16}$$

This function is characterized by a long-lived oscillation that is initially strongly damped and a phase shift compared to a Cosine function with the same argument. A physical scenario that is typically described by such a function is incommensurate spin density wave system [143].

4.5 Fast Fourier Transform in μSR

Performing a fast Fourier transform (FFT) of the muon spin polarization function is a common and useful procedure to promptly have an approximate visual illustration or a picture of the internal magnetic field distribution. It also provides a quick comparison of the measured μSR signal with the best-fit theory function from the time domain. This is done by integrating the time-domain polarization function such that the field distribution is then given by,

$$\rho(B) = \int_0^\infty \widetilde{P}(t) e^{-i(\gamma_\mu B t + \phi)} dt \tag{4.17}$$

where $\widetilde{P}(t) = P_x(t) + iP_y(t)$.

The real part of the Fourier transform reflects the local-field distribution.

There are however some limitations to the measured time spectrum that introduce statistical noise and ringing in the FFT spectrum. Such limitations are due to the finite lifetime of the muon thereby resulting to fewer counts at later times, or due to finite counting rates so the length of the time spectrum is also finite. These unwanted features are smoothed out by introducing an apodization function.

Apodization can also be called as data windowing, wherein the asymmetry spectrum is multiplied by a weighting function which varies between one and zero to suppress the ringing in the FFT spectrum.

5 Structural and Magnetic Properties of T'-La_2CuO_4

Recently for the first time, bulk undoped $La_2CuO_{4+\delta}$ was stabilized in the metastable T'-structure by a low-temperature synthesis method [44, 144]. We determined its crystal structure by synchrotron powder diffraction and thermal neutron scattering measurements. Then its magnetic properties were profoundly examined via cold neutron scattering, bulk μSR, and NMR. These are combined efforts from LMU-PSI, TU Darmstadt, and TU Dresden encompassing a collaborative project to extensively investigate structural and magnetic properties of body-centered tetragonal (BCT) cuprates in general.

Investigations and findings on this compound can be a benchmark for further understanding of the magnetic properties of the mother compounds T'-RE_2CuO_4 (RE= Pr, Nd, Eu). Fundamental questions had long-confronted the rare-earth cuprates, specifically the influence of a polarizable magnetic ion on the underlying interactions that define their magnetic structure and characteristic magnetic properties. In the T'-La_2CuO_4 (T'-LCO), the complex magnetic interactions between the CuO_2 and the rare-earth subsystems is eradicated since La is nonmagnetic. This makes T'-LCO the ideal system among the BCT cuprates to study the magnetic interactions of the CuO_2 plane alone.

Another of our objective is to determine the role of the reduction process and its effects on oxygen stoichiometry and on magnetism of the rare-earth cuprate mother compounds. Reducing the as-grown materials has dramatic consequences for the magnetic and conducting properties in electron-doped cuprates. However, this is also dependent on which oxygen site is vacated. This topic will be addressed and discussed in the succeeding chapters. For T'-LCO, we found and will herein present, that the as-grown compound is already stoichiometric and annealing is not necessary to remove oxygen. In addition, since it is metastable, subjecting it to higher temperature would transform it to the orthorhombic T-phase.

5.1 Structural Characterization

The crystallographic properties of T'-LCO are thoroughly examined by several techniques. Synchrotron powder diffraction had been performed to initially verify the homogeneity of the T'-phase.[1] Analysis of the oxygen stoichiometry of T'-LCO was independently performed with neutron scattering measurements at the thermal neutron powder diffractometer, HRPT, SINQ, PSI. The obtained data had been Rietveld refined using different refinement software packages done by the author and the collaborating groups to crosscheck the obtained results. At the end of this structural characterization section is a publication exhibiting the combined works about the structural properties and oxygen occupancies of T'-LCO. The analysis of the oxygen stoichiometry was done with the use of TOPAS, GSAS, and Fullprof refinement software packages.[2]

5.1.1 Synchrotron Powder Diffraction

Polycrystalline monophasic T'-La$_2$CuO$_4$ (T'-LCO) was obtained at 653 K in a CsOH flux, as described in Ref. [44]. The large size of the cesium ions make it a good flux medium since it does not enter into the La$_2$CuO$_4$ structure. The resulting powder was then washed with flowing argon and deionized water. This step had to be undertaken in order to dissolve the flux before it was filtered off and dried overnight at 343 K in vacuum. However, it was then later on found out that this washing step had resulted to the presence of a very minimal amount of a second phase (less than 2%) identified to be La(OH)$_3$. Despite this, the obtained compound is without a coexisting T-phase as revealed by the synchrotron powder diffraction pattern shown in Figure 5.1, collected with a wavelength of λ = 99.9615 pm and a Ge(111) monochromator at DESY/Hasylab B2 beamline with the use of a 0.5 mm boron-silica-glass capillaries. Rietveld refinement was performed using the TOPAS software package. Available data for Nd$_2$CuO$_4$ [145] was initially used as a template, and for the impurity La(OH)$_3$ structure data was obtained from [146]. Table 5.1 shows the positional parameters used in the TOPAS refinement and Table 5.2 shows the refined lattice parameters. The synchrotron results gave preliminary structural analyses for the T'-LCO. Further investigations primarily about the oxygen stoichiometry were performed using thermal neutrons due to their higher sensitivity to oxygen. This will be discussed in the next section.

---

[1] T'-La$_2$CuO$_4$ samples were synthesized by Roland Hord, our collaborator from the group of Prof. Barbara Albert and under the supervision of Prof. Lambert Alff of the Technical University of Darmstadt, Germany.

[2] These packages implement the Rietveld refinement method and the instruction guide for each software is readily available in their respective webpages.

Table 5.1: Positional parameters of T'-La_2CuO_4 for the synchrotron data refined by TOPAS.

Atom	Wyck.	x/a	y/b	z/c
La	4e	0.00000	0.00000	0.3512(5)
Cu	2a	0.00000	0.00000	0.00000
O1	4c	0.00000	0.50000	0.00000
O2	4d	0.00000	0.50000	0.25000

Table 5.2: Lattice constants (in Å) of T'-LCO refined by TOPAS

a	b	c
4.0091(1)	4.0091(1)	12.5443(5)

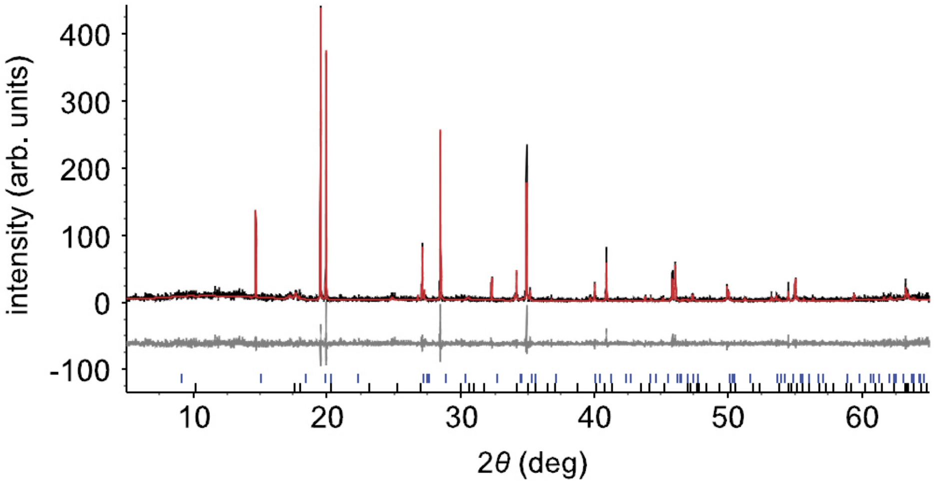

Figure 5.1: Synchrotron powder diffraction profile of T'-La_2CuO_4 at room temperature.

5.1.2 Thermal Neutron Scattering Measurements on T'-La_2CuO_4

Neutron scattering is an important tool to refine the structural parameters of our samples. High-resolution neutron powder diffraction was performed at the thermal neutron HRPT Powder Diffractometer of the Swiss Spallation Source (SINQ), PSI, in order to determine the exact structure and oxygen occupation of T'-La_2CuO_4. The sample was placed in a rotating cylindrical 6mm-diameter vanadium sample holder. Monochromated neutrons with wavelengths 1.1545 Å and 1.494 Å, respectively, were utilized using a Ge(hkk) focusing monochromator. The use of two wavelengths is strategic and useful as this allows one to get both correct definition of very small occupancies and of the anisotropic displacement parameters (ADP). In addition, doing this can provide better resolution for low Q peaks from larger wavelength. Neutron diffraction patterns were collected from $2\theta = 3$ to 180 degrees.

Refinement analysis, particularly the Rietveld method, extracts the needed information from the neutron diffraction measurements. A profile analysis program called Fullprof was primarily used. A detailed explanation and description of the parameters are outlined on the Fullprof website. Rietveld refinement is done by minimizing the weighted squared difference between the observed and the calculated patterns of the crystal (and/or magnetic structure). In the case of the electron-doped cuprates crystallizing in the I4/mmm space group, the structure data of Nd_2CuO_4 [145] was initially used as a template. Since there is an impurity phase of $La(OH)_3$, this was added as a second phase. A pseudo-voigt profile function was used to fit the Bragg peaks. The background can be manually added or it can also be modeled or generated as a polynomial function. An example of a Fullprof pcr code file for T'-La_2CuO_4 refinement is given in the appendix. The space group I4/mmm has a total multiplicity of 32. The atoms are positioned in symmetry-allowed sites. In the refinement, O(3) position was manually put since it is a defect site for T'-structures. The O(2) and O(3) isotropic factors are made to correlate in the refinements, since the small occupation of the O(3) site does not allow for an individual refinement. The z-coordinate for the O(3) position was then fixed to the value that obtained a reasonable Cu-O(3) distance.

Figure 5.2 displays the refined neutron diffraction profile. Tables 5.3 and 5.4 summarize the refined structural parameters for T'-LCO.

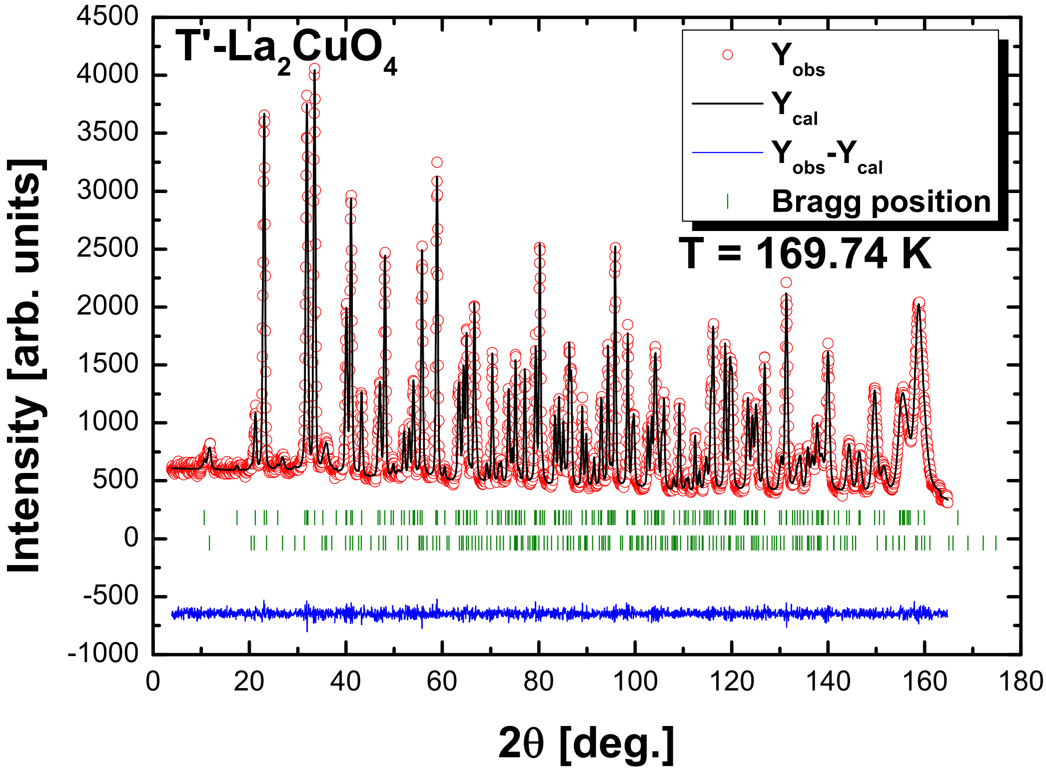

Figure 5.2: Thermal neutron diffraction pattern for T'-LCO at $T = 169.74$ K.

Table 5.3: Lattice Constants (in Å) of T'-LCO refined by Fullprof

a	b	c
4.00624(5)	4.00624(5)	12.5324(3)

Table 5.4: T'-LCO positional parameters and occupation sites

Name	Wyck.	x/a	sx	y/b	sy	z/c	sz	occ.	socc
La1	4e	0.00000	(0)	0.00000	(0)	0.35220	(9)	1.010	(2)
Cu1	2a	0.00000	(0)	0.00000	(0)	0.00000	(0)	1.000	(0)
O1	4c	0.00000	(0)	0.50000	(0)	0.00000	(0)	1.020	(2)
O2	4d	0.00000	(0)	0.50000	(0)	0.25000	(0)	1.010	(2)
O3	4e	0.00000	(0)	0.00000	(0)	0.10000	(0)	0.040	(2)

From the Rietveld refinement in Table 5.4, the presence of a minute O(3) can be negligible. A full occupation is 1. Thus, e.g. in the O(3) site, this very minute occupation can be accounted to systematic effects incurred in the refinement or fitting process.

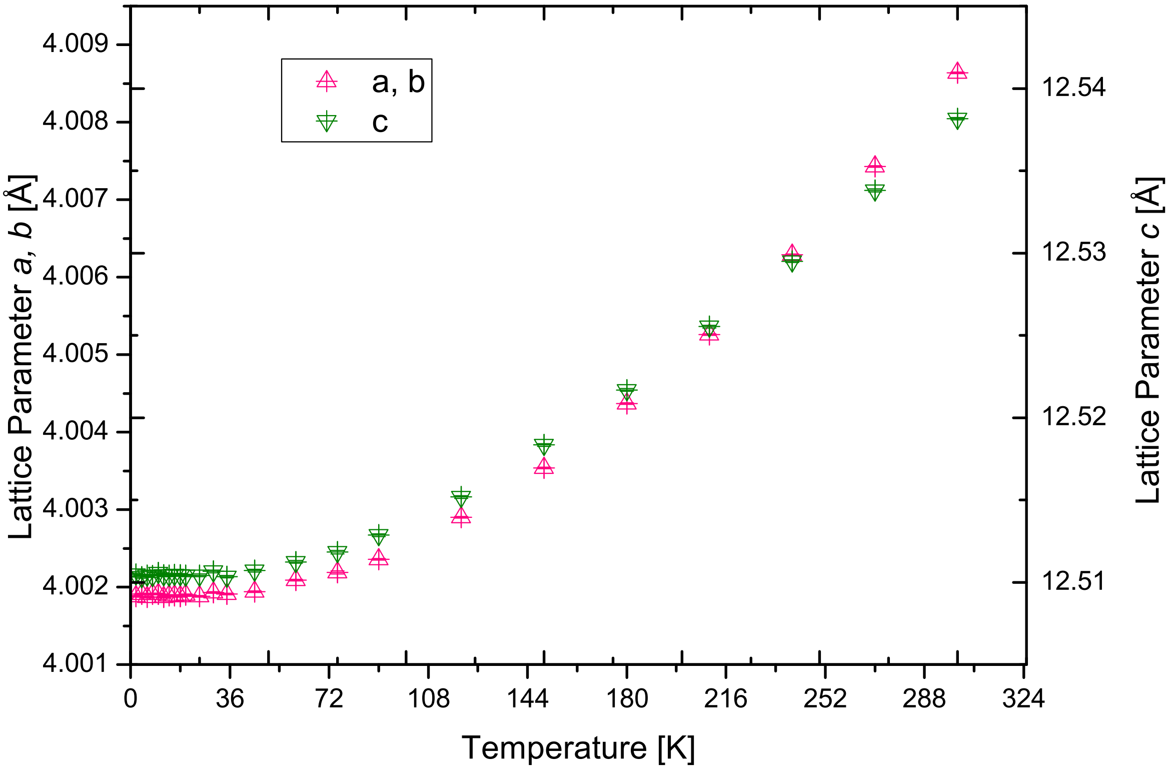

Figure 5.3: Temperature dependence of the lattice parameters of T'-La_2CuO_4.

In addition, measurements to obtain the temperature dependence of the lattice constants were also performed and the results are shown in Figure 5.3. An expansion of the lattice constants with increasing temperature is a normal behavior, i.e. it does not show any anomalies indicating structural phase transitions.

The neutron results are in good agreement with the synchrotron data but obtained much more precise occupancies. The comparison of these results is given in Table 5.5.

Table 5.5: Data collection and TOPAS refinement results for La_2CuO_4 (tetragonal symmetry, space group *I4=mmm*) comparing synchrotron and neutron data. R_p is the profile R parameter, R_{wp} the weighted profile R parameter, R_{exp} is the best possible R_{wp} or expected R parameter, and GOF is the goodness of fit.

Method	Synchrotron (at 300 K)	Neutron (at 170 K)
a, b (pm)	400.91(1)	400.624(5)
c (pm)	1254.43(5)	1253.24(3)
$V/10^{-6}$ (pm^3)	201.61(2)	201.144(6)
Calculated density (g cm^{-3})	6.6923(5)	6.8963(2)
Measuring range (2θ)	5-65	3-180
R_p	28.41	4.03
R_{wp}	37.2	5.22
R_{exp}	36.74	4.42
GOF	1.01	1.18

Other Rietveld refinement programs like TOPAS and GSAS had also been used for the investigation of the possible presence of apical oxygen O(3). In any refinement, it is imperative to firstly refine the zero point of the diffractometer. Then the background parameters were also refined. Thereafter, the lattice parameters, the positional parameter and the occupancy were refined. The results obtained using different refinement softwares were summarized in Table 5.6.

Table 5.6: T'-LCO positional parameters and occupation sites obtained by neutron diffraction and refined using several programs.

				TOPAS		GSAS		Fullprof	
Atom	Wyck.	x/a	y/b	z/c	occ.	z/c	occ.	z/c	occ.
La	4e	0	0	0.35195(7)	1.035(7)	0.35224(7)	1.003(5)	0.3522(9)	1.01(2)
Cu	2a	0	0	0	1.010(1)	0	1.010(1)	0	1.00
O1	4c	0	0.5	0	1.040(1)	0	1.000(7)	0	1.02(2)
O2	4d	0	0.5	0.25	1.040(1)	0.25	1.000(7)	0.25	1.01(2)
O3	4e	0	0	0.15(2)	0.013(8)	–	–	0.1	0.04(2)

For the refinement with TOPAS, a copper to apical oxygen bond length of z/c = 0.195 which is comparable to other rare earth cuprates, was assumed in order to determine a correct positional parameter value for the inserted O(3). The results from the refinement with TOPAS obtained an unreasonably decrease of copper to oxygen bond length to ~ 1.88 Å as the positional parameter z/c for the O(3) position had changed its value from 0.195 to 0.15(2). When the O(3) position was set and fixed to a value that provided reasonable Cu-O distance and when the occupancies of La, Cu, O(1) and O(2) were set to 1, the value of the occupancy of O(3) became zero (0.0005(48)). An even shorter bond length was obtained from Fullprof results. For the GSAS refinement, a positional parameter of z/c= 0.35 was obtained when O(3) was inserted. This directly corresponds to the La position. Thus, this too is an unreliable and unreasonable result leading to the conclusion that it is not possible to refine an occupancy parameter for O(3) because it yields unphysical results. In addition, there was an increase of the statistical average χ^2 upon inclusion of O(3) position implying that the structure model including O(3) is not true. On a good note, without inserting the O(3) position in GSAS, a nominal stoichiometry for all elements within an error below 0.01 was obtained.

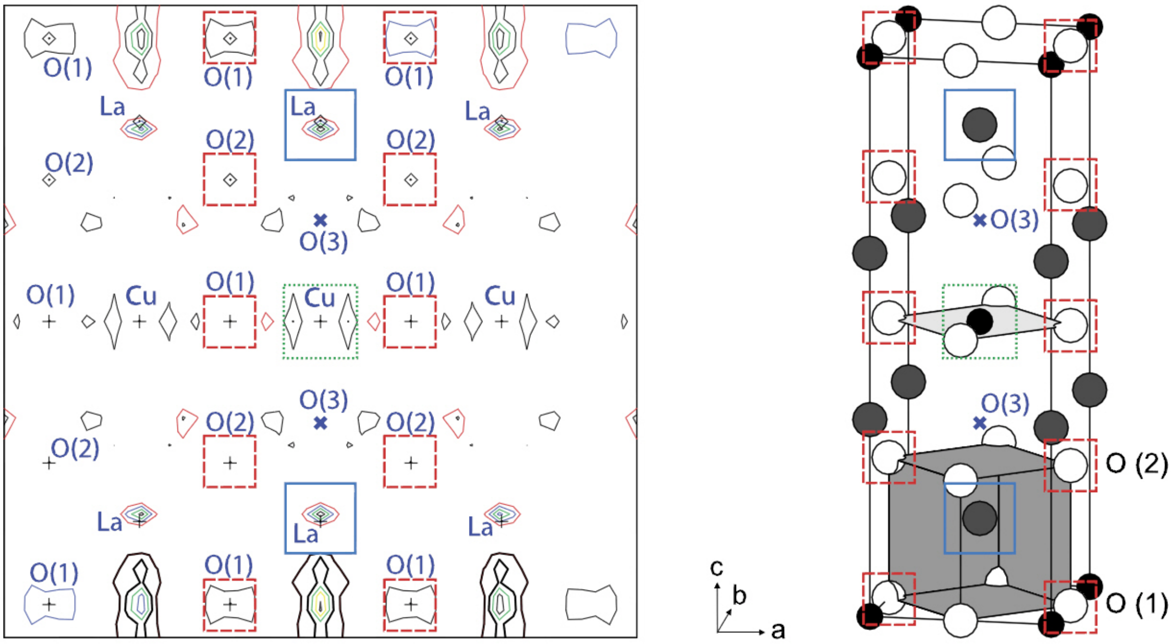

Figure 5.4: Residual scattering density (symbolized by clouds) in the ac-plane centered around the copper ion as obtained from neutron diffraction data using GSAS. The contour lines are drawn between 0.09 and 0.43 e Å^{-3}. The contour interval is 0.09 e Å^{-3}. Reproduced from Reference [147].

The GSAS refinement results giving a stoichiometric T'-LCO is further reinforced by the residual neutron scattering density map. Figure 5.4 displays the scattering density in the *ac*-plane with the copper ion in the center. The corresponding positions in the unit cell are as well labelled in the figure. Focusing on the O(3) position which are expected above and below the Cu site, one can see that there were no residual scattering density obtained at all. The highest residual scattering densities are visibly around the La position, and in between oxygen sites.

In conclusion, from our high resolution neutron scattering data on the T'-La_2CuO_4 compound, we find that the low-temperature synthesis yields a stoichiometric La_2CuO_4 compound without a detectable occupation of the apical O(3) defect site. This is very remarkable since the usually used high temperature solid state reaction technique yields always specimens with well measurable O(3) occupation.

The investigation of the oxygen stoichiometry of T'-LCO was concluded in a recent publication in the Superconductor Science and Technology journal (R. Hord, G. Pascua, et al. Oxygen stoichiometry of low-temperature synthesized metastable T'-La_2CuO_4. Supercond. Sci. Technol. **26** (2013) 105026 (6pp)). This is displayed in the next pages.

IOP Publishing — Superconductor Science and Technology

Supercond. Sci. Technol. **26** (2013) 105026 (6pp) doi:10.1088/0953-2048/26/10/105026

Oxygen stoichiometry of low-temperature synthesized metastable T'-La_2CuO_4

R Hord[1], G Pascua[2], K Hofmann[1], G Cordier[1], J Kurian[3], H Luetkens[2], V Pomjakushin[2], M Reehuis[4], B Albert[1] and L Alff[3]

[1] Eduard-Zintl-Institute of Inorganic and Physical Chemistry, Technische Universität Darmstadt, Darmstadt, Germany
[2] Paul-Scherrer-Institute (PSI), Villigen, Switzerland
[3] Institute of Materials Science, Technische Universität Darmstadt, Darmstadt, Germany
[4] Helmholtz-Zentrum Berlin (HZB), Berlin, Germany

E-mail: alff@oxide.tu-darmstadt.de

Received 3 June 2013, in final form 1 August 2013
Published 12 September 2013
Online at stacks.iop.org/SUST/26/105026

Abstract

We have investigated the oxygen stoichiometry of low-temperature synthesized metastable T'-La_2CuO_4 bulk samples by neutron scattering. T'-La_2CuO_4 is the parent compound of electron-doped high-temperature superconductors that is chemically closest to the parent compound of the hole-doped superconductor T-La_2CuO_4. While usually all electron-doped cuprates require strong reduction to approach stoichiometry, the low-temperature synthesis directly yields fully stoichiometric compounds. This result makes low-temperature grown T'-La_2CuO_4 the ideal material to perform a comparison of the two parent compounds of hole- and electron-doped cuprates.

(Some figures may appear in colour only in the online journal)

1. Introduction

It is still a dream of high-temperature superconductivity research to have a material that can be both hole *and* electron doped without structural change to obtain a unified superconductivity phase diagram. Only in the compound $Y_{1-z}La_z(Ba_{1-x}La_x)_2Cu_3O_y$, the region around zero-doping could be explored at both sides of the phase diagram revealing different magnetic behavior, however without reaching the superconducting state, neither by electron doping nor by hole doping [1]. The physics of electron and hole doping has therefore been discussed based on a phase diagram of structurally and chemically very different materials. In this phase diagram, for hole-doped cuprates the antiferromagnetic interaction is rather rapidly suppressed upon doping, while in electron-doped cuprates the antiferromagnetic phase survives to higher doping concentrations, leading to a much narrower superconducting region [2]. In the system La_2CuO_4 hole doping can be realized by substituting the trivalent La by a divalent element (e.g. Ba, Sr, Ca), whereas electron doping can be achieved in the system RE_2CuO_4 (RE = Pr, Nd etc) by substitution of RE by a tetravalent element (Ce, Th). However, hole and electron-doped compounds always have a different crystal structure: hole-doped materials grow in the so-called T-structure, while electron-doped cuprates grow in the so-called T'-structure (see figure 1). Since the T'-form of La_2CuO_4 is metastable, electron doping induced superconductivity was mostly studied in the compounds T'-$RE_{2-x}Ce_xCuO_4$ with RE = Nd and Pr [3, 4]. Recently, by combining differential scanning calorimetry, high-temperature oxide melt solution calorimetry, and transposed temperature drop calorimetry, the amount of enthalpy by which the T'-form of La_2CuO_4 is less stable than the orthorhombic form at room temperature has been directly measured to be 1.40 ± 0.56 kJ mol^{-1} [5]. This relatively small difference in energy is the reason why the metastable compound is accessible to synthesis by circumventing thermodynamic equilibrium. After early attempts to grow T'-La_2CuO_4 [6], it was in thin films that the phase diagram of T'-$La_{2-x}Ce_xCuO_4$ became available [7, 8]. The phase diagram of electron-doped $La_{2-x}Ce_xCuO_4$ shows much more similarity to the phase diagram of hole-doped $La_{2-x}Sr_xCuO_4$, proving that the early phase diagrams based on $Nd_{2-x}Ce_xCuO_4$ were not generic [9]. The importance

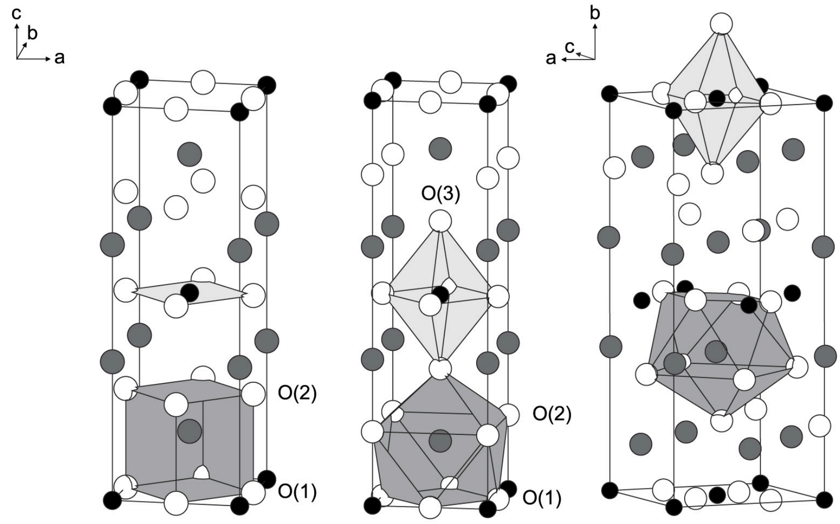

Figure 1. Unit cells of T'-, K_2NiF_4-type (both space group $I4/mmm$, No. 139), and orthorhombic (space group $Cmce$, No. 64) modifications of La_2CuO_4 (from left to right). Small black dots symbolize copper, large black dots lanthanum, and white dots oxygen.

of the compound T'-La_2CuO_4 lies in the fact that it is the parent compound of electron-doped cuprates. In contrast to the T-modification where the copper atoms are octahedrally coordinated by oxygen, the T'-modification forms sheets of Cu–O squares with fourfold coordination (see figure 1). Recently, it has been shown by muon spin rotation that T'-La_2CuO_4 is an antiferromagnetic insulator and shows a strikingly different magnetic behavior due to its enhanced two-dimensionality [10]. Within the T'-family, the absence of a magnetic lanthanide such as Pr or Nd reduces strongly the interplanar magnetic coupling between adjacent copper oxide layers. In T'-La_2CuO_4 two distinct temperatures are observed associated with a slowing down of antiferromagnetic fluctuations at $T_{N1} \approx 200$ K, and finally static order at $T_{N2} \approx 115$ K [10]. In contrast, in T-La_2CuO_4 the octahedral oxygen environment of copper suppresses antiferromagnetic fluctuations and enhances antiferromagnetic long-range order, so that $T_{N1} \approx T_{N2} \approx 300$ K. Since T_N strongly depends on doping, it is of utmost importance to have stoichiometric samples. While different soft-chemical synthesis routes have been applied to obtain T'-La_2CuO_4 [10, 11], the bulk synthesis of the doped compound T'-$La_{2-x}Ce_xCuO_4$ is still elusive.

It is a remarkable feature of the synthesis of electron-doped cuprates that a strong oxygen reduction is necessary to obtain superconducting samples [12]. One possible reason is that during synthesis small amounts of oxygen populate an interstitial defect site corresponding to the apical oxygen site in the T-structure (so-called O(3) position). Since oxygen stoichiometry implies charge carrier doping, unrevealed oxygen off-stoichiometry can lead to physical misinterpretation of data. We now summarize corresponding oxygen stoichiometry studies for electron-doped materials and their parent compounds. Estimations showed that the total amount of removed oxygen during the reduction step lies between 0.01 and 0.04 [13–16]. Previous neutron diffraction studies on $Nd_{2-x}Ce_xCuO_4$ confirmed the picture that reduction decreases the amount of oxygen at the O(3) defect position while the slightly deficient O(1) (within the copper oxygen plane) and O(2) (within the charge reservoir layer) sites hardly differ for as-grown (nonsuperconducting) and reduced (superconducting) samples [15, 17, 18]. Investigations of the Nd-based parent compound Nd_2CuO_4 showed O(1) and O(2) deficiencies of about 2.5% each for as-grown samples. After oxidation O(1) is fully occupied, however, O(2) is still 2.5% deficient and O(3) (apical oxygen) is unoccupied [19]. Neutron diffraction studies of Nd_2CuO_4 single crystals report O(3) occupancies of $\sim$0.1 (oxidized) and $\sim$0.04 (reduced), while O(1) and O(2) are not fully occupied [20]. Apparently, there is almost no difference in O(1) and O(2) occupancies between reduced and oxidized crystals. Refined Cu–O(3) bond lengths of 2.45 Å (oxidized) and 2.49 Å (reduced) are comparable with copper to apical oxygen bond lengths of other cuprates. In comparison to undoped Nd_2CuO_4, single crystals of electron-doped $Nd_{2-x}Ce_xCuO_4$ have O(3) occupancy values of 0.06(1) for oxidized and 0.04(1) for reduced crystals [21]. In addition to oxygen off-stoichiometry, it has also been found in as-grown samples that a considerable amount of in-plane Cu vacancies can occur which disappear upon annealing [22]. However, also in these samples the oxygen O(1) occupation deviates by about 0.05 from the stoichiometric value. It has been shown that Nd_2CuO_4 and Pr_2CuO_4 are antiferromagnetic Mott insulators [2, 20], however, there are also some reports about superconductivity in such 'undoped' compounds [23]. For $La_2CuO_{4+\delta}$ a complex phase diagram as a function of δ including hole-induced superconductivity has been established [24]. Therefore, the correct knowledge of oxygen stoichiometry is necessary and crucial for understanding the physics of high-temperature superconductors.

Bulk material of undoped RE_2CuO_4 and electron-doped $RE_{2-x}Ce_xCuO_4$ (RE = Pr, Nd etc) is typically obtained via solid-state reaction in air at high temperatures. Regardless of whether doped or undoped, these compounds crystallize in the T'-modification (Nd_2CuO_4 structure type). However, solid-state reaction of La_2O_3 and CuO at high temperatures leads to the orthorhombic modification (see figure 1). T'-La_2CuO_4 is metastable and transforms to the high-temperature T-modification upon heating [25]. It is not possible to obtain T'-La_2CuO_4 directly via high-temperature synthesis, but only using low-temperature approaches, e.g. using a flux medium [10]. This paper reports a detailed neutron diffraction study of low-temperature synthesized T'-La_2CuO_4 to identify the oxygen occupancies in this important material.

2. Experimental details

Crystalline powder of T'-La_2CuO_4 was prepared by mixing stoichiometric amounts of La_2O_3 and CuO and heating them to 653 K in a CsOH flux [25, 10]. After drying, the chemicals were ground using an agate mortar. The gray mixture was placed as thin pellets in open silver crucibles which were heated in a furnace under purified argon at 653 K for 24 h. After cooling to room temperature the black reaction cake was removed mechanically from the bottom of the crucible and ground in an argon glovebox. The black powder was washed under flowing argon with deionized water in order to dissolve the flux before it was filtered off and dried at 343 K in vacuo overnight.

Infrared spectroscopy was used to show the absence of CsOH and H_2O. The measurements showed an unwanted, weak but sharp absorption band at $\nu = 3610\ \mathrm{cm}^{-1}$ that can be assigned to $La(OH)_3$. The absence of elements other than La, Cu, and O was shown by energy dispersive x-ray spectroscopy. In particular, no Cs has been incorporated into the sample. Synchrotron x-ray diffraction patterns of the powder samples were collected at room temperature at DESY/Hasylab (beamline B2, $\lambda = 99.9615$ pm, Ge(111) monochromator) using 0.5 mm boron–silica-glass capillaries. Neutron diffraction patterns were collected at 169.74 K from 3° to 180° in 2θ at the high-resolution powder diffractometer for thermal neutrons (HRPT) of the Paul-Scherrer-Institute [26]. Monochromated neutrons with a wavelength of 115.450 pm were obtained using a Ge(hkk) focusing monochromator. The sample was placed in a rotating cylindrical vanadium sample holder with 6 mm diameter. Rietveld refinements were performed using different program packages TOPAS [27], GSAS [28], and FullProf [29].

3. Results and discussion

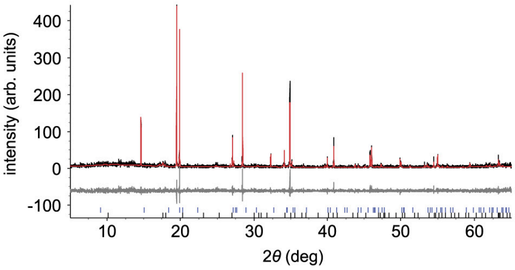

Figure 2. Observed and calculated synchrotron powder patterns of Rietveld refined T'-La_2CuO_4 at room temperature. The gray curve is the difference curve. Vertical dashes indicate the positions of the reflections of the Nd_2CuO_4 structure model (top) and the by-product $La(OH)_3$ (bottom).

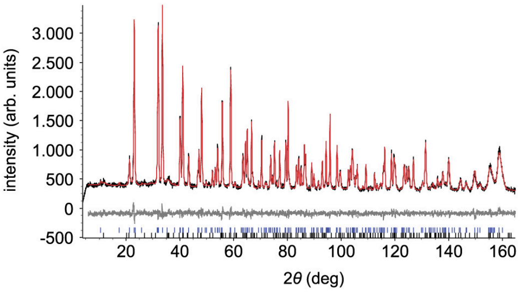

Figure 3. Observed and calculated neutron powder-diffraction patterns of Rietveld refined T'-La_2CuO_4 at 169.74 K. The gray curve is the difference curve. Vertical dashes indicate the positions of the reflections of the Nd_2CuO_4 structure model (top) and the by-product $La(OH)_3$ (bottom).

Table 1. Positional parameters of T'-La_2CuO_4 (space group No. 139) for the synchrotron data refined by TOPAS.

Atom	Wyck.	x/a	y/b	z/c
La	4e	0	0	0.3512(5)
Cu	2a	0	0	0
O(1)	4c	0	0.5	0
O(2)	4d	0	0.5	0.25

Both synchrotron and neutron data show weak additional peaks of $La(OH)_3$ among those of the major phase T'-La_2CuO_4. These impurity reflections were not visible in x-ray diffraction patterns collected by conventional laboratory equipment (powder-diffraction system STADI P (Fa. STOE) in transmission geometry) at room temperature on flat plate holders using monochromated cobalt radiation ($\lambda = 178.896$ pm). Available structure data of Nd_2CuO_4 [30] and $La(OH)_3$ [31] were used as starting parameters for refinement. Experimental and calculated powder x-ray diffraction patterns are shown in figure 2 (synchrotron data) and figure 3 (neutron data). A pseudo-Voigt profile function was used to fit the peaks and the background was modeled with a second order function. The lattice parameters were refined before zero correction was carried out. After fixing them, positional parameters and occupancies were refined. The refinement results and the positional parameters are shown in tables 1 and 2. In the following discussion we will focus on the neutron scattering data which are in complete

Table 2. Positional parameters and occupancies of T'-La_2CuO_4 (space group No. 139) obtained by neutron diffraction and refined using several programs.

				TOPAS		GSAS		FullProf	
Atom	Wyck.	x/a	y/b	z/c	Occ.	z/c	Occ.	z/c	Occ.
La	4e	0	0	0.351 95(7)	1.035(7)	0.352 24(7)	1.003(5)	0.3522(9)	1.01(2)
Cu	2a	0	0	0	1.01(1)	0	1.01(1)	0	1
O(1)	4c	0	0.5	0	1.04(1)	0	1.00(7)	0	1.02(2)
O(2)	4d	0	0.5	0.25	1.04(1)	0.25	1.00(7)	0.25	1.01(2)
O(3)	4e	0	0	0.15(2)	0.013(8)	—	—	0.1	0.04(2)

Table 3. Data collection and TOPAS refinement results for La_2CuO_4 (tetragonal symmetry, space group $I4/mmm$) comparing synchrotron and neutron data. R_p is the profile R parameter, R_{wp} the weighted profile R parameter, R_{exp} is the best possible R_{wp} or expected R parameter, and GOF is the goodness of fit.

Method	Synchrotron (at 300 K)	Neutron (at 170 K)
a, b (pm)	400.91(1)	400.624(5)
c (pm)	1254.43(5)	1253.24(3)
$V/10^{-6}$ (pm^3)	201.61(2)	201.144(6)
Calculated density (g cm^{-3})	6.6923(5)	6.8963(2)
Measuring range (2θ)	5–65	3–180
R_p	28.41	4.03
R_{wp}	37.2	5.22
R_{exp}	36.74	4.42
GOF	1.01	1.18

Table 4. The 20 positional parameters with the highest residual scattering densities obtained by GSAS from neutron diffraction data.

	ρ	x	y	z
1	0.511	0.0000	0.0000	0.5000
2	0.459	0.0000	0.0000	0.3418
3	0.285	0.0000	0.0000	0.4282
4	0.228	0.0000	0.2660	0.1766
5	0.178	0.0000	0.1523	0.0000
6	0.167	0.0000	0.3948	0.5000
7	0.148	0.0000	0.3120	0.0000
8	0.131	0.0000	0.1307	0.4530
9	0.127	0.1917	0.1917	0.0000
10	0.101	0.0000	0.1505	0.2124
11	0.090	0.0000	0.0000	0.2535
12	0.088	0.2113	0.2113	0.2248
13	0.076	0.0256	0.2766	0.2384
14	0.075	0.1386	0.1386	0.1004
15	0.075	0.0000	0.5000	0.2500
16	0.073	0.1465	0.2957	0.3125
17	0.070	0.0000	0.1701	0.3819
18	0.068	0.1163	0.2449	0.0667
19	0.067	0.0000	0.4146	0.2790
20	0.064	0.0000	0.1671	0.1148

agreement with synchrotron data, but yield much more precise occupancies.

For the investigation of the possible presence of apical O(3) oxygen, we have added the corresponding defect site manually to the Nd_2CuO_4 structure model. To determine a correct positional parameter value for the inserted O(3) oxygen, we assumed a copper to apical oxygen bond length comparable to other rare earth cuprates, $z/c = 0.195$. After refining the background, lattice parameters, and zero correction the positional z/c parameter and the occupancy were freely refined. The results of these refinements as obtained from the different refinement programs are shown in table 2. Using TOPAS, the positional parameter z/c for the O(3) position changes its value from 0.195 to 0.15(2). This results in an unreasonably short copper to apical oxygen bond length of ~1.88 Å. The occupancies of all atoms were refined freely together with the positional parameters given in table 2. This results in an unreasonable Cu–O(3) distance. When the O(3) position was fixed on a value that ensures a reasonable Cu–O distance, and when the occupancies of La, Cu, O(1), and O(2) were fixed to the value one, the occupancy of O(3) became zero (0.0005(48)). FullProf refinement gives an even shorter bond length. When O(3) oxygen is included in the GSAS refinement, a positional parameter of $z/c = 0.35$ is obtained corresponding exactly to the La position. This is also an unreasonable result, and, thus, it is not possible to refine an occupancy parameter for O(3). We note that the inclusion of the O(3) position leads to an increase of the statistical average χ^2, suggesting also that the structure model including O(3) is not true. Without offering the O(3) position as a refinement parameter, GSAS yields the nominal stoichiometry within an error below 0.01. We have summarized lattice parameters and discrepancy indices of the synchrotron and neutron data in table 3.

So far, the diffraction data and their Rietveld refinement clearly suggest that T'-La_2CuO_4 is stoichiometric. For more details, we discuss the residual neutron scattering density, ρ, map as obtained from GSAS. In figure 4 such a map is shown corresponding to the scattering density in the ac plane with the copper ion in the center. The corresponding positions in the unit cell are also indicated in figure 4. The positions with the highest residual scattering densities are especially around the La position, above/below La, and between oxygen sites. The here discussed O(3) position is above/below the Cu site where no residual scattering density is obtained at all. In table 4 the 20 positions with the highest residual scattering density are given. None of these positions corresponds to a reasonable O(3) position ($x/a = 0, y/b = 0$, and $z/c \sim 0.195$). A tiny value of $\rho = 0.090$ is observed on the eleventh place with position parameters $x/a = 0, y/b = 0$, and $z/c = 0.2535$. However, this would correspond to a copper to apical oxygen bond length of 3.17 Å, which is clearly too large as compared to similar compounds. We therefore conclude that neutron and synchrotron diffraction indicate a fully

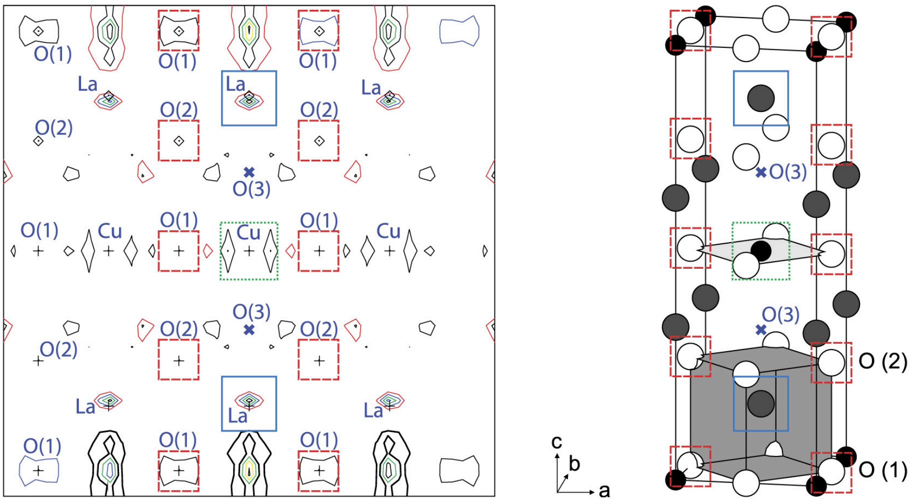

Figure 4. Residual scattering density (symbolized by clouds) in the *ac*-plane centered around the copper ion as obtained from neutron diffraction data using GSAS. The contour lines are drawn between 0.09 and 0.43 e Å^{-3}. The contour interval is 0.09 e Å^{-3}.

stoichiometric compound T'-La$_2$CuO$_4$ without measurable interstitial oxygen defects. Note also that the Cu occupation (see table 2) is the nominal one within an error of ±0.01. Effects from in-plane copper vacancies as discussed in literature [22] are not relevant for the low-temperature synthesized samples.

4. Conclusion

The oxygen stoichiometry and occupancy of the apical oxygen position in T'-La$_2$CuO$_4$ was analyzed by a detailed refinement of synchrotron x-ray and neutron diffraction data using the Rietveld programs TOPAS, GSAS, and FullProf. The inclusion of apical oxygen as interstitial defect site O(3) yields unphysical values of the corresponding bond length. There is no indication that residual scattering density at any interstitial site has to be taken into account. We conclude that the low-temperature synthesis gives, as a free gift, stoichiometric compounds with an experimental error below 0.01, making additional reduction or annealing steps obsolete. The 'real' parent compound of the electron-doped cuprates, T'-La$_2$CuO$_4$, is also an antiferromagnetic insulator as T-La$_2$CuO$_4$, but with different magnetic behavior due to the difference in crystal structure. Low-temperature synthesized samples allow an intrinsic comparison of the physical disparities of the two parent compounds of hole and electron-doped cuprates.

Acknowledgments

This work was supported by DFG (Deutsche Forschungsgemeinschaft) Grant Nos Al536/9 and Al560/9.

References

[1] Segawa K, Kofu M, Lee S-H, Tsukada I, Hiraka H, Fujita M, Chang S, Yamada K and Ando Y 2010 *Nature Phys.* **6** 579
[2] Luke G M *et al* 1990 *Phys. Rev.* B **42** 7981
[3] Tokura Y, Takagi H and Uchida S 1989 *Nature* **337** 345
[4] Alff L, Krockenberger Y, Welter B, Schonecke M, Gross R, Manske D and Naito M 2003 *Nature* **422** 698
[5] Lilova K I, Hord R, Alff L, Albert B and Navrotsky A 2013 *J. Solid State Chem.* **204** 91–4
[6] Chou F C, Cho J H, Miller L L and Johnston D C 1990 *Phys. Rev.* B **42** 6172
[7] Naito M and Hepp M 2000 *Japan. J. Appl. Phys.* **39** L485
[8] Sawa A, Kawasaki M, Takagi H and Tokura Y 2002 *Phys. Rev.* B **66** 014531
[9] Krockenberger Y, Kurian J, Winkler A, Tsukada A, Naito M and Alff L 2008 *Phys. Rev.* B **77** 060505(R)
[10] Hord R *et al* 2010 *Phys. Rev.* B **82** 1805081
[11] Houchati M I, Ceretti M, Ritter C and Paulus W 2012 *Chem. Mater.* **24** 3811
[12] Takagi H, Uchida S and Tokura Y 1989 *Phys. Rev. Lett.* **62** 1197
[13] Tarascon J-M *et al* 1989 *Phys. Rev.* B **40** 4494
[14] Takayama-Muromachi E, Izumi F, Uchida Y, Kato K and Asano H 1989 *Physica* C **159** 634
[15] Suzuki K, Kishio K, Hasegawa T and Kitazawa K 1990 *Physica* C **166** 357
[16] Kim J S and Gaskell D R 1993 *Physica* C **209** 381
[17] Izumi F, Matsui Y, Takagi H, Uchida S, Tokura Y and Asano H 1989 *Physica* C **158** 433
[18] Kwei G H, Cheong S-W, Fisk Z, Garzon F H, Goldstone J A and Thompson J D 1989 *Phys. Rev.* B **40** 9370
[19] Marin C, Henry J Y and Boucherie J X 1993 *Solid State Commun.* **86** 425
[20] Radaelli P G, Jorgensen J D, Schultz A J, Peng J L and Greene R L 1994 *Phys. Rev.* B **49** 15322
[21] Schultz A J, Jorgensen J D, Peng J L and Greene R L 1996 *Phys. Rev.* B **53** 5157
[22] Kang H J, Dai P, Campbell B J, Chupas P J, Rosenkranz S, Lee P L, Huang Q, Li S, Komiya S and Ando Y 2007 *Nature Mater.* **6** 224

[23] Krockenberger Y, Yamamoto H, Tsukada A, Mitsuhashi M and Naito M 2012 *Phys. Rev.* B **85** 184502

[24] Wells B O, Lee Y S, Kastner M A, Christianson R J, Birgeneau R J, Yamada K, Endoh Y and Shirane G 1997 *Science* **277** 1067

[25] Hord R, Cordier G, Hofmann K, Buckow A, Pascua G, Luetkens H, Alff L and Albert B 2011 *Z. Anorg. Allg. Chem.* **637** 1114

[26] Fischer P *et al* 2000 *Physica* B **276–278** 146

[27] Topas 4.2 2009 *Bruker AXS*

[28] Larson A and van Dreele R 2001 *General Structure Analysis System* (Los Alamos, USA: Los Alamos National Laboratory)

[29] Rodriguez-Carvajal J 1990 *Abstract of the Satellite Meeting on Powder Diffraction of the XV Congress of the IUCr* (Toulouse: International Union of Crystallography) p 127

[30] Makarova I P, Simonov V I, Blomberg M K and Merisalo M J 1996 *Acta Crystallogr.* B **52** 93

[31] Zachariasen W H 1948 *Acta Crystallogr.* **1** 265

5.2 Magnetic Properties

In the following, I will thoroughly describe the magnetic properties of the bulk T'-La_2CuO_4 (T'-LCO) using combined cold neutron scattering, μSR, and ^{139}La-NMR techniques. Detailed analysis of μSR data is reinforced by the determination of the muon site. In the end, a physical scenario is proposed with the unified efforts and understanding from the results of the mentioned techniques.

5.2.1 Cold Neutron Scattering Measurements on T'-La_2CuO_4

Cold neutron scattering measurements were done at the DMC diffractometer at PSI in order to investigate the magnetic structure of the sample. The measurements were done at three temperature regimes; at room temperature 300 K, at an intermediate temperature of 60 K, and base temperature of 1.7 K. Figure 5.5 shows the diffraction pattern of the sample. A decrease and a shift of the intensity peaks at the two extreme temperatures, 300 K and 1.7 K, were observed as lattice constants also expand with increasing temperature. However, it gives an apparently strange behavior at the intermediate temperature as the nuclear peaks give the highest intensities.

No concrete findings can be drawn from the measurements since there were no evident magnetic peaks detected at the expected positions. This could be due to the small magnetic moments of our sample which neutrons cannot detect or this could also be due to diffuse background signal due to the presence of a 7% impurity phase of $La(OH)_3$. Hydrogen has a large incoherent scattering length and this had produced the relatively high background. There was, however, the apparent observation of a tiny unknown peak at $2\theta = 10.9$, which was a bit far from the expected nuclear peak at $2\theta = 11.26^\circ$. In addition, two other smaller peaks were seen which are presumed to be magnetic peaks since they are essentially absent at 300 K, see the inset of Figure 5.5 pointed by the two right blue arrows. Unfortunately, these peaks could not be indexed by any magnetic model and their origin is therefore unclear at the moment. Since the $La(OH)_3$ phase is a product obtained after the synthesis and only when the sample had to be washed with water, then future works would attempt to wash the samples with heavy water D_2O instead. This should drastically reduce the diffuse scattering and therefore allow clear determination of magnetic peaks from ordered magnetic Cu moments as small as 0.3 μ_B which seems to be not possible with the present sample containing $La(OH)_3$.

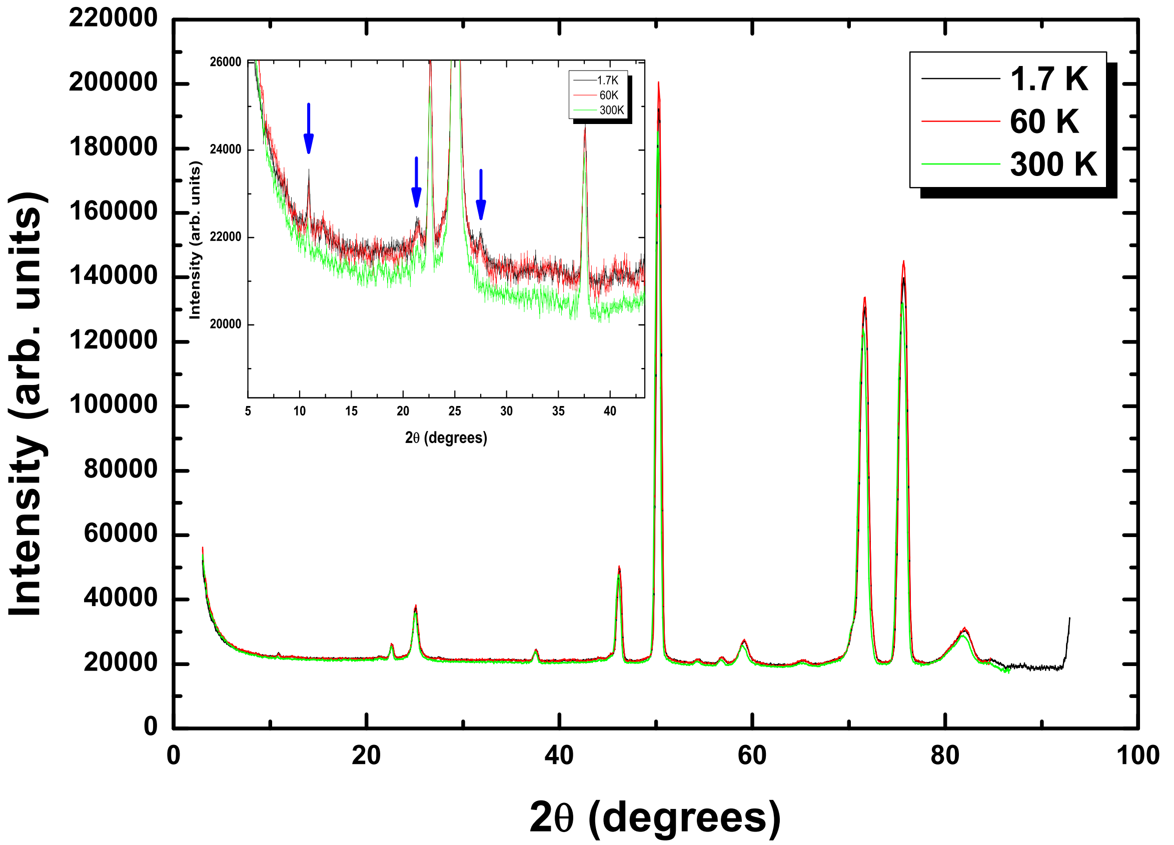

Figure 5.5: Diffraction patterns at temperatures 1.7 K, 60 K, and 300 K from DMC of T'-LCO. Inset: The two right blue arrows point at unknown peaks that are presumably magnetic peaks which disappear at increasing temperatures.

5.2.2 μSR Measurements on T'-La$_2$CuO$_4$

The magnetic properties of T'-La$_2$CuO$_4$ were investigated by muon-spin rotation and relaxation (μSR) using the General Purpose Surface muon spectrometer (GPS) of the πM3 beamline at the Paul Scherrer Institute (PSI), Switzerland. The data were analyzed using the Musrfit program [148].

Zero-Field μSR (ZF-μSR) Measurements on T'-LCO

ZF-μSR was performed on T'-LCO to microscopically examine its magnetic properties. Representative ZF-spectra at 10, 70, 115, 180, 220, and 300 K are shown in Figure 5.6. At the highest temperature, T'-La$_2$CuO$_4$ is in the paramagnetic state and the muon spin polarization *P(t)* is well-described by the Gaussian Kubo-Toyabe function[142] which is given in Equation 4.7.

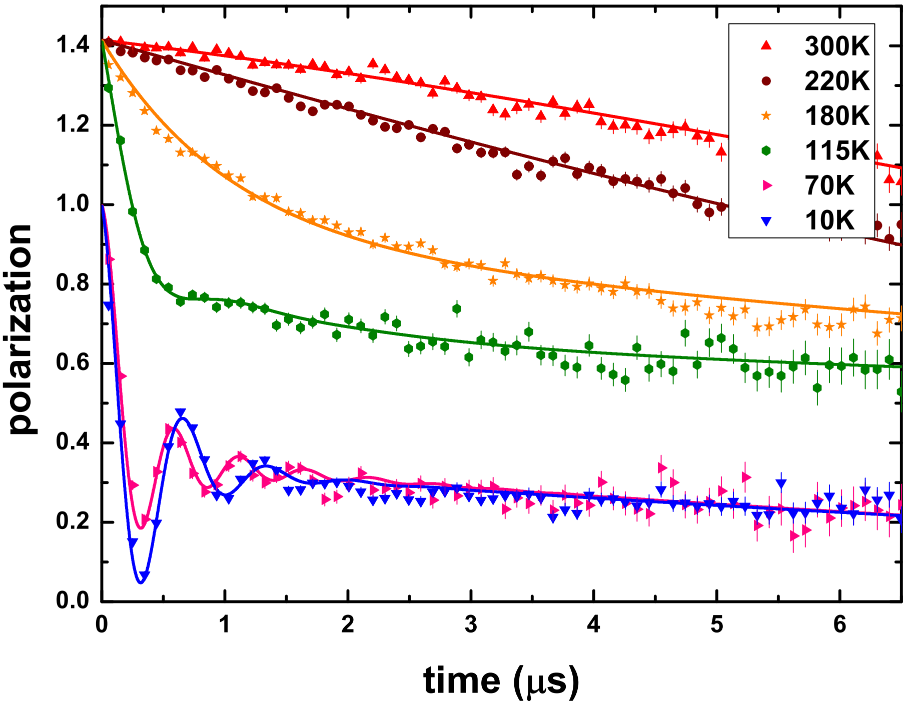

Figure 5.6: Zero-field spectra at 10, 70, 115, 180, 220, 300 K. The plot was shifted by +0.4 for T= 115, 180, 220, and 300 K for display clarity purposes.

In this typical functional form, the depolarization originates from the interaction of the muon spin with static and randomly oriented nuclear magnetic moments. The paramagnetic Cu 3d moments are rapidly fluctuating resulting to a depolarization, given by the field averaged over the muon lifetime, with a small relaxation rate compared with the nuclear contribution.

Then at a slightly lower temperature, an exponential depolarization emerges. Magnetism starts to develop at 220 K as shown in Figure 5.7a. In addition, an increase in the transverse relaxation rate λ_T at this temperature is observed, as shown in Figure 5.7c. Please note that λ_T includes static as well as dynamic contributions to the transverse relaxation. On top of it, in Figure 5.7d, λ_L also starts to increase at 220 K and this is given only by the dynamic contributions. This means that magnetic correlations start to build up but that at the same time the system continues to be weakly (slowly) dynamic. Hence, at this intermediate temperature range, T'-La_2CuO_4 is said to be in the quasistatic regime due to the presence of dynamics on top of a static signal. This fact is already visible from the raw data where a clear strong relaxation of the 2/3 component (transverse relaxation) and a slow relaxation of the 1/3 tail (longitudinal relaxation) is visible. This is, of course, reflected in the corresponding fit parameters shown in Fig. 5.7 where the λ_T is always larger than λ_L by a factor 5. Note that for fast fluctuations the relaxation function would be given by a single exponential function ($\lambda_T = \lambda_L$), which is clearly not the case here. The presence of weak dynamics is also obtained from longitudinal field measurements as exemplified in Figure 5.8 for a temperature of 155 K. At all fields, the spectra are characterized by a clear long time relaxation indicating the presence of magnetic dynamics (compare to Chapter 4). At this temperature, the data are best-fitted with a dynamic Lorentz-Kubo-Toyabe function. As a reference, the corresponding static theory functions are displayed which clearly do not reproduce the observed decoupling behavior .

With decreasing temperature, the fluctuations further slow down which increases the observable depolarization. Both the transverse as well the longitudinal relaxation increases indicating that the size of the quasi-ordered magnetic Cu moments grows towards lower temperatures and that the fluctuation rate of the internal field decreases in this temperature range, respectively.

Below $T_{\mathrm{N2}} = 115\ K$, the electronic moments get static on the scale of the muon lifetime, prompting the muons to precess in the static local fields produced by the Cu moments. This is shown in Figure 5.7b, wherein the frequency starts to grow at 115 K. Correspondingly, λ_L peaks at this temperature signifying the onset of the static regime. Note that this peak corresponds to the famous $1/T_1$ peak usually observed in NMR experiments at second order phase transitions. Below this temperature, a broad field distribution resembling that of the Overhauser-field distribution is observed, see Figure 5.9. Hence, the muon spin precession

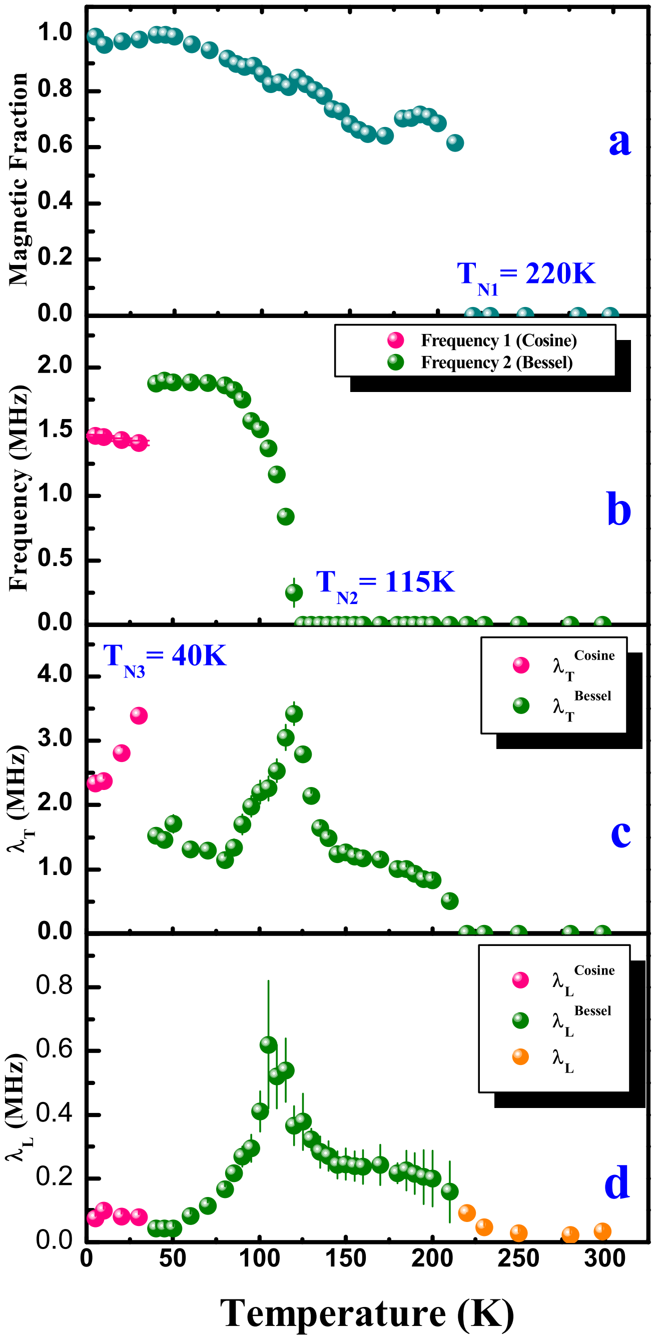

Figure 5.7: ZF-μSR fit results for T'-La_2CuO_4: a) The magnetic volume fraction as a function of temperature of T'-La_2CuO_4, b) the frequency dependence as a function of temperature, c) the transverse relaxation rate, and d) the longitudinal relaxation rate.

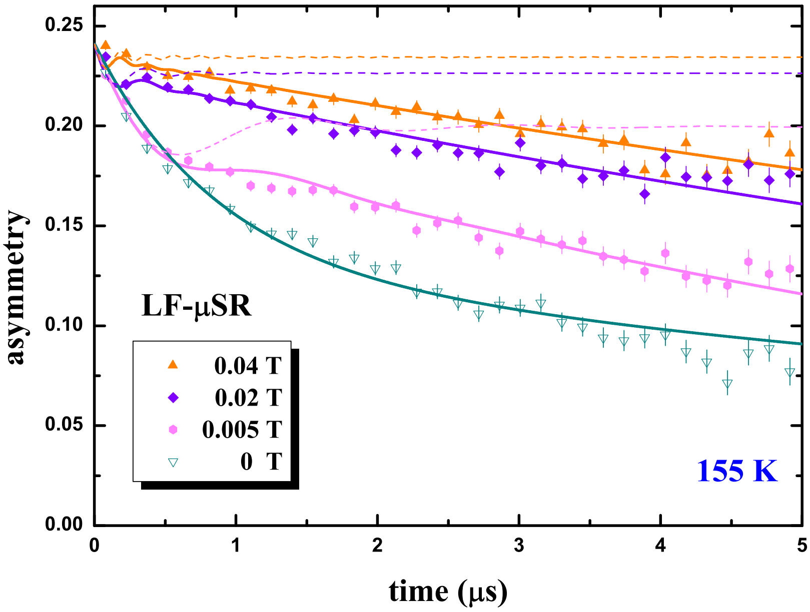

Figure 5.8: Longitudinal field μSR at 155 K with 0, 0.005, 0.02, and 0.04 Tesla applied fields. At this temperature, the data are best-fitted with a dynamic Lorentz-Kubo-Toyabe function. The dashed lines are the theoretical fits considering static fields.

observed in this powder magnetic material at this temperature regime can be well-described with a zeroth-order Bessel function. This function is characterized by a phase shift compared to a cosine function and an initially strongly damped oscillation. The muon polarization has the functional form:

$$P(t) = \frac{2}{3}e^{-\lambda_T t}\mathrm{j}_0(2\pi f t) + \frac{1}{3}e^{-\lambda_L t} \tag{5.1}$$

where j_0 is the zeroth-order Bessel function and $f_\mu = \gamma_\mu / (2\pi)\, B_{\mathrm{loc}}$. The observation of a 2/3 oscillating μSR signal fraction and 1/3 non-oscillating fraction comes from spatial averaging of powder samples where 2/3 of the local field components are perpendicular to the initial muon spin and cause a precession, while 1/3 of the local fields are parallel and do not cause a precession. As said above, the relaxation of the oscillating signal, λ_T, includes both static and dynamical effects. Effectively, the transverse relaxation results from the intrinsic width of the Overhauser field distribution, and in addition static magnetic disorder and dynamics. On the other hand, the relaxation of the second term, λ_L, is solely due to dynamic magnetic fluctuations.

Interestingly, at 40 K, there is an abrupt change of the field distribution and the data can be well-described, down to lowest temperatures, with a standard cosine function having the polarization function:

$$P(t) = \frac{2}{3} e^{-\lambda_T t} \cos(2\pi f t) + \frac{1}{3} e^{-\lambda_L t} \tag{5.2}$$

Astoundingly, the amplitudes of the signal fractions of the respective Bessel and Cosine components really show an impetuous transition, if these parameters are both initially left free in the data fitting analysis. Additionally, the mere time-spectra e.g. in Figure 5.9(left), already shows out-of-phase oscillations at the different temperature regions below and above 40 K. To further illustrate this abrupt change in the field distribution, a Fast Fourier Transform (FFT) at temperatures above and below 40 K is plotted in Figure 5.9(right).

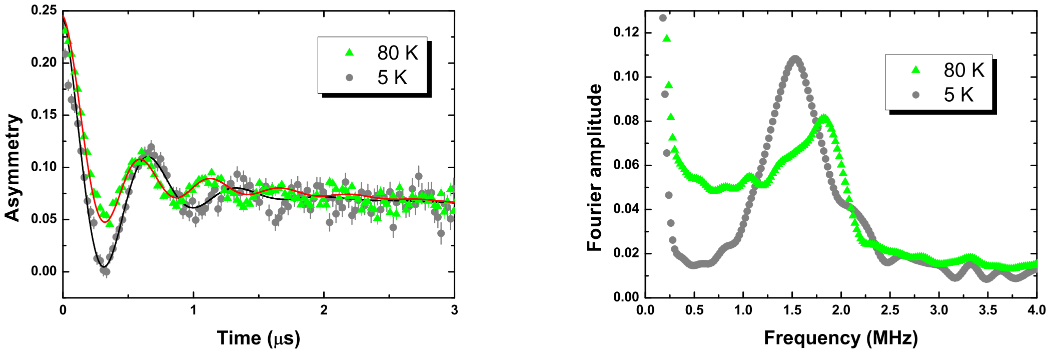

Figure 5.9: Time spectra for 80 K and 5 K and their respective Fourier plots giving each field distribution.

It is visible from the FFT plots in Figure 5.9(right), that the low-temperature regime displays a field distribution that is symmetric and Lorentzian in form in contrast to the broad field distribution which has a higher maximum frequency and spectral weight to lower frequencies at higher temperatures. The sharp peak appearing near zero frequency is due to the slowly decaying asymmetry of the 1/3 tail in time space that was not subtracted from the signal before performing the FFT.

LF-μSR Measurements on T'-La$_2$CuO$_4$

Longitudinal field (LF) measurements can neatly distinguish a static and a dynamic scenario [142] for magnetism. For the static case, with reasonably applied external LF, the static internal fields can be overcome and the polarization stays the same while for dynamic fields, there are still spin flip processes which decrease the polarization with time.

The LF-μSR decoupling measurements for T'-LCO were performed at different temperature regimes under 0.005, 0.02, and 0.04 Tesla applied fields. As highlighted before, Figure

5.8 shows a typical decoupling measurement at T = 155 K showing that at this temperature, the relaxation has clearly a dynamic component. Figure 5.10 displays these measurements for various selected temperatures including the zero-field measurements for comparison and reference. From these plots, a qualitative description of the data can already be drawn. In the present case, no quantitative evaluation of the spectra could be performed since no theoretical fit function is available for well-defined internal magnetic fields and a fit with a dynamic Kubo-Toyabe function with zero average magnetic internal field (as done in Fig. 5.8) would only produce wrong fluctuation rates.

At 80 K, a clear signature of static magnetism is exhibited from the decoupling behavior with typical horizontal tail with recovery of the muon spin polarization with increasing external magnetic fields. On the contrary, a dynamic magnetism is exhibited by the data e.g. at 155 K and 180 K, with a relaxing tail at all applied fields.

In order to have an overview of the dynamic and static nature of magnetism of the sample at different temperature regimes, a temperature scan with an applied field of 0.04 T has been done. The obtained relaxation rate is depicted in Figure 5.11 that yields a peak at the transition temperature T_{N2}. The peak signifies that at low temperatures the relaxation rate is low because the magnetic system is statically-ordered, while at high temperatures the relaxation rate is low because the magnetic system fluctuates relatively fast compared to the Larmor frequency. The peak is observed at the temperature where the fluctuation rate matched the muon Larmor frequency. Note that the peak in the dynamic relaxation rate is observed at the same temperature where the ZF μSR oscillations first appear.

There are two possible reasons why a magnetic system could be dynamic as seen by muons at higher temperatures. Either the magnetism itself is dynamic or the muon is dynamic. The latter depends on the binding potential of the muon in the crystal. This scenario can be ruled out in this particular case since usually, in oxides, the muon is bound to oxygen atoms [149]. This as well will be further shown in our muon site analysis for T'-LCO to be elaborated in section 5.4.1. Moreover, at high temperature, e.g. at 250 K, the spectra are well described by a Gaussian-Kubo-Toyabe function, a signal for a static field distribution. This proves that at high temperatures the muon does not diffuse. Since diffusion is a thermally activated process, it is highly unlikely that the muon might diffuse at lower temperatures where the dynamic relaxation is observed.

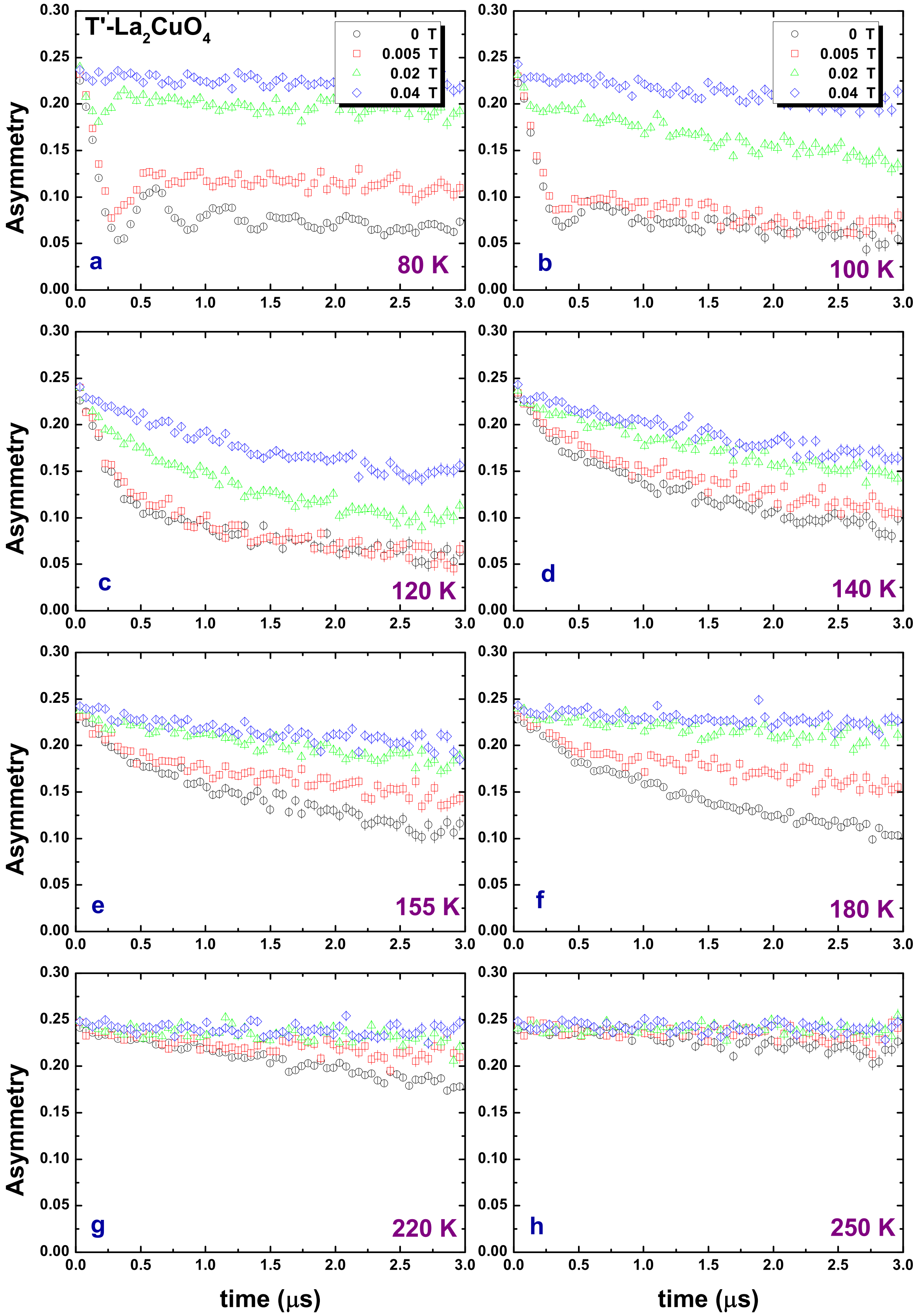

Figure 5.10: Decoupling measurements at various temperatures with 0, 0.005, 0.02, and 0.04 Tesla applied fields.

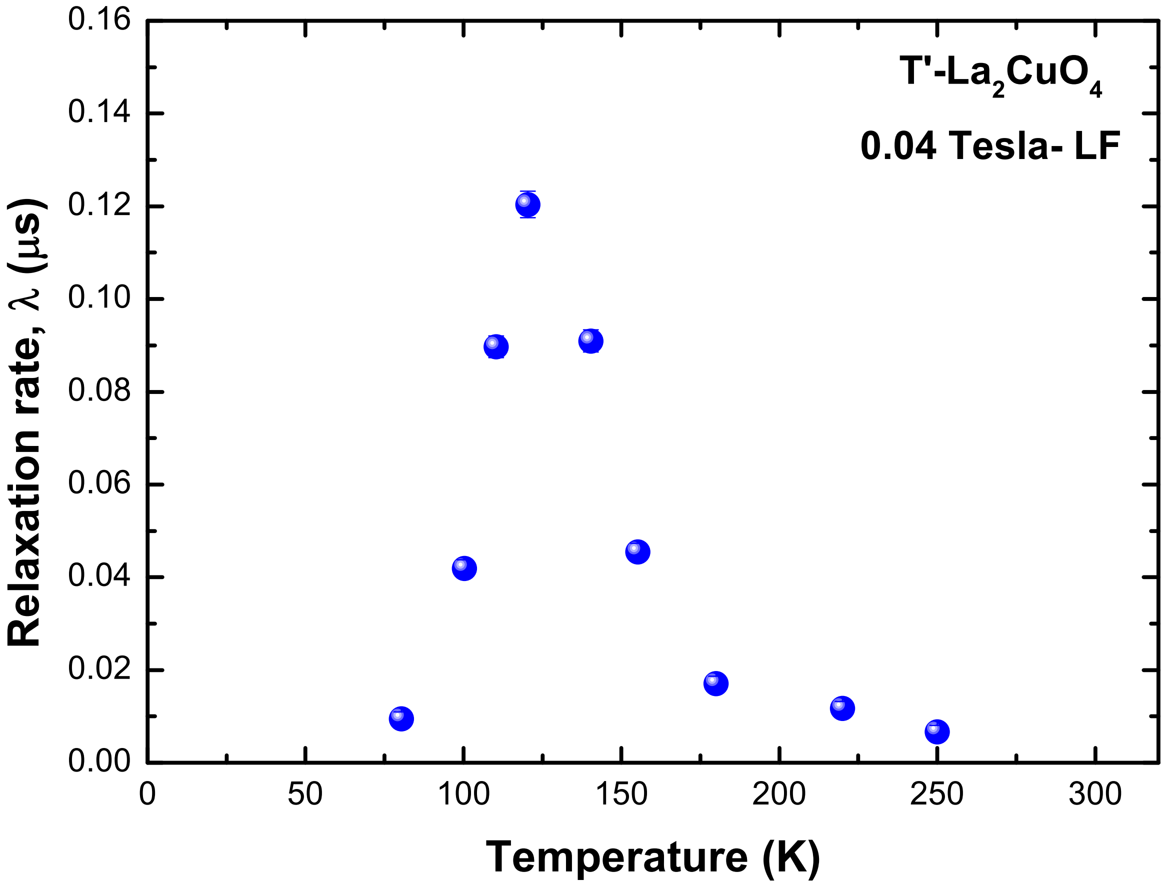

Figure 5.11: Temperature dependence of the dynamic relaxation rate given by LF-μSR measurement with an applied field of 0.04 T. A simple exponential function was used to fit the data at all temperatures.

5.2.3 ^{139}La-NMR Measurements on T'-La$_2$CuO$_4$

To reinforce our understanding on the rich transitions observed by μSR, ^{139}La-NMR field sweep and spin-lattice relaxation experiments at resonance frequency 30.7 MHz were performed from 241 K down to 10 K.[3] Fieldsweep spectra at 21, 100, 150, 206, and 241 K are given in Figure 5.12.

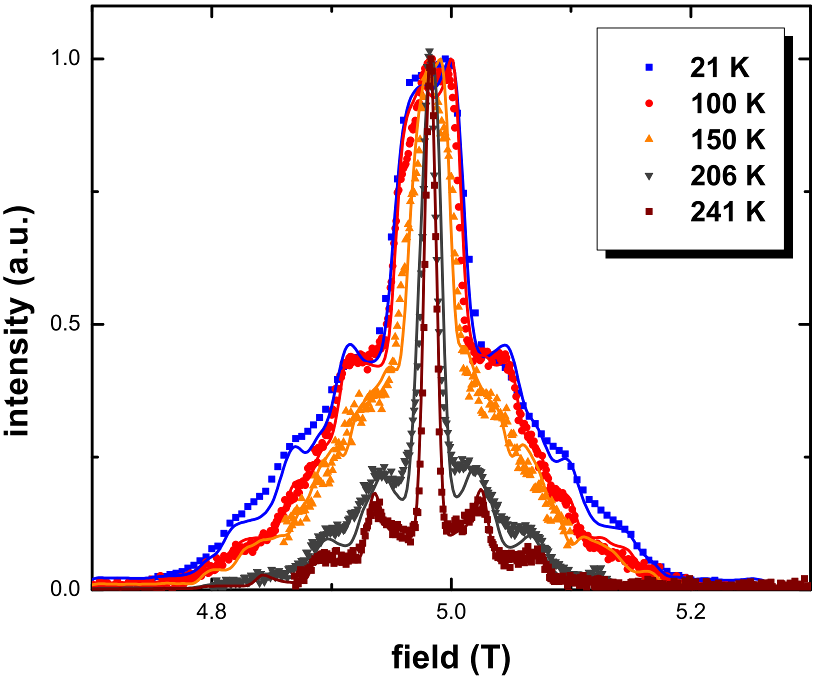

Figure 5.12: ^{139}La-NMR field sweep spectra at resonance frequency 30.7 MHz.

Different experimental techniques give distinctive magnetic fluctuation and relaxation time scales but nonetheless provide complementary information in unfolding and drawing up a plausible physical picture. Such is the case with our ^{139}La-NMR (in milliseconds) and μSR (in microseconds) experimental results. Despite this difference, there are certain behaviors observed at the same characteristic temperature regimes. The salient experimental μSR findings revealing the sequence of transitions are proven to be real effects as anomalies were similarly observed at the same characteristic temperatures in the ^{139}La-NMR measurements. This is namely the onset of a local field at the La site and a peak in $1/T_1$ at $T = 220$ K , a change of the fluctuation behavior as indicated by β, the exponent of the stretched exponential fit to T_1, at $T = 115$ K, and a minimum in $1/T_2$ at $T = 40$ K. Figure 5.13 exhibits these said transitions. The observation of anomalies in the NMR data at the same temperature as observed by μSR at completely different time scales indicates that the transitions are

---

[3] This was performed and analyzed by Marco Günther, from our collaborating group of Prof. Dr. Hans-Henning Klauß of the Institut für Festkörperphysik, TU Dresden, Germany.

real transitions in a thermodynamic sense. The reason why ^{139}La-NMR is apparently less sensitive to the measured transitions and why no drastic changes are observed in the NMR spectra lies in the fact of a nearly symmetric position of the La nucleus with respect to the magnetic Cu system. This fact will be further illuminated by the dipole field calculations for the muon and La site presented in section 5.4.2.

After summarizing the main experimental observations, the next sections will attempt to draw a physical picture of the sequential magnetic ordering at each of the abovementioned characteristic temperature regimes for T'-LCO.

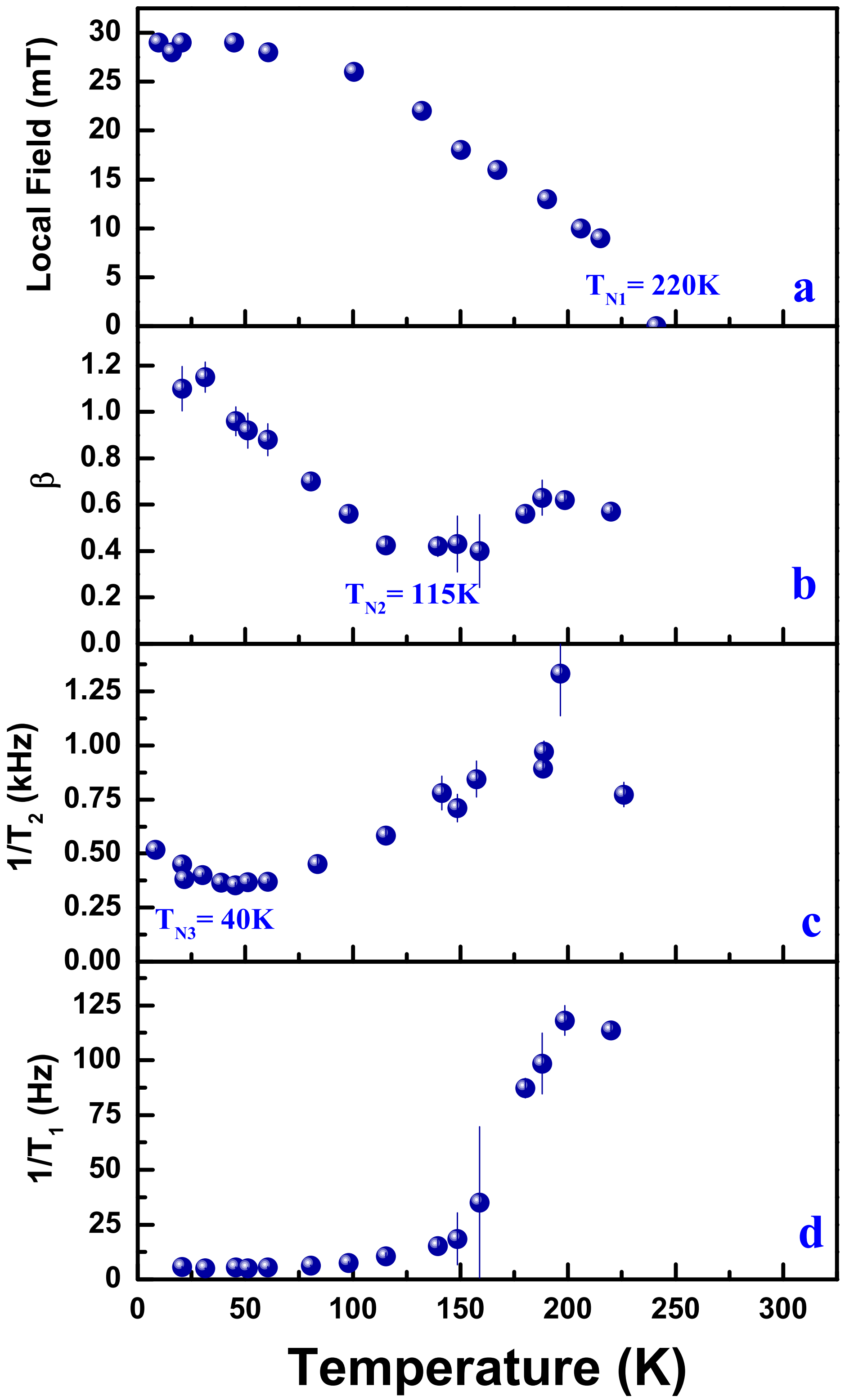

Figure 5.13: NMR results showing a) the magnetic order parameter of T'-La_2CuO_4 represented by hyperfine fields $|\boldsymbol{B}_{\mathrm{local}}|$ derived from field sweep spectra simulation, b) the stretched exponent β, c) the transverse relaxation, $1/T_2$, d) the longitudinal relaxation, $1/T_1$.

5.3 Key Experimental Observations on T'-La_2CuO_4

Structural characterization techniques such as synchrotron X-ray diffraction and thermal neutron scattering had revealed that our La_2CuO_4 adheres to the T'-modification and is monophasic, with a minute amount of an impurity $La(OH)_3$ phase that resulted from the washing out of any remaining flux in the sample with the use of deionized water. The lattice parameters are refined and they exhibit a normal increase as a function of increasing temperature. More importantly, the oxygen occupations were analyzed and it was found that no apical oxygen O(3) was present in the structure. Finally, the fact that the low-temperature synthesized T'-La_2CuO_4 is stoichiometric provides a remarkable conclusion from the structural characterization investigations since this is not the case for all other rare-earth cuprates synthesized by a high-temperature method.

The recapitulation of the main results from zero-field μSR measurements provide the magnetic features of T'-La_2CuO_4 and is discussed in the following. At the highest temperatures, 300 K down to 230 K, T'-La_2CuO_4 is in its paramagnetic state. The Gaussian-Kubo-Toyabe shape of the μSR relaxation additionally proves that the muon is static (not diffusing) up to the highest measured temperatures.

At intermediate temperatures, 220 K down to 120 K, a quasistatic magnetism is probed by μSR seemingly in contrast to the well-defined local field at the La nucleus as measured by ^{139}La-NMR below 220 K. Simulation of the NMR spectra prove that the Cu moments are aligned in the CuO_2 plane below T_{N1} indicating a strong easy-plane anisotropy. μSR reveals a gradual slowing down of magnetic fluctuations below T_{N1}= 220 K, and true static magnetic order below T_{N2}= 115 K in sharp contrast to La_2CuO_4 in the T-structure where $T_{N1} \approx T_{N2} \approx 300$ K is found by μSR.

Also interestingly, in the temperature interval of 115 K down to 40 K, the data fits well with a Bessel function due to an Overhauser-like internal field distribution. Although the idea of incommensurability is a possibility signifying a fit with the Bessel function, it is a better option that in this particular case, it is more plausible that the characteristic field distribution is produced by a different effect. An alternative magnetic spin structure would later be presented in the succeeding section. Here I only would like to point out that the broad asymmetric distribution of internal fields has to be produced by a corresponding distribution of local magnetic environments, e.g. by a distribution of relative spin orientation angles of neighboring Cu planes.

An interesting and notable feature is observed at T_{N3}= 40 K since an abrupt change of the field distribution is observed and the data can be simply and best-described by a Cosine function down to the lowest temperature. The Fourier transform reveals a field distribution with one narrow symmetric line. Even without assuming any particular microscopic magnetic model one can conclude that in this low temperature phase a well defined, long-range-ordered magnetic structure is adapted by the system.

According to the above summarized observations for the different temperature regimes the three characteristic temperatures T_{N1}, T_{N2}, and T_{N3} are defined as follows. T_{N1} signifies the build up of magnetic correlations and this is illustrated e.g. by the increase of the magnetic fraction in Figure 5.7 and the strong increase of the transverse and longitudinal relaxation. On the other hand, this is seen as the onset of a rather well-defined local field from ^{139}La-NMR results. What we call T_{N2} is the onset temperature of spontaneous muon spin precession indicating static magnetic order, shown in Figure 5.7*b* corroborated by a peak in the dynamic relaxation rate at the same temperature shown in Figure 5.11. Then what was denoted as T_{N3} is the temperature at which there is an observed abrupt change of the shape of the field distribution from an asymmetric broad distribution at higher temperatures to a narrow symmetric one at lower temperatures.

Weak anomalies are found in the ^{139}La-NMR data at the same temperatures at which strong changes in the μSR spectra are observed even though both techniques measure at completely different time scales. This indicates that at these temperatures, transitions in a thermodynamic sense take place. A reason why NMR is apparently much less sensitive to the observed transitions will be satisfactorily explained also in the following sections.

5.4 Coming up with a Physical Scenario for the Magnetic Ordering

In the following, I will sequentially describe the steps undertaken in coming up with a physical scenario for T'-LCO from the combined experimental observations. This is initiated by considering symmetry-allowed magnetic structure models for T'-cuprates, as defined in the introduction chapter, section 2.3.7. Using these models, magnetic dipole field calculations were performed. An intermediary and significant step that will be discussed in the following, is the determination of the muon site which is then included in the calculations.

5.4.1 Muon Site Analysis in T'-La$_2$CuO$_4$

The relevant quantitative information that can be extracted with the positive muon as a local probe can be augmented by knowing exactly the interstitial site where the muon is sitting. The final stage of the muon's deceleration process in matter takes place by electrostatic interactions with the sample and, from a few eV to zero kinetic energy, the muon travels $\sim 1 \mu m$ before coming to rest in an interstitial site [150]. Thus, inspecting the electrostatic potential shape can provide physical intuition for the final muon site. Nonetheless, in insulators, the positive muon tends to form bonds with the atomic species present in the host material. This is mainly due to the absence of conduction electrons that could contribute to the screening of the positively charged particle. For this reason, the final interstitial position can be different from the minimum of the electrostatic potential.

To this aim for our T'-LCO, *ab initio* strategy based on density functional theory (DFT) calculations had been implemented to identify local minima corresponding to possible interstitial muon sites for T'-LCO.[4] A detailed description of the computational analysis and complete results from the calculations will be published later by our collaborators. Here, I will only give a concise description that outlines the significant points that derive the muon site for our magnetic dipole field calculations that will be presented in the next section.

---

[4] This was done by Pietro Bonfà, from our collaborating group of Prof. Roberto De Renzi of Dipartimento di Fisica e Scienze della Terra and Unità CNISM di Parma, Università Degli Studi Di Parma, Italy

Brief Computational Background

The T'-LCO electrostatic potential has absolute minima close to the oxygen atoms in the LaO planes, the charge reservoir layer. There are also other narrow relative minima of different planes and close to the O atoms in the CuO planes. If the muon were not forming chemical bondings with the O atoms, the minima of the potential would roughly correspond to the interstitial sites. On the other hand, the formation of μ^+-O bonds leads to the formation of three symmetry inequivalent interstitial sites. It has to be noted that the most energetically favorable path for the muon to pass through the material is close to the reservoir layer.

To obtain the description of the possible interstitial muon sites, the method described in Ref. [151] had been used. In this method, the generalized gradient approximation (GGA) functional [152] had been used to the DFT and the pseudopotential-based plane wave method. This has the advantage of correctly predicting the antiferromagnetic insulating ground state of T'-LCO. The present calculations indicate the existence of a spin polarized solution with an antiferromagnetic moment of $\sim 0.47\ \mu_B$ per Cu atom. A supercell approach is implemented in order to approximate the effect of one impurity in the system and avoid the spurious contributions from the replica of the impurity introduced by periodic boundary conditions. Different supercell sizes were checked, e.g. $2\sqrt{2}$ x $2\sqrt{2}$ x 2 and $3\sqrt{2}$ x $3\sqrt{2}$ x 2, and it was found that they give almost identical results.

To simulate a positively charged muon, a hydrogen atom was introduced, an electron from the system was removed, and a compensating background was added. This is routinely done when simulating the effect of charged interstitial impurities from first principles. Starting from random interstitial positions, the muon's position and the surrounding crystal lattice were relaxed. Three possible symmetry inequivalent sites were obtained, labeled A, B and C in Figure 5.14. In the figure, the final interstitial site are sketched in the $\sqrt{2}$ x $\sqrt{2}$ x 1 cell. Note here that this unit cell is rotated by 45° from the typical tetragonal cell presented in this thesis.

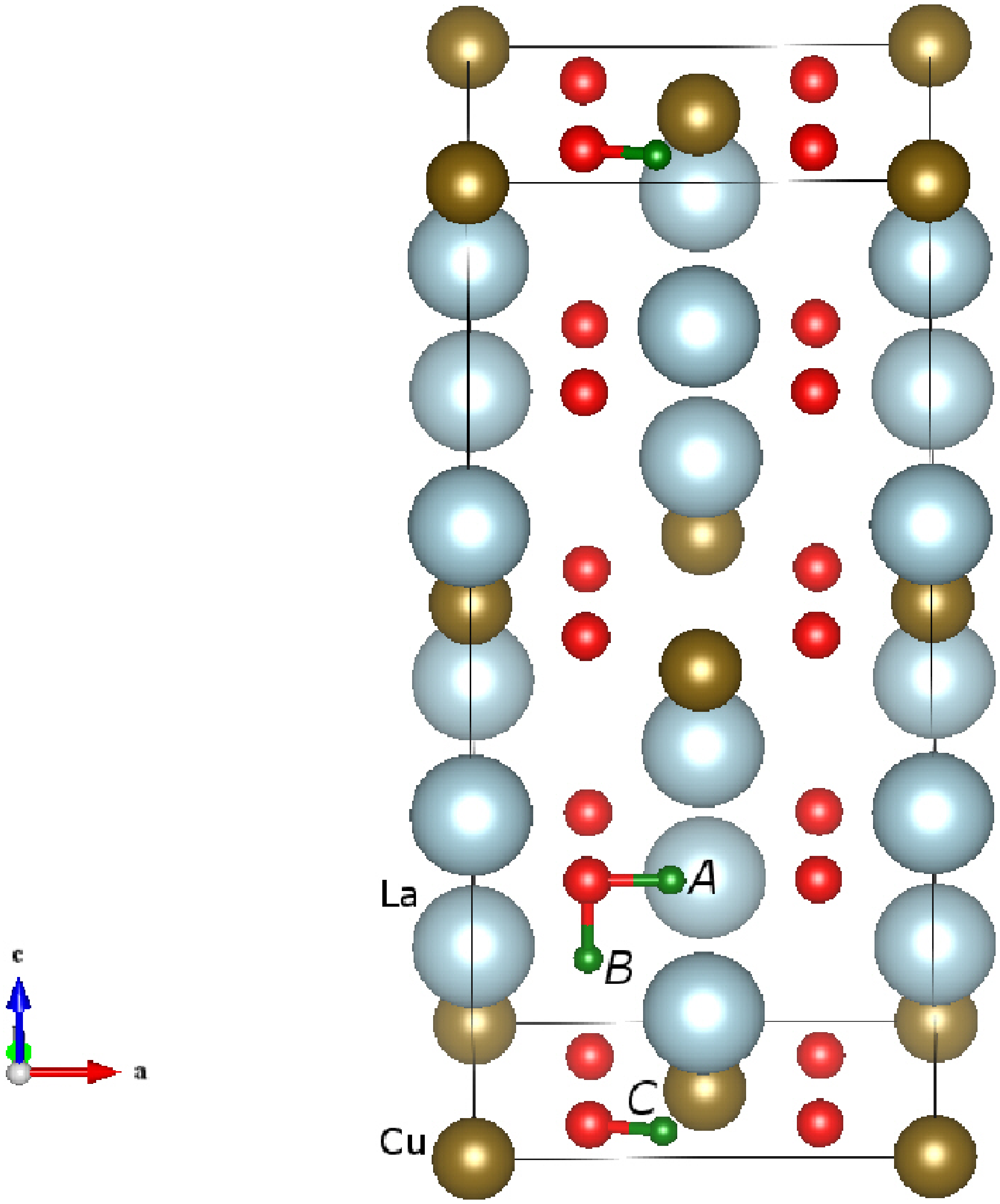

Figure 5.14: Schematic representation of the possible final interstitial muon sites labeled A, B and C. The gray balls are the La atoms, the dark yellow balls are the Cu atoms, and the red balls are the oxygen atoms.

To confirm that site A is a trapping site, zero point vibration energy (ZPE) of the muon is calculated for the case for a muon in site A. The potential felt by the muon is extracted by performing small displacement from its equilibrium position.

A description of the perturbation of the muon on the lattice structure for site A is displayed in Figure 5.15.

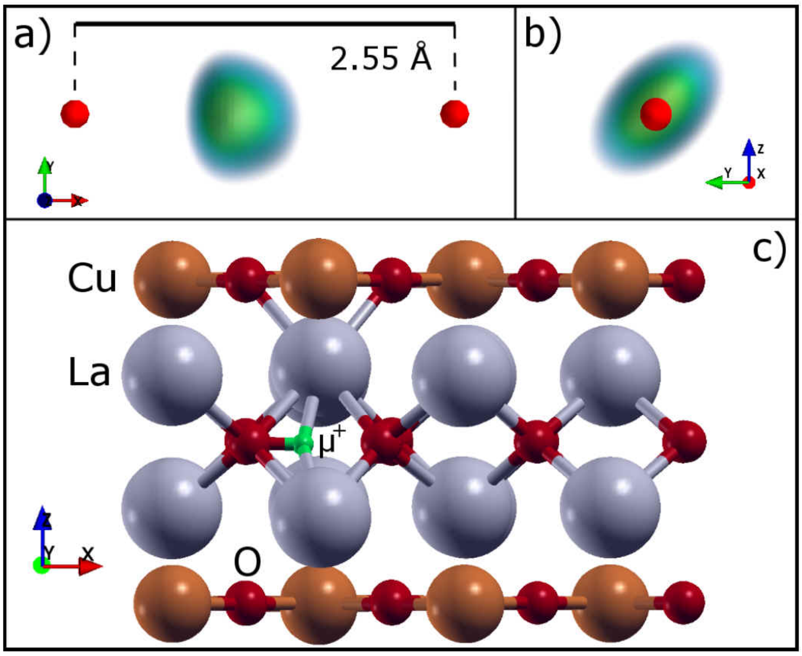

Figure 5.15: a) and b) Probability density for the muon in site A. The colored shadows represent the muon probability density distribution with a linear scale from blue to red. A cutoff is set to 1 tenth of the maximum probability density. c) Final muon position and lattice distortions.

The oval shape of the probability density in the xy plane in Figure 5.15a is due to the anharmonicity of the potential while the elliptic shape in the yz plane is a consequence of the neighboring La atoms. The large area explored by the muon is a well known consequence of its light mass compared to the proton. Quite notably, the most probable position for the muon is shifted from the potential minimum by ~ 0.07 Å along the bond direction away from the closest oxygen. Thus, the most probable position for the μ^+ in site A is located at 1.10 Å away from one relaxed oxygen and 1.185 Å from the original O(2) position in the O(2)-O(2) bond direction in the charge reservoir LaO layer. Its location in the in the usual tetragonal cell is (0.285, 0.205, 0.249) . With 90% probability, the muon resides within a sphere of radius 0.26 Å centered at the maximum probability point.

Conclusion: Muon Site Analysis for T'-La$_2$CuO$_4$

DFT calculations had identified three local minima corresponding to possible interstitial muon sites. By taking into account the zero point energy (ZPE) of the muon, we can confirm that site A is a trapping site and that the most probable position is located along the O(2)-O(2) bond, 1.10 Å far from one oxygen in the LaO plane of T'-LCO.[5] This means that in the tetragonal unit cell there are 8 structurally equivalent muon sites, see Figure 5.16.

---

[5] A publication with the details of the muon site analysis of T'-LCO will follow soon.

5.4.2 Magnetic Dipole Field Calculations

Combining the data obtained from μSR and ^{139}La-NMR allows us to attempt to formulate a plausible and consistent physical picture, considering calculation of magnetic dipole fields at the muon sites and the La-site. [6] Hyperfine fields at the respective muon and the La-sites are analyzed by means of a local dipole summation. The muon site derived from the *ab-initio* calculations in the previous section is included as an input in the calculations. Dipole field calculations were done as well at the La-site at (0, 0, 0.3528).

As illustrated in chapter 2 section 2.3.7, various spin geometries possible for body-centered tetragonal cuprates with the two experimentally-found antiferromagnetic propagation vectors within τ_3 and τ_5 IR, respectively, were adapted in the dipole field calculations. The geometry of the Cu spins is already given in Figure 2.11 with the definition of the rotation angles of spins in the different planes, notably the α and β. As mentioned, α is the angle of rotation of the in-plane spins (blue spin in the figure), β is the angle of rotation of the spin in the neighboring plane (red spin in the figure).

The two collinear structures originating from K_1 and K_2 propagation vectors are energetically degenerate domains so if the spin structure originating from K_1 propagation vector is entirely rotated by 90°, one obtains the other domain originating from the K_2 propagation vector. These collinear domains, also called 90°-domains, are always there in a powder and they result in an equivalent absolute local field at the muons site. Note also that with respect to symmetry operations, e.g. inversion of all Cu moments: NCol II$^{(+)}$ $\rightarrow$ -NCol II$^{(+)}$, being 180° domains with respect to each other. So in the same way, the noncollinear structures denoted with the (+) and (-) are also 90°-domains. Thus for each IR, we have the represented structures denoted as Col I and Col II, NCol I and NCol II. Hence, one need not show the calculations for each magnetic structures with K_1 and (+) since, as justified, the corresponding K_2 and (-) are always 90°-domains providing the same field at the muon site.

In T'-LCO, four sets of parallel moments are considered. These are shown in Figure 5.16. They are represented by $\mathbf{m}_{11}$ = $-\mathbf{m}_{12}$, and $\mathbf{m}_{21}$ = $-\mathbf{m}_{22}$. Here, interplanar antiferromagnetism is already assumed due to the strong antiferromagnetic coupling J within the CuO_2 plane. Essentially, there are pairs of fields sensed at the muon sites (1, 5), (2, 6), (3, 7), and (4, 8) with equal magnitude of local field for all α and β angles. The magnitude of the field is shown in Figure 5.17 as a color map for all angles α and β. Interplanar moments $\mathbf{m}_{11}$ and $\mathbf{m}_{21}$ are parameterized by α and β, respectively. The magnetic field can be described by an

---

[6] With the input of the suggested magnetic models from our side (see chapter 2,section 2.3.7), the actual calculations were performed by Marco Günther, from our collaborating group of Prof. Dr. Hans-Henning Klauß of the Institut für Festkörperphysik, TU Dresden, Germany.

effective coupling to the moments on the Cu sites. Thus, $|\mathbf{B}_{dipol}(\boldsymbol{r})| = |\mathbf{a}(\boldsymbol{r},\alpha,\beta)\ \mathbf{m}_{Cu}|$, with $\mathbf{a}(\boldsymbol{r},\alpha,\beta)$ being the coupling tensor.

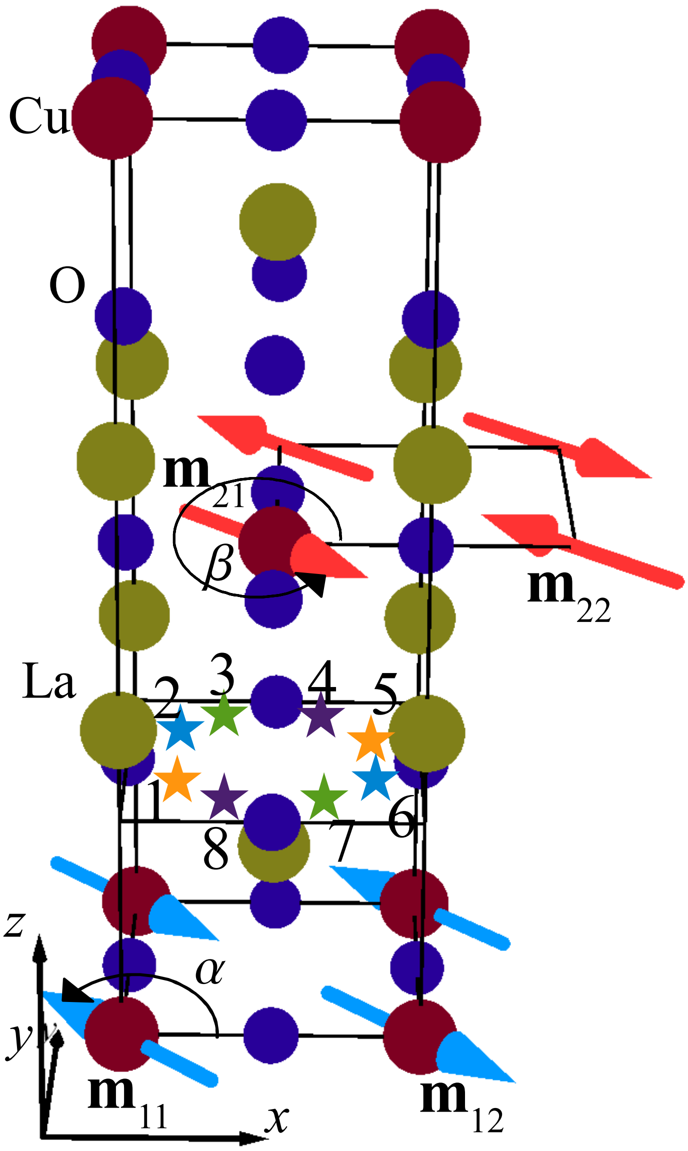

Figure 5.16: Definition of angles, Cu moments and muon sites used for the magnetic dipole calculations. See text for a detailed explanation.

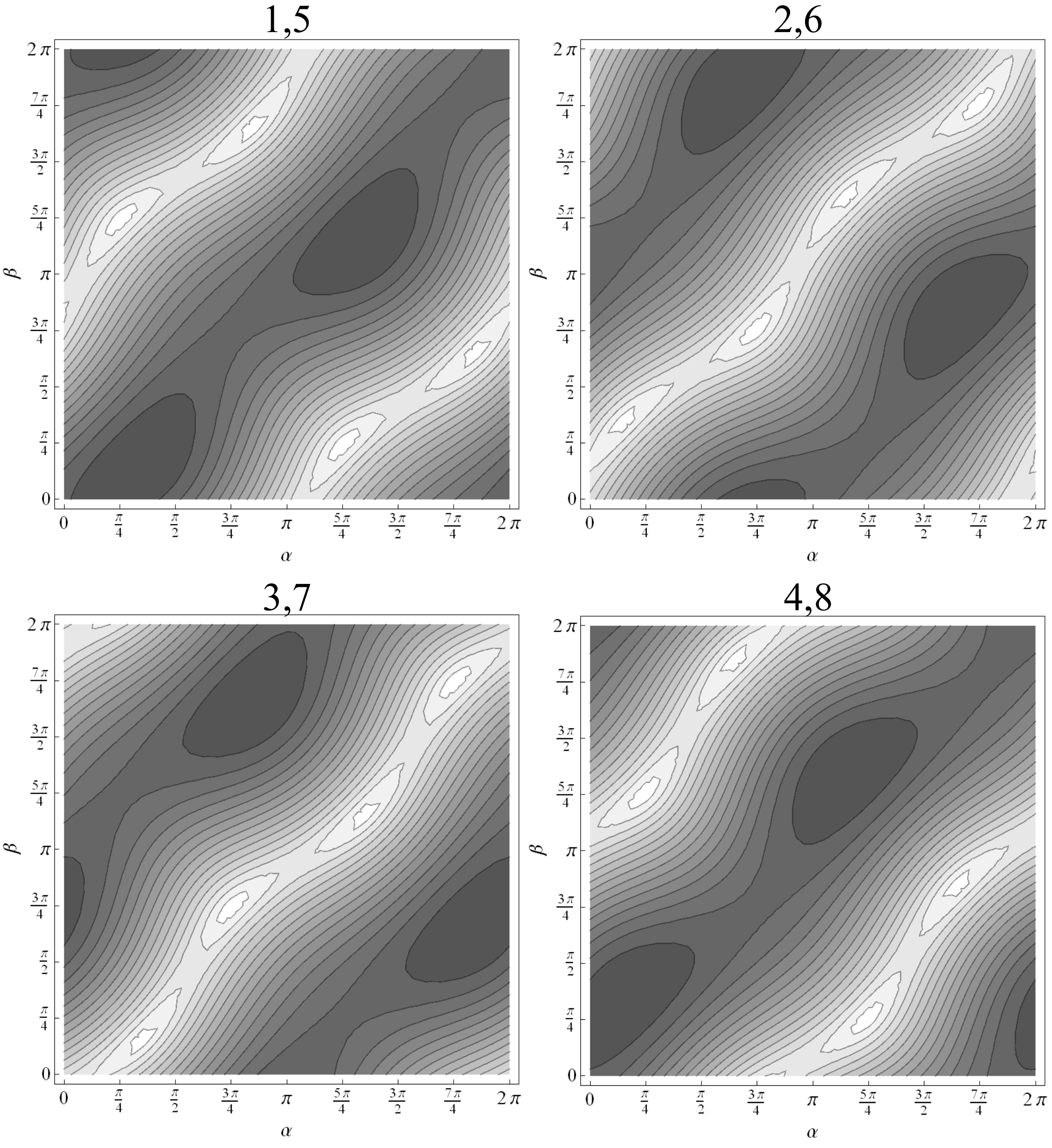

Figure 5.17: Coupling map of all 8 pairs of fields at the muon sites. There are pairs with the same magnitude of local field for all α and β at the muon sites. These are the fields (1,5), (2,6), (3,7), and (4,8) .

Figure 5.18 shows the coupling map at the muon and La sites, respectively, as a function of α and β for comparison. Please note the small variations of the field at the La site in contrast to the ones calculated for the muon sites.

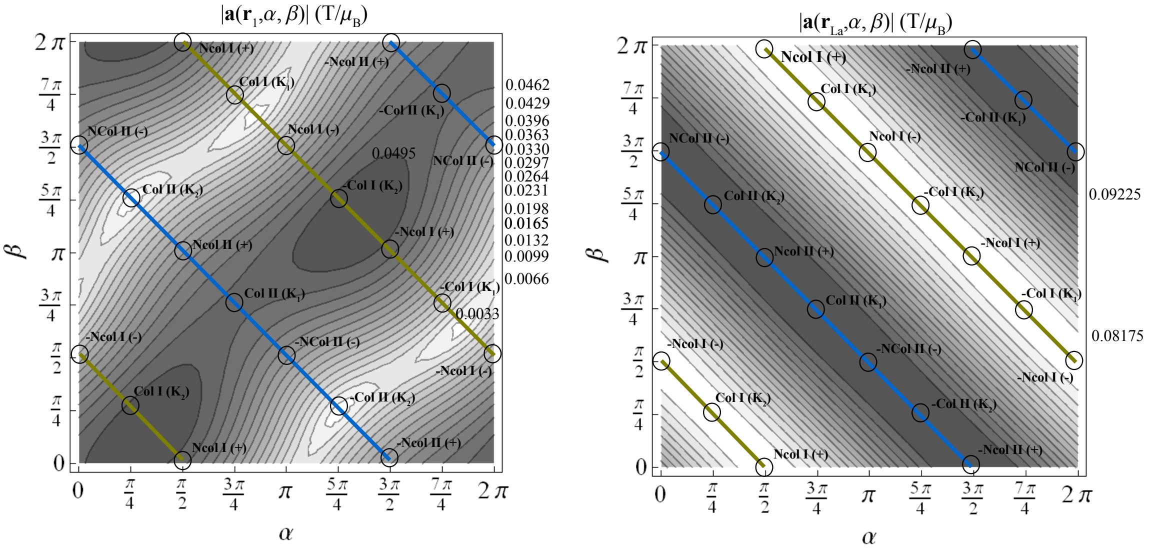

Figure 5.18: (left) Coupling map of the pair of field (1,5) at the muon site as a function of α and β. Some particular models of magnetic order are highlighted, i.e. the fields on the green line correspond to magnetic structure models belonging to the τ_3 IR while the ones on the blue line belong to the τ_5 IR, (right) Coupling map of the La site at r_{La} as a function of α and β. Only small changes of the dipolar coupling occur at the La site. Please note especially, that all magnetic structure models belonging to the same IR produce the same magnetic field at the La site. Among all possible magnetic models there is only a difference of 10% in the magnitude of the dipole fields at the La site while there is a variation of 100% on the muon sites.

In the following, I will be showing the obtained dipole field maps within the z= 0.25 plane of the unit cell of the special case models, Col I, Col II, NCol I, and NCol II in order to discriminate which among the models can best-describe the low-temperature regime that will be discussed in more detail in the next section. Muon sites with different magnitudes of the magnetic dipole field are shown as stars of different color in the maps. The number of magnetically-inequivalent muon sites and the magnitudes of the fields are given in the caption of the figures.

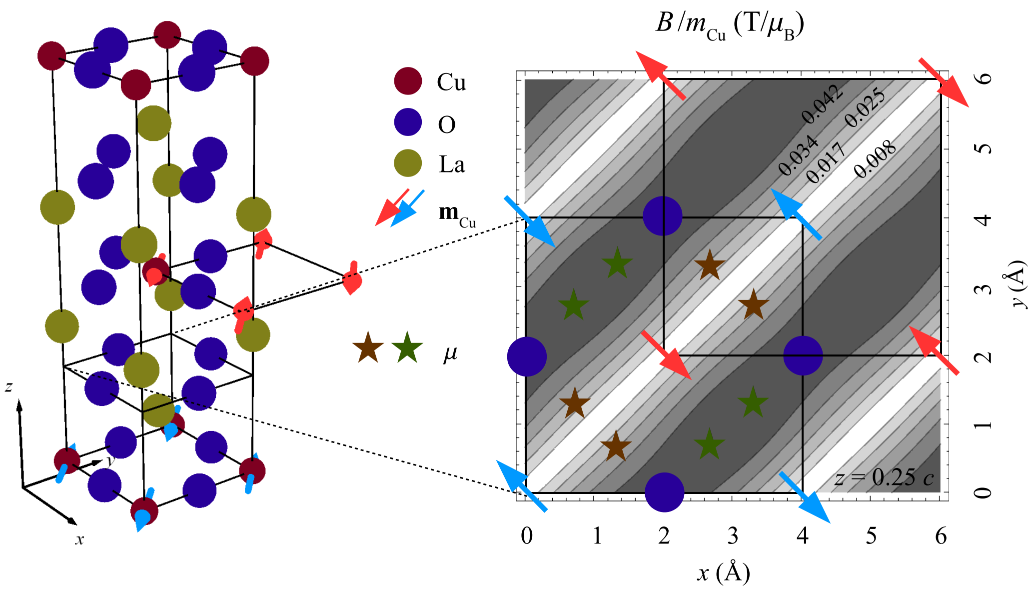

Figure 5.19: Dipolar coupling map of magnetic order Col I (K$_1$). Here, $\alpha = 3/4\pi$ and $\beta = 7/4\pi$. There are two sets of magnetically equivalent muon sites (1,4,5,8) and (2,3,6,7) that obtains the coupling, 0.0125 T/μ_B and 0.0510 T/μ_B, respectively for each set of sites.

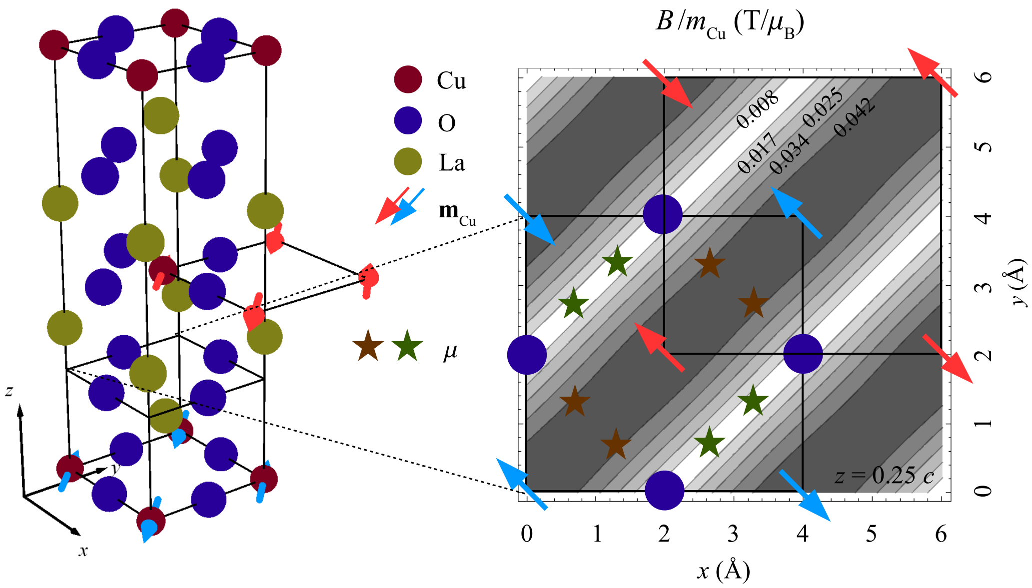

Figure 5.20: Dipolar coupling map of magnetic order Col II (K$_1$). Here, $\alpha = 3/4\pi$ and $\beta = 3/4\pi$. There are two sets of magnetically equivalent muon sites (1,4,5,8) and (2,3,6,7) that obtains the coupling, 0.0006 T/μ_B and 0.0480 T/μ_B, respectively for each set of sites.

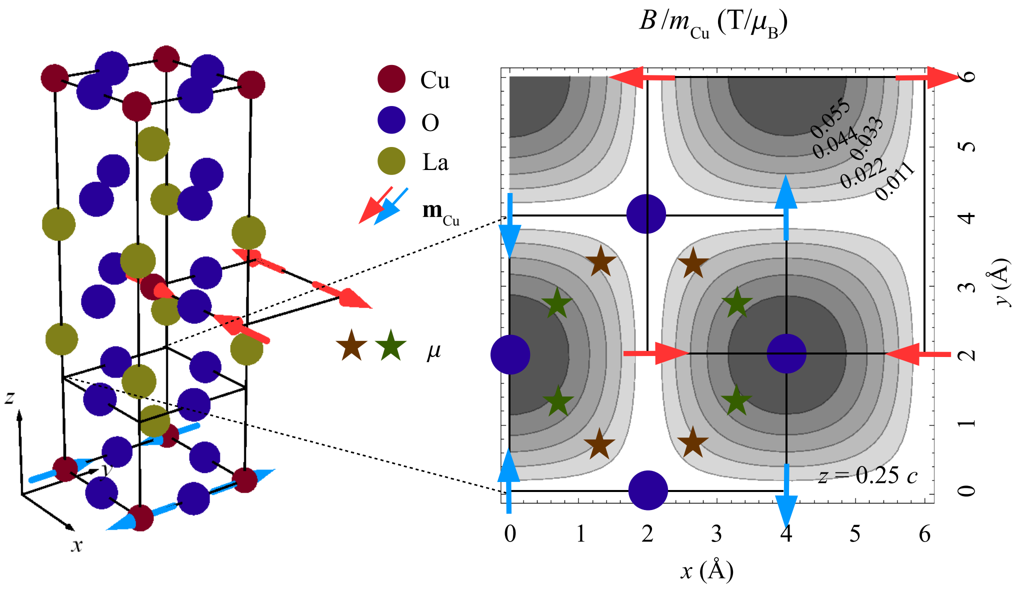

Figure 5.21: Dipolar coupling map of magnetic order NCol I($^+$). Here, $\alpha = 1/2\pi$ and $\beta = 0$. There are two sets of magnetically equivalent muon sites (1,2,5,6) and (3,4,7,8) that obtains the coupling, 0.0449 T/μ_B and 0.0272 T/μ_B, respectively for each set of sites.

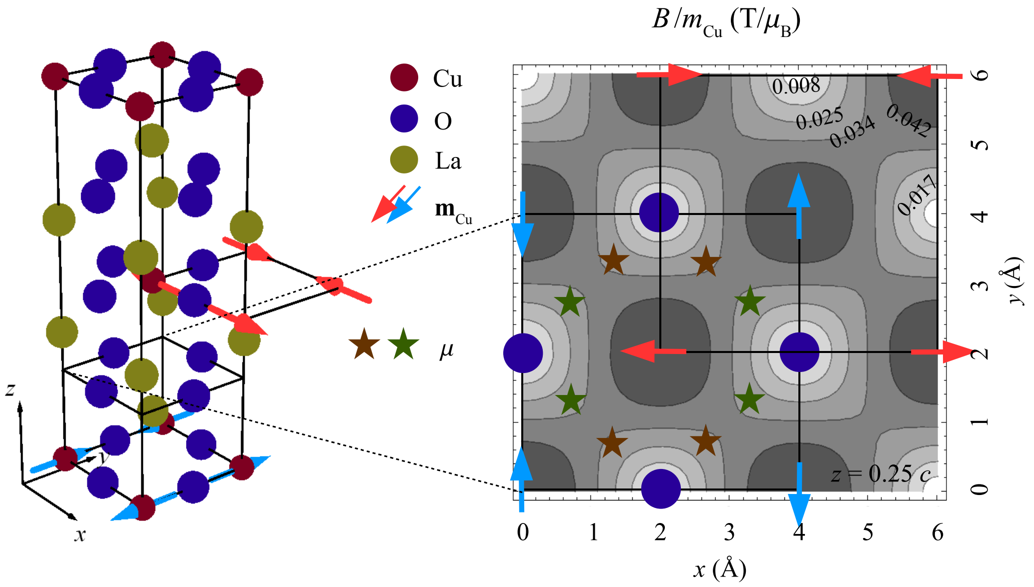

Figure 5.22: Dipolar coupling map of magnetic order NCol II($^+$). Here, $\alpha = 1/2\pi$ and $\beta = \pi$. There are two sets of magnetically equivalent muon sites (1,2,5,6) and (3,4,7,8) that obtains the coupling, 0.0335 T/μ_B and 0.0343 T/μ_B, respectively for each set of sites.

Five models for the dipole field calculations were implemented to attempt to come up with plausible physical scenarios depicting the broad field distribution at high temperatures. Therefore the following models assume a variation of different magnetic structures within the sample. This produces locally different magnetic environments for different muons within the sample. The magnetic field distribution that would be measured by the muon ensemble is then obtained by histogramming the local fields for the various local magnetic structures. This physical situation is e.g. possible if at a given temperature the anisotropy in the CuO_2 plane is not strong enough to stabilize a preferred direction of the Cu spins and random spin alignments between neighboring planes are realized. It turns out from the simulations that next-nearest Cu planes have only little influence on the field at the muon site. Therefore, the obtained field distributions are virtually identical if the relative spin orientation between neighboring planes γ varies smoothly along a spatial direction, e.g. by a continuous increase of the angles α and β or if γ is randomly distributed within the sample. In the following some models are presented, each of which results in a different field distribution that later should be compared to the experimentally-observed Overhauser-like distribution obtained in the static magnetic regime between 40 K and 115 K by μSR.

Model 1: Random plane model. All possible models of the α-β plane are realized. Figure 5.23 shows a histogram of the parameter plane normalized as a probability density function (PDF) sampled on a 100x100 grid.

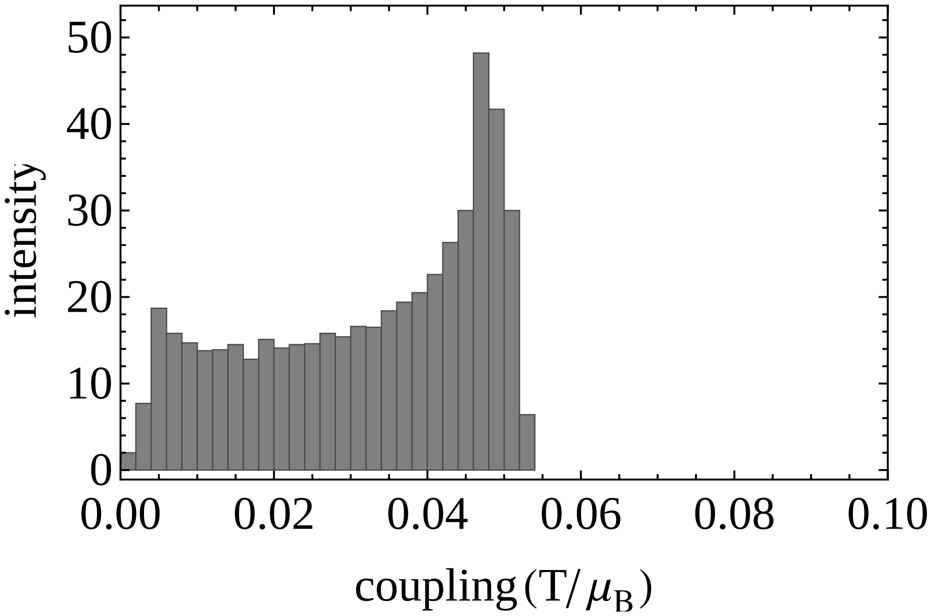

Figure 5.23: Local field histogram of the whole α-β-plane sampled on 100x100 grid. This is a model describing the situation of no coupling between neighboring planes and no preferred orientation within the CuO_2 plane.

Model 2: Collinear models with correlated rotations. Collinear models in this subset are generated by applying likewise rotations to all Cu planes and are situated on a straight line in the α-β-plane. This model therefore assumes a coupling between neighboring planes that forces the spins to be collinear, but with no restriction of the orientation of the spins within the plane (no large enough anisotropy). Note that the various magnetic structures in this model do not belong to the same IR.

The left figure of Figure 5.24 shows a plot along the section of the model in the parameter space. The two sets of muon sites (1,4,5,8) and (2,3,6,7) give equivalent fields. In addition, all the collinear models within different IRs give the same histograms, see the right figure of Figure 5.24. The field at the La-site is also included and it is displayed in the figure with a dark yellow line that is almost constant at 0.09 T/μ_B.

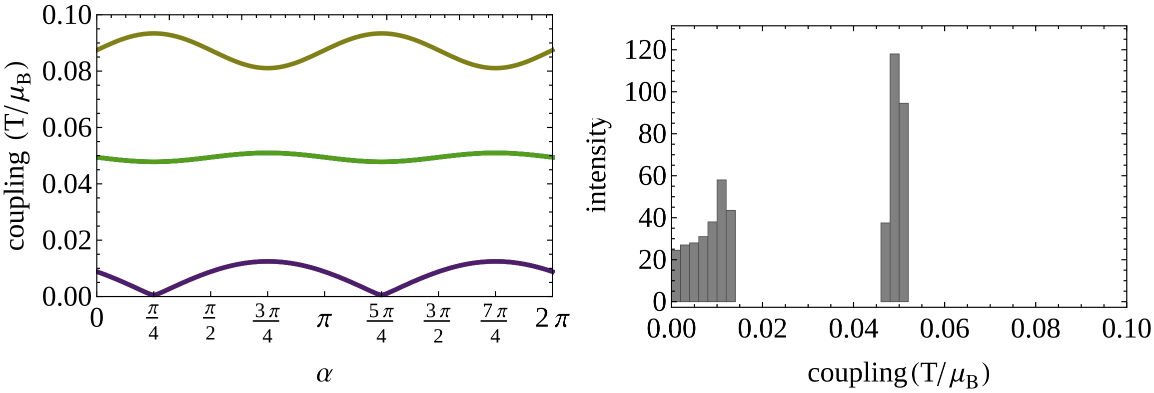

Figure 5.24: (left) Local fields for a selection section of all local probe sites along $\beta = \pi + \alpha$. The dark yellow line comes from La. The purple line comes from muon sites 1,4,5,8. The green line comes from muon sites 2,3,6,7. (right) Probability density function along $\beta = \pi + \alpha$.

Model 3: Noncollinear models with correlated rotations. This set of models is defined by $\beta = \pi/2 + \alpha$. Again all noncollinear models are connected by likewise rotations, therefore resulting in equivalent histograms of local fields/coupling. This model is similar to the previous model 2 with the difference that the relative orientation between neighboring planes is fixed to 90°. Here, the two sets of sites result into a broad field distribution not tangenting zero field. The field at the La-site, like in Model 2, is almost constant.

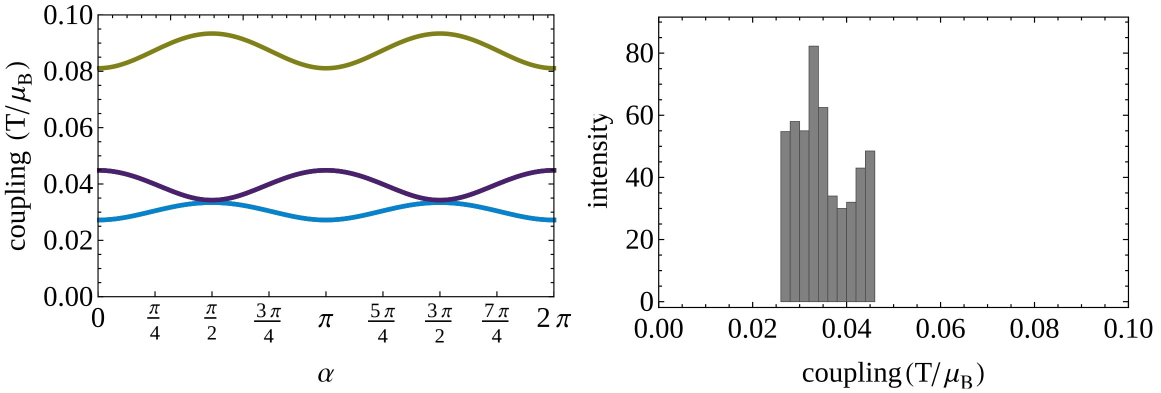

Figure 5.25: (left) Section of all local probe sites along $\beta = \pi/2 + \alpha$. Dark yellow line: La. Purple line: muon sites 1,2,5,6. Blue line: muon sites 3,4,7,8. (right) PDF along $\beta = \pi/2 + \alpha$.

Model 4: Correlated but antilikewise rotation within τ_3 IR. Here, $\beta = \pi/2 - \alpha$. This defines the set of models generated by antilikewise α and β rotations, respectively, within the τ_3 IR. These structures produce magnetic fields at the muon and La sites that lie on the green line in Figure 5.18. A broad field distribution is generated as shown in the right figure of Figure 5.26. The left figure is a section showing four sets of α-shifted muon sites. The field at the La-site is constant.

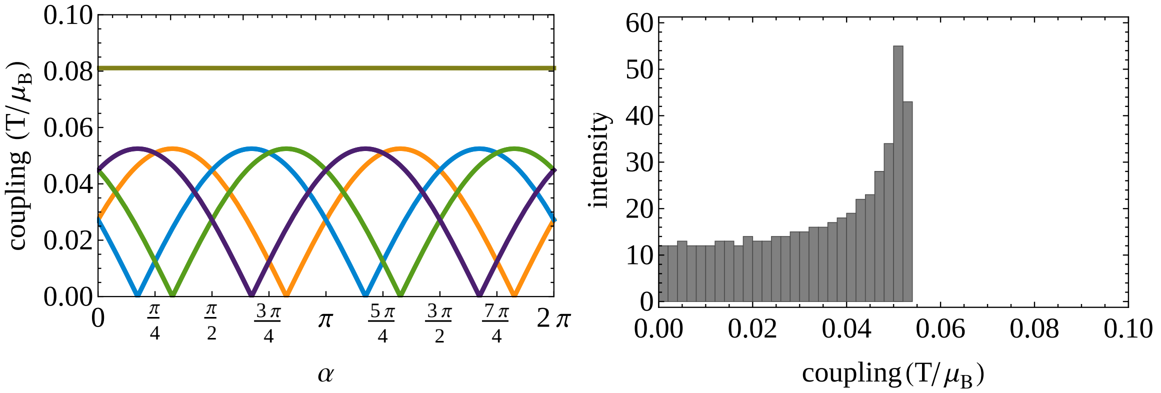

Figure 5.26: (left) Section of all local probe sites along $\beta = \pi/2 - \alpha$. Dark yellow line: La. Orange line: muon sites 1,5. Blue line: muon sites 2,6. Green line: muon sites 3,7. Purple line: muon sites 4,8. (right) PDF of τ_3 along $\beta = \pi/2 - \alpha$.

Model 5: Correlated but antilikewise rotation within the τ_5 IR. This model connecting the magnetic structure models within τ_5 IR is defined by $\beta = 3\pi/2 - \alpha$ in the parameter space. The physical interpretation of this model is equivalent to the one of model 4 with the difference that only magnetic structures allowed within the τ_5 IR are adopted. These structures produce fields indicated as blue line in Figure 5.18. The section is characterized by four sets of fields at the muon sites but form two effective sets as shown in the left figure of Figure 5.27. Near $\alpha = n\pi/2$, where n is a natural number, all fields form a single effective field at the muon site. The field at the La-site is constant.

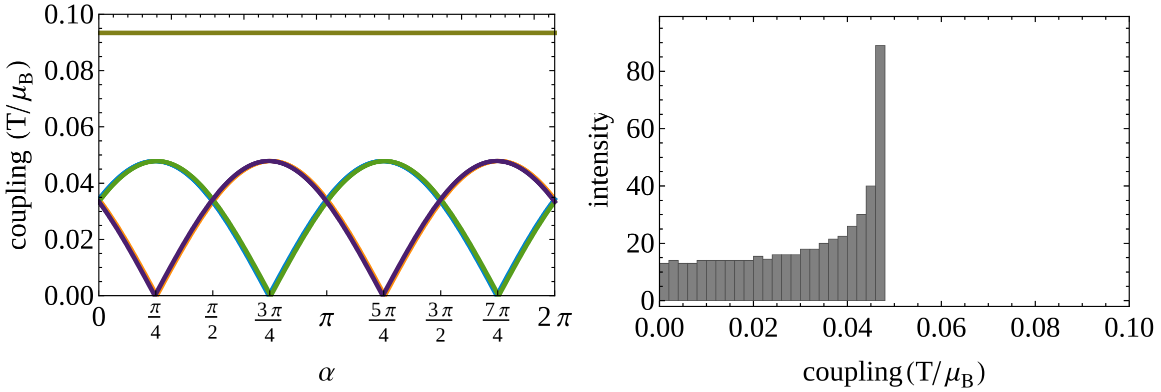

Figure 5.27: (left) Section of all local probe sites along $\beta = 3\pi/2 - \alpha$. Dark yellow line: La. Orange line: muon sites 1,5. Blue line: muon sites 2,6. Green line: muon sites 3,7. Purple line: muon sites 4,8. (right) PDF along τ_5 along $\beta = 3\pi/2 - \alpha$.

5.4.3 Plausible Physical Scenario for Each Characteristic Temperature Regime

In the following, each of the characteristic temperature regimes will be thoroughly discussed including the discussed magnetic dipole field calculation results aimed at reproducing the experimental field distributions to come up with plausible physical scenarios of the magnetic ordering.

230 K $\leq T \leq$ 300 K, Paramagnetic Regime

It was found by zero-field μSR measurements that at the highest temperatures 300 K down to 230 K, T'-La$_2$CuO$_4$ is in its paramagnetic state. One of the crucial considerations with the μSR technique is the possibility of the muon to diffuse within some systems obscuring interpretation of data. However, analysis show that in this particular system, muon diffusion scenario is definitely ruled out. The Gaussian Kubo-Toyabe signal at this temperature region is a proof of a static field distribution and our muon site analysis is a proof that it is bound to an oxygen atom, similar to other related works on the calculation of the muon site in cuprates [149]. Hence, the muon is not diffusing within the system. The paramagnetic fluctuations are too fast to be measurable with μSR.

120 K $\leq T \leq$ 220 K, Quasistatic Regime

The increase in the transverse relaxation rate sensed by the muon signify the building up of magnetic correlations and at the same time, there is also an observed increase of the longitudinal relaxation rate that imply the presence of dynamics. Thus, the order is only quasistatic. On the other hand, the dipole field sensed at the La-site seems to suggest that there is a rather conventional magnetic ordering below 220 K. The reason for this is that the La nucleus is sitting in a symmetric site and does not strongly see fluctuations nor static changes as evidenced by the dipole field calculations. Hence, independent of the magnetic structure, the field at the La-site is always very similar.

Dipole field calculations on the La-site shown in the right figure of Figure 5.18 really prove that regardless of the magnetic structure model, only small changes of the dipolar coupling is obtained. Thus, ^{139}La-NMR is not sensitive to changes in the magnetic structure nor to fluctuations within the system. Staying in the same IR magnetic structure even do not change at all the local field at the La site as evidence by the blue-violet and yellow-green line in Figure 5.18. The difference in local fields at the La site between two arbitrary magnetic models with the moments in the ab-plane is only 11%. On the contrary, the left figure of

Figure 5.18 displays the dipole fields sensed at the muon site in which minute changes in the structure or field distributions can be distinguishable by the muon. This is because the muon sits on a non-symmetric interstitial site and can therefore observe changes between different magnetic structures. The smooth built up of a well-defined local field at the La nucleus below 220 K is therefore satisfactorily explained, as long as the magnetic moments lie within the CuO_2 plane.

In the following, I will attempt to explain plausible scenarios regarding this quasistatic behavior of T'-LCO which is essentially a 2D system at high temperatures, but finally has to order in a 3D magnetic structure at low temperatures.

Scenario 1: At intermediate temperatures, 220 K down to 120 K, the magnetic correlations are already built up as seen by NMR but are still fluctuating as given by the weak dynamics sensed by muons. The exponential depolarization function has its *tail* going to 1/3, indicative of a quasistatic magnetic signal, i.e. the transverse relaxation is much faster than the longitudinal relaxation. This depolarization signal, as well picks up in addition weak dynamic signals. These results could imply that the CuO_2 planes order (seen by NMR), and still the alignment between the planes is fluctuating as seen by the slow dynamics in the time window of the muons. These already-ordered planes has a correlation length that is rather very long (e.g. 272 lattice constants at T_{N1}, this will be discussed in the next section), but are still fluctuating against every other layer.

As previously discussed, the BCT cuprates magnetic properties are very well-described by the isotropic Heisenberg model in two dimensions and the dominant energy is the isotropic exchange energy between nearest-neighbor spins in adjacent planes. For systems with tetragonal symmetry, the mean field exerted by one layer on the adjacent layer vanishes and there is classical degeneracy. Yildirim [72] had discussed that there is a strong second neighbor antiferromagnetic interaction and weaker first neighbor interaction on a body-centered cubic geometrical arrangement of spins. In such a case, the classical exchange field at any site on one sublattice due to the spins in the other sublattice is zero. Thus, the effective quantum interaction between the two subsystems are decoupled [72]. In a BCT antiferromagnet, symmetry allows an interaction of the next nearest-neighboring sublattice that would uniquely fix the orientation of all, say, even-numbered layers with respect to one another.

Thus, a physical scenario that one can infer from the above explanation is that below 220 K, there is an antiferromagnetic coupling between the Cu moments within the planes and the coupling to the next plane is weak due to frustration. Hence, the relative orientation between the planes can be random and even fluctuating. The 3D magnetic ordering transition that appears at 220 K might be due to the coupling of every second plane which is ferromagnetic.

This scenario gets more and more plausible as J' gets smaller. In the T'-LCO case, it might be the smallest yet observed. This will be further discussed in the last section of this chapter.

Scenario 2: This quasistatic behavior may be one of those compelling evidences for the long-documented quasi-2D (and dimensional crossover) behavior of the cuprates. This behavior is at first marked with fluctuations which have essentially a 2D-like character and very near to the phase transition, when the correlation lengths is sufficiently large, they crossover to their ultimate 3D behavior. It may be a provocative conjecture, but another scenario might be that this quasistatic regime could be a signature of a Kosterlitz-Thouless transition. This would imply that at $T_{\mathrm{N1}} = 220$ K the system undergoes a transition from a 2D Heisenberg model to an effective 2D XY model, as it might be suggested by our NMR measurements which indicate that the moments are in plane below T_{N1}. From the Mermin-Wagner theorem, there is no phase transition in a 2D XY model but nonetheless exhibit a kind of phase transition called the Kosterlitz-Thouless (KT) transition. This transition is characterized by two phases: a disordered high-temperature phase where the correlation-function decays exponentially, and a low-temperature phase with a quasi-long range order and the correlation-function decays with a power law. However, if the system directly undergoes an ordering in 3D XY (in the presence of quantum fluctuations) at higher temperatures and the correlation length follows a power law behavior, the KT transition may not be observed.

40 K $\leq T \leq$ 115 K, Static Regime

At this temperature range, T'-LCO is in the true static regime in which the μSR signal is described by a zeroth-order Bessel function. This indicates the presence of a broad and asymmetric field distribution that may imply different scenarios for the realized spin structure.

A distribution of internal fields sensed by the muons in this temperature regime indicates a distribution of local magnetic environments.

This broad field distribution at this intermediate temperature can give a physical picture which could be thought that the system is consisting of grains possessing all different spin structures which are allowed by symmetry. Another possible scenario is a spin density wave with a continuous modulation of the relative angle between neighboring planes along the c-direction from unit cell to unit cell.

Three among the five models depicted in the dipole field calculations section can reproduce a broad field distribution with a pronounced tail to low fields as typical for an Overhauser distribution. To obtain a consistent picture from both the La-NMR and the μSR measurements, magnetic field distributions at the muon sites have been calculated for each model assuming the Cu moment $\mathbf{m}_{Cu}$ that is obtained by the La-NMR measurement within the same model. The comparison of these model calculations with the actual experimental μSR data is illustrated in the following.

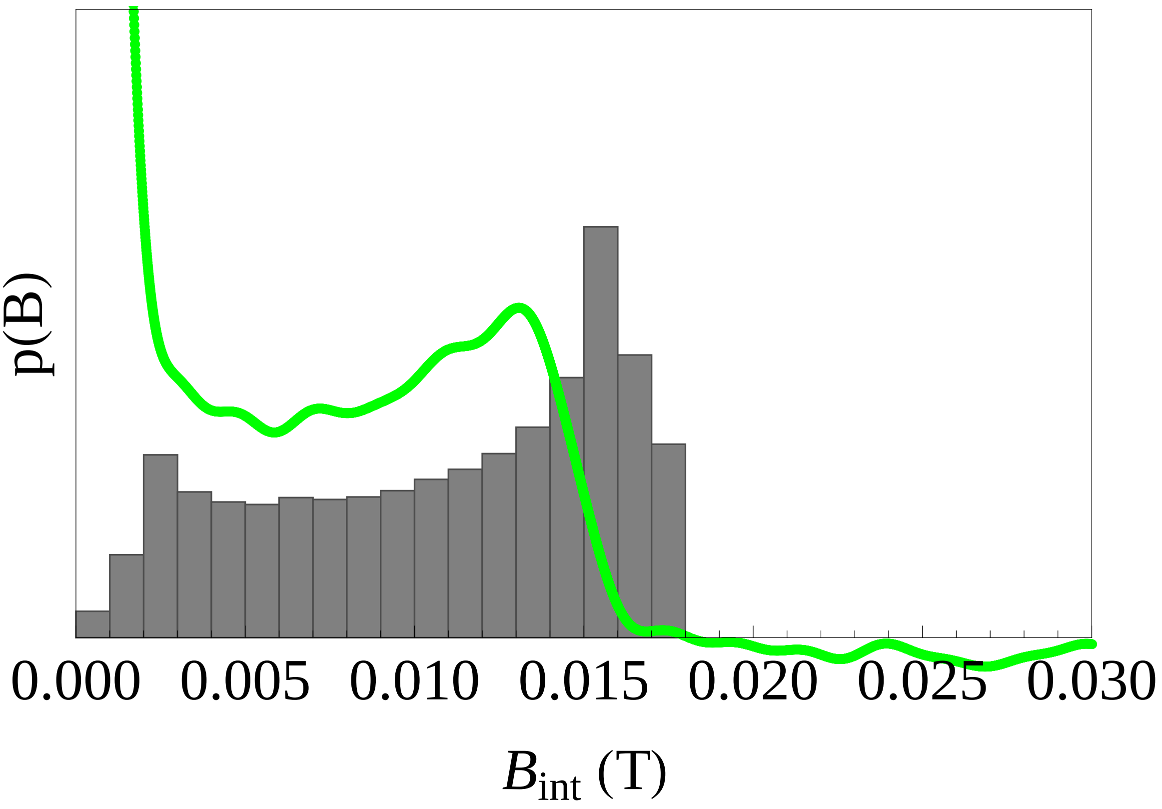

Figure 5.28: Comparison of the μSR experimental data (apple-green line) and the model with random orientation of planes (shown as Model 1 in the dipole field section). Here, $\mathbf{m}_{Cu}$= 0.335 μ_B was chosen to calculate the field at the muon sites as deduced from the ^{139}La-NMR measurement within this model.

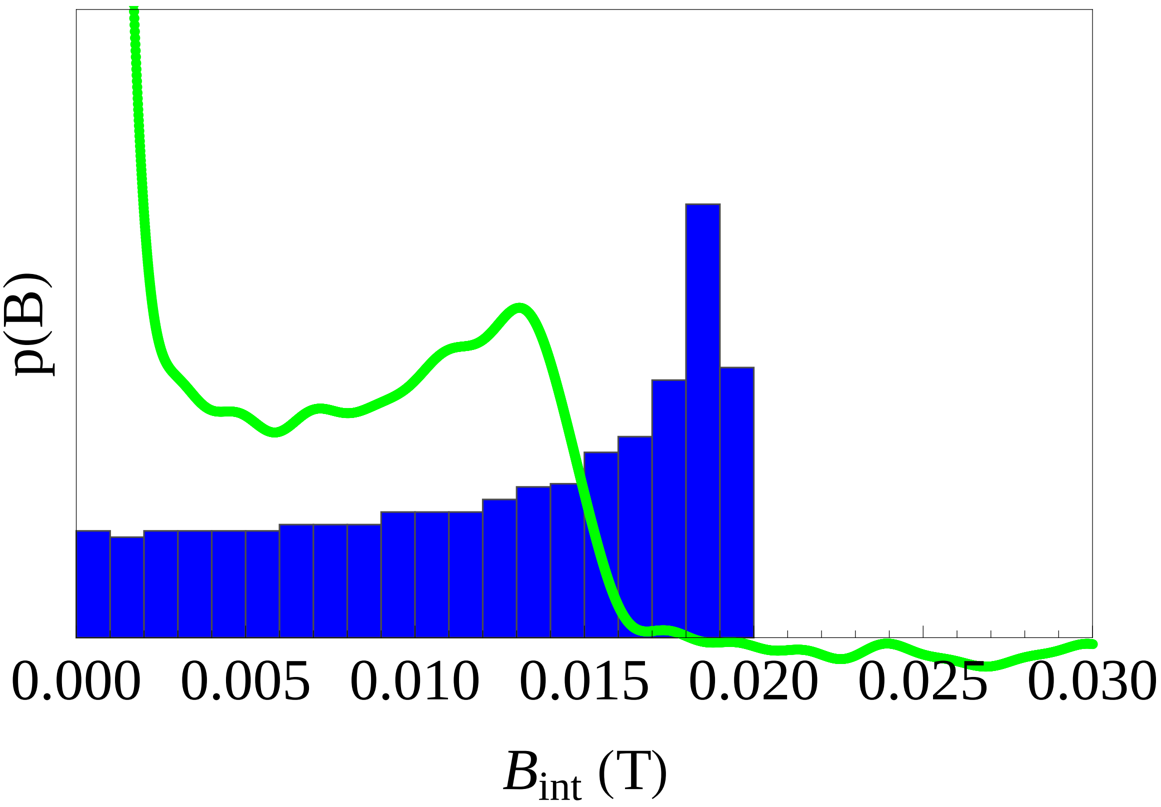

Figure 5.29: Comparison of the μSR experimental data (apple-green line) and the model illustrating rotation within the τ_3 IR (shown as Model 4 in the dipole field section). Here, $\mathbf{m}_{Cu}$= 0.36 μ_B as deduced from the ^{139}La-NMR measurement within this model.

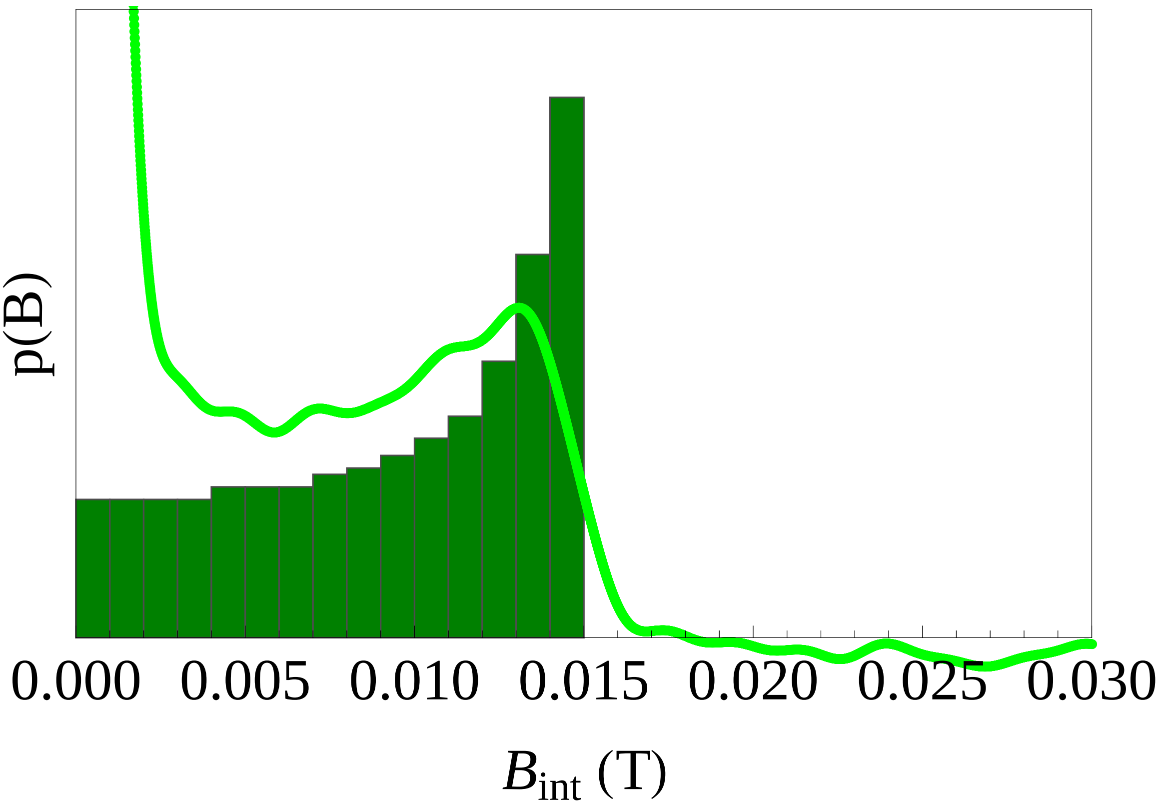

Figure 5.30: Comparison of the μSR experimental data (apple-green line) and the model illustrating rotation within the τ_5 IR (shown as Model 5 in the dipole field section). Here, $\mathbf{m}_{Cu}$= 0.31 μ_B as deduced from the ^{139}La-NMR measurement within this model. This model fits best the experimental data. The additional smoothing/broadening of the data compared to the model can well be explained by some degree of magnetic disorder/imperfections. Note that the upturn of $p(B)$ for the experimental data at low field values is an artefact of the fast fourier transformation since the time-independent (zero frequency) tail of the powder μSR data are also transformed.

From the simulations, even though all three models qualitatively results to a broad field distribution, the model with the symmetry-allowed variation of relative angles within the τ_5 IR (Model 5) is evidently the model that best-describes the experimental data at this particular temperature region. Note that the τ_5 magnetic structure models are those that are illustrated, e.g. in Figures 2.13 and 2.15. The distribution of magnetic structures that are present at different spatial locations in the sample are therefore characterized by different relative orientations (γ angles) of neighboring CuO_2 planes with a rigorous antiferromagnetic coupling in each plane. Whether all even and odd planes are coupled ferromagnetically can not be decided by the simulation. Nevertheless, this seems plausible since this magnetic coupling is weak, but not frustrated by geometry. The variation of the γ angle across the sample implies both that the coupling between neighboring planes is extremely weak and that at these temperatures, there is no strong enough magnetic anisotropy in the plane compared to the thermal energy $k_B T$ to impose a preferred orientation. The fact that nature obviously selects only magnetic structures that belong to the same IR of the symmetry group anyhow shows that a weak coupling of neighboring layers exists. The underlying physical interaction responsible for this behavior is not clear at the moment.

$T \leq 40\ K$, ***Lock-in*** **Regime**

The single symmetric Lorentzian field distribution seen below 40 K is simulated using the special cases of the models previously described. Figure 5.31 summarizes all four models (Col I, NCol I, Col II, and NCol II) in comparison with our low-temperature μSR data. In all four models, there are always two magnetically non-equivalent fields at the muon sites in the z = 0.25c plane. For model NCol II, the coupling for both sets is very close and may be seen as one single effective line in an experiment, unlike the other models that give two splitting fields at the muon site. Thus, this NCol II is the most-probable model for the low-temperature regime. A magnetic moment at the Cu sites $m_{Cu} = 0.332\ \mu_B$, very similar to the $m_{Cu} = 0.31\ \mu_B$ determined from the La-NMR measurements by applying the NCol II model, will result in a muon precession frequency of about f $\approx$ 1.5 MHz, in excellent agreement with the observed frequency at low temperatures $T < 40$ K. In addition, it should be noted that also the fact that the full amplitude of the μSR signal is precessing with one frequency clearly speaks for the NCol II model.

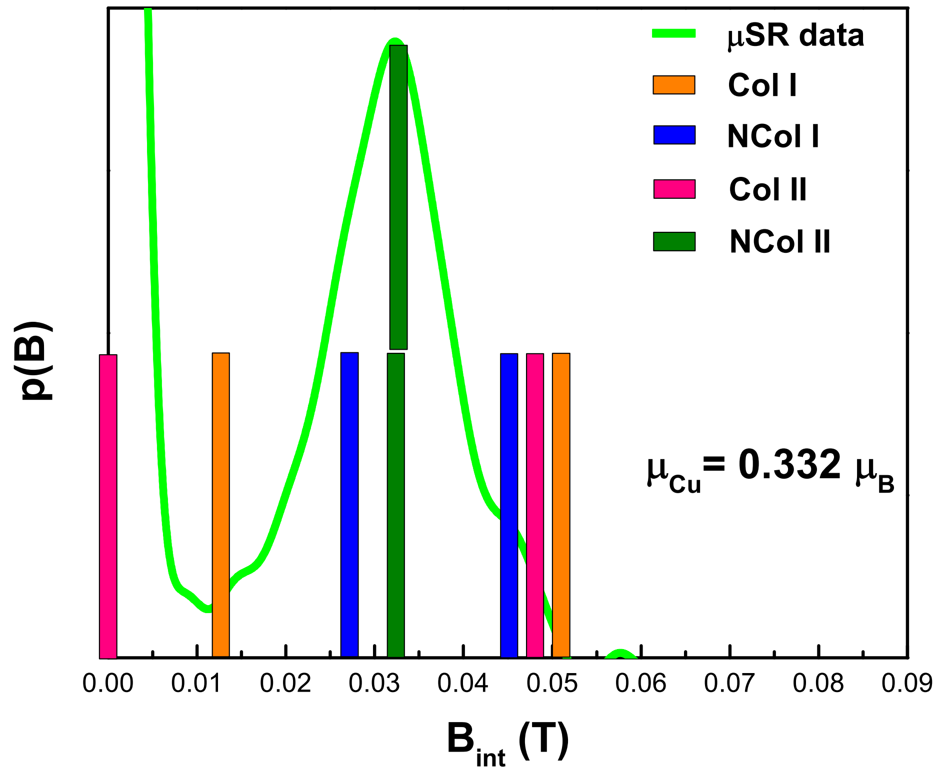

Figure 5.31: The different models in comparison with the experimental data at low temperatures. The values of the two relatively inequivalent fields sensed by the muon for the same model are labeled with the same color accordingly. Note that the upturn of $p(B)$ for the experimental data at low field values is an artefact of the fast fourier transformation since the time independent (zero frequency) tail of the powder μSR data are also transformed. The full amplitude of the oscillating μSR data is present below the peak at about 0.032 T. The NCol II model shows an excellent agreement of the μSR (from which a Cu magnetic moment of 0.332 μ_B is obtained) and NMR data (from which a Cu magnetic moment of 0.31 μ_B is obtained).

In conclusion, below $T_{\mathrm{N3}} = 40$ K, the spin structure locks-in to the magnetic model NCol II. This is the preferred alignment of the system which may be due to the small anisotropy in the CuO plane, as proven by the single μSR frequency (with quantitative agreement of the dipole field and signal amplitude). Interestingly, the NCol II model also belongs to the τ_5 IR as the model 5 that was deduced to be realized in the temperature range from 115 K down to 40 K. This makes the lock-in scenario even more plausible, since the high temperature model with a variation of relative orientations γ can freely rotate into the low temperature phase without leaving the IR. This is in line with the concept that thermal magnetic excitations should take place within the same IR. Apparently, at $T_{\mathrm{N3}} = 40$ K the anisotropy energy within the plane becomes comparable to the thermal energy and the magnetic structure locks-in into the energetically preferred NCol II structure. A possible justification of this spin alignment has been given by Petitgrand et al. [83] who derived the magnetic anisotropy on the basis of pseudo-dipolar interactions. Also interestingly, it is the very same NCol II structure that is adapted by Nd_2CuO_4 at low temperatures [59] indicating that this magnetic structure might be the generic ground state of BCT cuprates independent of the presence of a magnetic rare-earth ion or not.

Table 5.7 summarizes the results of the dipole field calculations on both the La-site and the muon sites for both the low- and high-temperature regimes. Please note that the moment slightly decreases with decreasing temperature, as exhibited by the temperature dependence of the usual order parameter.

Table 5.7: Table of coupling constants and effective moments for each magnetic structure model

	^{139}La		μ_{field1}		μ_{field2}	
	T < 40 K	T > 40 K	T < 40 K	T > 40 K	T < 40 K	T > 40 K
Experimental	29 mT	29 mT	1.5 MHz	1.9 MHz	1.5 MHz	1.9 MHz
Col I Coupling (T/μ_B)	0.0811	-	0.0125	-	0.0510	-
effective Cu moment (μ_B)	0.36	-	0.89	-	0.22	-
NCol I Coupling (T/μ_B)	0.0811	-	0.0449	-	0.0272	-
effective Cu moment (μ_B)	0.36	-	0.25	-	0.41	-
Col II Coupling (T/μ_B)	0.0934	-	0.0480	-	0.0006	-
effective Cu moment (μ_B)	0.31	-	0.23	-	18.5	-
NCol II Coupling (T/μ_B)	0.0934	-	0.0335	-	0.0343	-
effective Cu moment (μ_B)	0.31	-	0.332	-	0.324	-
Model 4:						
rotation τ_3 Coupling (T/μ_B)	-	0.0811	-	0.0525	-	0.0525
effective Cu moment (μ_B)	-	0.36	-	0.268	-	0.268
Model 5:						
rotation τ_5 Coupling (T/μ_B)	-	0.0934	-	0.0479	-	0.0479
effective Cu moment (μ_B)	-	0.31	-	0.294	-	0.294
Model 1:						
random angles Coupling (T/μ_B)	-	0.08725	-	0.047	-	0.047
effective Cu moment (μ_B)	-	0.335	-	0.30	-	0.30

5.5 3D Magnetic Ordering Temperatures

The kind of order a physical system can undergo is profoundly influenced by its dimensionality. Conventional long-range order is common in three-dimensional systems at low temperature. However, as previously mentioned in the Hohenberg-Mermin theorem, the true long-range order in an ideal 2D Heisenberg system having continuous symmetry is destroyed by thermal fluctuations at any finite temperature. The quasi-2D magnetic compounds undergo 3D magnetic ordering that is attributed to slight deviations from an ideal 2D system brought about by the interlayer coupling [153] or spin anisotropy of XY symmetry [154].

In this present work, the most interesting result is that our T'-La_2CuO_4 has strongly reduced Néel temperatures compared with the orthorhombic T-La_2CuO_4, and with other members of the T'-Ln_2CuO_4 e.g. Pr_2CuO_4 and Nd_2CuO_4 systems. An attempt to explain and discuss the possible origin of this strong reduction of the Néel temperatures is presented in the following. Moreover, the implications of our results on the 3D ordering in the long-studied lamellar tetragonal systems is indeed a challenge to elucidate. Nonetheless, I will still naïvely discuss plausible explanations that encompass the magnetic interactions of T'-LCO, in the light of known magnetic features of the insulating antiferromagnetic parent compounds of the cuprates e.g. isotropic and anisotropic couplings, frustration, and other competing or cooperating interactions.

The Néel temperatures of T-La_2CuO_4 are $T_{\mathrm{N1}} \approx T_{\mathrm{N2}} \approx 300$ K as compared to $T_{\mathrm{N1}} = 220$ K and $T_{\mathrm{N2}} = 115$ K for the T'-La_2CuO_4. As previously mentioned, the T-La_2CuO_4 has the CuO_6 octahedra with the lanthanum ions that are ninefoldly-coordinated in a monocapped square antiprisms [155]. Thus, a first qualitative argument for the reduced Néel temperatures in the T'-La_2CuO_4 compared with the T-La_2CuO_4 is simply due to the notion that the octahedral copper environment stabilizes the antiferromagnetic order in the copper oxygen plane. Although the T'-modification has wider in-plane lattice spacings in the copper oxide plane, the rigid oxygen octahedra in the T-phase seemingly augments the energy cost of a copper spin flip as oppose to a planar coordination. In addition, the presence of an orthorhombic distortion of the lattice breaks the tetragonal symmetry, partially lifting the interplanar frustration, and paving way to Dzyaloshinskii-Moriya (DM) interaction leading to weak ferromagnetism. The transition to 3D ordering in T-La_2CuO_4 was attributed to the finite coupling between the planes and the antisymmetric DM spin exchange anisotropy. Note that this anisotropy is absent in tetragonal lamellar systems.

Now comparing the obtained Néel temperatures for the T'-La_2CuO_4 with $T_{\mathrm{N1}} = 220$ K and $T_{\mathrm{N2}} = 115$ K to other T' cuprates like Nd_2CuO_4 and Pr_2CuO_4 with $T_{\mathrm{N1}} \approx 250$ K, the former has still much more reduced T_{N}s. This strong reduction we account to two factors. One, the increase of lattice parameters along both the a- and c -axes, as shown by the progression of the lattice parameters for the T' systems in Figure 5.32. Second and more interestingly, the reduced T_{N} compared to other T'-$\mathrm{RE_2CuO_4}$, e.g. $\mathrm{Nd_2CuO_4}$ or $\mathrm{Pr_2CuO_4}$, with $T_{\mathrm{N1}} \simeq 250$ K and $T_{\mathrm{N2}} \simeq 170$ K can be explained in a different way, i.e. the presence of a magnetic rare-earth ion which has a striking influence on the interlayer interactions in the T'-$\mathrm{RE_2CuO_4}$. These two accounts will be discussed in more detail in the following.

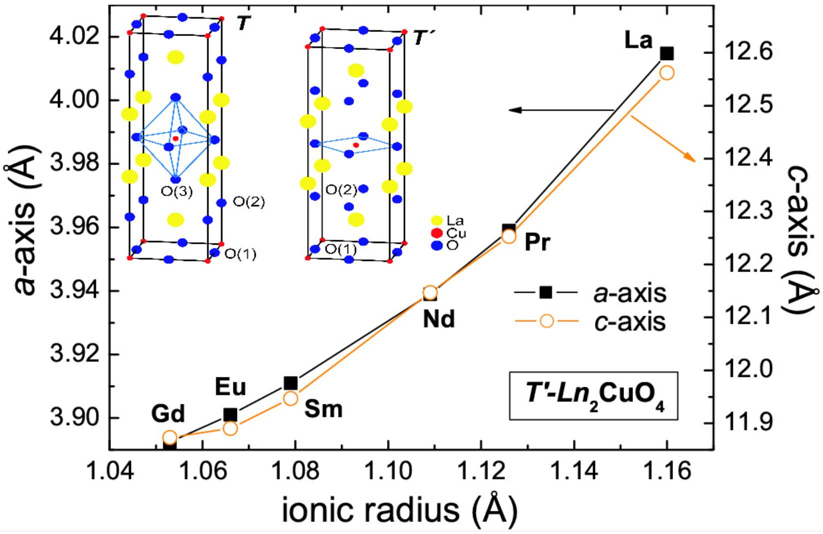

Figure 5.32: Lattice constants for T'-$\mathrm{RE_2CuO_4}$ systems. The inset once again compares the comparison between a T and a T' structure, to note that these $\mathrm{RE_2CuO_4}$ systems adhere to the T'-structure. Reproduced from Ref. [44].

The increased lattice constants should consequently reduce both the in-plane coupling constant (J) as well as the coupling between the $\mathrm{CuO_2}$ planes (J'). The cuprates are commonly characterized by small ratios of J'/J. Thus, the cuprates are considered to be ideal approximations of a 2D Heisenberg antiferromagnet. With this notion, one can use the 2DQNLσ model to predict the long-range order and to discuss the dynamic and static properties of these systems. Within this model, the magnetic correlation length can be estimated from $\xi_{2D} \simeq 0.5a$ exp (1/x) [1- x/2 + O(x^2)], with the lattice constant a and $x = k_B T/(1.13J)$. The 3D ordering temperature is then governed by the interplanar coupling as given by $J'(N_0/S)^2(\xi_{2D}/a)^2 \simeq k_B T_N$. $\mathrm{N_0/S} \simeq 0.36$ denotes the staggered magnetization at T= 0 due to quantum fluctuations and ξ_{2D} is the magnetic correlation length. Considering once again the phase diagram of the QNLσ model in Figure 2.5 in chapter 2, for the case when a long-range order at T= 0 is assumed, the system is in the renormalized classical regime. Renormalization group analysis results to an exponentially diverging correlation length as a function of temperature with T→0.

The increase in lattice constants, in principle, can be considered as the initial rationale behind the strong reduction of the T_{N} in T'-LCO. However, experiments have proven that the in-plane coupling J for the T- and T'-cuprates depends only weakly on the lattice constant a [156, 157]. The in-plane coupling J follows a power-law dependence. Thus, $J = J_0\ (a_0/a)^4$ with $J_0 = 0.13$ and $a_0 = 382$ pm. Henceforth, there is an approximately 5% reduced coupling in the T'-LCO in comparison with the Pr compound ($J_{La} = 0.95\ J_{Pr}$) and $J \approx 0.11$ eV can be calculated. The implication of this result suggests that if T_{N} would be determined by J like in a 3D Heisenberg magnet ($J \simeq \mathrm{k}_B T_{\mathrm{N}}$, which sets the upper limit for the influence of J on T_{N} in the 2D system), one would suppose a maximally 5% reduction that would still be much smaller than the observed difference ($T_{\mathrm{N1}}^{Pr} \approx 250$ K and $T_{\mathrm{N1}}^{La} \approx 220$ K). Additionally, this estimation of J can also allow us to work out the abovementioned equations for ξ_{2D} to determine the interplanar coupling. This points out that having a low T_{N} in T'-LCO results from an approximately ten times smaller J' compared to other T' cuprates ($J'_{La} \approx 0.08\ J'_{Pr}$). This effect appears to be large, keeping in mind the increase in the c-axis by only 2%. Up to a certain qualitative point, this result can be interpreted in a different way.

The body-centered tetragonal cuprates which include a magnetic (NCO) or nearly magnetic (PCO) rare-earth element in their structure possess qualitatively very different magnetic structures. It is well-established that a noncollinear magnetic structure is realized [33] for the rare-earth BCT cuprates in contrast to T-LCO and another tetragonal cuprate SCCO possesing the collinear arrangement. This suggests that the interaction of the Cu and the rare-earth subsystems greatly modifies their magnetic properties. In such a noncollinear structure, the weak pseudo-dipolar interaction which derives from the slight polarization of the magnetic RE angular momenta by the antiferromagnetic ordered Cu spins plays an important role [83]. For the here-studied T'-LCO, La^{3+} is a closed-shell nonmagnetic ion which does not permit for such a polarization that therefore results to a reduced coupling of the $\mathrm{CuO_2}$ planes. The derived result of a ten times decrease of the interplanar coupling can possibly be attributed to the missing polarizable ion in our T'-$\mathrm{La_2CuO_4}$. In a simpler description, the substitution of La by a Nd or Pr is equivalent to putting in some of the magnetic *glue* between the $\mathrm{CuO_2}$ layers. This finding and claim will later on be reinforced by a study on $\mathrm{La_{1.85}Sm_{0.15}CuO_4}$ to be discussed in the next chapter where some "magnetic glue" has been added to T'-$\mathrm{La_2CuO_4}$ on purpose to study this effect.

The main points discussed above were wrapped up in a publication, see Phys. Rev. B. **82**, 180508(R) (2010).

RAPID COMMUNICATIONS

PHYSICAL REVIEW B **82**, 180508(R) (2010)

Enhanced two-dimensional behavior of metastable T'-La$_2$CuO$_4$, the parent compound of electron-doped cuprate superconductors

R. Hord,[1] H. Luetkens,[2] G. Pascua,[2] A. Buckow,[3] K. Hofmann,[1] Y. Krockenberger,[4] J. Kurian,[3] H. Maeter,[5] H.-H. Klauss,[5] V. Pomjakushin,[6] A. Suter,[2] B. Albert,[1] and L. Alff[3]

[1]*Eduard-Zintl-Institute, Technische Universität Darmstadt, Petersenstr. 18, 64287 Darmstadt, Germany*
[2]*Laboratory for Muon Spin Spectroscopy, Paul-Scherrer-Institute (PSI), 5232 Villigen, Switzerland*
[3]*Institute of Materials Science, Technische Universität Darmstadt, Petersenstr. 23, 64287 Darmstadt, Germany*
[4]*Cross-Correlated Materials Research Group (CMRG), RIKEN Advanced Science Institute, Wako 351-0198, Japan*
[5]*Institut für Festkörperphysik, TU Dresden, D-01069 Dresden, Germany*
[6]*Laboratory for Neutron Scattering, PSI, ETHZ, CH-5232 Villigen PSI, Switzerland*

(Received 22 October 2010; published 10 November 2010)

We synthesized crystalline bulk samples of lanthanum cuprate in the metastable T' phase using cesium hydroxide flux. Its crystal structure was determined as space group $I4/mmm$, no. 139, a=401.02 pm, c=1252.66 pm. Muon spin rotation reveals a gradual slowing down of magnetic fluctuations below $T_{N1} \approx 200$ K, and static magnetic order below $T_{N2}=115$ K, in sharp contrast to La$_2$CuO$_4$ in the T structure where $T_{N1} \approx T_{N2} \approx 300$ K. Our result shows that the strikingly different magnetic behavior of the two parent compounds has its origin in the two crystal structure modifications. In addition, we find that T'-La$_2$CuO$_4$ has strongly reduced magnetic interactions compared to the other T' materials Nd$_2$CuO$_4$ and Pr$_2$CuO$_4$, where Nd^{3+} and Pr^{3+} are magnetic ions in contrast to the nonmagnetic La^{3+}.

DOI: 10.1103/PhysRevB.82.180508 PACS number(s): 74.72.Cj, 74.25.Ha, 74.62.Bf, 74.72.Ek

La$_2$CuO$_4$ is the parent compound of hole- and electron-doped high-temperature superconductors of the form La$_{2-x}A_x$CuO$_4$, e.g., with A=Ba for hole doping and Ce for electron doping. Since all hole-doped cuprates crystallize in the so-called T phase, T-La$_2$CuO$_4$ is their parent compound. In contrast, all electron-doped cuprates crystallize in the so-called T' phase, which means that lanthanum cuprate in its metastable T' modification is their true parent compound. Most studies of electron-doped cuprates have been restricted to nonlanthanum based systems such as Nd$_2$CuO$_4$ or Pr$_2$CuO$_4$—materials which have no equivalent on the hole-doped side of the phase diagram.[1,2] Revealing the intrinsic magnetic and superconducting properties of hole- and electron-doped cuprates requires therefore also a comparison of T-La$_2$CuO$_4$ and T'-La$_2$CuO$_4$. The structure of T-La$_2$CuO$_4$ is similar to the tetragonal K$_2$NiF$_4$-structure type but reported to be orthorhombically [space group (s.g.), *Bmab*, no. 64] (Refs. 3 and 4) or even monoclinically distorted (s.g., *Bm*11, no. 8) as observed by neutron scattering in almost untwinned single crystals.[5] It exhibits static antiferromagnetism with reported Néel temperatures between 296 K (Ref. 6) and 316 K.[5] In the T'- or Nd$_2$CuO$_4$ structure ($I4/mmm$, no. 139), copper ions are not coordinated octahedrally but form layers consisting of CuO$_4$ squares. The magnetic properties of T'-La$_2$CuO$_4$ have not been investigated in detail so far, simply due to the lack of available bulk samples of this metastable compound. Magnetic studies of Nd$_2$CuO$_4$ and Pr$_2$CuO$_4$ have been performed[7] but are complicated by the presence of the additional magnetic ions Nd^{3+} and Pr^{3+}.

Using conventional bulk methods, only Pr$_{1-x}$LaCe$_x$CuO$_4$ could be synthesized with maximally half of the Pr sites occupied by La ions.[8] The parent compound T'-La$_2$CuO$_4$ itself is difficult to access because of the higher stability of the T modification. Only recently, Kato *et al.*[9] reported soft-chemical techniques to synthesize oxide superconductors and mentioned a successful preparation of T'-La$_2$CuO$_4$ as bulk material with lattice parameters a=402 pm and c=1249 pm employing NaOH/KOH melts at 350 °C.[10] Here we describe a cesium hydroxide flux based synthesis route to high-quality bulk samples of T'-La$_2$CuO$_4$, and determine its basic magnetic properties using the muon spin rotation technique.

Stoichiometric amounts of copper oxide CuO (Fluka >99%) and lanthanum oxide La$_2$O$_3$ (Merck KGaA Darmstadt 99.5%) were mixed using a ball mill at 15 Hz for 18 min, ground and put in an open silver crucible together with cesium hydroxide CsOH (monohydrate, Fluka >95%), the oxides/hydroxide molar ratio being approximately 1:3. The crucible was placed in a furnace and heated under purified argon flow to 653 K for 24 h. After cooling to room temperature, the reaction cake was ground in an argon glove box, and then, under flowing argon, washed with distilled (deionized) water to dissolve the hydroxide. A black powder was filtered off and dried at 343 K in vacuum over night. The absence of elements (particularly Cs) other than La, Cu, and O in the samples was shown by energy dispersive x-ray spectroscopy. X-ray diffraction patterns of the products on flat plate holders were collected at room temperature, using a powder-diffraction system STOE STADI P with monochromatized cobalt radiation (λ=178.896 pm) in transmission geometry. A Rietveld refinement [program GSAS (Ref. 11)] was performed using structure data from Nd$_2$CuO$_4$ (Ref. 12) as starting parameters. Powder patterns, both experimental and calculated, are shown in Fig. 1. Table I gives the results of the structure determination of T'-La$_2$CuO$_4$. Figure 2 shows the evolution of the a and c axes of T'-Ln_2CuO$_4$ following the lanthanide (Ln) contraction.

We have derived the site occupancies of oxygen in T'-La$_2$CuO$_4$ including the defect site O(3) of apical oxygen on an identically fabricated sample. We have found in-plane

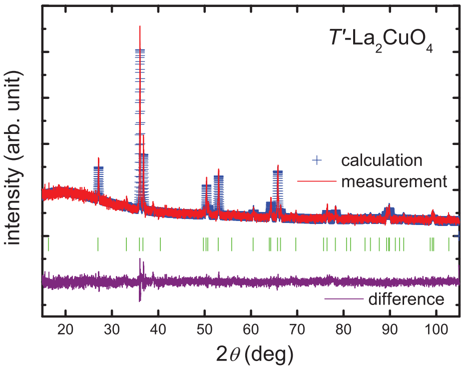

FIG. 1. (Color online) Observed, calculated powder pattern, and difference curve (bottom) for T'-La_2CuO_4. Vertical dashes indicate the positions of the reflections.

oxygen O(1) 2.000(12), out-of-plane O(2) 1.938(11), and apical oxygen O(3) 0.018(5). Comparing this result to literature values,[15] our samples are close to the reported values of the best reduced samples. This shows that the low-temperature synthesis yields about stoichiometric compounds without additional reduction step. While it is difficult to tell whether the small O(3) value is significant without having large single crystals, it is interesting to note that there seem to be vacancies on the O(2) site. Again, this has been also found in Nd_2CuO_4.[15]

TABLE I. Details on the structure refinement of T'-La_2CuO_4. Numbers in brackets are standard deviations that refer to the last digit. U_{iso} values (in picometer square) are defined as one third of track of the orthogonalized tensor U_{ij}. Wyckoff sites for La, Cu, O(1), and O(2), respectively, are 4*e*, 2*a*, 4*c*, and 4*d* (Ref. 13).

Formula unit		La_2CuO_4
Temperature (K)		293(2)
Crystal system		Tetragonal
Space group		$I4/mmm$
a,b (pm)		401.02(2)
c (pm)		1252.66(9)
$V/10^{-6}$ (pm^3)		201.45(3)
Calculated density (g/cm^3)		6.683
No. of reflections (measured)		70
No. of parameters (refined)		10
$\rho_{min/max}$		−3.256/4.458
R_p		0.0741
R_{wp}		0.0945
$\chi 2$		0.9468
Atom	$x\ y\ z$	U_{iso} or U_{11}, U_{22}, U_{33}, U_{12}, U_{13}, U_{23}
La	0 0 0.3528(4)	0.024(2), 0.024(2), 0.037(3), 0, 0, 0
Cu	0 0 0	0.023(6), 0.023(6), 0.048(9), 0, 0, 0
O(1)	0 0.5 0	0.025
O(2)	0 0.5 0.25	0.05(2)

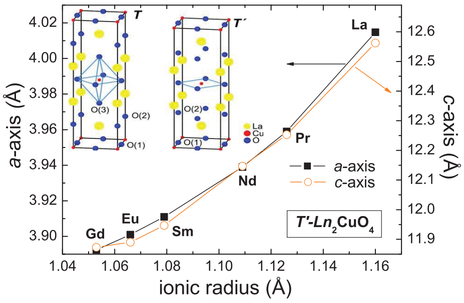

FIG. 2. (Color online) Lattice constants for T'-Ln_2CuO_4. The data points for $Ln \neq$ La are taken from literature (Ref. 14). Inset: comparison of the T and the (tetragonally idealized) T' structures of La_2CuO_4.

The choice of CsOH as flux medium is important to ensure an *undoped* compound T'-La_2CuO_4. Since the La position is eightfold coordinated, the ionic radius of La^{3+} is about 116 pm. Sodium with an ionic radius of 118 pm therefore is a good substitution and (hole) dopant. In T-La_2CuO_4 sodium doping leads to similar superconducting critical temperatures of up to 40 K as the classical doping by Sr^{2+}.[16] Doping with potassium (ionic radius of 151 pm) is more difficult and superconducting T-structure samples were not reported.[16] For Cs^+ with an even larger ionic radius of 174 pm doping in both the T and T' structures can be excluded due to the huge difference in size between Cs^+ and La^{3+}.

T'-La_2CuO_4 is an electrical insulator, i.e., in pressed bulk pellets the resistivity in a standard four-probe setup was too high to be measured. We investigated the magnetic properties of T'-La_2CuO_4 by muon spin rotation and relaxation (μSR).[17]

In the inset of Fig. 3 we show representative zero-field μSR data at 10, 130, 180, and 220 K. At the highest

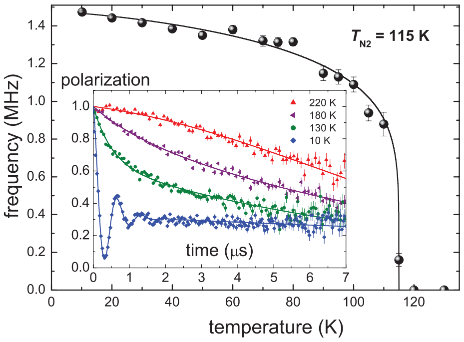

FIG. 3. (Color online) Temperature dependence of the magnetic order parameter as measured by the μSR precession frequency (the solid line is a guide to the eyes). Inset: representative zero-field μSR spectra for 10, 130, 180, and 220 K.

temperature the muon spin polarization $P(t)$ is well described by the Gaussian Kubo-Toyabe (GKT) function $P(t)=\frac{1}{3}+\frac{2}{3}[1-(\sigma t)^2]\exp(-\frac{1}{2}\sigma^2 t^2)$.[18] The small relaxation rate σ and the functional form are typical for static and randomly oriented magnetic fields originating from nuclear moments only. This means that at 220 K, T'-La$_2$CuO$_4$ is in the paramagnetic state and that the electronic Cu $3d$ moments are rapidly fluctuating so that the resulting depolarization, given by the field averaged over the muon lifetime (2.2 μs), is small compared with the nuclear contribution. Below temperatures of $T_{\mathrm{N1}}\approx 200$ K an additional exponential depolarization gradually develops with decreasing temperature on the cost of the paramagnetic GKT signal which can be fitted to $P(t)=\exp(-\lambda t)$ with a relaxation rate λ. In principle this relaxation could stem from static or slowly (in the megahertz region) fluctuating electronic moments. Longitudinal field (LF) μSR experiments can distinguish between these two scenarios.[18] Our LF-μSR measurements prove the predominantly dynamic character of the depolarization. With decreasing temperature the fluctuation slows down, thereby bringing the fluctuation rate into the time window of the muon ($10^{-6}-10^{-11}$ s), which increases the observable depolarization. Below $T_{\mathrm{N2}}=115$ K, the electronic moments become static on the scale of the muon lifetime, causing the muon spins to precess in the static local fields B_{loc} produced by the Cu moments.

A translationally invariant antiferromagnet possesses a well-defined local field B_{loc} at the muon site. Correspondingly a single Larmor precession frequency $2\pi f=\gamma_\mu B_{\mathrm{loc}}$ (muon gyromagnetic ratio $\gamma_\mu=8.531\times 10^8$ rad s^{-1} T^{-1}) is found which in an insulator is proportional to the staggered magnetization, i.e., the magnetic order parameter. The observed damped oscillation is indicative of long-range order with a moderate degree of magnetic disorder.[17] At lowest temperatures the μSR data of T'-La$_2$CuO$_4$ can be well described by $P(t)=\frac{2}{3}e^{-\lambda_T t}\cos(2\pi f t)+\frac{1}{3}e^{-\lambda_L t}$ with λ_T and λ_L being the transverse and longitudinal relaxation rate. Interestingly, in the temperature interval of 40 to 115 K the low-temperature fit function does not describe the data well. This might indicate some more complicated magnetic state in this temperature range. The temperature dependence of the μSR precession frequency is shown in Fig. 3. The observation of a 1/3 nonoscillating μSR signal fraction proves that 100% of our sample orders since in a fully magnetic powder 1/3 of the local fields are parallel to the initial muon spin direction and do not cause a precession. This information is only obtainable with a local probe like μSR and is indispensable for the absolute determination of the Cu magnetic moment by subsequent neutron-diffraction studies. However, since μSR is a *local* probe, the Cu spin structure cannot be determined directly by our measurements and awaits neutron scattering. The observed μSR frequency is a bit smaller than, but of the same order as, that in other members of the T'-Ln_2CuO$_4$ family.[8,19]

The difference between T_{N1} and T_{N2} is most pronounced for the here reported parent compound T'-La$_2$CuO$_4$. However, qualitatively the same picture was also previously observed for other members of the T'-Ln_2CuO$_4$ family. For example, slow magnetic fluctuations below T_{N1} and the appearance of static magnetic order below T_{N2} has been also observed in Pr$_{1-x}$LaCe$_x$CuO$_4$ and Nd$_2$CuO$_4$.[8,20] It has been shown on identical samples that T_{N1} as sensed by muons corresponds to the temperature $T_{\mathrm{N}}^{\mathrm{neutron}}$, where the magnetic peak intensity starts to develop in elastic neutron-scattering experiments.[21] Taking into account the different time scales of μSR and neutron scattering a clear physical picture emerges from the complementary information of the two techniques: below $T_{\mathrm{N1}}\approx T_{\mathrm{N}}^{\mathrm{neutron}}$ long-range antiferromagnetic correlations build up in the systems which are quasistatic on the time scale of the neutron measurement but still slowly fluctuating in the longer μSR time window while below T_{N2} true static order develops on the time scale of the muon measurement. Please note that this scenario also naturally explains the unusually fast (almost first order) increase in the observed μSR frequency below T_{N2} (see Fig. 3).

The most interesting result is that T'-La$_2$CuO$_4$ has strongly reduced Néel temperatures $T_{\mathrm{N1}}\approx 200$ K and $T_{\mathrm{N2}}=115$ K (static order) compared to T-La$_2$CuO$_4$ with $T_{\mathrm{N1}}\approx T_{\mathrm{N2}}\approx 300$ K. Our result suggests that the octahedral copper environment stabilizes the antiferromagnetic order in the copper oxygen plane. It is likely that the energy cost of a copper spin flip in the rigid oxygen octahedra is enhanced compared to the planar coordination. This simple picture gives a first qualitative argument for a reduced T_{N} in T'-La$_2$CuO$_4$ compared to T-La$_2$CuO$_4$, which even has wider in-plane lattice spacings in the copper oxide plane.

Also compared to other T' cuprates such as Nd$_2$CuO$_4$ and Pr$_2$CuO$_4$ with $T_{\mathrm{N1}}\approx 250$ K,[19,22] T'-La$_2$CuO$_4$ has the lowest Néel temperatures T_{N1} and T_{N2} (the onset temperature of spontaneous muon spin precession indicating static magnetic order). Taking, e.g., the data of Fujita *et al.*[8] on Pr$_{1-x}$LaCe$_x$CuO$_4$ T_{N2} extrapolates for $x=0$ (corresponding to PrLaCuO$_4$) to approximately 170 K. In the following, we discuss a possible origin of this strong reduction in T_{N} in some detail. In principle, this can be anticipated from the increase in the lattice parameters along both the c and a axes as shown in Fig. 2 which should reduce both the in-plane coupling constant (J) as well as coupling between the CuO$_2$ planes (J'). Generally, the cuprates are characterized by small ratios of J'/J, therefore they can be regarded as nearly two-dimensional (2D) magnetic systems. The magnetic ground state of such a 2D system has been extensively studied since the discovery of high-T_{C} cuprates. It has been shown that the 2D Heisenberg model can be mapped onto a quantum nonlinear sigma model.[23] The three-dimensional (3D) magnetic ordering temperature is determined by the small interplanar coupling and T_{N} can be estimated from $J'(N_0/S)^2(\xi_{2D}/a)^2\simeq k_B T_{\mathrm{N}}$. $N_0/S\simeq 0.36$ denotes the reduced staggered magnetization at $T=0$ due to quantum fluctuations and ξ_{2D} is the magnetic correlation length. Within this model and in the so-called renormalized classical regime, for which experiments suggest applicability for the cuprates,[24,25] the magnetic correlation length can be written as $\xi_{2D}\simeq 0.5a\exp(1/x)[1-x/2+O(x^2)]$ with the lattice constant a and $x=k_B T/(1.13J)$. It has been shown experimentally[26,27] that the in-plane coupling J for T and T' cuprates depends only weakly on the lattice constant a. It follows a power-law dependence $J=J_0(a_0/a)^4$ with $J_0=0.13$ eV and $a_0=382$ pm. Therefore, in T'-La$_2$CuO$_4$ the coupling is reduced by approximately 5% compared to the Pr compound

($J_{\mathrm{La}}=0.95J_{\mathrm{Pr}}$) and amounts to $J\approx 0.11$ eV. This means that if T_{N} would be determined by J like in a 3D Heisenberg magnet ($J\approx k_{\mathrm{B}}T_{\mathrm{N}}$, which represents an upper limit for the influence of J on T_{N} in the 2D system), one would expect a reduction of maximally 5% which would be still much smaller than the observed difference ($T_{\mathrm{N1}}^{\mathrm{Pr}}\approx 250$ K and $T_{\mathrm{N1}}^{\mathrm{La}}\approx 200$ K). On the other hand, this estimate of J now allows us to determine the interplanar coupling from the combination of the above equations using the measured $T_{\mathrm{N}}=T_{\mathrm{N1}}\approx 200$ K and $a=401$ pm. This means that such a low T_{N} results from an approximately ten times smaller J' compared to other T' cuprates ($J'_{\mathrm{La}}\approx 0.08J'_{\mathrm{Pr}}$).

This effect seems to be large bearing in mind the increase in the c axis by only 2%. At least qualitatively this result can be understood in a different way. It is well established that in contrast to T-La$_2$CuO$_4$ the T'-Ln_2CuO$_4$ compounds possess a noncollinear magnetic structure, see, e.g. Ref. 28. In such a noncollinear structure the static and dynamic magnetic properties are governed by weak pseudodipolar interaction which derives from the slight polarization of the rare-earth angular momenta by the antiferromagnetic ordered Cu spins.[29] In contrast to other lanthanides in T'-Ln_2CuO$_4$ the La^{3+} is a closed-shell nonmagnetic ion which does not allow for such a polarization therefore leading to a reduced coupling of the CuO$_2$ planes. In other words, the substitution of La by, e.g., Pr or Nd is equivalent to taking out some of the magnetic "glue" between the 2D CuO$_2$ layers. As a result, only the direct comparison of T and T'-La$_2$CuO$_4$ (without the interference of additional magnetic ions) reveals the true structural effect on the *intrinsic* magnetic properties. One may speculate that the observed enhanced two dimensionality ($J'/J\approx 2\times 10^{-6}$) and the corresponding increase in magnetic fluctuations favors a faster transition into a superconducting phase upon doping. Indications of such behavior were found previously in bulk[30] and in molecular beam epitaxy grown thin films[31] of T'-La$_{2-x}$Ce$_x$CuO$_4$, where superconductivity occurred even at slightly lower doping values than on the hole-doped side of the phase diagram. Recent electronic-structure calculations also indicate a more metallic character of the T' structure.[32] Furthermore, the doping of maximal critical temperature in La$_{2-x}$Ce$_x$CuO$_4$ is about $x_{\mathrm{opt}}=0.09$, which is well reduced compared with the optimal doping concentration in La$_{2-x}$Sr$_x$CuO$_4$, where $x_{\mathrm{opt}}=0.15$.[31] However, these results have to be confirmed by bulk samples.

In conclusion, bulk material of crystalline T'-La$_2$CuO$_4$ was synthesized at moderate temperatures and its crystals structure was determined. Muon spin rotation measurements indicate a slowing down of weakly dynamic antiferromagnetism below $T_{\mathrm{N1}}\approx 200$ K and static order below $T_{\mathrm{N2}}=115$ K, which is strongly reduced compared to T-La$_2$CuO$_4$ and the other members of the T'-Ln_2CuO$_4$ family. Within the T' compounds this reduction in T_{N} can be traced back to a ten times decrease in the interplanar coupling possibly due to the missing polarizable lanthanide ion in T'-La$_2$CuO$_4$. Our result can be used as test for a realistic theoretical modeling of the parent compounds of the electron- and hole-doped high-temperature superconductors, taking into account their different crystalline structure.

The authors acknowledge the support by the DFG under Projects No. AL536/9-1 and No. AL560/9-1. Part of this work was performed at the Swiss Muon Source (Villigen, Switzerland).

---

[1] Y. Tokura *et al.*, Nature (London) **337**, 345 (1989).
[2] L. Alff *et al.*, Nature (London) **422**, 698 (2003).
[3] B. Grande *et al.*, Z. Anorg. Allg. Chem. **428**, 120 (1977).
[4] For a review see: Hk. Müller-Buschbaum, J. Alloys Compd. **349**, 49 (2003).
[5] M. Reehuis *et al.*, Phys. Rev. B **73**, 144513 (2006).
[6] M. Braden *et al.*, Physica C **223**, 396 (1994).
[7] W. Henggeler *et al.*, Phys. Rev. Lett. **80**, 1300 (1998).
[8] M. Fujita *et al.*, Phys. Rev. B **67**, 014514 (2003).
[9] M. Kato *et al.*, Mater. Sci. Eng., B **148**, 53 (2008).
[10] Y. Imai *et al.*, Chem. Mater. **19**, 3584 (2007).
[11] A. C. Larson and R. B. Von Dreele, program GSAS, Los Alamos, USA, 1985.
[12] I. P. Makarova *et al.*, Acta Crystallogr., Sect. B: Struct. Sci. **52**, 93 (1996).
[13] Structure data available at http://www.fiz-karlsruhe.de/request_for_deposited_data.html, CSD 421550.
[14] J. T. Markert *et al.*, Phys. Rev. Lett. **64**, 80 (1990).
[15] P. G. Radaelli *et al.*, Phys. Rev. B **49**, 15322 (1994).
[16] M. A. Subramanian *et al.*, Science **240**, 495 (1988).
[17] P. Dalmas de Réotier and A. Yaouanc, J. Phys.: Condens. Matter **9**, 9113 (1997).
[18] R. S. Hayano *et al.*, Phys. Rev. B **20**, 850 (1979).
[19] G. M. Luke *et al.*, Phys. Rev. B **42**, 7981 (1990).
[20] T. Kubo *et al.*, Physica C **378-381**, 354 (2002).
[21] T. Uefuji *et al.*, Physica C **378-381**, 273 (2002).
[22] T. R. Thurston *et al.*, Phys. Rev. Lett. **65**, 263 (1990).
[23] S. Chakravarty *et al.*, Phys. Rev. B **39**, 2344 (1989).
[24] B. Keimer *et al.*, Phys. Rev. B **46**, 14034 (1992).
[25] F. Borsa *et al.*, Phys. Rev. B **45**, 5756 (1992).
[26] P. E. Sulewski *et al.*, Phys. Rev. B **41**, 225 (1990).
[27] S. L. Cooper *et al.*, Phys. Rev. B **42**, 10785 (1990).
[28] I. W. Sumarlin *et al.*, Phys. Rev. B **51**, 5824 (1995).
[29] D. Petitgrand *et al.*, Phys. Rev. B **59**, 1079 (1999).
[30] Y. Koike *et al.*, Jpn. J. Appl. Phys., Part 1 **31**, 2721 (1992).
[31] Y. Krockenberger *et al.*, Phys. Rev. B **77**, 060505(R) (2008).
[32] H. Das and T. Saha-Dasgupta, Phys. Rev. B **79**, 134522 (2009).

To recapitulate, T'-LCO has a body-centered tetragonal structure at all temperatures and the nearest-neighbor interlayer exchange is fully frustrated, significantly reducing the effective interplanar coupling. However, such frustration can be removed by quantum fluctuations that can be due to spin-orbit interaction giving rise to a small in-plane anisotropy [158]. Additionally, unlike T-LCO, no orthorhombic distortion exists in T'-LCO, thus DM interaction is absent that dominates the T-LCO. The 3D-ordering in a body-centered tetragonal systems is governed by other type of interactions such as the magnetic dipole interaction, magnetic anisotropy, and biquadratic exchange interactions, which may compete with the effective interactions due to quantum disorder [72]. In addition, quantum fluctuations produce antifferomagnetic interaction between alternate layers and zero point fluctuations favor collinear structures, which obviously in our case is not the dominant effect since a noncollinear structure is obtained at lowest temperatures.

A sequential progression among the other members of the T'-RE$_2$CuO$_4$ (RE= rare earth e.g. La, Pr, Nd) puts this novel parent compound T'-La$_2$CuO$_4$ to be in trend as it qualitatively exhibit the same picture, specifically, the observation of slow magnetic fluctuations below T_{N1} and the emergence of static magnetic order below T_{N2} are similarly the case for Pr$_{1-x}$LaCe$_x$CuO and Nd$_2$CuO$_4$ [109, 159].

The difference between T_{N1} and T_{N2} and the designation of the true 3D magnetic order is significant at the same time debatable in our T'-LCO. It leads us to question when does the 3D magnetic ordering actually occurs. At T_{N1}, the order is only quasistatic. Although, a plausible physical interpretation of the quasistatic behavior of T'-LCO could be another strong evidence of a dynamical layer decoupling and quasi-2D behavior in the cuprates. Yildirim [72] supports the idea that the more two-dimensional the system becomes, it is more plausible that the nearest-neighbor sublayers becomes decoupled due to frustration but the next nearest neighbors are coupled ferromagnetically thus leading to 3D order. If one takes T_{N2} as the true 3D ordering temperature, then our T'-LCO will be one of the most-two dimensional system ever-studied. To illustrate, if one assumes ideal 2D Heisenberg behavior, then one can calculate essential parameters according to the 2DQNLσ model and allows us to compare our T'-LCO to other notable 2D square-lattice quantum Heisenberg antiferromagnet systems as shown in Figure 5.33.

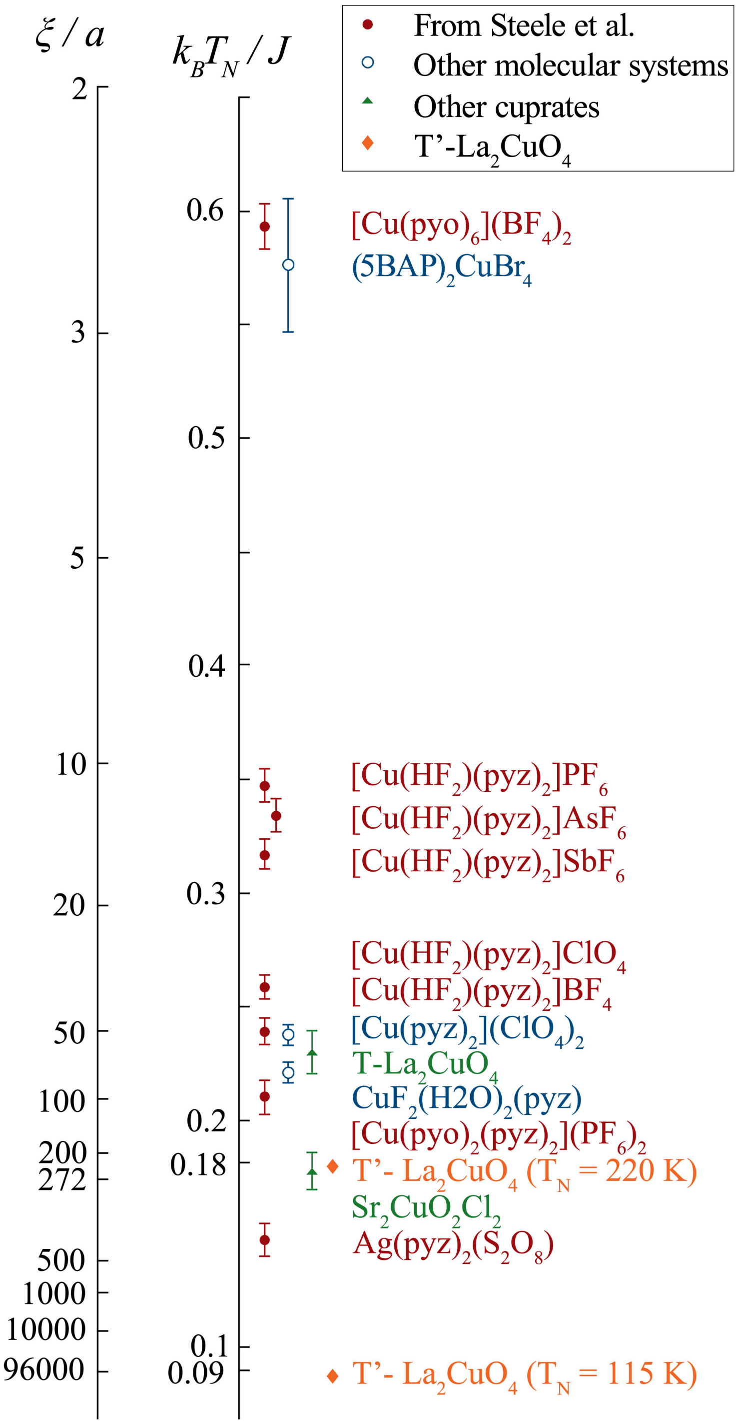

Figure 5.33: Quantification of the two-dimensionality of the notable 2D square-lattice quantum Heisenberg antiferromagnet systems, e.g. molecular magnets studied by Steele et al. [160], other molecular systems, other cuprates, and inserting our T'-LCO in the trend. The figure is reproduced from Ref. [160]. The location of T'-La_2CuO_4 in this plot depends on the assignment of the real 3D ordering temperature which could be either $T_{N1} = 220$ K or $T_{N2} = 115$ K.

However, for the T'-LCO, the observed phase transition temperatures within our designated range of T_{N1} and T_{N2} may also possibly bracket the crossover of the 2D XY to Kosterlitz-Thouless transition, as this system may exhibit 2D Heisenberg to 2D XY behavior and then from 2D XY to a 3D XY transition. Indeed, if we are correct, then this material should be an ideal candidate to further study KT transitions.

Unfortunately, these pool of ideas remain speculative about the true sequence of magnetic ordering in T'-LCO. Further quantitative predictions and extensive experimental evidences must be further obtained to extend our current understanding on the rich transitions exhibited by this novel BCT cuprate.

.

5.6 Outlook

Our T'-La$_2$CuO$_4$ is also a true mother compound of the electron-doped cuprates. The findings presented herein will add up to the database of body-centered tetragonal cuprates that can be made superconducting by electron-doping. In the future, this system doped with electrons by e.g. Ce substitution should provide for the first time a reasonable comparison with its hole- doped counterpart T-La$_{2-x}$Sr$_x$CuO$_4$. However, this work still awaits successful attempts to dope our T'-La$_2$CuO$_4$ so the superconducting derivatives are still underway and would not be a scope of this work.

Single crystal T'-LCO samples will certainly be also useful to elucidate the magnetic properties because single crystal samples have the advantage that one not only can probe the magnitude of the fields but also the field directions with the μSR technique.

6 The Effect of Rare-Earth Substitution on T'-La_2CuO_4 and Oxygen Reduction on $La_{1.85}Sm_{0.15}CuO_4$

In the previous section, the 2-dimensionality of T'-La_2CuO_4 is highlighted and discussed, and we found that the newly-synthesized metastable T'-La_2CuO_4 exhibits much lower T_N and increased magnetic fluctuations compared to other parent compounds of electron-doped superconductors like Nd_2CuO_4 or Pr_2CuO_4.

The next step is to investigate the possible reasons for the observed effects of the increased fluctuations and much lower T_N in the mother compound T'-La_2CuO_4 [44]. Namely, the role of the magnetic rare-earth ion which might effectively enhance the magnetic coupling in the c-direction will be discussed. Secondly, the influence of the reduction annealing on the oxygen occupancies, e.g. the effect of excess oxygen on the apical defect site or from the copper oxygen plane of the substituted compound, e.g. $La_{1.85}Sm_{0.15}CuO_4$, will be focused upon. To address these, a series of measurements on isovalent substitution with magnetic rare-earth i.e. $La_{2-x}RE_xCuO_4$ (RE= rare-earth ion), and comparison of as-grown and reduced samples are carried out.

$La_{1.85}RE_{0.15}CuO_4$ (RE= Sm, Tb, Ho, Er) samples were synthesized and are hoped to help us understand how and if the magnetic rare-earth ions stabilize the magnetism in the T'-structure and enhance the magnetic coupling along the crystallographic c-axis. As the as-grown samples tend to contain excess oxygen in the T'-structures, the removal of these by reduction annealing is well-known to give access to the superconducting regime [28, 35] and would clearly unfold some intrinsic electronic properties. However, there are different scenarios discussed in other related studies on how oxygen reduction can also effectively reduce disorder and therefore impurity scattering, suppress the long-range antiferromagnetic order, and provide itinerant carriers for superconductivity [161, 162, 115, 163, 114, 113, 112, 97] . Hence, it is imperative that the as-grown samples undergo reduction annealing.

In the following sections, the structural and magnetic properties of the bulk samples will be discussed.

6.1 Structural Properties of $La_{1.85}RE_{0.15}CuO_4$ (RE= Sm, Tb, Ho, Er)

$La_{1.85}RE_{0.15}CuO_4$ (RE= Sm, Tb, Ho, Er) samples were synthesized via the same route as the undoped T'-La_2CuO_4 [44]. The structural quality of the as-grown samples were investigated by High-Temperature Xray Diffraction (HT-XRD) performed by our collaboration from Technische Universität Darmstadt, Germany. As an example, the XRD pattern for the as-grown $La_{1.85}Sm_{0.15}CuO_4$ is given in Figure 6.1. The structural parameters were refined and obtained from Rietveld Refinement using the TOPAS Refinement software. In order to gauge how good the Rietveld refinements are, the R-factors are discrepancy values that provide the criteria for judging the quality of Rietveld fits. Table 6.1 shows the R-factors of all the measured as-grown compounds. Rp is the profile R parameter, Rwp is the weighted profile R parameter, and GoF is the goodness of fit. For a discussion about the details and significance of these R-factors in Rietveld analysis, see Refs. [164, 165].

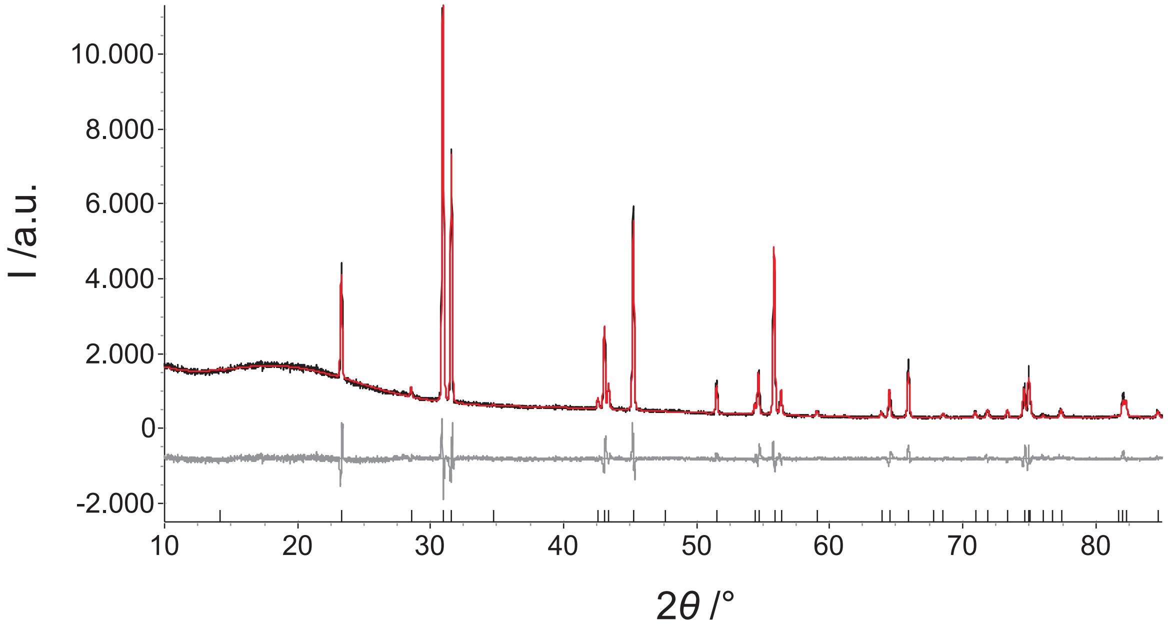

Figure 6.1: X-Ray diffraction pattern for the as-grown $La_{1.85}Sm_{0.15}CuO_4$

Table 6.1: R-factors for the as-grown samples

Sample Name	La_2CuO_4	LSmCO	LTbCO	LHoCO	LErCO
Rp	12.97	4.78	4.30	5.67	5.52
Rwp	9.84	7.81	5.87	9.42	9.00
GoF	0.9468	2.19	1.24	2.39	2.30

Albeit good quality of the Rietveld fits, the more significant results are the parameters displayed in Table 6.2 that can draw-up conclusive results for the structural properties of the abovementioned as-grown compounds.

Table 6.2: La-RE ratio, lattice parameters a and c, and volume

Sample Name	La:RE ratio	Ionic radius RE^{3+} [Å]	lattice parameter a [Å] c[Å]	unit cell volume [$Å^3$]
La_2CuO_4		1.16	4.0102(2) 12.5266(9)	201.45(3)
$La_{1.85}Sm_{0.15}CuO_4$	La: 92.5% Sm: 7.5%	1.079	4.00337(6) 12.4997(3)	200.333(7)
$La_{2-x}Tb_xCuO_4/TbO_{1.81}$	La: 92.5% Tb: 7.5%	1.04	4.00797(6) 12.5167(3)	201.066(8)
La_2CuO_4/Ho_2O_3	La: 92.5% Ho: 7.5%	1.015	4.00585(6) 12.5187(3)	200.886(7)
La_2CuO_4/Er_2O_3	La: 92.5% Er: 7.5%	1.004	4.00737(7) 12.5149(3)	200.977(8)

Taking the undoped compound T'-La_2CuO_4 as a reference for the XRD data, a significant change is observed only for the Sm-substituted compound $La_{1.85}Sm_{0.15}CuO_4$. Since no lattice change is observed for the other compounds of $La_{1.85}RE_{0.15}CuO_4$ (RE= Tb, Ho, Er) especially in the c-direction, the inclusion of the rare-earth within the system may not have been effective. Please note that when the substitution is not effective, the rare-earth is not included in the chemical formula of the compound, given in the table is e.g. La_2CuO_4/Ho_2O_3. It could be that when there is a bigger difference in the ionic radii between the rare-earth used for the isovalent substitution and the reference compound with La^{3+}, then the substitution is not effective. The magnetic properties of these systems were also studied by μSR and they exhibit the same general characteristics as the mother compound. However, due to the inhomogeneity of the rare-earth impurity inclusions, this had added complications in discriminating the physical meaning of the strongly-damped signal that may have come from the rare-earth ions in μSR. Therefore, I will focus on the homogeneously-substituted $La_{1.85}Sm_{0.15}CuO_4$ sample in the following discussion. Unfortunately, neutron diffraction measurements were also done on our as-grown bulk samples only except for the $La_{1.85}Sm_{0.15}CuO_4$. Materials containing rare-earth elements like Gd, Sm , Eu, or Dy are strongly neutron-absorbing. Hence, no neutron measurement were done particularly for the $La_{1.85}Sm_{0.15}CuO_4$.

Since only the as-grown $La_{1.85}Sm_{0.15}CuO_4$ exhibited promising results from the XRD measurements, it was the focus of study to elucidate whether the substitution of a magnetic rare-earth ion will enhance the magnetic coupling along the c-axis direction. In addition, the study of the effect of reduction on the magnetism is a second aim. Thus, the as-grown $La_{1.85}Sm_{0.15}CuO_4$ has undergone reduction annealing at 550 °C, following the same procedure as in Ref. [166]. In addition, such a temperature was chosen because the compound transforms to the T-phase when it is heated above the synthesis temperature of 600 °C. As already mentioned, reduction annealing is an established step that is necessary for the electron-doped cuprates to instigate the appearance of superconductivity, which is in stark contrast with the hole-doped cuprates wherein static long-range antiferromagnetic order is quickly suppressed, the material becoming metallic and superconducting solely by hole-doping. The structural properties of the reduced sample were investigated with HT-XRD and structural parameters were also refined using the TOPAS software package. Table 6.3 gives the refinement results for both the as-grown and reduced $La_{1.85}Sm_{0.15}CuO_4$ samples in comparison with the pristine compound.

Table 6.3: Xray diffraction refinement results of the as-grown and reduced $La_{1.85}Sm_{0.15}CuO_4$ samples in comparison with the parent compound T'-La_2CuO_4

Sample Name	La_2CuO_4	as-grown LSmCO	reduced LSmCO
Lattice parameter	a= 4.0102(2)	a= 4.00305(7)	a= 4.00474(8)
	c= 12.5266(9)	c= 12.4988(4)	c= 12.4920(3)
Rwp	12.97	7.81	8.56
Rp	9.84	4.78	6.04
GoF	0.9468	2.19	1.29

The reduced $La_{1.85}Sm_{0.15}CuO_4$ sample has slightly expanded along the a- and b-directions and correspondingly contracted the c-direction in comparison to the as-grown material. This may imply that some deficient sites are filled-out or repaired, e.g. Cu sites, during reduction. It was believed that the high-temperature synthesis can cause Cu vacancies in e.g. NCCO [167, 168] and PLCCO [169]. Possibly, annealing could drive a redistribution of Cu in which the vacancies in other layers are filled. In addition, a similar situation illustrated by the two-step annealing scheme by Krockenberger and coworkers [125] may also be applicable in our case. It was believed that the as-grown material contains more than the stoichiometric amount of oxygen which are distributed at the apical sites. The first annealing step did not alter the lattice parameters but a significantly higher resistivity value was obtained. This was accounted to oxygen vacancies found in the CuO_2 plane. The second annealing was explained as a process of repairing those in-plane defects by relocating apical oxygen atoms to the planes [125]. Anyway one has to mention that the measurements of Krockenberger et al. have been performed on thin film specimens only which means that no true information on the oxygen site occupation using e.g. neutron scattering could be obtained. A decreased c-lattice parameter was anyhow also observed [125] which has also been associated to the removal of apical oxygen by previous neutron scattering measurements [114, 115] on Nd_2CuO_4 single crystal samples.

For the case of our reduced $La_{1.85}Sm_{0.15}CuO_4$, a combination of those abovementioned scenarios is very likely even though due to the presence of the absorbing Sm in our sample, neutron scattering measurements could also not be performed. Therefore, we can only argue in analogy to the previously studied systems. The decreased c-lattice parameter may imply that the intrinsic apical oxygen found in the as-grown samples had been relocated to the CuO_2 planes, therefore, increasing the a and b- lattice parameters. In addition, it is plausible that potential Cu defects are healed out at the same time.

However, in comparison with the mother compound, the substitution of Sm resulted in a decrease of the lattice parameters for both the as-grown and reduced samples in accordance with the lanthanoid contraction. These structural results are related with its magnetic and electronic properties which will be further discussed in the succeeding section.

6.2 Magnetic Properties of $La_{1.85}Sm_{0.15}CuO_4$

The magnetic properties of the samples had been investigated by bulk μSR using the General Purpose Spectrometer (GPS) of the πM3 beamline at the Paul Scherrer Institute (PSI), Switzerland.

Since only the $La_{1.85}Sm_{0.15}CuO_4$ samples gave promising results from HT-XRD, these samples had likely revealed more compelling μSR results also. Hence, only the magnetic properties for the as-grown and reduced $La_{1.85}Sm_{0.15}CuO_4$ samples are discussed as these are the most viable samples from which a significant conclusion can be drawn.

6.2.1 As-grown and Reduced $La_{1.85}Sm_{0.15}CuO_4$

In this subsection, the as-grown and reduced $La_{1.85}Sm_{0.15}CuO_4$ (LSmCO) samples are presented side-by-side for comparison and discussion. As mentioned above, the as-grown LSmCO had been reduced following the procedure done in Ref. [166] wherein the reduction procedure provides superconducting $La_{1.85}Sm_{0.15}CuO_4$ samples.

$La_{1.85}Sm_{0.15}CuO_4$ should also be undoped since La and Sm ions are both trivalent. The addition of the Sm is believed to stabilize the structure at high temperatures. We were not able to reproduce the data of Asai and coworkers [166] obtaining superconducting samples. Our sample remains magnetic but nonetheless exhibits notable differences from the as-grown compound.

The magnetic properties of both the as-grown and reduced $La_{1.85}Sm_{0.15}CuO_4$ samples are characteristically illustrated by the temperature dependence of the time evolution of the asymmetry in zero applied field, given in Figure 6.2. It is useful to note that to have a compelling picture and comparison with the mother compound T'-LCO, the analytic functions used to model the physical phenomena therein is adapted to the rare-earth substituted compounds as well.

At the highest temperatures, both samples are in the paramagnetic state described by a Gaussian Kubo-Toyabe polarization function that represents a relaxation originating from nuclear moments. Also obviously, the paramagnetic fluctuations are too rapid for the muon to see.

At a slightly lower temperature, at below $T = 220$ K, given in solid brown circles of Figure 6.2, the as-grown sample remained paramagnetic while the reduced sample deviated from Gaussian and developed an exponential-type relaxation. This change of depolarization from Gaussian to exponential suggests that the rapid fluctuation of the Cu^{2+} had slowed down and had gone into the time window of the muon. Although, one observes an increase in

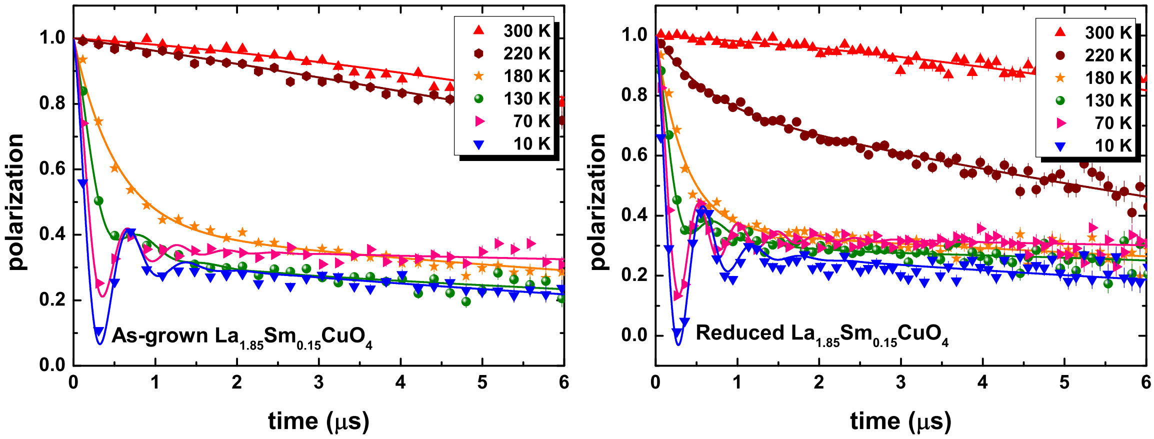

Figure 6.2: Zero-field spectra of the (left) as-grown and (right) reduced $La_{1.85}Sm_{0.15}CuO_4$ samples at 10, 70, 115, 180, 220, 300 K.

the dynamic relaxation rate λ_L, alongside the increase of the static relaxation rate λ_T, given in Figure 6.3. This indicates that at this temperature range, quasistatic antiferromagnetic order similar to the one in the mother compound LCO is realized. On the other hand, one has to note that the dynamic relaxation rate in LSmCO is a factor of 3 smaller than in LCO signifying that there are substantially slower magnetic fluctuations in this LSmCO. In other words, the Cu fluctuation rates are strongly reduced in LSmCO compared to LCO. The decoupling measurements which will be discussed in the succeeding paragraphs would verify this.

The results obtained for the rare-earth substituted compounds are compared with the mother compound. We have defined three characteristic temperatures: T_{N1} is the onset temperature where the exponential-type relaxation starts to appear, T_{N2} is the onset temperature where muon spin precession appears indicating static long-range order, and T_{N3} is the temperature at which there is an observed change of field distribution from an asymmetric broad one to a symmetric and more Lorentzian field distribution. Thus, from these definitions, our characteristic temperature T_{N1} is 220 K for the as-grown sample and 240 K for the reduced sample, respectively. This can be also seen in the increase in the magnetic volume fraction plot of Figure 6.3.

Further cooling down, precession frequency of the muon spin emerges and this proves the appearance of static magnetic order. This is observed below $T_{\mathrm{N2}} =$ 130 K for the as-grown sample and $T_{\mathrm{N2}} =$ 170 K for the reduced sample, respectively, as shown in Figure 6.3. This T_{N2} for both the as-grown and reduced samples, is nonetheless increased in comparison to the one obtained for the T'-La_2CuO_4 mother compound which is $T_{\mathrm{N2}} = 115$ K. This is also visible in the peak of the transverse relaxation rate. At this intermediate temperatures, a

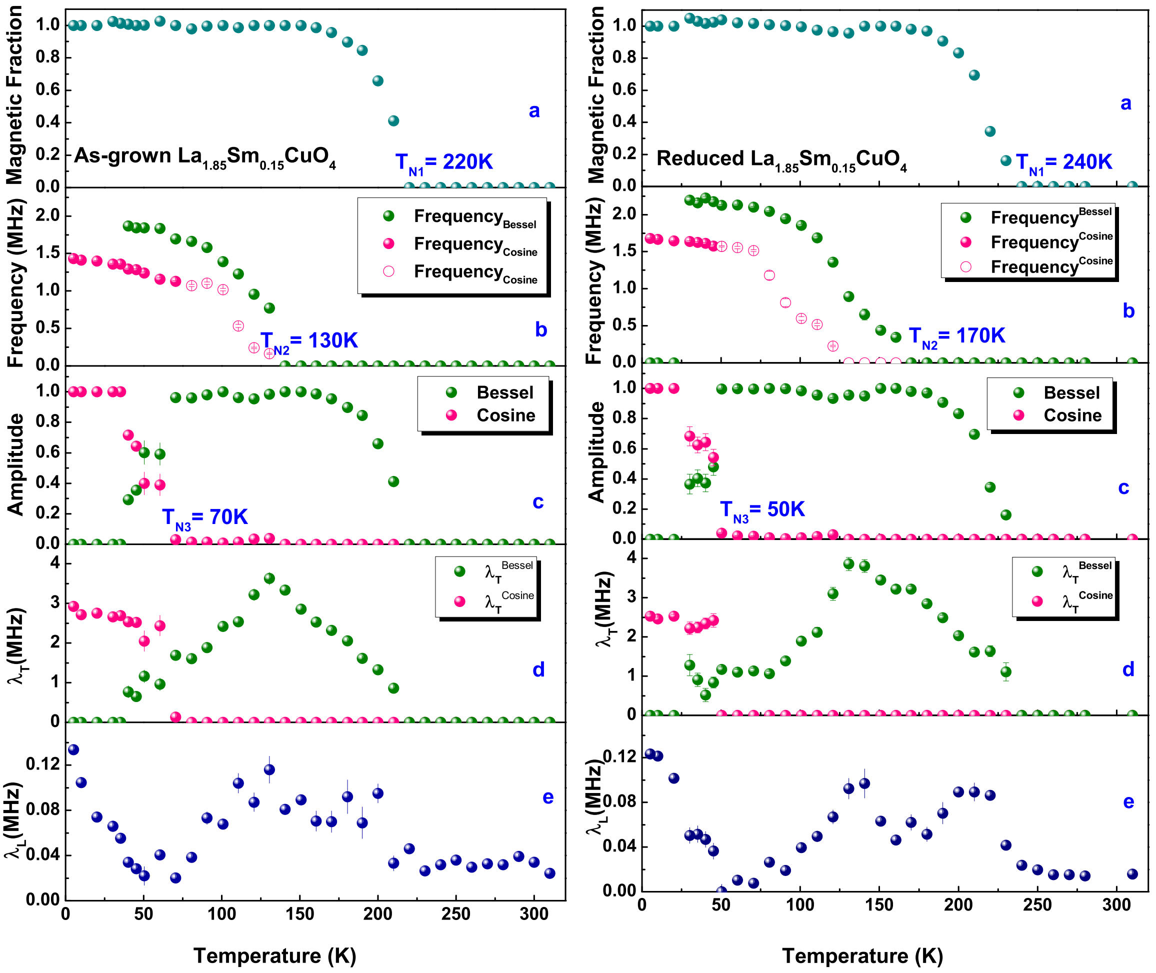

Figure 6.3: ZF-μSR fit results for (left) as-grown and (right) reduced T'-$La_{1.85}Sm_{0.15}CuO_4$ samples: a) The magnetic volume fraction, b) the frequency, c) the amplitude of each signal given by the two magnetic components, d) the transverse relaxation rate, and e) the longitudinal relaxation rate as a function of temperature.

peculiarly-looking broad field distribution is observed which requires a more complicated fitting model. A reasonable and better fit includes two magnetic fractions at this particular temperature region. This means that at this temperature interval, two inequivalent muon sites are detected giving two magnetic components that can be best fitted with Bessel and Cosine functions, respectively. However, as given by the amplitudes of each signal, the Cosine signal is very faint which is only about less than 5%, shown in Figure 6.3*c*.

In order to better visualize and compare the local field distributions at different temperature regions, the real part of the Fast Fourier Transform (FFT) is shown in Figure 6.4 for the as-grown and reduced samples. Each FFT plot includes representative temperatures at each of the three important characteristic regions, showing the evolution of the shape of the field distributions. The sharp peak appearing near zero frequency is the slowly decaying offset asymmetry in time space that was not subtracted from the signal. Comparing the as-grown and the reduced samples, specifically at the intermediate temperatures, one can immediately see that the reduced sample has sharper peaks which entails that there is less disorder in this system. The broad field distribution looking like an Overhauser field distribution is much more pronounced in the reduced sample, see e.g. the 90 K purple plot. These features are unfortunately not very well-captured by the fit parameters shown in Figure 6.3, e.g. the transverse relaxation rate is essentially the same for both samples. The probable reason for this behavior is the peculiar shape of the field distribution which could not be well-represented by the analytical fit functions.

Taking T_{N3} in focus, the cosine component gradually grows and the Bessel component dramatically decreases at $T_{\mathrm{N3}} = 70$ K for the as-grown, and at $T_{\mathrm{N3}} = 50$ K for the reduced compound, down to the lowest temperature. This is exhibited in Figure 6.3 by the amplitude of the two signals coming from the two different magnetic components. This is in contrast with the mother compound where a very abrupt change of the field distribution is observed at 40 K. For the reduced sample, the change happened in a more dramatic manner compared to the as-grown sample. However, both the as-grown and reduced LSmCO samples show a change in T_{N3} that is not as abrupt as in the mother compound.

To isolate static and dynamic nature of magnetism, longitudinal field- μSR (LF-μSR) measurements were carried out at 0.005, 0.02, 0.04, and 0.1 Tesla applied fields. The concept of decoupling was already depicted in detail in chapter 4. The decoupling experiment results are given in Figures 6.5 and 6.6, for the as-grown and reduced sample, respectively. These series of graphs can directly demonstrate that the internal fields are mainly static in nature in all the different temperature regions, and can be decoupled by an applied longitudinal field. Only in the temperature region between T_{N1} and T_{N2} a slight dynamic relaxation is notable as seen from the small damping of the spectra at long times. On the other hand, this dynamic relaxation is much smaller than in the case of the mother compound T'-LCO, see Figure 5.10. This supports our conclusion drawn already from the ZF data that the magnetic dynamics is much slower in LSmCO than in LCO. The difference of the dynamic behavior of the T'-LCO mother compound and the LSmCO samples can also be visualized by the temperature dependence of the dynamic relaxation rate at an applied field of 0.04 T shown in Figure 6.7. Especially at the intermediate region exhibiting a broader peak and a reduced by a factor of two on the longitudinal relaxation rate is observed for the LSmCO samples. In addition, the upturn observed at low-temperatures could imply the slowing down of the Sm moments at low-temperatures. It would be interesting to test with μSR if real static Sm order is achieved, but this had not been the focus of the present study.

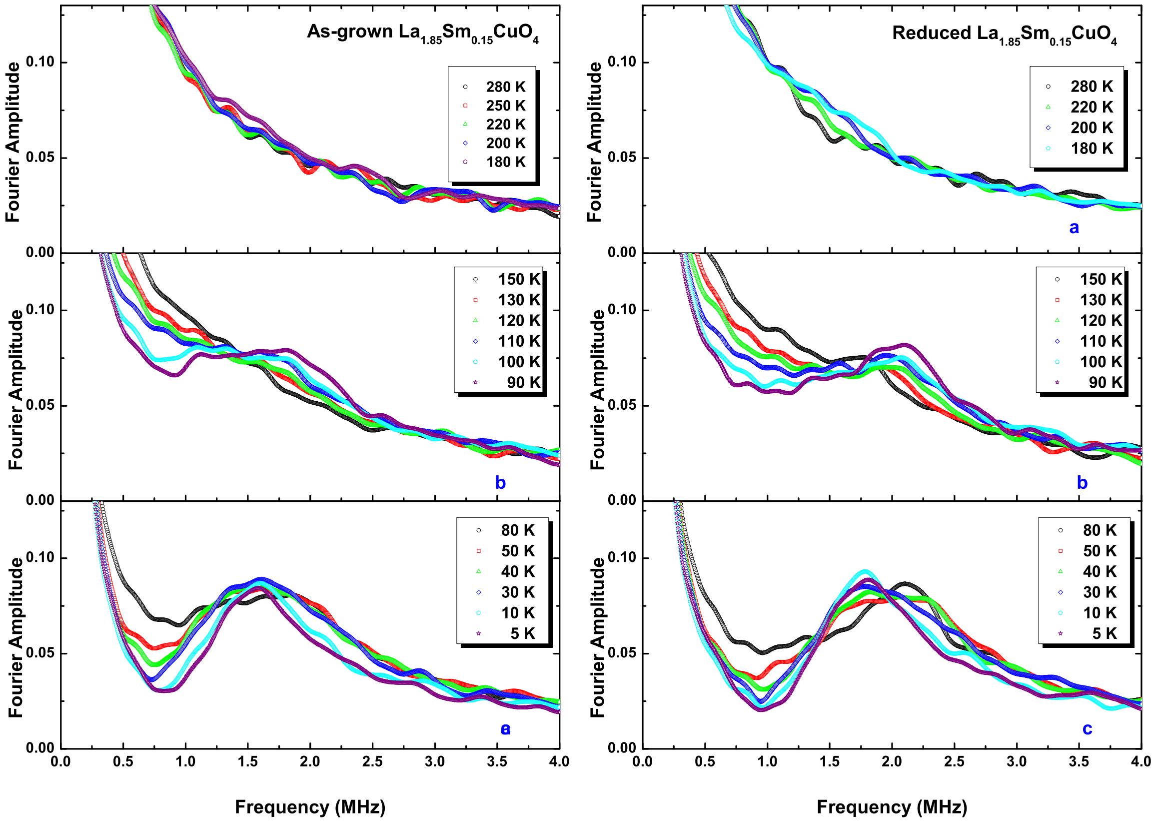

Figure 6.4: Field distributions for the (left) as-grown and (right) reduced $La_{1.85}Sm_{0.15}CuO_4$ at different temperature regions, a) high, b) intermediate, and c) low temperatures.

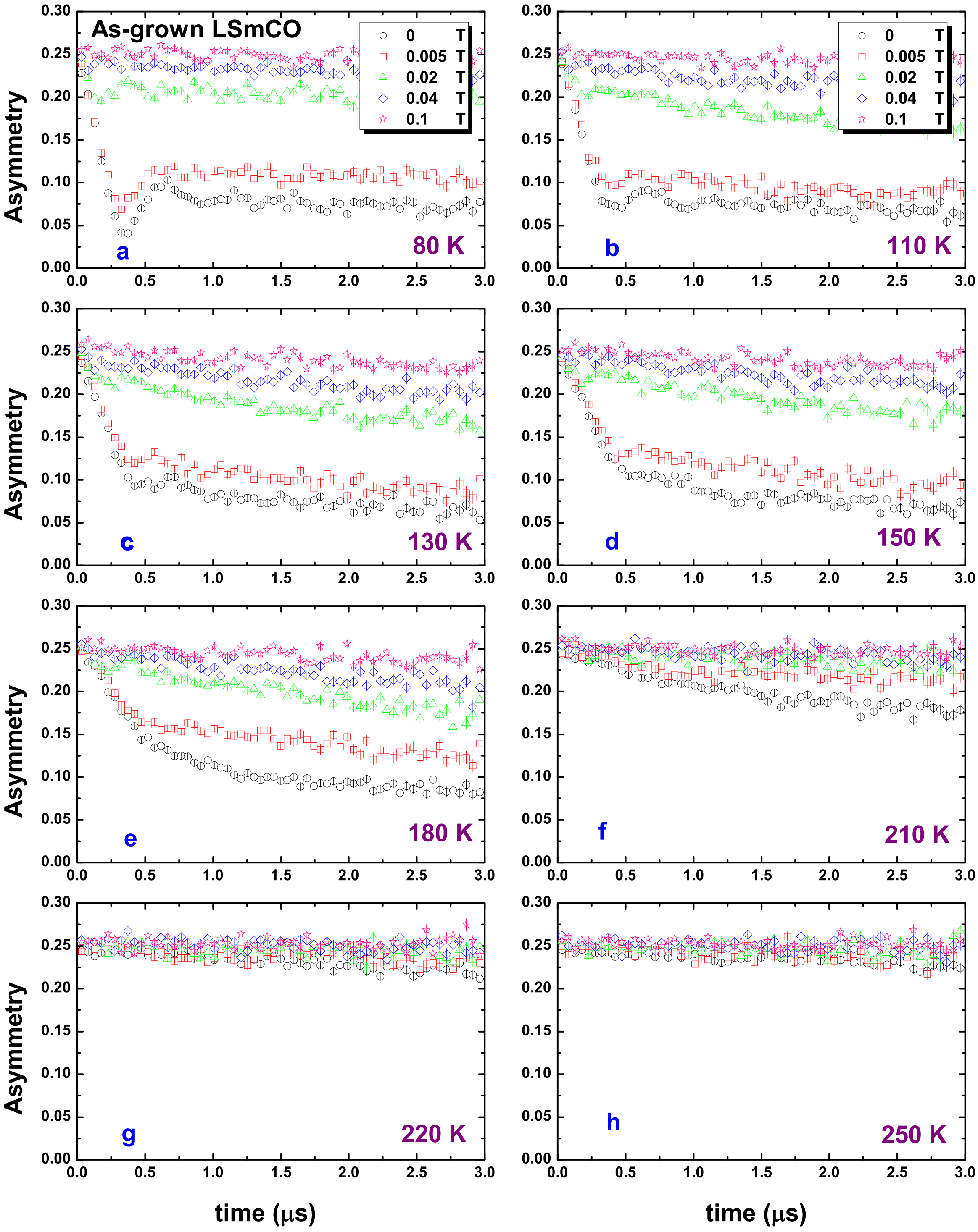

Figure 6.5: Decoupling measurements of as-grown LSmCO sample at various temperatures with 0, 0.005, 0.02, 0.04, and 0.1 Tesla applied fields.

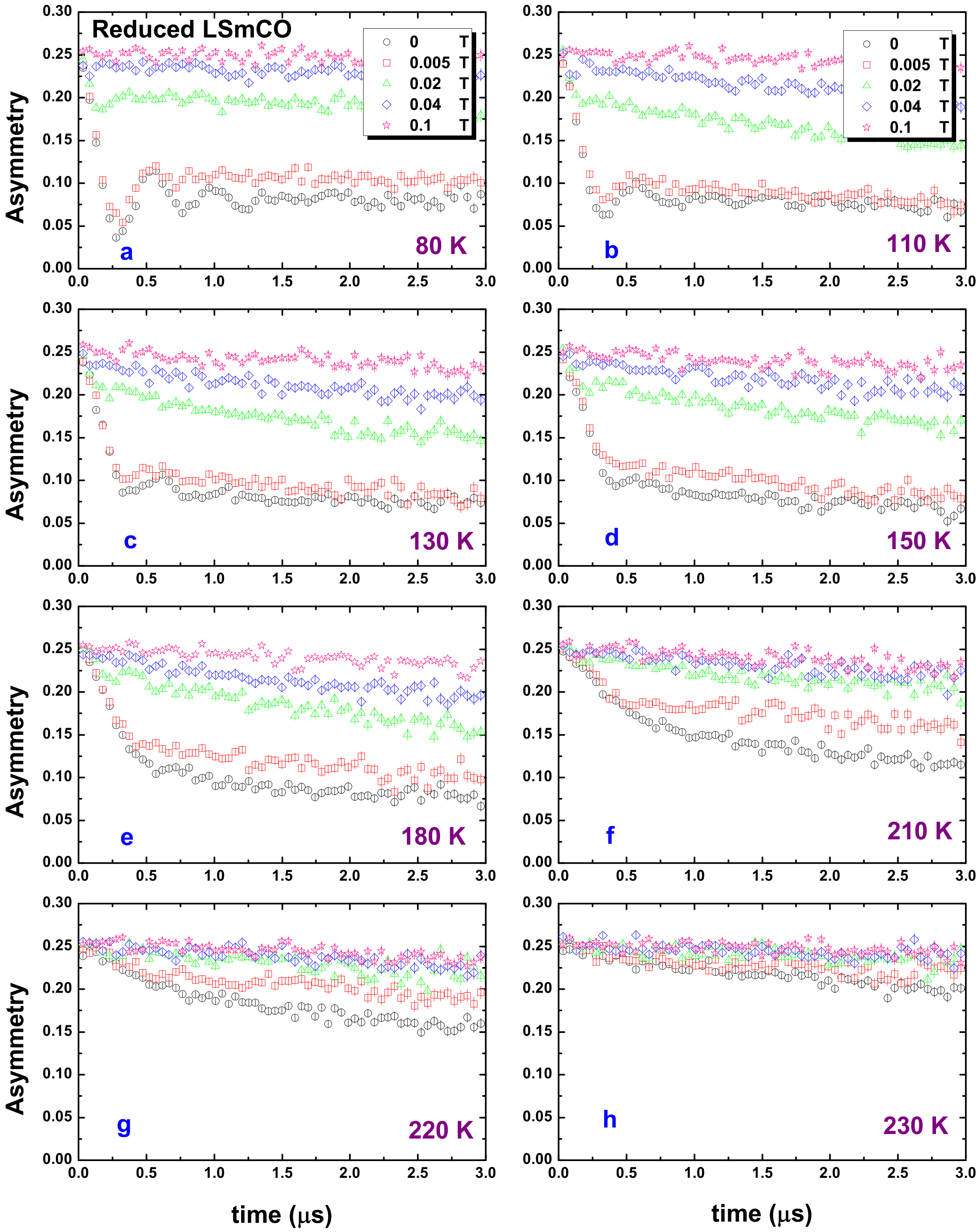

Figure 6.6: Decoupling measurements of reduced LSmCO sample at various temperatures with 0, 0.005, 0.02, 0.04, and 0.1 Tesla applied fields.

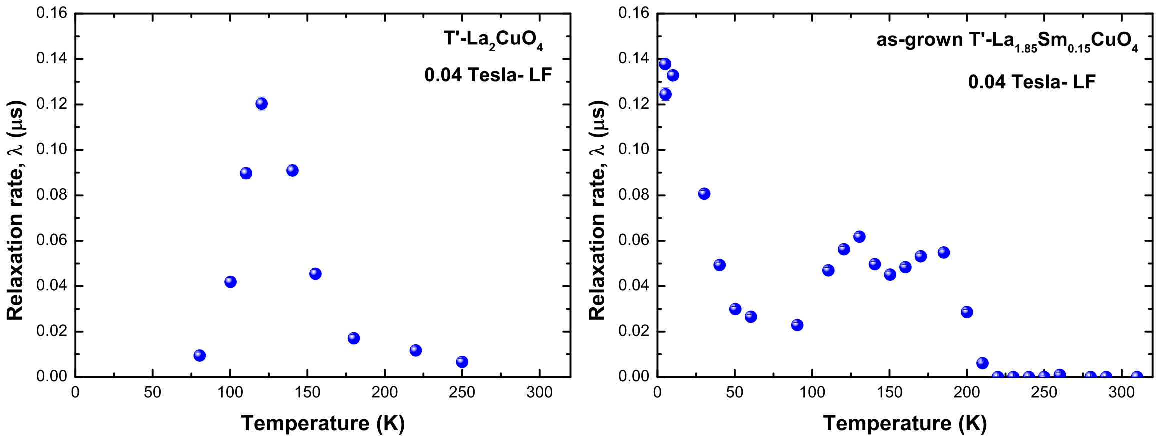

Figure 6.7: Temperature dependence of the dynamic relaxation rate given by LF-μSR measurement on T'-LCO (left side) and the T'-LSmCO (right side) compounds with an applied field of 0.04 Tesla.

Summary of Experimental Results for As-grown and Reduced $La_{1.85}Sm_{0.15}CuO_4$

Comparing the as-grown sample with the mother compound T'-La_2CuO_4, one can conclude that there are notable similarities and differences between the two compounds. Like in the mother compound, three magnetic transitions, T_{N1}, T_{N2}, and T_{N13}, are observed. These emphasize that the mother compound and the as-grown $La_{1.85}Sm_{0.15}CuO_4$ exhibit very similar overall behavior. The quasistatic ordering remained at the same temperature which is at $T_{N1}{\approx}220$ K, however, fluctuations are much more reduced in the as-grown $La_{1.85}Sm_{0.15}CuO_4$ compound. The static ordering was enhanced since the observed characteristic temperature T_{N2} had increased to 130 K for the as-grown sample compared to LCO. Loosely spoken, the introduction of the magnetic rare-earth Sm into the system is like adding a magnetic glue between the CuO_2 layers that enhances the interlayer coupling. This would be discussed more in detail in the next section.

Now comparing the as-grown and the reduced $La_{1.85}Sm_{0.15}CuO_4$ samples, T_{N1} and T_{N2} are both increased in the reduced sample. This could signify that the 3D ordering is more stable in the reduced sample than in the as-grown one.

Previously, we identified the T_{N3} regime in the mother compound as the temperature when the sample abruptly changes field distribution and this was interpreted as a temperature where it *locks in* to the NCol II configuration. In comparison to the mother compound, the change of field distribution in the as-grown LSmCO compound is gradual and it is enhanced as $T_{N3} = 70$ K. However, in the reduced LSmCO compound, this transition bounced back to a lower temperature as it slowly goes to $T_{N3} = 50$ K which is almost like in the mother compound where $T_{N3} = 40$ K. This is especially noteworthy since the T_{N1} of the reduced sample is actually increased compared to the as-grown sample.

Wrapping up the abovementioned observations, the magnetic transitions and overall behavior of both the as-grown and the reduced LSmCO are notably very akin to those transitions exhibited by the mother compound LCO. The key differences are the raised temperature at which these transitions occur within the characteristic regimes and the scaled down magnetic fluctuations in the Sm-substituted compound. The reduction process decreases the magnetic disorder and further increases the uppermost transition temperature T_{N1}.

6.3 Interpretation of Results for As-grown and Reduced $La_{1.85}Sm_{0.15}CuO_4$

It is interesting to understand whether the magnetic properties of T'-RE_2CuO_4 strongly depend on the type of RE ion and how strong is the influence of these RE ions on the copper magnetism. As already known, these materials have a tetragonal structure where the copper ions have a body-centered lattice configuration. Consequently, in the antiferromagnetic state, these copper ions in the adjacent CuO_2 planes do not interact in the mean-field approximation if one assumes conventional isotropic Heisenberg exchange coupling. Thus, some weak interactions may reveal or even impose themselves, which may not be common in other cuprates.

It is believed that in contrast to T-La_2CuO_4, the rare-earth cuprates T'-RE_2CuO_4 possess a noncollinear structure. This proposal is supported by neutron scattering studies in magnetic field confirming noncollinearity of the magnetic structure [33, 170, 84, 171, 102]. In such a noncollinear structure, the static and dynamic magnetic properties are steered by weak pseudodipolar interaction which derives from the slight polarization of the rare-earth angular momenta by the antiferromagnetic ordered Cu spins [83]. In the case of the Nd_2CuO_4, it was earlier established that the rather strong magnetic moment of the Nd ion couples with the Cu spins sublattice that can be accounted to the observed spin-reorientation transitions in this compound.

In this work, the enhancement of the interlayer coupling as evidenced by the increase of the Néel temperatures comparing the parent compound T'-La_2CuO_4 to the as-grown $La_{1.85}Sm_{0.15}CuO_4$, is accounted to the isovalent substitution of the magnetic rare-earth Sm ion in place of the nonmagnetic La ion. Contrapositively, this reinforces and confirms our previous claim on the low T_N of T'-LCO. Heuristically, the magnetic Sm ion acts as a polarizable magnetic *glue* that enhances the magnetic coupling of the CuO_2 planes. In addition, the presence of the Sm in the system slowed down magnetic fluctuations between the sublattices. Our results on the magnetism of LSmCO therefore actually support the conclusions about the exotic sequence of magnetic ordering in T'-LCO described in the previous chapter. A detailed theoretical description of all present magnetic interactions will be even more complicated in LSmCO due to the additional interactions between the Cu sublattice and randomly distributed magnetic Sm ions. Previously, the balance on the different interactions involving the RE-Cu, Cu-Cu, and RE-RE along with novel anisotropies were made responsible for the observed spin-reorientation in these body-centered tetragonal systems such as the case of the Nd_2CuO_4 [89, 90, 91, 92, 59, 93, 94, 60, 95]. Previous neutron scattering study on Sm_2CuO_4 by Lynn and coworkers did not show evidence of spin reorientation transition but the zero-field magnetic structure of the Cu sublattice is noncollinear which resembles that of the phase II of Nd_2CuO_4 [172], with the difference that the spin direction is rotated by 90°. The Sm magnetic moments are observed to order below 5.95 K. In a related work by Sumarlin, Skanthakumar, and Lynn, it was shown that the Sm magnetic structure of Sm_2CuO_4 consists of ferromagnetic sheets within the *ab*-planes, with the spin direction along the *c*-axis and spins in alternate sheets aligned antiparallel [173]. Of course it is anticipated that the randomly distributed Sm moments on the RE sublattice in LSmCO would (if at all) order at lower temperatures.

On the other hand, this present study on the $La_{1.85}Sm_{0.15}CuO_4$ exhibits rich transitions as the other tetragonal systems discussed herein. However, the quantification of the exact effect of the Sm awaits further explanation and will not be the scope of this work.

For the effect of the reduction annealing in the system, the increase of the observed Néel temperatures comparing the as-grown and reduced LSmCO samples, supports the combined notions of Kang *et al.* [121] and Krockenberger *et al.* [125], pointing to the repair of Cu and oxygen deficiencies in the CuO_2 plane. The annealing would therefore effectively reduce the disorder in the CuO_2 planes which strengthens the magnetic coupling. On the other hand, it was shown that the reduction/annealing process results in the suppression of antiferromagnetic order and the increase of the electron mobility, allowing superconductivity in these electron-doped cuprates [113, 112, 97]. It was even claimed that in the undoped T'-$La_{1.85}Sm_{0.15}CuO_4$ (the same stoichiometry as our compound), superconductivity could be induced by the annealing process [166]. The authors of that paper even claim that the perfectly annealed sample with a repaired CuO_2 plane is metallic and even superconducting in stark contrast to our findings.

These obvious discrepancies between different experimental results and their corresponding interpretation clearly call for a further experimental and theoretical investigation. In the next chapter, we try to shed more light on the magnetism of the BCT mother compounds and the effect of reduction annealing by making a systematic experimental investigation of T'-$\mathrm{Pr_2CuO_4}$ using various experimental techniques and different annealing conditions.

7 Structural and Magnetic Properties of T'-Pr_2CuO_4

To continue the series of measurements aimed at confirming the effect of a magnetic rare-earth element on the magnetism of the mother compounds of electron-doped cuprates, T'-Pr_2CuO_4 samples were grown and measured. In addition, it was already previously stated that reducing the as-grown materials has striking consequences for the magnetic and conducting properties and this is dependent on which oxygen site is vacated [53]. Note once more that in the T'-structure, there are three possible oxygen positions: O(1) is within the copper oxide plane, O(2) within the charge reservoir layer, and the third position O(3) is a defect position at the apical site.

The role and influence of excess oxygen on the magnetism is conjointly investigated in this compound. The oxygen content and site occupation of the sample before and after the reduction process were checked by high resolution neutron diffraction. The sample before the reduction is referred to here as the as-grown sample and the one after reduction annealing is the reduced sample. Magnetic neutron scattering were performed in order to investigate the magnetic structure of T'-Pr_2CuO_4.

Essentially, this chapter would present and discuss data for T'-Pr_2CuO_4 obtained from neutron diffraction and μSR measurements for the investigation of the material's structural and magnetic properties. The structural and proposed magnetic models were simultaneously investigated and refined for the data obtained from measurements at the HRPT and the DMC neutron diffractometers at PSI. Rietveld refinement analysis was employed with the use of the Fullprof software package. The magnetic properties were elaborated by the μSR measurements and data were analyzed using the Musrfit program [148]. Details of the measurements and data analysis will be further described in the subsections that follow.

The T'-Pr_2CuO_4 (T'-PCO) samples were synthesized by our collaborator from Technische Universität Darmstadt, R. Hord, following the high-temperature synthesis procedure from Reference [174]. Two sets of samples were measured, A and B. Each set has both as-grown and reduced samples. Set B is synthesized primarily for a more systematic study and further verification of the measurements done on Set A. Set B has three samples, one as-grown and two reduced. The effect of the reduction process were verified with the two reduced samples with different thermal treatments.

Table 7.1 gives the list of the studied samples with a brief description of each of their synthesis and reduction process undertaken. This will also serve as a guide in the nomenclature of the samples for the discussion.

Table 7.1: List of Samples

Set	Sample Name	Description
Set A	As-grown A	synthesized at 1100 °C
	Reduced A_{900-Ar}	reduced with Ar flow at 900 °C for 12 hours
Set B	As-grown B	synthesized at 1100 °C
	Reduced $B_{800-Vac}$	reduced at 800 °C in vacuum
	Reduced B_{900-Ar}	reduced with Ar flow at 900 °C for 10 hours

7.1 Structural Characterization

7.1.1 Thermal Neutron Scattering Measurements on T'-Pr_2CuO_4

High resolution neutron powder diffraction data have been collected from thermal neutrons HRPT diffractometer, SINQ, PSI, Villigen, Switzerland. The measurements have been carried out on both sets of samples at $T = 300$ K or $T = 310$ K. The samples were placed in a rotating cylindrical vanadium sample holder with 6 mm diameter. In most of the samples, refinement analysis were done with a combined fit of two datasets taken from measurements with two neutron wavelengths, 1.1545 Å and 1.494 Å, respectively. For the As-grown A sample, only one wavelength, 1.494 Å, was used. Like in the T'-La_2CuO_4 sample, available structure data for Nd_2CuO_4 [145] were used as initial refinement parameters. As such, T'-PCO then has the same positional parameters and Wyckoff sites as it is also belonging to the I4/mmm space group.

The same refinement approach is used for the T'-PCO as the one described for the T'-LCO. A pseudo-voigt profile function was used as a fitting function for the reflections. The background was generated by a polynomial function and was also refined. All the other parameters like the lattice constants, site occupation and isotropic factors were simultaneously refined. An example of the Fullprof pcr code file is shown in the appendix.

Figure 7.1 depicts the neutron powder diffraction profile at $T = 310$ K (paramagnetic state) for the As-grown B sample. Refinement results for the other samples are shown in the appendix. From the Rietveld refinement, the lattice parameters were obtained along with the positional parameters and site occupations. These are tabulated in Table 7.2 and Table 7.3. The values in parentheses are the errors for each obtained parameter. If there is an error bar of zero, this indicates that the corresponding parameter has been fixed to the given value in the analysis.

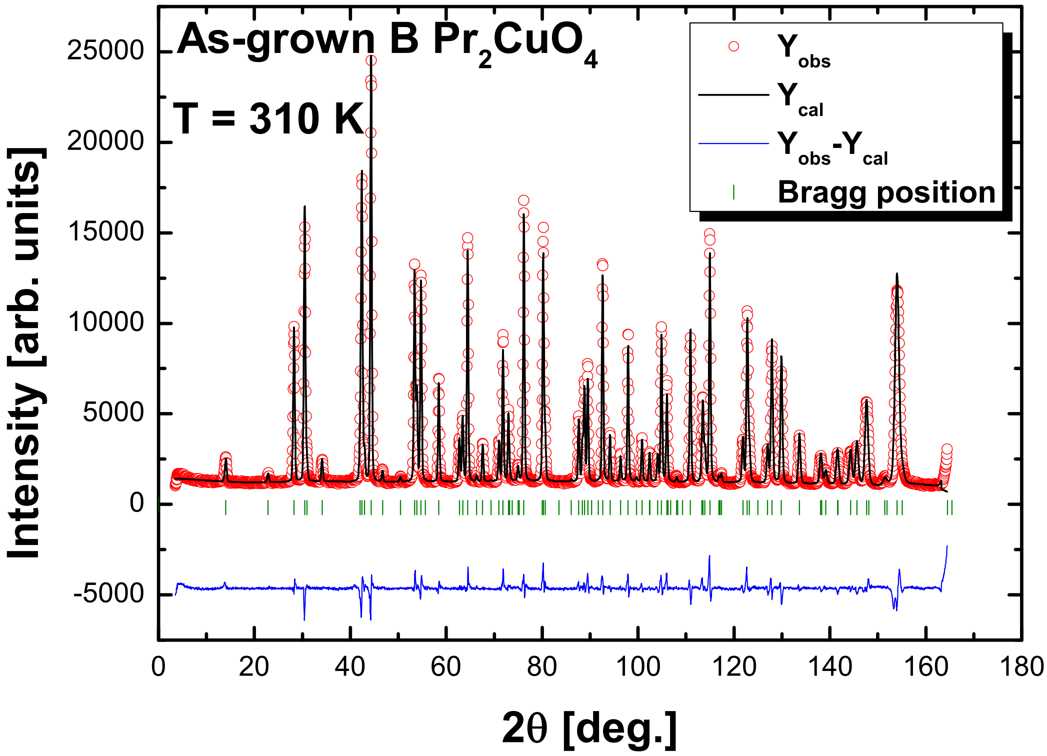

Figure 7.1: Diffraction pattern for sample As-grown B at $T = 310$ K.

Table 7.2: As-grown B: Lattice Constants

a	b	c
3.96168(2)	3.96168(1)	12.24115(7)

Note that in Table 7.3, full occupation for each atom should be: Pr = 2.000, Cu= 1.000, and O(1) = O(2) = O(3) = 2.000. O(2) and O(3) were correlated in refining the isotropic factors. This is also true for all the other samples, presented in the Appendix.

The as-grown sample was then reduced at 900 °C in Argon flow for 12 hours. Like the as-grown sample, the reduced sample, named as Reduced A_{900-Ar}, was also measured at HRPT

Table 7.3: As-Grown B: Positional parameters and site occupations

Name	x	sx	y	sy	z	sz	B	sB	occ.	socc
Pr1	0.00000	(0)	0.00000	(0)	0.35161	(7)	0.268	(15)	2.000	(0)
Cu1	0.00000	(0)	0.00000	(0)	0.00000	(0)	0.289	(12)	1.000	(0)
O1	0.50000	(0)	0.00000	(0)	0.00000	(0)	0.563	(12)	2.000	(0)
O2	0.00000	(0)	0.50000	(0)	0.25000	(0)	0.404	(14)	2.018	(9)
O3	0.00000	(0)	0.00000	(0)	0.19063	(498)	0.404	(14)	0.024	(5)

diffractometer for investigation of its structural parameters. The data refinement was done in an analogous procedure to the as-grown sample. The background points were automatically generated with a polynomial function. No systematic result can be drawn from the Set A samples since the As-grown A sample was unfortunately measured with only one neutron wavelength. Thus, Set B samples were synthesized with two different reduction annealing conditions.

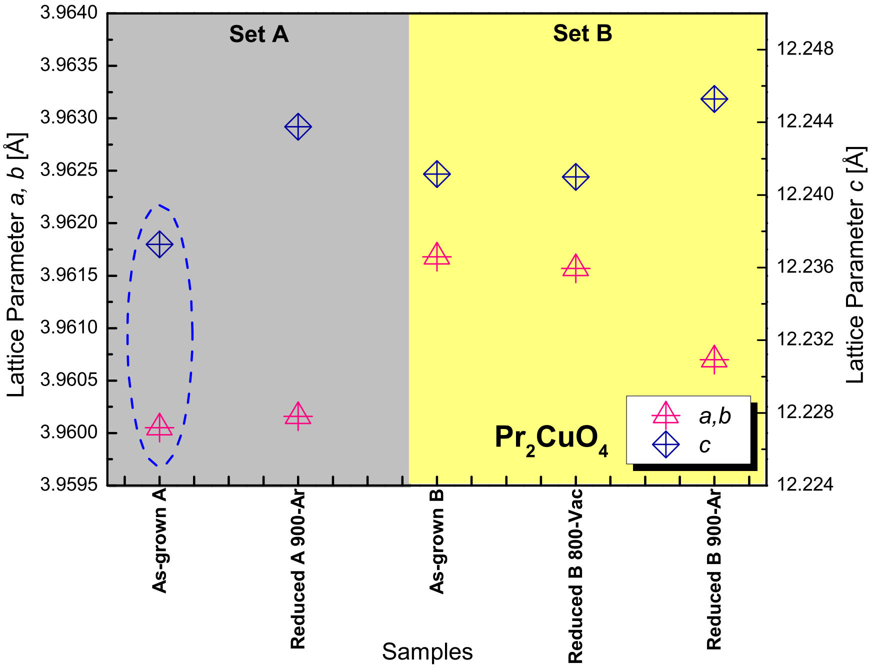

Figure 7.2: Summary of lattice constants for all the measured Pr_2CuO_4 samples. The As-grown A sample has been measured only with one neutron wavelength. Therefore, only a limited q-range has been available for the analysis. This substantially reduces the reliability of the results shown in the dashed ellipse.

Figure 7.2 shows the lattice parameters of all the measured T'-Pr_2CuO_4 samples. The dashed ellipse in the figure is to note that for As-grown A sample, there is only one dataset used in the refinement coming from the measurement with only one wavelength, as mentioned previously. Hence, this dataset cannot be directly compared with its reduced counterpart. However, a more reliable trend can be obtained from the Set B samples.

The Reduced $B_{800-Vac}$ sample did not seem to show a distinct change in the lattice parameters compared to the As-grown B sample. However, taking As-grown B in comparison with the Reduced B_{900-Ar}, an increase in the c lattice parameter and a decrease in the a and b lattice parameters, are evidently observed. Table 7.4 presents the summary of the refinement of lattice parameters including the volume for all the studied samples.

Table 7.4: Lattice parameters a,b and c, and volume of the T'-Pr_2CuO_4 samples

Sample Name	lattice parameter a,b [Å]	lattice parameter c[Å]	Unit cell volume [Å^3]
As-grown A	3.96005(2)	12.23728(10)	191.905(0.002)
Reduced A_{900-Ar}	3.96016(1)	12.24376(6)	192.018(0.001)
As-grown B	3.96168(2)	12.24115(7)	192.124(0.001)
Reduced $B_{800-Vac}$	3.96157(1)	12.24099(6)	192.111(0.001)
Reduced B_{900-Ar}	3.96070(1)	12.24528(5)	192.094(0.001)

In these T'-structures, the O(2) and O(3) oxygen positions should be cautiously regarded since these play a key role in the structural and conducting properties of the compound. It is then imperative to note them. Table 7.5 compiles the refinement results for all the as-grown and the reduced Pr_2CuO_4 samples.

Table 7.5: Occupation sites O2 and O3 f the T'-Pr_2CuO_4 samples

Sample Name	O2	O3
As-grown A	2.048(19)	0.029(12)
Reduced A_{900-Ar}	2.014(8)	0.007(4)
As-grown B	2.018(9)	0.024(5)
Reduced $B_{800-Vac}$	2.018(9)	0.009(5)
Reduced B_{900-Ar}	1.993(8)	0.004(4)

Comparing the Fullprof refinements in both sets of the as-grown and the reduced Pr_2CuO_4 samples, all the heat treatment conditions to eradicate O(3) can be considered efficient since, as presented in Table 7.5, the O(3) occupation site was vacated. This is the case in both sets of samples. Focusing on the more systematic set B samples, however, the two different annealing conditions gave a different result regarding O(2). For the case of the Reduced $B_{800-Vac}$ sample, only the O(3) was taken out from the structure while O(2) was unchanged. On the other hand, both the O(2) and O(3) were drastically taken out for the Reduced B_{900-Ar} sample consequently reducing its unit cell volume.

7.1.2 Key Experimental Observations from Thermal Neutron Diffraction Measurements

Two sets of samples were synthesized for neutron scattering measurements, namely Set A and Set B. Tables 7.4 and 7.5 summarizes the essential structural Rietveld refinement results from Fullprof of both sets of samples. The structural investigations via powder diffraction measurements with thermal neutrons reveal the presence of O(3) in the as-grown samples. Set B samples provided a more systematic study and evidently gave more reliable results, thus, conclusions were drawn from our Set B samples.

For the Set B samples, two reduction conditions were implemented. One sample is reduced at 800 °C in vacuum and the other one at 900 °C in flowing Ar gas. In comparison to the as-grown sample, the Reduced $B_{800-Vac}$ sample did not exhibit distinct changes in the structural lattice parameters while the Reduced B_{900-Ar} sample had exhibited an increase in the c-lattice parameter and a decrease in the a and b lattice parameters. In order to further understand the reduction effect on magnetism, it is useful to note the O(2) sites, which are the sites in the charge reservoir layer. The site occupations of O(2) and O(3) for the Set B samples are depicted in Table 7.5. The Reduced $B_{800-Vac}$ sample had only taken out the O(3) while the O(2) was unchanged while the Reduced B_{900-Ar} sample had drastically taken out the oxygens from the O(2) and the O(3) sites. Additionally, it is observed that the volume of the latter sample is reduced due to the removal of these O(2) and O(3) sites.

The abovementioned neutron scattering experimental observations can already directly point out that the reduction annealing conditions influence the crystallographic properties of the material. The observed crystallographic properties certainly have influence on the magnetic properties. This will be presented in the succeeding sections.

7.2 Magnetic Properties

7.2.1 Cold Neutron Scattering Measurements on T'-Pr_2CuO_4

Besides the structural investigations on the HRPT instrument discussed in the previous section, neutron diffraction experiments were also performed on the cold neutron powder diffractometer DMC at the Swiss Spallation Neutron SINQ (PSI Villigen, Switzerland). This is primarily done in order to investigate the magnetic structures of T'-Pr_2CuO_4. The proposed structures will be included in the discussion in the following. The experiments were performed at temperatures of 1.5 K to 300 K using neutrons with a wavelength of $\lambda = 4.207$ Å. The Fullprof program was once again used to analyze and to model the diffraction data.

Magnetic Bragg peaks were observed in cold neutron scattering measurements. These peaks can be indexed at superstructure positions which are also found in all the other tetragonal RE_2CuO_4 (RE= Pr, Nd, Sm, and Eu), namely indices ($h/2$, $k/2$, l), where h, k are odd integers and l is any integer. Figure 7.3 shows the evolution of the magnetic Bragg peak at (-1/2 1/2 1), (1/2 -1/2 1) with increasing temperature. Two indices were given but these pertain to the same peak position. Only the (1/2 1/2 1) peak is plotted here but in fact, there is another magnetic peak observed at (1/2 1/2 2) that was being described by the magnetic model used. The magnetic peaks vanish at the Néel temperature $T_N = 285$ K.

Magnetic refinements were performed with the Fullprof package on the obtained data from DMC. In the Fullprof pcr file, the crystallographic and the magnetic structures are both included. As a starting model for the refinement, a simple magnetic structure model belonging to space group $P\overline{1}$ was used to refine the magnetic peaks. The magnetic reflections can be described with an antiferromagnetic wave vector **k**= (1/2, 1/2, 0). A k-vector of (1/2, 1/2, 0) implies that there is no modulation along the c-direction but a doubling along the a and b directions. An example of a pcr file is shown in the appendix.

As discussed in chapter 2, neutron powder measurements are not able to resolve the ambiguity of the various different collinear and noncollinear spin structures shown in Figures 2.14 and 2.15. This essentially stems from the fact that magnetic structures with the k-vectors $\mathbf{K}_1$= (1/2 1/2 0) and $\mathbf{K}_2$= (-1/2 1/2 0) can not be distinguished by powder neutron diffraction. In addition, the collinear and noncollinear structures also give the same powder diffraction pattern. This is problematic, since on the one hand, in a real sample always both 90°-domains of collinear structures would be present due to their energetic degeneracy in a tetragonal system and the noncollinear structures on the other hand can be regarded as a coherent superposition of these two collinear structures, see e.g. Figure 2.12. In single crystals anyhow, neutron diffraction can distinguish between the different models but only if a

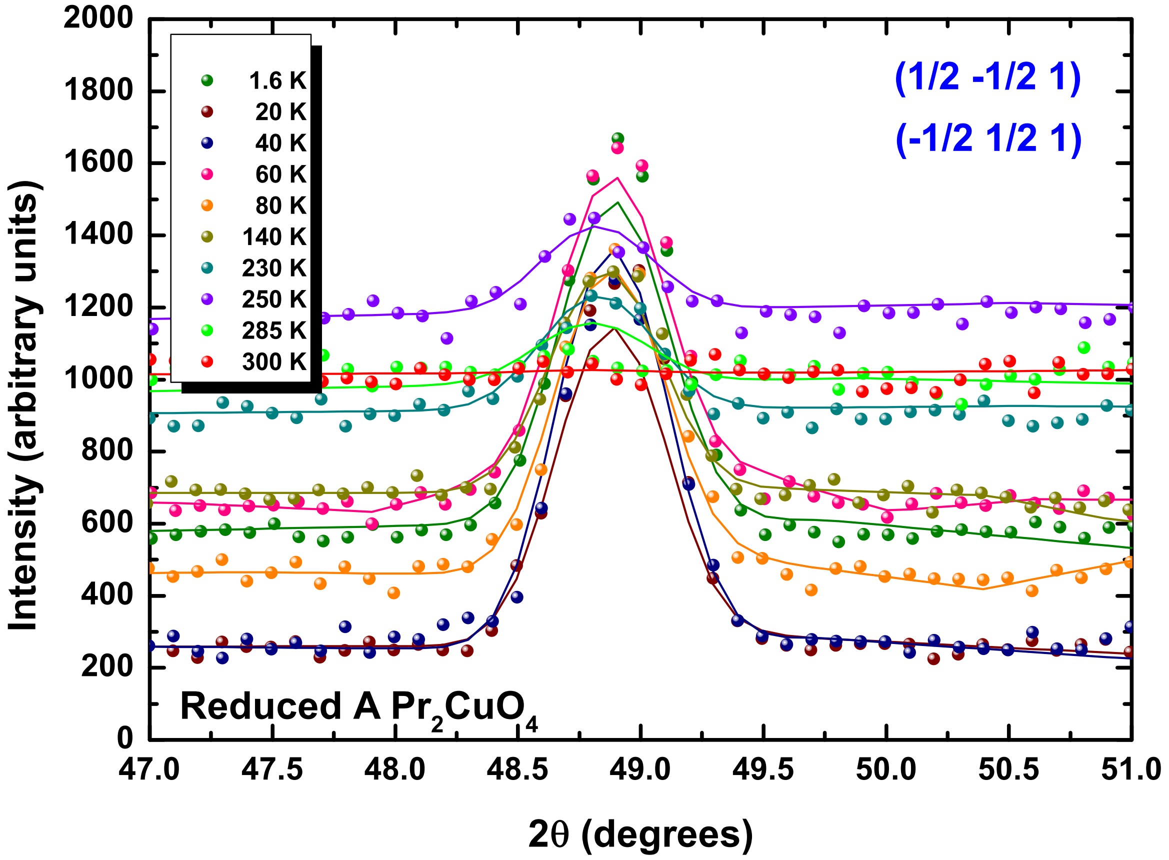

Figure 7.3: Temperature dependence of the magnetic Bragg peak (-1/2 1/2 1), (1/2 -1/2 1) of the Reduced A T'-Pr_2CuO_4 sample. The temperature dependent shift of the flat baseline has been attributed to a problem in the detector of the diffractometer after the measurements. This baseline shift anyhow did not disturb the fitting of the magnetic peak intensity.

symmetry breaking magnetic field or uniaxial pressure is applied [33, 99]. Please note that due to the very same reasons, powder neutron diffraction is also not sensitive to transitions between the different spin arrangements. Despite not being able to discern the correct spin structure, one information verified is the magnetic order parameter obtained from the temperature dependence of the intensity of the magnetic Bragg peaks. The data in Figure 7.4 show the temperature dependence of the intensity of the (1/2 1/2 1) Bragg peak for each of the measured samples displaying a transition temperature at $T_N = 285$ K. The As-grown A sample was not measured on DMC but its reduced counterpart, which is Reduced A_{900-Ar} was measured and gave preliminary ideas for a more systematic study on this compound which was afterwards done on sample Set B. If one looks closely, especially in plot d) of Figure 7.4, the curve is not very smooth but has a *dent* or discontinuity at ~150 K. Additionally, Sumarlin and coworkers [33] had observed a similar behavior on single crystals of PCO, shown in Figure 7.5.

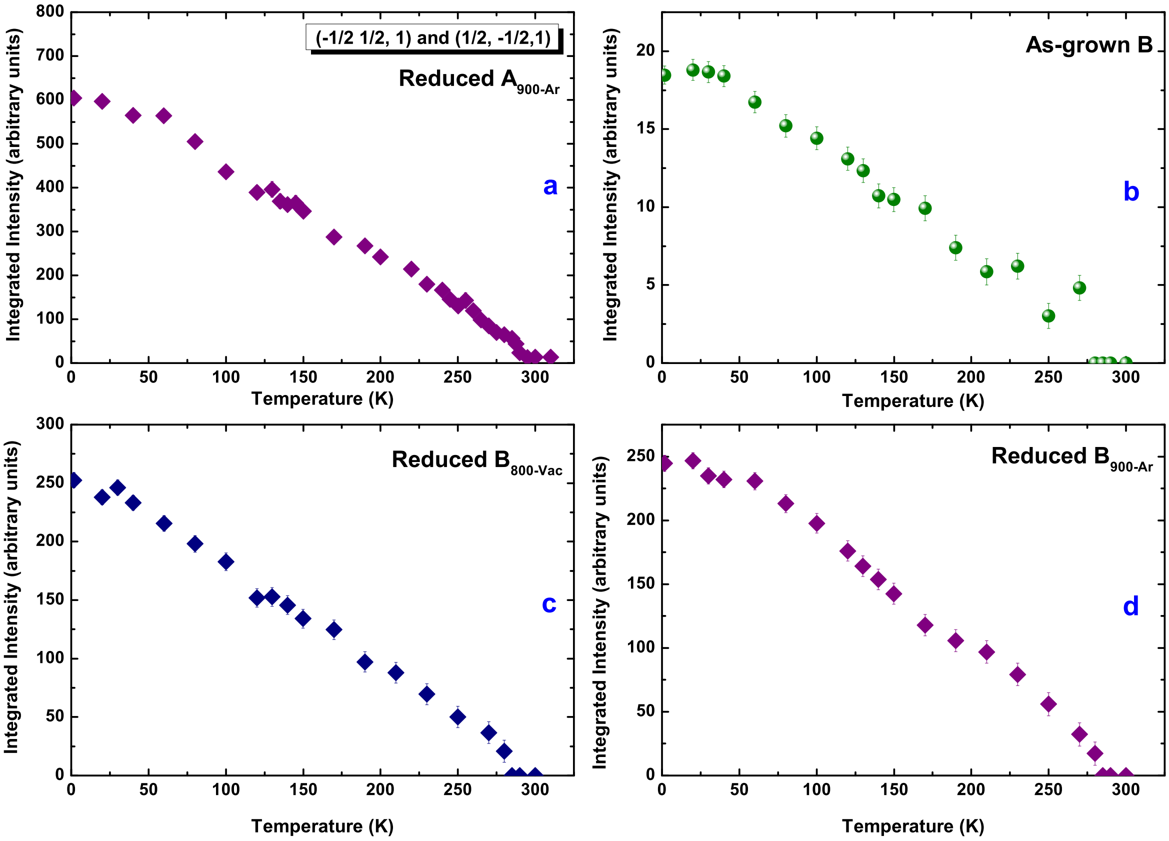

Figure 7.4: Temperature dependence of the integrated intensity of the (1/2 1/2 1) magnetic Bragg peak of a) Reduced A_{900-Ar} sample, b) As-grown B sample, c) Reduced $B_{800-Vac}$ sample, d) Reduced B_{900-Ar} sample.

Sumarlin *et al.* [33] claimed that the overall temperature dependence of the Cu sublattice magnetization is adequately described by a power-law behavior over the full temperature range, given as a solid curve in Figure 7.5. The additional scattering intensity which can be seen below 200 K has been interpreted to stem from small Pr moments which are induced by the ordered Cu spins via an exchange field at the Pr sites. The Pr moments themselves have also been shown to order subsequently at lowest temperatures [59].

As we will see in the following, the μSR data on T'-PCO show a series of magnetic transitions as a function of temperature. The behavior is similar, but more complex than the one observed in LCO which has no polarizable magnetic rare earth element in the structure. Therefore, it seems unlikely that the induced magnetic polarization in the RE magnetic system is at the heart of the explanation for the observed transitions, but add only another degree of freedom to the complex magnetic interactions in the CuO_2 plane. It is more likely that the magnetic transitions that are observed with μSR are not easily visible with standard neutron diffraction techniques without polarization analysis. The kink in the neutron powder diffraction data shown in Figure 7.4 d) might be therefore an indication of one of the magnetic transitions observed by μSR at around 150 K. This will be shown in the next section. In addition, an anomalous *reemergence* (seen like a *bubble*) of the intensity at higher temperatures was observed in the neutron data of Plakhty and coworkers, see Figure 7.6. Their discussion, however, did not include the origin of this feature. A rather similar feature is seen by μSR at high-temperatures, which will be discussed in the later sections.

Yet another proof for the complex magnetic behavior of T'-PCO is the appearance of new history-dependent magnetic peaks in the diffraction data which I will discuss in the following.

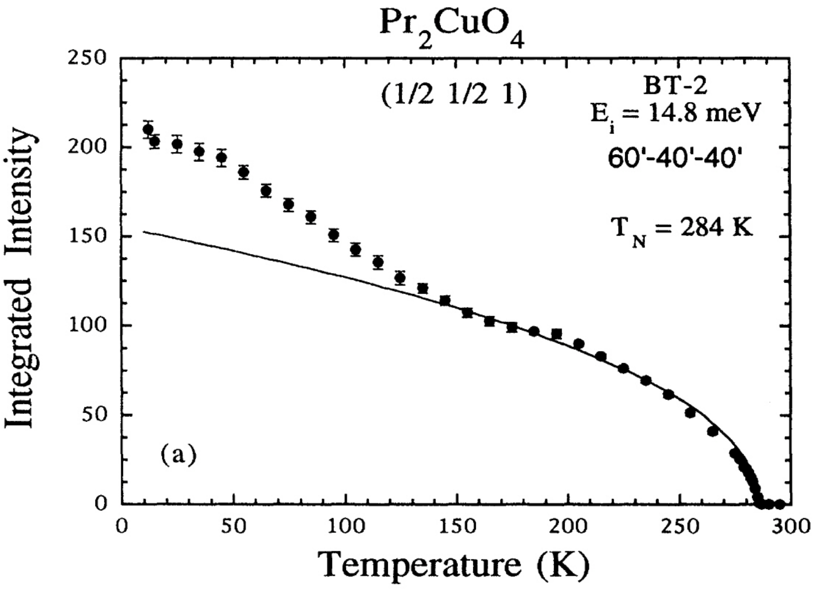

Figure 7.5: Temperature dependence of the integrated intensity of the (1/2 1/2 1) magnetic Bragg peak of the neutron work of Sumarlin and coworkers [33] on a single crystal of PCO.

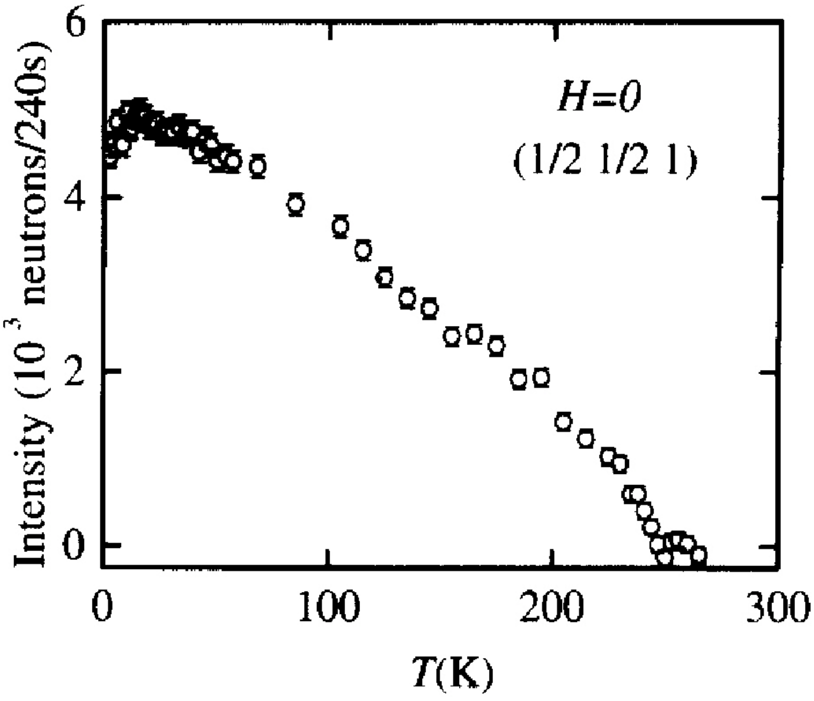

Figure 7.6: Temperature dependence of the integrated intensity of the (1/2 1/2 1) magnetic Bragg peak of the neutron work of Plakhty and coworkers [175] on T'-PCO. Note the tiny *reemergence* of the intensity at high-temperatures.

Temperature history dependent magnetic diffraction peaks at 40 K

In Figure 7.7, neutron diffraction data of the Reduced A_{900-Ar} PCO sample are shown for $T = 40$ K. At this temperature, we observed clear magnetic peaks that were not observed at any other temperature. Any electronic problem of the DMC diffractometer can be excluded from clearly defined peaks. Within our used magnetic structure model $P\overline{1}$ one of the peaks could be identified to be (1/2 1/2 3), while the other one could not be indexed within this model. An attempt to reproduce these peaks in a second temperature cycle failed as it is also shown in Figure 7.7. This implies that the occurrence of these magnetic peaks either strongly depends on the thermal history of the sample or that the corresponding magnetic structure only appears in an extremely small temperature interval which had been missed in the second attempt.

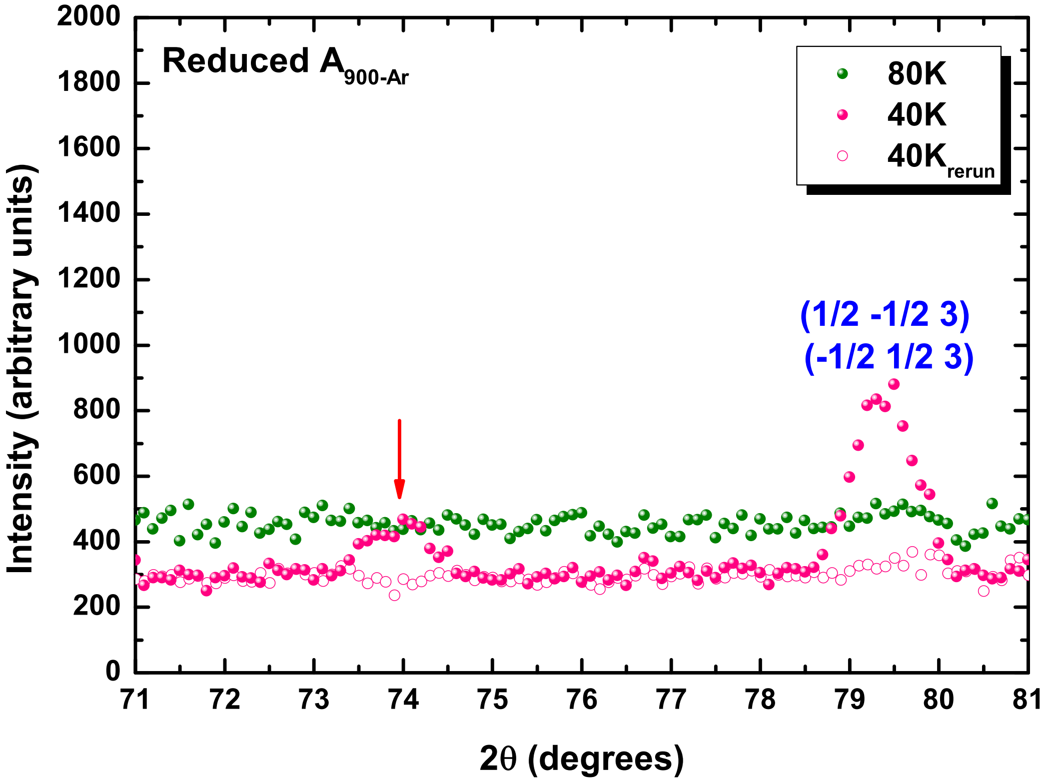

Figure 7.7: Anomalous peaks observed on the Reduced A_{900-Ar} PCO sample at 40 K showing the (1/2 1/2 3) magnetic Bragg peak and another undefined peak at $2\theta \simeq 73.9$ degrees pointed by the red arrow.

As I will show in the following chapters, μSR reveals a magnetic reorientation or lock-in transition at 40 K very similar to the already discussed transition observed in T'-LCO. Therefore, it is reasonable to assume that the sporadically-observed magnetic neutron scattering peaks at 40 K are related to this transition in the sense that they belong to a narrow intermediate phase bridging between the high and low temperature magnetic phase. The fact that the 40 K data were not reproducible might indicate that the corresponding magnetic phase is only metastable and not the true magnetic ground state. Please note anyhow that the peaks are narrow and well-defined which points to a well-ordered magnetic structure of a spatial domain size larger than the neutron coherence length.

Further understanding about the magnetic properties of the samples can be left for our other techniques to elucidate since, as explained above, powder neutron scattering has limitations. In addition to the discussed inability to differentiate between different magnetic domains, powder neutron diffraction is not the technique of choice to determine magnetic dynamics which could be better done on single crystals. As we will show later, also in T'-PCO we observe magnetic dynamics well below the highest magnetic transition temperature (similar to the case of T'-LCO). Since large single crystals are available for T'-PCO it would be interesting to search for the collective dynamics of 2D magnetically ordered planes which should be observable by a broadening of the magnetic peaks in q_z direction. For the powder samples used in our investigation, it is anyhow imperative to complement the neutron studies with local probe techniques like NMR or μSR.

7.2.2 μSR Measurements on T'-Pr_2CuO_4

μSR experiments were carried out using the Dolly and the GPS instruments located at the πE1 and πM3 beamlines, respectively, of the Swiss Muon Source, Paul Scherrer Institute, Villigen, Switzerland.

In the following, I will describe and peruse the magnetic properties of the as-grown T'-Pr_2CuO_4 (PCO). Then the effect of the different annealing treatments on magnetism will be expounded subsequently.

As-grown T'-Pr_2CuO_4 Properties

Zero-Field μSR (ZF-μSR) measurements were performed on both sets of the as-grown and reduced samples of T'-Pr_2CuO_4 (T'-PCO) to microscopically investigate their magnetic properties.

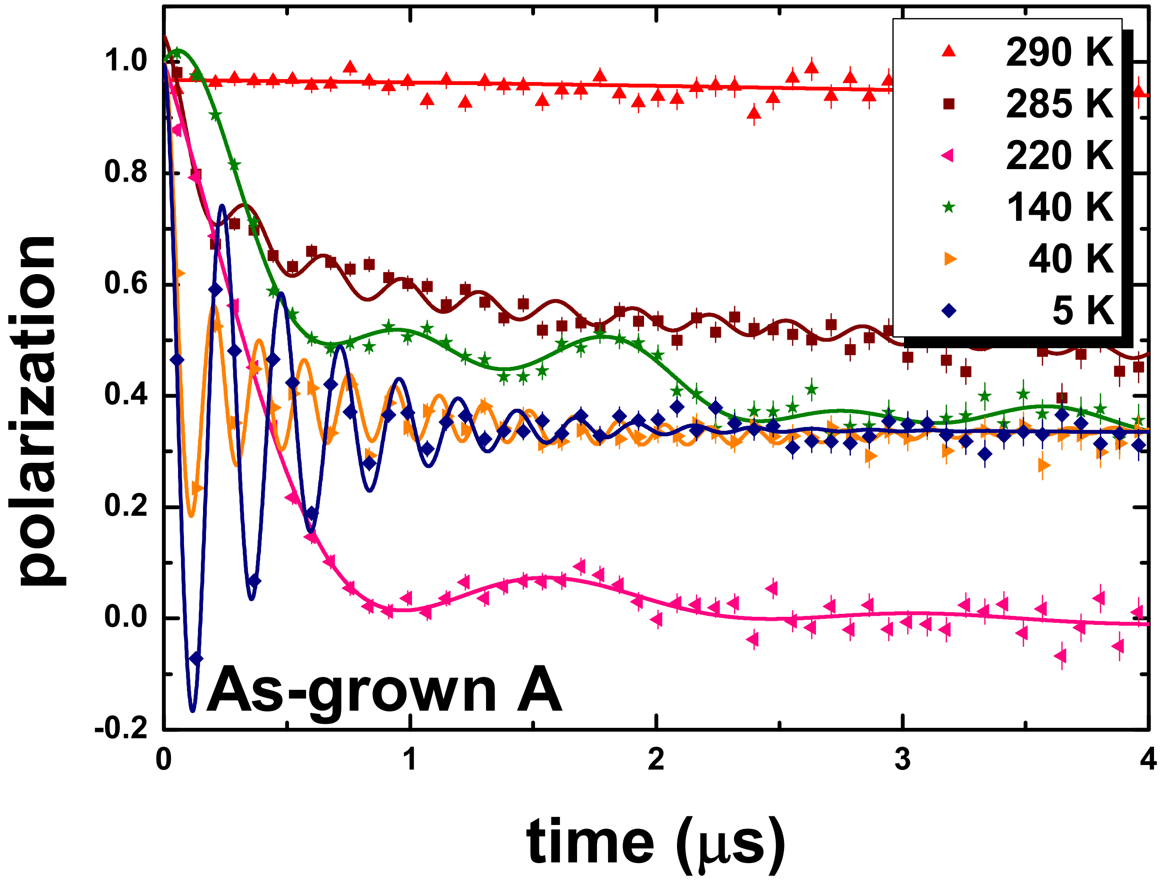

Figure 7.8: Zero-field spectra at 5, 40, 140, 220, 285, and 290 K of the As-grown A T'-PCO sample.

Representative ZF-spectra of the As-grown A sample are shown in Figure 7.8. It is noteworthy to mention that the analytical functions to model the T'-LCO were also adopted for the T'-PCO. At the highest temperature, T'-Pr_2CuO_4 exhibits a paramagnetic signal that is described by a Gaussian-Kubo Toyabe function above T= 290 K indicating paramagnetism.

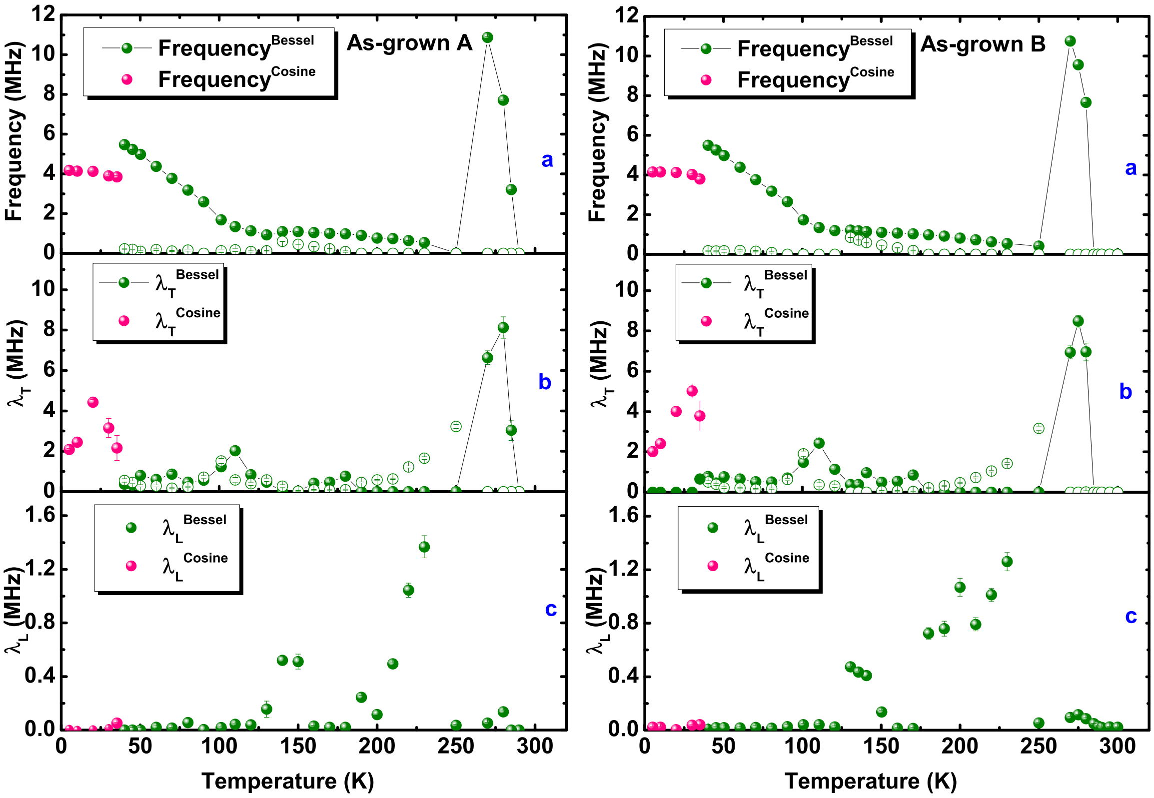

Figure 7.9: a) The ZF-μSR frequency, b) the transverse relaxation rate, and c) the longitudinal relaxation rate as a function of temperature of the As-grown A (left-side figure) and the As-grown B (right-side figure) samples, respectively.

Then incredibly, starting at $T =$ 285 K, fast oscillations at early times of the signal start to emerge. The muon spin precession can be well-fitted with a zeroth-order Bessel function at this temperature regime. The fast oscillations are not nicely seen in Figure 7.8 due to the strong binning of the data. Later, I will discuss the high frequency phase in more detail and raw data will be shown in Figure 7.15 more clearly. Figure 7.9 shows the μSR fit parameter results for both the as-grown samples A and B. The data are virtually identical proving the reproducibility of the synthesis procedure. Figure 7.9 *a*) displays an increase of the muon precession frequency and at the same time, the transverse relaxation rate, λ_T, given by Figure 7.9 *b*), also increased. This increase in λ_T reflects that the internal field sensed by the muon at this temperature regime increased and that therefore the absolute width of the field distribution is enhanced. The observed frequency peaks at $T =$ 280 K. The high-frequency had suddenly completely receded at $T = 250$ K. The signal is, however, still magnetic as demonstrated by the flat tail of the relaxation signal going to 1/3. Please note that this fast muon frequency of the T'-PCO in a very narrow temperature interval near T_N may be comparable to the previously shown neutron data by Plakhty *et al.* [175], see again Figure 7.6.

With decreasing temperature, the frequency gradually starts to develop again as shown in Figure 7.9 *a*). However, at the intermediate region, from $120\,K \leq T \leq 250\,K$, two magnetic components fitted with two Bessel functions were used to describe the data. This appearance of a two-component relaxation function indicates two magnetically different muon sites in the crystallographic structure. This is e.g. clearly seen from the beating of the μSR spectrum at 140 K in Figure 7.8. From below 250 K down to 180 K, only one frequency can be clearly resolved from these two magnetic components and in addition an increase of the dynamic relaxation rate is observed at this region. This is also very well visible in the raw data plotted in Figure 7.8 since the time dependent asymmetry drops well below the 1/3 tail at 220 K. Then at a bit lower temperature, from 170 K down to 130 K, a branching out to two frequencies is clearly seen. Moreover, a second peak in λ_L is also observed at 130 K. This means that at this temperature, fluctuations are on the scale of the muon Larmor frequency. This means that the described magnetic transitions are all accompanied by magnetic fluctuations within the time window of μSR. This is interesting, since it again shows that the magnetic system can not be characterized by a continuous slowing down of magnetic fluctuations with decreasing temperature, but that in contrast real magnetic transitions are observed at the different characteristic temperatures.

A better visualization of the field distributions at each characteristic temperature regions are given by the Fast Fourier Transform (FFT) plots shown in Figure 7.10. Like in the FFT plots in the previous chapter, the sharp peak appearing near zero frequency is the slowly decaying offset asymmetry in time space that was not subtracted from the signal. The high-temperature region plot in Figure 7.10 *a*) clearly exhibits the peaks at high frequencies at around 10 MHz. Then at the intermediate regime, one can see a broad field distribution that is suitably fitted with one or two zeroth-order Bessel functions.

Below $T = 120$ K, the frequency starts to grow smoothly like the usual order parameter and like in the case of the T'-La_2CuO_4. Correspondingly, a peak in λ_T is seen at 110 K. Again, the field distribution in this temperature regime is broad and pronounced asymmetric. Hence, a zeroth-order Bessel function still best describes the data.

Interestingly, once more at 40 K, a switch of field distribution happens below which a standard cosine function can better describe the data. Figure 7.10 *c*) clearly displays the evolution of the low-temperature field distributions starting at 40 K. The field distributions below 40 K show a shape that are symmetric, Lorentzian in form and are shifted to a bit lower frequency compared to the higher temperatures. Like in the T'-La$_2$CuO$_4$, this sudden change in the field distribution we ascribe to a lock-in transition into one simple well-defined magnetic structure. As in T'-LCO we find only one internal magnetic field. Following the discussion of T'-LCO, we can ascribe this only to the NCol II magnetic phase since in all other possible simple magnetic structures, two well separated magnetic internal fields should be observed.

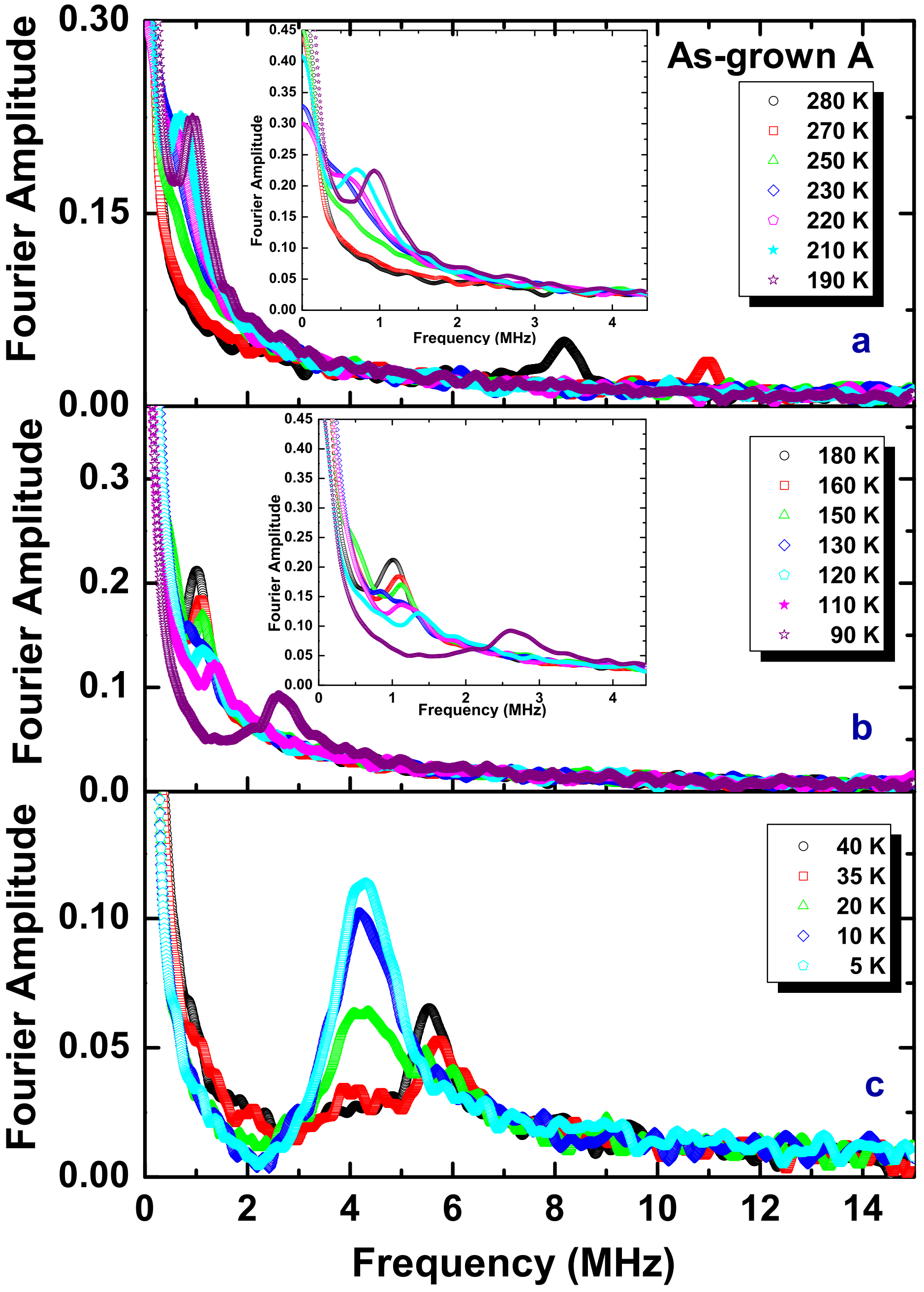

Figure 7.10: FFT plots of each characteristic temperature region of As-grown A sample.

LF-μSR Measurements on the As-grown A Sample

These observed μSR oscillations above 150 K and especially the high frequencies observed around 280 K of the T'-Pr_2CuO_4 are in stark contrast to the predominantly dynamic character of the depolarization in T'-La_2CuO_4 at the same temperature range. Therefore, it is important to investigate also the dynamic magnetic properties of the T'-PCO sample. This can be done by the decoupling measurements performed at various temperature regimes under 0.005, 0.02, 0.04, and 0.1 Tesla applied fields. Figure 7.11 shows these measurements plotted including the zero-field measurements for comparison and reference. Since no theoretical fit function is available for decoupling measurements with well-defined internal magnetic fields, I will restrict myself to a qualitative description of the data.

Clearly, static magnetism can be concluded for the 80 K spectra from the nice decoupling behavior with the stereotypical horizontal tail with recovery of the muon spin polarization with increasing external magnetic fields. In contrast, the data at e.g. 120 K and 220 K clearly display a dynamic behavior with a relaxing tail at all fields. Interestingly, at the intermediate temperature of 180 K the system is obviously static again.

To obtain an overview of the dynamic and static temperature regimes, a temperature scan with an applied field of 0.1 Tesla has been performed. The obtained dynamic relaxation rate is depicted in Figure 7.12. As already obtained from the analysis of the ZF data, two clearly dynamic temperature regions can be identified by the peaks of the relaxation rate. As discussed above, the appearance of two peaks in the dynamic relaxation rate speaks against a continuous slowing down of the spin dynamics and evidences the presence of distinct phase transitions. The strong change of the internal field distribution favors spin reorientation transitions between qualitatively very different magnetic structures. This will be further interpreted in section 7.2.4 of this chapter.

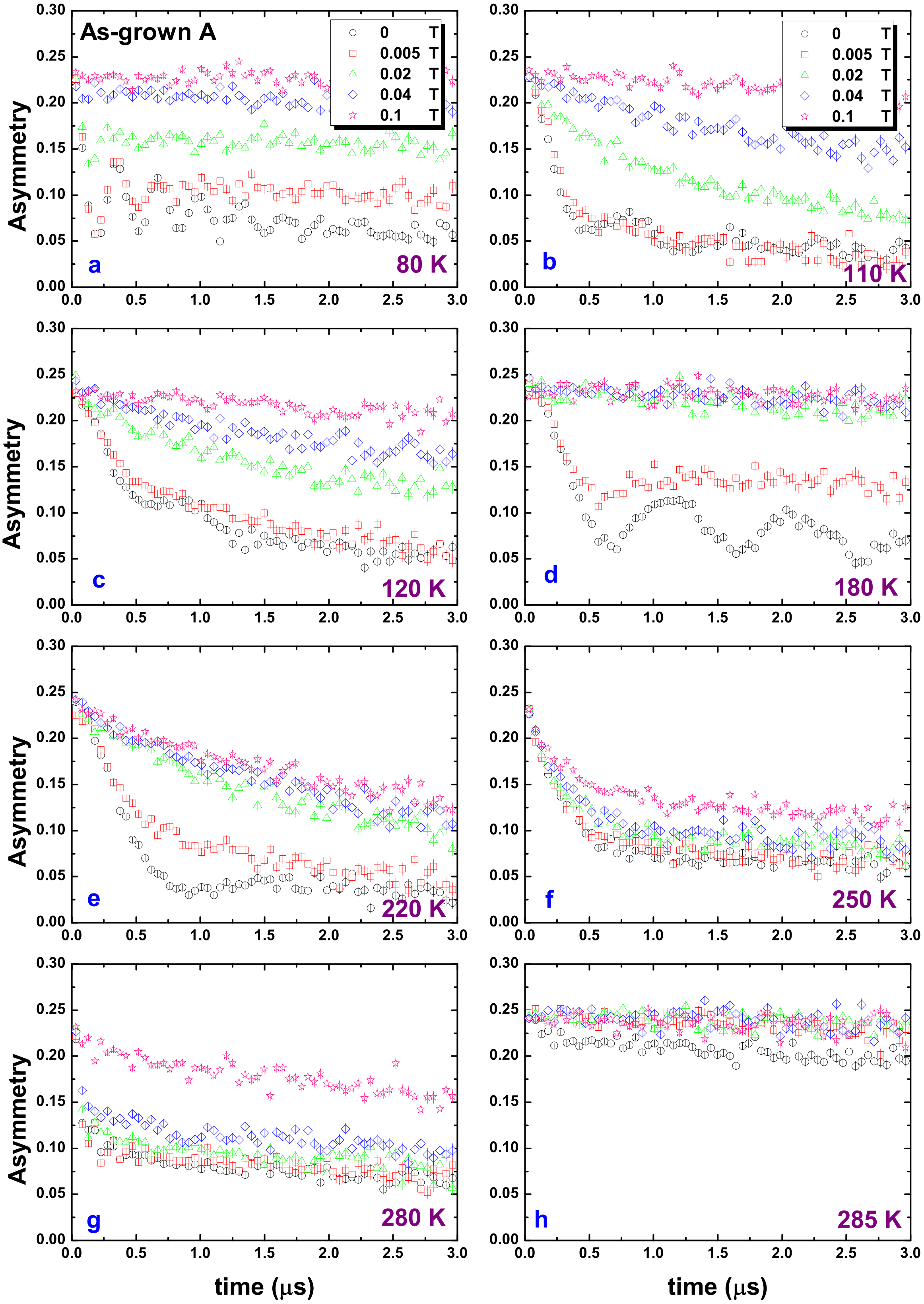

Figure 7.11: Decoupling measurements at various temperatures with 0, 0.005, 0.02, 0.04, and 0.1 Tesla applied fields.

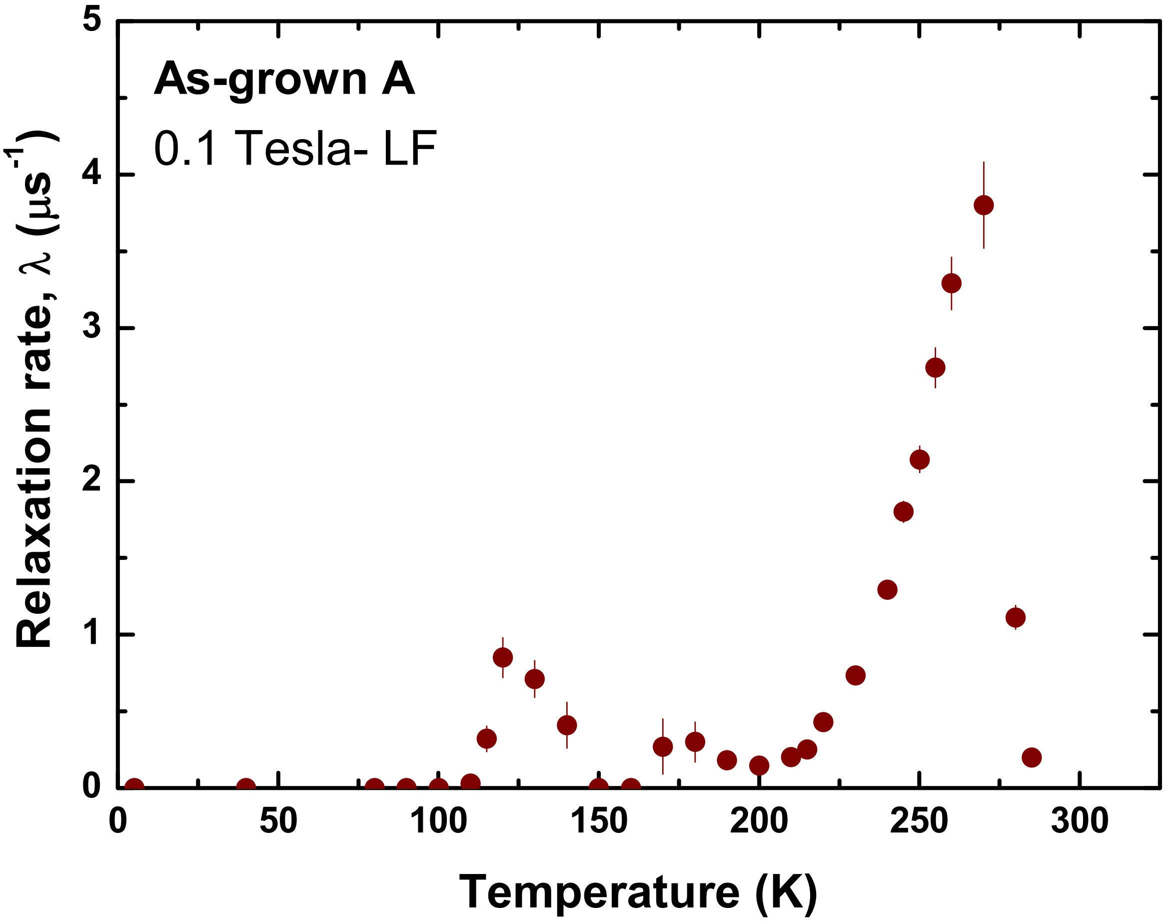

Figure 7.12: Temperature scan with an applied 0.1 Tesla longitudinal fields of the As-grown A sample.

Effect of Annealing at 800 °C in Vacuum

As depicted in Figure 7.9, the same features as for the sample As-grown A and the remarkable transition temperatures are consistently seen for the sample As-grown B. This is expected since the two samples are grown at the same conditions. But astoundingly, the same characteristics are also manifested by the sample Reduced B$_{800-Vac}$ wherein a reduction at 800 °C under vacuum conditions did not seem to drastically affect magnetism in the system, see the μSR fit parameter in Figure 7.13 . Structurally, it is only the O(3) site that is vacated but no evident difference on the O(2) site is observed among these three samples as given by high-resolution powder neutron diffraction results, see again Table 7.5. Therefore, one has to conclude that the small amount of apical oxygen present in the as-grown samples does not affect the magnetism of T'-PCO. This is very important, since exactly this oxygen is generally believed to play a major role in the occurence of superconductivity in the electron-doped cuprates, see chapter 2.

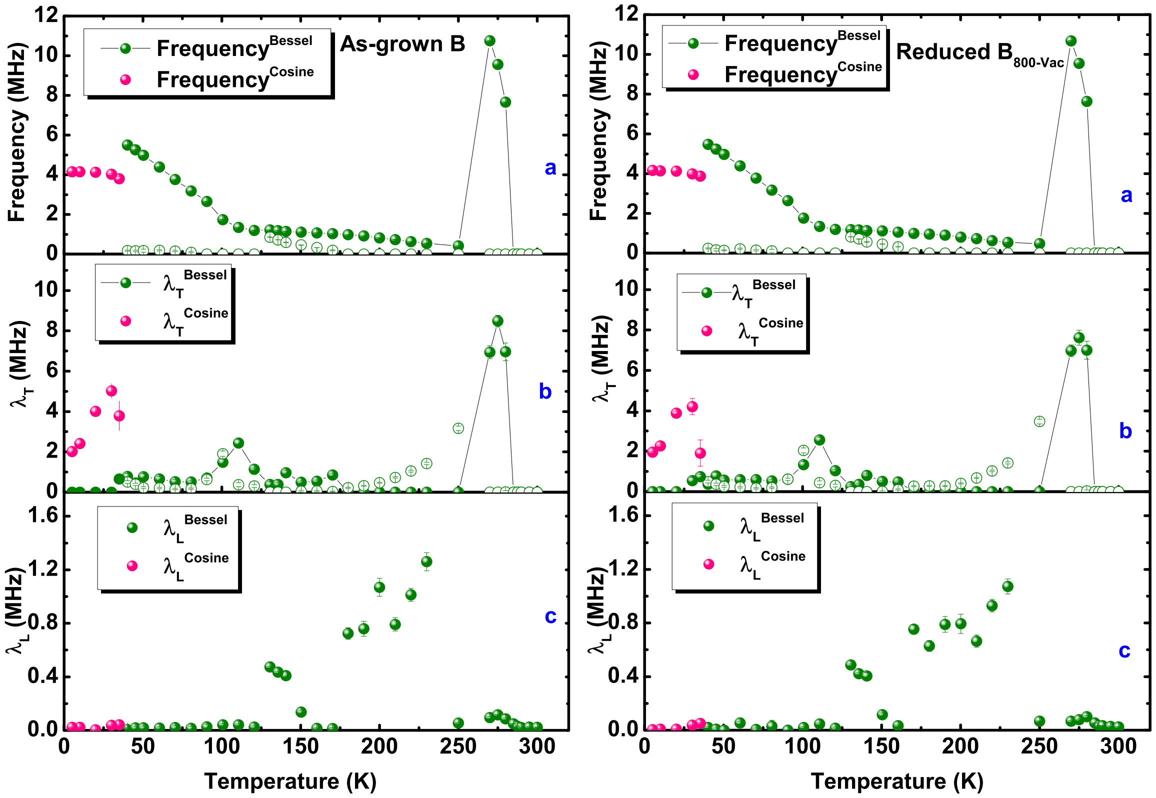

Figure 7.13: ZF-μSR fit results for samples T'-Pr$_2$CuO$_4$ As-grown B and Reduced B$_{800-Vac}$: a) The frequency, b) the transverse relaxation rate, c) the longitudinal relaxation rate as a function of temperature.

Effect of Annealing at 900 °C in Ar flow for 12 hours

In order to continue the investigation of the influence of oxygen reduction conditions on the magnetism in T'-Pr_2CuO_4, we compare μSR measurements of the as-grown and the reduced sample annealed at 900 °C in Ar flow for 12 hours. Representative ZF-spectra of the As-grown A and the Reduced A_{900-Ar} samples are shown side-by-side in Figure 7.14. Elaborating on the distinctive transitions at particular temperature regimes and comparing the two samples, evident differences are observed even by merely looking at the spectra. Once more, the same fit model is used for both compounds like in the case of T'-LCO. At the highest temperature, a paramagnetic signal is displayed. A Gaussian-Kubo Toyabe function fits the signal.

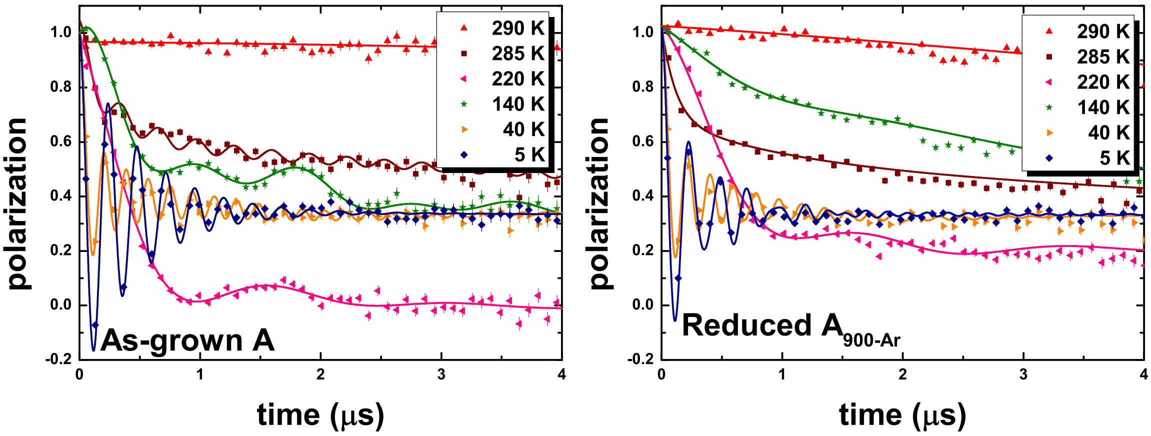

Figure 7.14: Zero-field spectra at 5, 40, 140, 220, 285, and 290 K of the As-grown A and Reduced A_{900-Ar} samples.

Then at a slightly lower temperature, there is an obvious and remarkable observed difference between the two compounds. The presence of the high-frequency observed at high temperatures in the as-grown sample had diminished in the reduced sample, and only a damped signal is seen in the reduced sample. In Figure 7.14, the 285 K data (brown) are shown with a relatively strong binning, the difference at the high-temperature regime is better-highlighted in Figure 7.15. The inset displays the rapidly-oscillating signal at very early times in the time spectra. Please note that both samples show quasi-static magnetism at this temperature, but that sample As-grown A possesses a much more homogenous magnetic state since the μSR oscillations are visible. This means in turn, that obviously the high-temperature reduction process causes disorder in the Cu magnetic system. The 220 K signal is also very distinct, see pink data in Figure 7.14. The as-grown sample shows a more dynamic signal in comparison to the more static signal exhibited by the reduced sample. This is very clearly seen from the raw data since the tail is much more strongly damped in the as-grown sample (λ_L ~ 1 MHz) than for the Reduced A_{900-Ar} sample (λ_L ~ 0.4 MHz). Therefore, one has to conclude that the reduction process changes magnetic dynamics of the system. Also in the intermediate-temperature regime at 140 K depicted as the green data points in Figure 7.14, a noticeable oscillation is observed in the as-grown sample while the reduced sample exhibited an exponential depolarization. This again is a proof for the introduced magnetic disorder by the high-temperature reduction process.

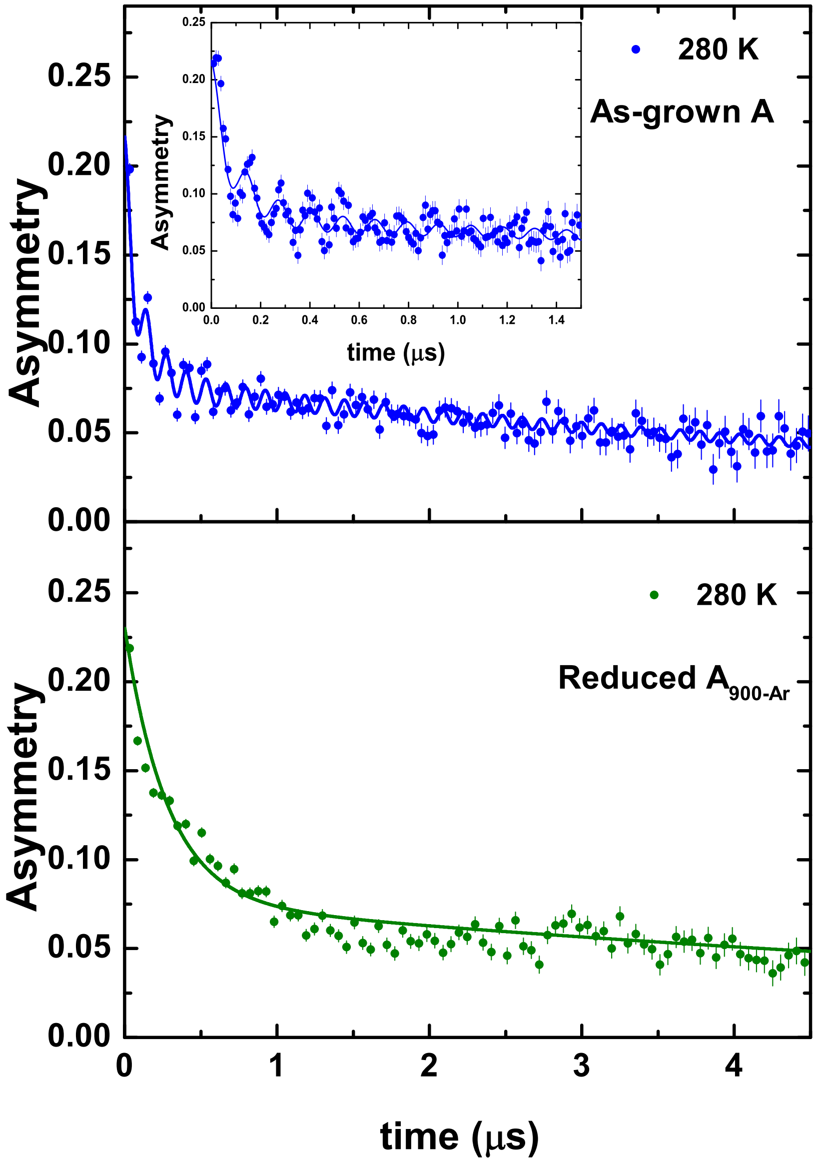

Figure 7.15: Zero-field spectra at 280 K of the As-grown A and Reduced A_{900-Ar} samples.

One can immediately see the evolution of the shape of field distribution at different temperature regimes as illustrated in Figure 7.16. At the high-temperature regime, Figure 7.16 *a*) further shows that the high-frequency that was before seen in the as-grown compound is no longer evident, please compare to Figure 7.10. The disappearance of this frequency at high temperatures may suggest that there is a different magnetic structure or a considerably increased magnetic disorder exhibited by the reduced compound at this temperature regime in comparison to the as-grown sample.

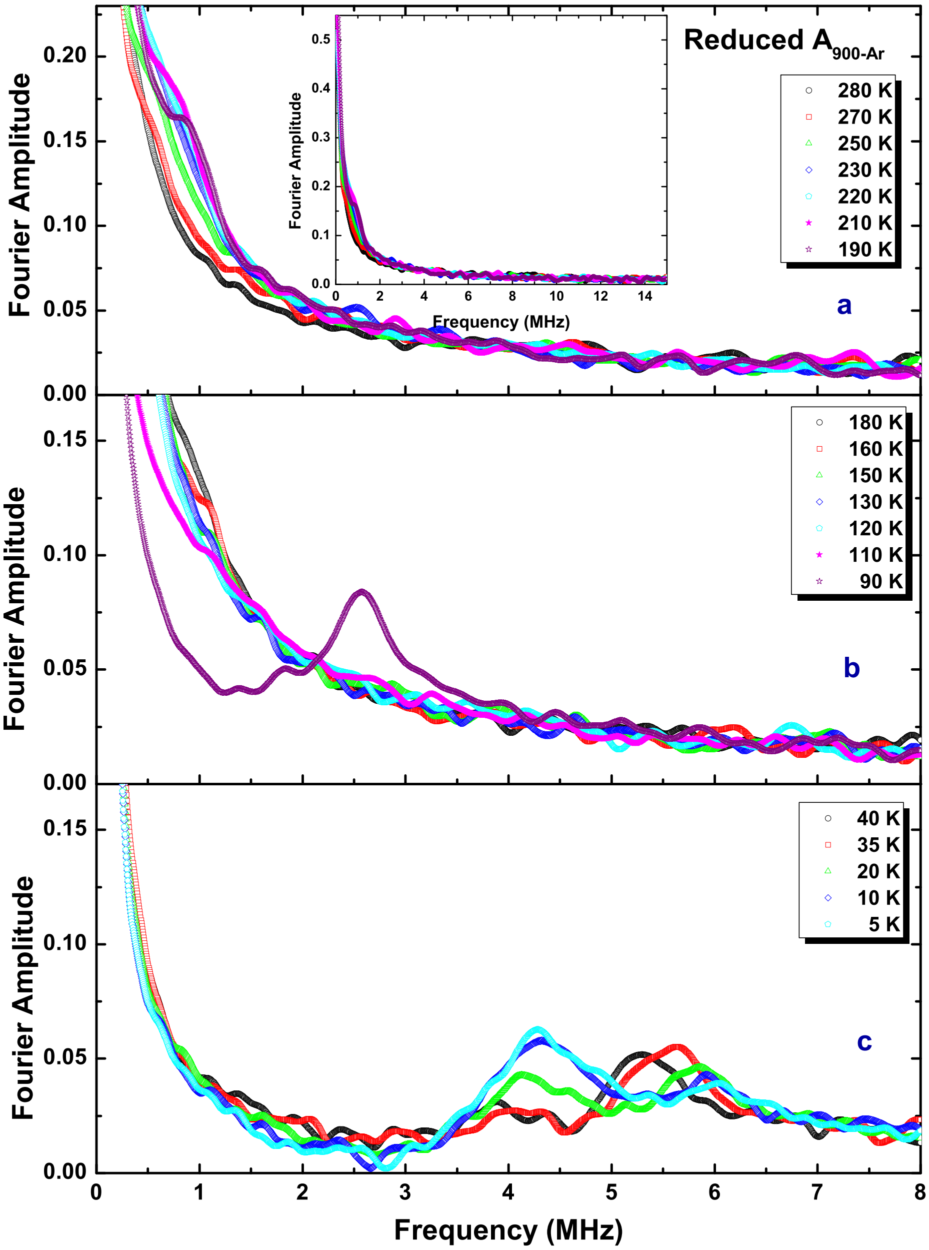

Figure 7.16: FFT plots at each characteristic temperature region of Reduced A_{900-Ar} sample.

Then at a bit lower temperature, a low frequency starts to emerge at $T = 275$ K as shown in Figure 7.17 a). With decreasing temperature, fluctuations go into the time window of the muon at below 250 K as shown by an increase in the longitudinal relaxation rate in Figure 7.17 c). Then at 230 K down to 160 K, the depolarization can be better fitted with two frequencies but with the same relaxation rates. This two-frequency region is somehow shifted in comparison with the as-grown sample. This is also seen as a broader field distribution at the intermediate region in Figure 7.16 b) starting at 150 K down to 120 K. Then at 150 K, the oscillation fades and only an exponential depolarization is observed.

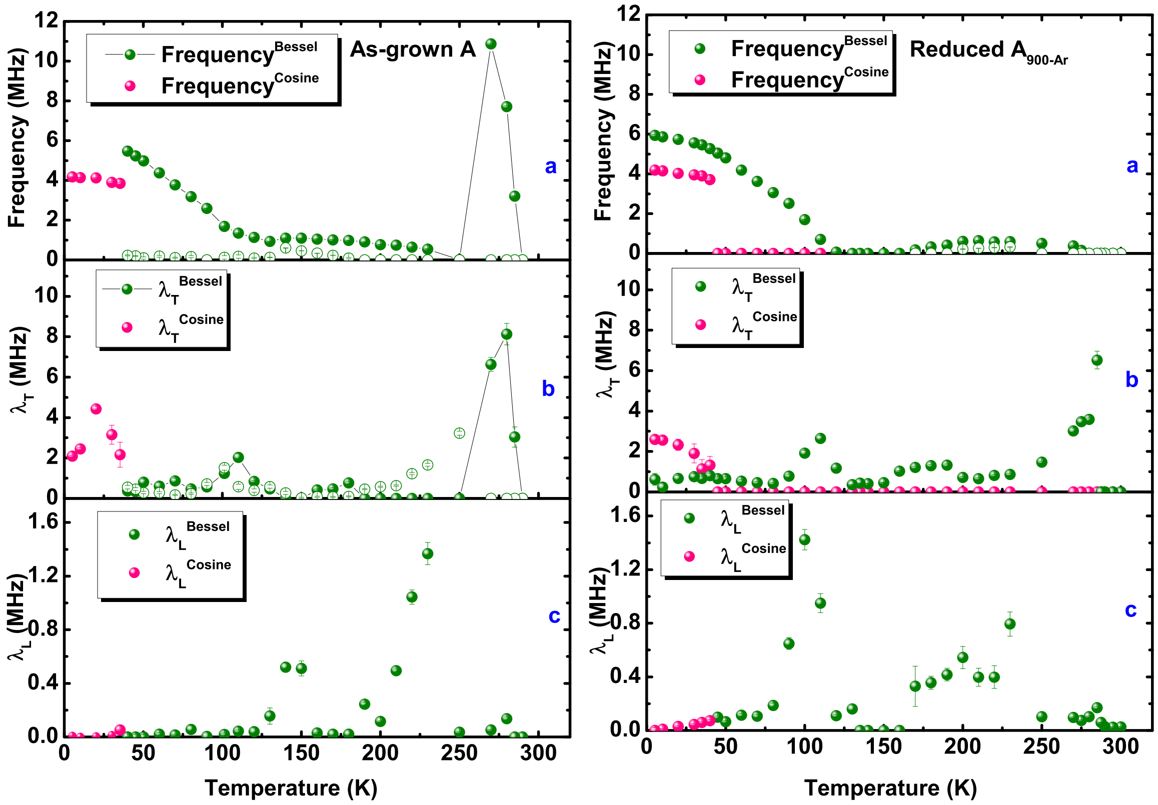

Figure 7.17: ZF-μSR fit results for T'-Pr_2CuO_4: a) The frequency, b) the transverse relaxation rate, and c) the longitudinal relaxation rate as a function of temperature of the As-grown A (left-side figure) and the Reduced A_{900-Ar} (right-side figure) samples, respectively.

Below 120 K, reemergence of an oscillating signal is observed and it grows like a usual order parameter like in the case of the as-grown sample. The dynamic relaxation rate, λ_L peaks and then decreases. This means that the system is again entering a static regime from a highly fluctuating one. The data in this region is well-described with the zeroth-order Bessel function.

Below 40 K, the field distribution pictured in Figure 7.16 has an unconventional shape. A sum of both the Cosine and Bessel magnetic fractions best fits this field distribution. This is in contrast to the well-defined single Lorentzian field distribution in the as-grown sample.

LF-μSR Measurements for Reduced A_{900-Ar} Sample

Like the As-grown A sample, the dynamic nature of the magnetism of the Reduced A_{900-Ar} sample was verified by the decoupling measurements performed at various temperature regimes under 0.005, 0.02, 0.04, and 0.1 Tesla applied fields. Figure 7.18 shows these measurements. Also, to obtain an overview of the dynamic and static temperature regimes, a temperature scan with an applied field of 0.1 Tesla applied longitudinal field is performed giving the transition regions exhibited by the peaks of Figure 7.19. Interestingly the dynamic relaxation rate λ_L of the Reduced A_{900-Ar} sample is virtually identical to the one of the as-grown sample, please compare to Figure 7.12. It shows two peaks at ~120 K and ~270 K indicating two phase transitions at these temperatures, respectively. It should be noted anyhow that for the Reduced A_{900-Ar}, the lower temperature peak was seen in ZF at about 100 K. This indicates that even a small magnetic field of 0.1 Tesla can modify the magnetism of the reduced sample considerably and apparently can remove the differences between the as-grown and reduced sample. This is probably again a manifestation of the very small differences in the total energy of the various magnetic states the system can adopt.

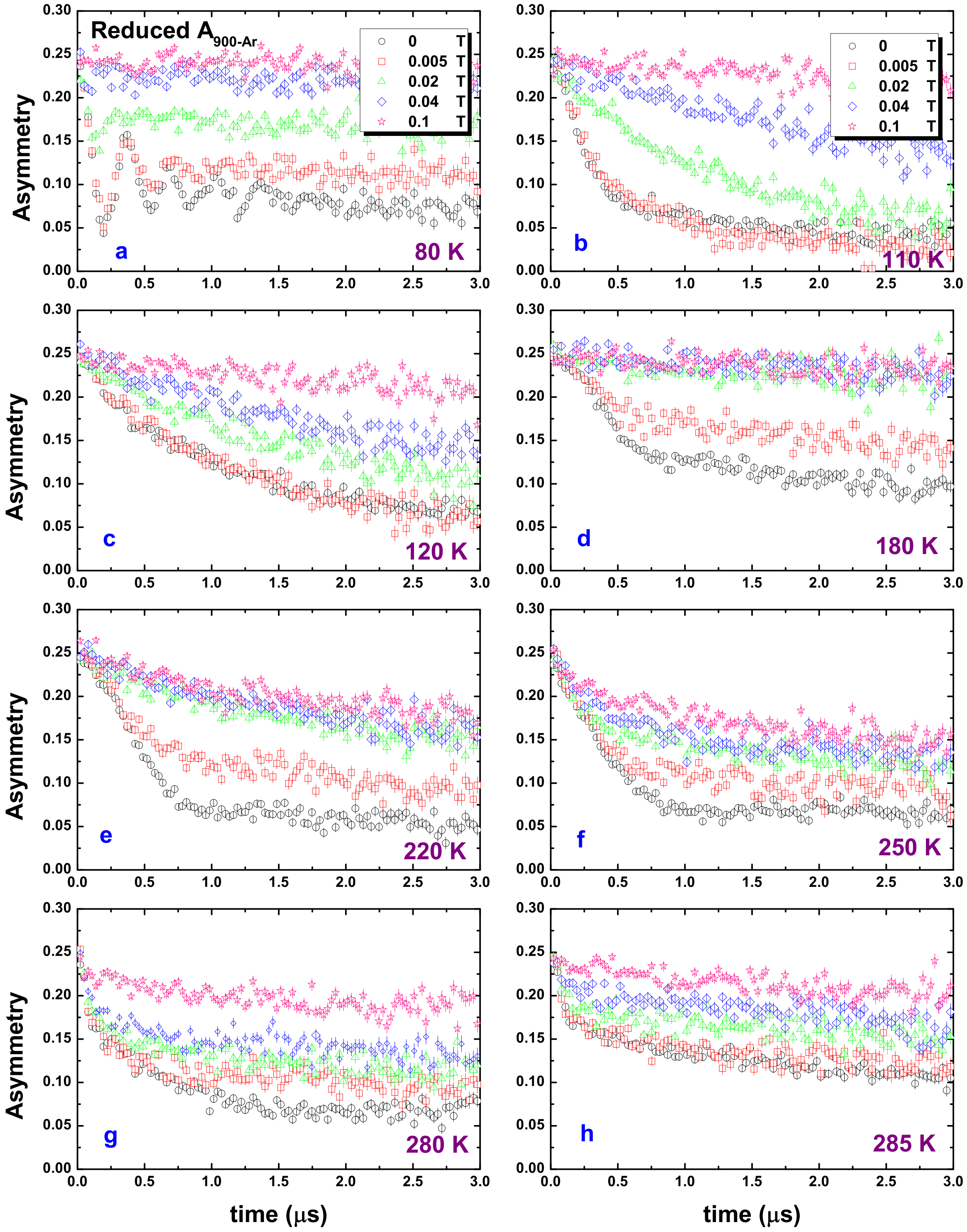

Figure 7.18: Decoupling measurements at various temperatures with 0, 0.005, 0.02, 0.04, and 0.1 Tesla applied fields.

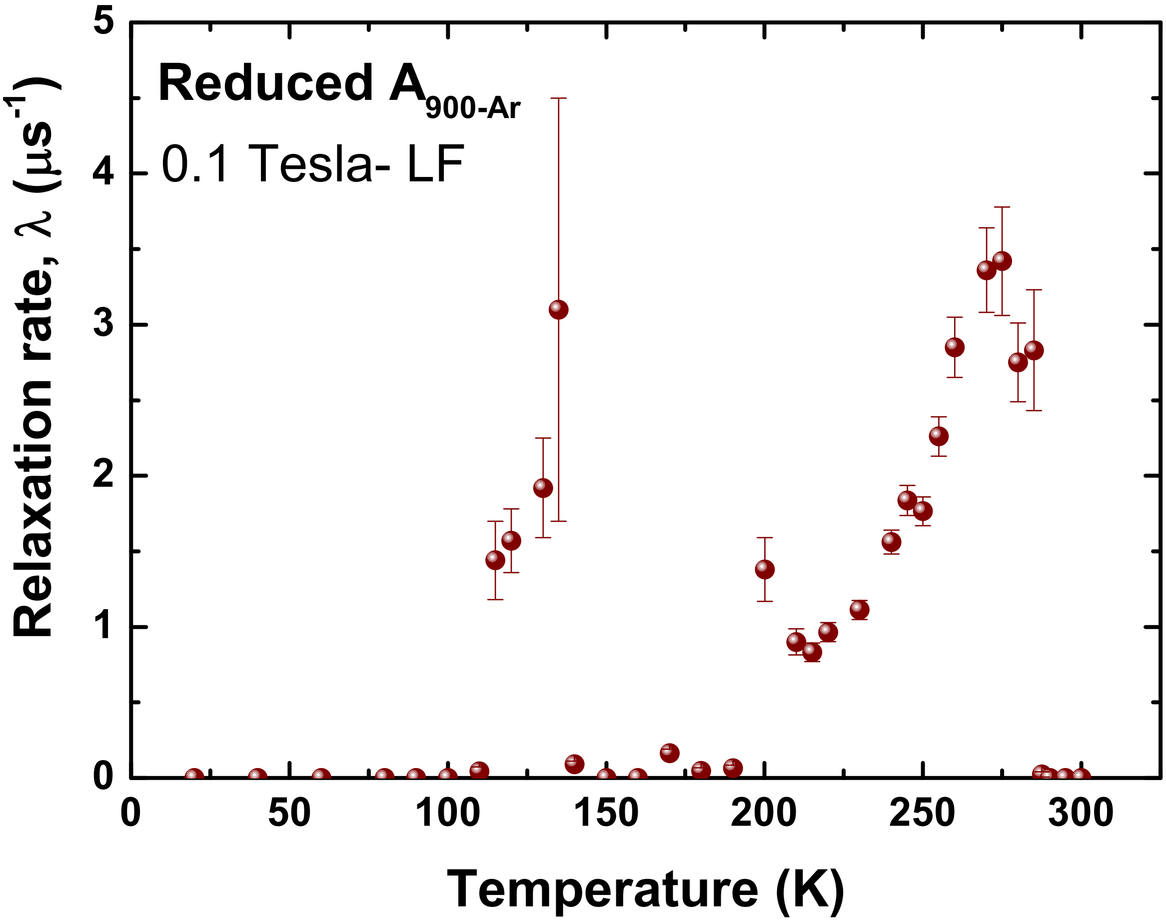

Figure 7.19: Temperature scan of the Reduced A_{900-Ar} PCO sample with an applied 0.1 Tesla longitudinal fields.

Effect of Annealing at 900 °C in Ar flow for 10 hours - a slightly shorter annealing time

For the Reduced B_{900-Ar} sample, there are slight differences observed especially at lower temperatures in comparison to the previously described Reduced A_{900-Ar} sample. It is significant to mention that with this sample, the annealing time is a little bit shorter than the Reduced A_{900-Ar} sample (10 hours in comparison to 12 hours).

The overall characteristic of this sample resembles the one of the Reduced A_{900-Ar} sample. A notable difference is on the low temperature region. The data below 80 K can be better fitted with two cosine functions plus another fast relaxing signal. Actually, the data has a broad field distribution that is not very pronounced which makes the signal more challenging to fit and capture with the analytical fit functions.

This result directly exemplifies that longer annealing times and/or higher temperatures could lead to more homogeneous samples. For completeness the μSR fit results are depicted in Figure 7.20.

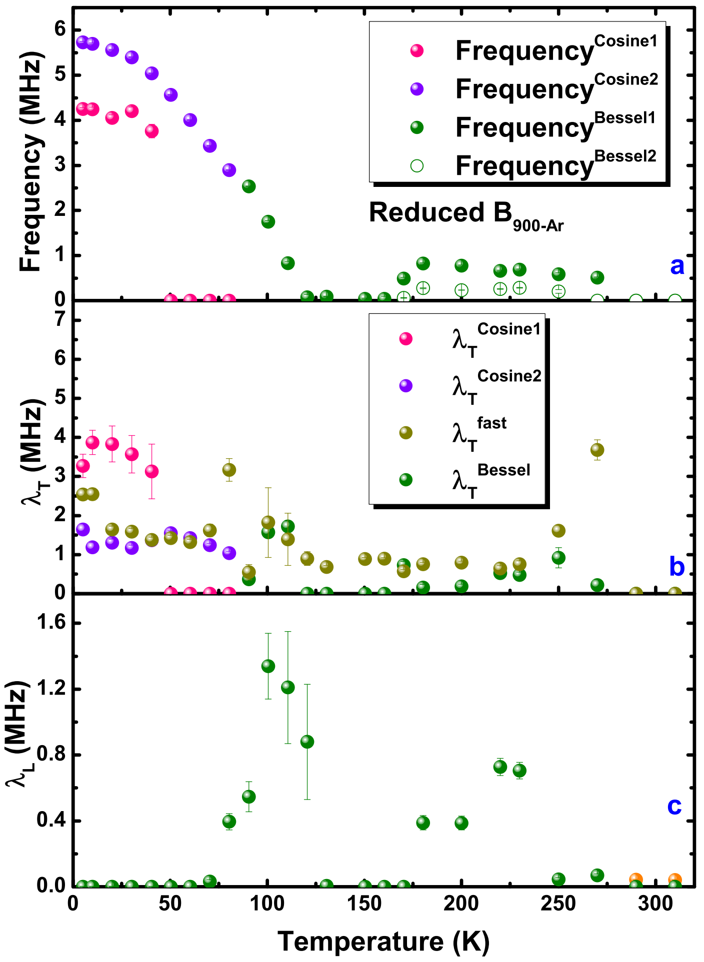

Figure 7.20: ZF-μSR fit results for Reduced B_{900-Ar} T'-Pr_2CuO_4 sample: a) The frequency, b) the transverse relaxation rate, and c) the longitudinal relaxation rate as a function of temperature.

7.2.3 Key Experimental Observations and Interpretations from μSR Results

As a recap, a total of five samples of bulk T'-$\mathrm{Pr_2CuO_4}$ (T'-PCO) were measured in μSR. These are divided into two sets of samples, Set A and Set B, and each set has both the as-grown and the reduced sample. Both as-grown samples A and B demonstrated virtually identical characteristics proving the reproducibility of the synthesis procedure. The annealing conditions for the reduced samples were all different, as previously described. μSR results revealed that the reduction annealing conditions influence the magnetism of the system.

With the rich series of transitions observed in T'-$\mathrm{Pr_2CuO_4}$, one can deduce that this is very similar to T'-$\mathrm{La_2CuO_4}$ (T'-LCO). There are, nonetheless, remarkable observed differences between the two compounds. From the cold neutron scattering results, the magnetic peak intensities vanished at $T_\mathrm{N} = 285$ K. This higher T_N compared to the e.g. $T_\mathrm{N1} = 220$ K of T'-$\mathrm{La_2CuO_4}$ (T'-LCO) clearly demonstrates that the magnetism in T'-PCO is less two-dimensional than in T'-LCO and also in comparison to the as-grown and reduced T'-LSmCO with $T_\mathrm{N1} = 220$ K and 240 K, respectively. As discussed in the previous chapter for the case of the T'-LSmCO, this can be traced back to the presence of a polarizable magnetic RE moment, and in this system the Pr moment. Another remarkable difference is the appearance of slow oscillations at high temperatures up to 250 K in T'-PCO in sharp contrast to the predominantly dynamic character of the depolarization in T'-LCO at a similar temperature range below T_{N1}. Even more astonishingly, in the as-grown T'-PCO sample, fast ZF-μSR oscillations (much faster than at lowest temperatures) are observed, a phenomenon completely absent for T'-LCO.

Now to focus on the magnetic transitions observed in the T'-$\mathrm{Pr_2CuO_4}$, the interesting features for both the as-grown and the reduced samples will be sorted in the following. Table 7.6 summarizes the striking differences of the as-grown and reduced samples at characteristic temperature regimes. Note once more that the sample annealed at 800 °C in vacuum demonstrated the same behavior as the as-grown samples. In the discussion below, the reduced sample referred to here is mostly the more homogeneous sample, the Reduced A_{900-Ar} sample (and not Reduced B_{900-Ar}).

Both the as-grown and the reduced samples show paramagnetism at the highest temperatures. Starting at 285 K down to 250 K, a very distinct difference is displayed by the fast oscillations of the ZF-μSR signal in the as-grown sample in stark contrast to a fast transverse damping of the signal in the reduced sample. In addition, an increase in the transverse relaxation rate is observed as a function of increasing temperature for both samples signi-

Temperature	As-grown & Reduced$_{800-vac}$	Reduced$_{900-Ar}$
300 K - 285 K	- Gauss-Kubo-Toyabe relaxation	- Gauss-Kubo-Toyabe relaxation
285 K - 250 K	- fast μSR oscillations - peak in dynamic relaxation rate (1000 G LF)	- fast transverse damping - peak in dynamic relaxation rate (1000 G LF)
250 K - 180 K	- 1 Bessel frequency increasing	- 2 Bessel frequency with maximum at 210 K and decreasing to zero below
170 K - 130 K	- 2 Bessel frequencies - peak in dynamic relaxation rate (1000 G LF) - peak in dynamic relaxation rate at 150 K (ZF)	- no frequencies, low transverse damping - peak in dynamic relaxation rate (1000 G LF)
120 K - 40 K	- 1 Bessel frequency increases like an order parameter	- 1 Bessel frequency increases like an order parameter - peak in dynamic relaxation rate at 100 K (ZF)
40 K - 0 K	- 1 Cosine frequency	- 1 Bessel and 1 Cosine frequency

Table 7.6: Comparison of the fit results for the As-grown and the reduced samples (800 °C, vacuum) on the one hand and the stronger reduced samples (900 °C, Ar) on the other hand.

fying that the internal field sensed by the muon at this temperature regime increased, thus, the absolute width of the field distribution is enhanced. The observation of an oscillation in the as-grown sample shows that the as-grown sample is more ordered than the reduced one. Thus, this means that high-temperature reduction annealing can bring about disorder in the Cu magnetic system. Note, however, that both samples exhibit only quasistatic magnetism at this temperature and the LF-μSR measurements with an applied field of 0.1 T therefore revealed a peak in the dynamic relaxation rate at this temperature region. As a matter of fact, there is another peak at the intermediate temperature but this will be discussed later.

From 250 K down to 120 K, two magnetic components fitted with two Bessel functions were used to describe the data. This two-component relaxation functions indicates two magnetically different muon sites in the crystallographic structure. However, on the interval from 250 K down to 180 K, only one frequency is observed in the as-grown sample while two frequencies but with the same relaxation rates, can be observed in the reduced sample. The frequency has a maximum at around 210 K and fades to zero below that. Below 170 K down to 130 K, there are two frequencies observed in the as-grown sample while in the similar temperature range between 150 K down to 120 K, only a low transverse damping of the signal is observed for the reduced sample. A second peak in the dynamic relaxation rate in the LF-μSR with 0.1 T applied field measurement is observed at 130 K for the as-grown sample while this is seen at around 120 K for the reduced sample. Although it should be pointed out once more that this second peak was seen in ZF at about 150 K for the as-grown and 100 K for the reduced sample, respectively. This then indicates that a minute field of even a 0.1 T can alter the magnetism and equalize some differences between the as-grown and reduced sample. The appearance of the two peaks in the dynamic relaxation rate as a function of temperature rather points to the presence of distinct phase transitions, and not to a continuous slowing down of the spin dynamics.

Then at 120 K down to 40 K, the previously two-component frequency of the as-grown sample merges into one that smoothly grows like the usual order parameter. This very same behavior was also demonstrated by the T'-LCO at the same temperature region. The reduced sample then regains the diminished frequency and follows a similar behavior. As the field distribution at this temperature region is again broad and asymmetric, a zeroth-order Bessel function still best describes the data for both samples.

A switch of field distribution, like in the case of the T'-LCO, happens at 40 K and below which a standard Cosine function can better describe the data. In contrast, a broader field distribution is observed in the reduced sample that can be best-fitted with a sum of two magnetic fractions using the Cosine and Bessel functions. Thus, one can deduce that the as-grown sample similarly demonstrates the magnetic reorientation or *lock-in* transition at 40 K as the one observed in T'-LCO, i.e. it *locks-in* to the NCol II magnetic structure. In contrast, the reduced sample does not show this *lock-in* behaviour. It is however, plausible that the reduced T'-PCO adopts one of the other special models discussed for T'-LCO in section 5.4.2. Especially, the two models Col I and NCol I are reasonable candidates since they both possess two distinct and non-zero internal magnetic fields at the muon sites. Again, the different magnetic behavior of the as-grown and reduced samples shows that the high temperature annealing at 900 °C has a significant influence on the magnetism of the sample.

The still magnetic electron-doped $RE_{2-x}Ce_xCuO_4$ cuprates only become non-magnetic and superconducting after a reduction process [110]. In this work, it is shown that also the magnetism of the undoped mother compounds is influenced by a high temperature reduction process. Due to the systematic investigation of the magnetic and structural properties of the very same samples for different reduction conditions, it is now possible to try to relate the magnetic changes to the structural modifications especially the occupation of the different oxygen sites. As discussed in chapter 2, it is common sense (which is not necessarily true), that reduction annealing should only remove the apical oxygen O(3) while the in-plane O(1) and the charge-reservoir layer O(2) should remain intact. A common reasoning is that the presence of this O(3) in BCT cuprates hinders the emergence of superconductivity as these empirically serve as strong scatterers as well as pair-breakers. Madelung potential calculations, reinforced by experimental results, found that below a certain level of doping, e.g. $x < 0.08$, it was the out-of-plane O(2) that is taken out [113, 112]. This is consistent with our results on the reduction annealing at 900 °C in Ar flow, but not with the annealing at 800 °C in vacuum where the apical oxygen O(3) is removed. On the other hand, there are experimental findings that suggest the elimination of oxygen from the CuO_2 plane [112, 113]. Astonishingly, this would have allowed superconductivity to flourish contrary to expected notion on the critical importance of an intact CuO_2 plane. A positive outcome when O(1) is removed is the emergence of a secondary phase which does not contain Cu ions, but these zones act as Cu reservoirs for the Cu that migrate into the CuO_2 planes during the reduction process, effectively reducing Cu vacancies and therefore, eliminating pair-breaking sites [27]. This then allows superconductivity to emerge. Kang and coworkers illustrated that there are intrinsically Cu deficiencies in the as-grown materials and that reduction annealing can *heal out* or *repair* these deficiencies along with the appearance of an impurity phase [121]. In our case, reduction annealing at 900 °C in Ar flow can drastically disorder the system. The disorder may have come possibly from the presence of Cu vacancies which were brought about by the relatively high annealing temperature. The decrease in the *a*- and *b*- lattice parameters for these 900 °C-reduced compounds can also reinforce this notion. This effect could anyhow also be produced by missing oxygen O(2) from the RE-O layer that had been taken out by the high temperature annealing. The redistribution of the O(2) may then have caused the magnetic disorder. In contrast, annealing at 800 °C maintains the same magnetic structures and transition temperatures. Although an excess of O(2) was observed which was unchanged compared to the as-grown sample, the apical oxygen was removed after this reduction. Therefore, one has to conclude that the small amount of apical oxygen present in the as-grown samples does not affect the magnetism of T'-PCO. Perhaps a second annealing as the one suggested by Krockenberger and coworkers [125] can redistribute these oxygens to site deficiencies in the CuO_2 plane. As mentioned earlier, in their thin film samples, even superconductivity could be observed in the nominally undoped samples by this procedure. This second annealing would be therefore a promising route for further investigations on these systems.

In addition to the reduction annealing temperature, the annealing time can also influence the system primarily on the homogeneity aspect. The sample Reduced B_{900-Ar} annealed for only 10 hours in contrast to the 12-hour annealed sample, Reduced A_{900-Ar}, illustrated magnetic inhomogeneities especially in the low-temperature region.

Coming back to the general magnetic behavior of as-grown as well as reduced T'-PCO, one has to conclude that all samples display a complex magnetic behavior very different from the simple magnetic ordering that one would deduce from powder neutron diffraction data shown in this thesis and in the literature. Several experimental observations point to a series of transitions between partially very different magnetic structures as a function of temperature. These are namely temperature intervals with very different number and sizes of internal magnetic fields and transverse and longitudinal relaxation rates. The observation of two peaks in the dynamic relaxation rate as a function of temperature also clearly speaks in favor of distinct transitions. Additionally, the behavior of the series of magnetic transition as a function of temperature for T'-PCO appears similar but more complex than the one observed in T'-LCO for which we could resolve the lower two magnetic phases. Therefore, it seems unlikely that the induced magnetic polarization in the RE magnetic system is at the core of explanation for the observed transitions. But certainly, the presence of a polarizable moment can add complexity on the magnetic interactions in the CuO_2 plane. In the following, the possibility of spin reorientation transitions is discussed.

7.2.4 Spin Reorientation in T'-Pr_2CuO_4

The investigation of the interesting magnetic behavior involving both the rare-earth and the copper spins can be substantiated in the T'-Pr_2CuO_4 compound. As with the other rare-earth cuprates with a body-centered tetragonal structure, the proposed magnetic structures for this compound have been illustrated and described in chapter 2, which are either collinear or noncollinear magnetic structures. Experimental evidences from neutron scattering support the noncollinear Cu spin order for these systems [33, 59]. So far, there are no accounts of spin reorientation on T'-Pr_2CuO_4 at ambient pressure. However, under small hydrostatic pressures, T'-Pr_2CuO_4 revealed two magnetic phase transitions that are also ascribed to spin reorientations [99]. Akimitsu et al. had performed μSR measurements on single crystal $Pr_{2-x}Ce_xCuO_{4-\delta}$ in zero external fields in which the authors proposed two spin-reorientation phase transitions [100] wherein the magnetic moments of the Cu atoms order in an antiferromagnetic noncollinear cross like structure including a, up to then, hidden canting of the spin arrangement. The said authors proposed a low-temperature phase (T $\leq$ 40 K) and a high-temperature phase (40 K $\leq T \leq$ 110 K) [100]. These somehow have similarities to our observed transitions. Their results did not elaborate nor include the appearance of the fast oscillations at the high-temperature region that we observed, and also were not able to account for the abrupt change of the shape of field distribution at $T \leq$ 40 K.

In this work, the appearance of two peaks in the dynamic relaxation rate is interpreted as an evidence of the presence of distinct phase transitions. The strong change of the internal field distribution can be attributed to spin reorientation transitions between qualitatively very different magnetic structures. Especially the appearance of the high μSR frequency around 280 K in the as-grown sample is intriguing. As it is clear from the magnetic dipole field calculations presented in section 5.4.2 in Figure 5.17, no such high fields can be produced by magnetic models in which the Cu moments are aligned within the plane. Therefore one has to conclude that in this temperature interval, the magnetic moments must have a component out-of-plane which can increase the field at the muon site dramatically. This configuration may possibly be similar to the magnetic structure proposed for T'-Sm_2CuO_4 [172]. This is interesting since usually a rather strong easy-plane anisotropy is assumed.

At the intermediate temperature region between 150 K and 250 K, a broad asymmetric distribution of internal fields which can be fitted by two Bessel functions is obtained. It is therefore reasonable to assume that a similar distribution of angles γ between the spin structures of neighboring Cu planes is adopted as in T'-LCO, see section 5.4.2. Anyhow there is a qualitative difference between the phase between 150 K up to 250 K and the phase between 40 K and 120 K. The latter being very similar to the one observed in T'-LCO at the corresponding temperature interval, namely a distribution of magnetic structures all belonging to the same IR τ_5. Again, one can conclude that also in T'-PCO the coupling between the neighboring CuO_2 planes is very weak and that the anisotropy in the plane must also be very weak compared to the temperature such that no well defined spin orientation is adopted. Having identified the phase between 40 K and 120 K in analogy to the T'-LCO compound, it is mandatory to ask the question what can be different for the higher temperature phase between 150 K and 250 K if at the lower temperatures the spin orientation angles are anyway distributed? One possible answer might be that in the higher temperature phase magnetic models only belonging to the τ_3 IR are adopted. As said earlier these different groups of magnetic structures differ in their anisotropy energy. A transition between these groups of structures would imply a temperature dependence (and sign change) of the anisotropy constant. In this way, the spin reorientation transitions in T'-Nd_2CuO_4 have been explained [83]. In principle, the distinction between these groups of magnetic structures can also and maybe best be made by μSR on single crystals. It turns out that according to our dipole field calculations the magnetic fields at the muon sites for *all* magnetic structures belonging to the τ_3 IR point along the crystallographic c-axis, while all structures belonging to the τ_5 IR produce magnetic fields within the ab-plane. Very recently, we performed orientation dependent μSR on as-grown single crystals of T'-Pr_2CuO_4 revealing that actually the above speculation is correct and that the high temperature phase must belong to structures from the τ_3 IR while in the lower temperature phase a distribution of structures from the τ_5 IR is realized.

As mentioned above, at temperatures below 40 K, it is plausible that the as-grown and weakly reduced T'-PCO adopt the NCol II structure as it is the case for T'-LCO. The high-temperature annealed samples anyhow show considerably more magnetic disorder and no clear *lock-in* transition (narrowing of the field distribution) is observed. The presence of two μSR frequencies (one Bessel and one Cosine) may indicate that rather predominantly either the NCol I or the Col I is realized, but in a phase separated manner due to the disorder.

Future work on our T'-Pr_2CuO_4 would involve magnetic neutron scattering with the application of magnetic fields in order to isolate and to resolve the possible magnetic phases determined by μSR.

8 Summary and Outlook

The structural and the magnetic properties of the investigated T'-RE$_2$CuO$_4$ (RE = La, La/Sm, and Pr) are discussed in separate chapters of this thesis. In all the investigated T'-RE$_2$CuO$_4$ (RE = La, La/Sm, and Pr) systems, a series of magnetic transitions has been found at different characteristic temperatures illustrated by the temperature dependence of the muon precession frequency in Figure 8.1. As discussed in the thesis, these transitions have been attributed to changes in the magnetic structure or spin reorientation transitions. The sensitivity of the μSR technique to such transitions is well-evidenced here while neutron scattering measurements on some of the compounds studied did not detect these transitions. In addition to the compounds studied in this thesis, in Figure 8.1, old μSR data [1] on Nd$_2$CuO$_4$ and Eu$_2$CuO$_4$ are shown. The data had been reanalyzed with the same analytic functions used for the other T'-cuprates. It is obvious that all compounds show a similar series of transitions even though details of the magnetic behaviors are slightly different.

The investigations on the novel and metastable T'-La$_2$CuO$_4$ are of striking significance in this work, mainly because our findings in this system had surprisingly revealed transitions even with the nonmagnetic ion La^{3+}. This undoubtedly challenged the common belief that the magnetic interaction between the Cu and the RE system is responsible for e.g. the spin reorientations observed in T'-Nd$_2$CuO$_4$ and thus, also questioned if the observed complex magnetic behavior is generic to all BCT cuprates independent of the magnetic state of the RE ion, and if the magnetic transitions might have been overlooked in some compounds e.g. due to the limitations of simple neutron diffraction experiments. Moreover, T'-La$_2$CuO$_4$ revealed a strongly-reduced Néel temperature compared to the orthorhombic T-La$_2$CuO$_4$ and to other T'-RE$_2$CuO$_4$ cuprates such as T'-Nd$_2$CuO$_4$ and T'-Pr$_2$CuO$_4$. This reduction can be traced back to a ten times decrease in the interlayer coupling possibly due to the missing polarizable lanthanide ion in T'-La$_2$CuO$_4$. This low interlayer coupling makes our newly synthesized compound to be the best realization of a cuprate 2D magnet. This finding addressed the influence of the magnetic rare-earth ion on the interlayer magnetic coupling and dynamics in the system and led to the synthesis of rare-earth substituted compounds,

---

[1] The data stem from early measurements of our collaborator, H.-H. Klauss, from the TU Dresden, Germany.

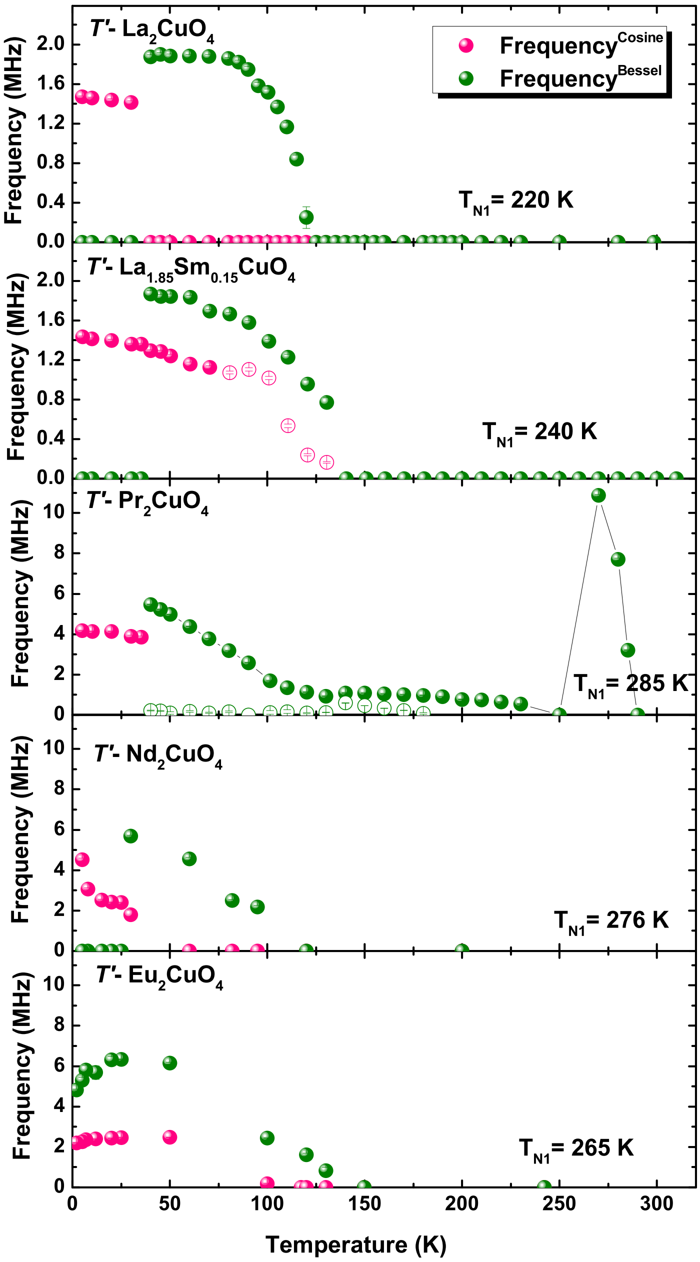

Figure 8.1: Temperature dependence of the muon precession frequency for all the as-grown T'-RE$_2$CuO$_4$ (RE= La, Pr, Nd, Eu) and La$_{1.85}$Sm$_{0.15}$CuO$_4$.

e.g. T'-$La_{1.85}Sm_{0.15}CuO_4$, which was found to have an increased T_N. Therefore, the results on T'-$La_{1.85}Sm_{0.15}CuO_4$ confirmed our notion that the magnetic coupling in the *c*-direction is enhanced with the substitution of a magnetically polarizable Sm ion in the T'-La_2CuO_4 which, loosely speaking, acts as a sort of magnetic glue between the layers. More formally, the magnetic ions strengthen the so-called pseudo-dipolar interactions in the system.

In order to draw a physical picture for the observed rich magnetic transitions, magnetic structure models for the T'-cuprates were defined. A crucial part on the thorough analysis of a μSR data is the determination of the muon site. For the T'-La_2CuO_4, the muon site was determined with the most probable position located along the O(2)-O(2) bond, 1.10 Å far from one oxygen in the LaO plane. Dipole field calculations have been implemented to model the different magnetic structures which all are characterized by an antiferromagnetic coupling of the Cu moments in the plane and different orientations of the spins within the planes. In addition, the models differ in the relative orientation of neighboring CuO_2 layers. Several plausible scenarios at three characteristic temperature regimes were tested and presented to elucidate the magnetic structure at the highest temperature regime between 220 K and 115 K where only a quasi-static order with slow (MHz) fluctuations is observed, a static regime with a broad asymmetric field distribution at the muon site between 115 K and 40 K, and a low temperature regime wherein an abrupt change to a narrow and symmetric field distribution is observed. The magnetic structure at intermediate temperatures could be identified to possess a distribution of symmetry-allowed relative spin orientations in adjacent CuO_2 planes. This observation indicates that the coupling between the layers is actually very weak and also additional anisotropies within the CuO_2 plane which determine the spin orientation within the plane are small compared to the thermal energy at these temperatures. At low-temperatures, our magnetic dipole calculations prove that T'-La_2CuO_4 *locks-in* to a well defined relative orientation of neighboring planes namely into a well defined noncollinear magnetic structure. This is again a remarkable result, since it was initially thought that in the absence of a magnetic RE ion, the system would adopt a collinear magnetic structure due to zero-point fluctuations of the spins leading to an order-by-disorder effect.

Experimental results on the T'-Pr_2CuO_4 and also the T'-$La_{1.85}Sm_{0.15}CuO_4$ demonstrated the important role of the oxygen content and oxygen site occupation on the magnetism. The observed differences between an as-grown sample and a reduced sample revealed that the annealing conditions can impose which oxygen site is vacated. The slight structural modifications induced by the annealing conditions have different effects on the static and dynamic properties of the Cu magnetism. Nevertheless, both as-grown and reduced samples possessed rich magnetic transitions as the other investigated compounds, with notable differences imposed by the reduction annealing conditions. The observation of a series of magnetic transitions in the T'-Pr_2CuO_4 is very astonishing since indications for spin reorientation transitions had not been accounted to this compound before. Again, it was believed that since Pr has a nonmagnetic ground state in the crystal field and has only other slightly polarizable low lying crystal field levels, it could not engage spin reorientation transitions. On the contrary, in this thesis it is shown that such a behavior is generic to the whole BCT cuprate family independent of the presence of a magnetic RE ion.

For the T'-Pr_2CuO_4, three different reduction annealing conditions were implemented. The sample annealed at 800 °C in vacuum demonstrated a virtually identical behavior as the as-grown samples while a slightly higher annealing at 900 °C resulted to a more magnetically disordered system. The as-grown sample displayed a striking feature at high-temperatures with the presence of fast ZF-μSR oscillations signifying a well ordered magnetic state, whereas the 900 °C-reduced sample did not show this behavior at the same temperature region. This led to the conclusion that a relatively high annealing temperature can drastically disorder the system. Our neutron scattering measurements show slightly different structural modifications for the different annealing conditions. Astonishingly, already the low-temperature annealing leads to the removal of the defect apical oxygen O(3) from the structure which had practically no effect on the magnetism in contrast to the general belief that it is exactly this defect site which is responsible for the appearance of magnetism and suppression of superconductivity in the electron-doped compounds. On the other hand, the high temperature annealing removes O(2) oxygen from the charge reservoir layer and creates magnetic disorder. Furthermore, the as-grown sample also displayed analogous behavior as the T'-LCO specifically at the intermediate temperature region manifested by a broad field distribution and the *lock-in* transition at the low-temperature region. On the contrary, the high-temperature reduced sample demonstrated an even more complex behavior at the said temperature regions probably due to the increased disorder which finally also leads to a different magnetic ground state as evidenced by the observation of two μSR frequencies instead of the one observed in as-grown and low temperature annealed samples.

The dynamic properties of T'-Pr_2CuO_4 have been studied by longitudinal field μSR as a function of temperature and for samples with different annealing conditions. Again, it is shown that the removal of the apical oxygen does not alter the magnetic dynamics present in the system, while the high-temperature annealed samples with removed O(2) ions showed a slightly different dynamic behavior. In both cases, the appearance of two peaks in the dynamic relaxation rate as a function of temperature further reinforced the evidence of the presence of distinct phase transitions in T'-Pr_2CuO_4. The strong change of the internal field distribution can be attributed to spin reorientation transitions between qualitatively very different magnetic structures. Plausible magnetic configurations for the different temperature regimes are discussed in the thesis. Astonishingly, very similar magnetic structures as compared to T'-La$_2$CuO$_4$ are deduced for T'-Pr$_2$CuO$_4$ while distinct differences are observed at high temperatures. The most remarkable difference occurs in a very narrow temperature interval for the as-grown T'-Pr$_2$CuO$_4$ sample where a canting of the Cu magnetic moments out of the CuO$_2$ plane is observed.

To wrap up the effect of the reduction annealing, it was observed that the T_N in T'-La$_{1.85}$Sm$_{0.15}$CuO$_4$ had increased after the reduction process. This is attributed to the healing out of the Cu sites and redistribution of oxygen that consequently strengthened the magnetism. It has to be noted that the annealing condition had to be delicately done at a temperature that the system would not transform into the T-phase, e.g. at 550 °C. In the case of the T'-Pr$_2$CuO$_4$, a higher annealing condition caused the removal of the O(2) which created magnetic disorder on the system. A slightly lower annealing temperature only removed O(3) but did not cause any strong effect on the magnetism of the system in contrast to general opinion that this apical defect site in T'-structures drives magnetism that obstructs the emergence of superconductivity.

Our investigations show that it is of paramount importance that systematic investigations are performed with an as large as possible number of suitable magnetic and structural experimental probes on the very same samples. Only this allows to draw correct conclusions on the interplay of magnetic and structural degrees of freedom in these systems. In this sense, it was of special advantage that in the present study, experimental techniques like NMR, μSR and neutron scattering, all possessing different time windows and sensitivities to different magnetic structures, had been used.

As an outlook, it would be interesting to extend the investigations to single crystal samples as these have the edge of not only probing the magnitude of the fields but also the field directions with the μSR technique. In addition, it would also be worthwhile to revisit other parent compounds of RE$_2$CuO$_4$, e.g. RE= Nd, Eu, Sm, Gd, and implement the same approach as was done in this work. Also, the completion of the phase diagram would be incessantly important, thus, it is highly recommended to extend our experimental approach to the superconducting systems especially on electron-doped bulk powders of T'-La$_{2-x}$Ce$_x$CuO$_4$ which would allow for the first time to compare these electron-doped compounds with their hole-doped counterparts T-La$_{2-x}$Sr$_x$CuO$_4$.

9 Appendix

9.1 Thermal Neutron Scattering Fullprof Refinement on T'-La$_2$CuO$_4$

The following is an example of a pcr code for the Fullprof software package used in the refinement of the neutron data from HRPT diffractometer, PSI.

```
0*COMM
! Current global Chi2 (Bragg contrib.) =      2.571
NPATT      2       1 1 <- Flags for patterns (1:refined, 0: excluded)
W_PAT   0.500 0.500
!Nph Dum Ias Nre Cry Opt Aut
   2   1   1   0   0   0   1
!Job Npr Nba Nex Nsc Nor Iwg Ilo Res Ste Uni Cor Anm Int
   1   5  -4   2   0   0   0   0   0   0   0   0   0   0  !-> Patt#:
1
   1   5  -4   2   0   0   0   0   0   0   0   0   0   0  !-> Patt#:
2
!
!File names of data(patterns) files
La2CuO4_HI_1p494_T=300_K_.dat
La2CuO4_HI_1p1545_T=300_K.dat
!
!Mat Pcr NLI Rpa Sym Sho
   1   1   0  -1   1   0
!Ipr Ppl Ioc Ls1 Ls2 Ls3 Prf Ins Hkl Fou Ana
   1   0   1   0   4   0   3   8   0   1   1  !-> Patt#: 1
   1   0   1   0   4   0   3   8   0   1   1  !-> Patt#: 2
!
! Lambda1  Lambda2    Ratio    Bkpos    Wdt    Cthm     muR   AsyLim
Rpolarz  2nd-muR -> Patt# 1
 1.494000 0.000000  0.00000   70.000  6.0000  0.0000  0.0000   30.00
0.0000  0.0000
!
! Lambda1  Lambda2    Ratio    Bkpos    Wdt    Cthm     muR   AsyLim
Rpolarz  2nd-muR -> Patt# 2
 1.154344 1.154344  0.00000   70.000  6.0000  0.0000  0.0000   30.00
0.0000  0.0000
!
!NCY  Eps  R_at  R_an  R_pr  R_gl
 10  0.05  0.80  0.80  0.80  0.50
!     Thmin        Step        Thmax     PSD    Sent0  -> Patt#: 1
     3.8500   0.050000   164.8000   0.000   0.000
!     Thmin        Step        Thmax     PSD    Sent0  -> Patt#: 2
     3.8500   0.050000   164.8000   0.000   0.000
!
! Excluded regions (LowT  HighT) for Pattern#  1
        0.00        6.00
      163.35      180.00
!
! Excluded regions (LowT  HighT) for Pattern#  2
        0.00        6.00
      163.35      180.00
!
!
      71    !Number of refined parameters
!
!  Zero    Code    SyCos    Code   SySin    Code  Lambda     Code
MORE ->Patt# 1
  0.00190   31.0  0.08556  311.0  0.00000    0.0 0.000000    0.00   0
!
!   Background coefficients/codes  for Pattern#  1  (Fourier cosine
series, up to 18 coefficients)
    1978.957     798.127    -148.491     238.169    -239.006
214.879
       21.00       51.00       41.00       71.00       81.00
91.00
    -191.970     188.040    -138.779     163.150    -102.032
96.993
      111.00      121.00      131.00      141.00      151.00
161.00
     -81.537      64.463     -49.142      47.974     -20.873
22.422
```

```
      221.00      231.00      241.00      251.00      211.00
201.00
!
!  Zero    Code    SyCos    Code   SySin    Code  Lambda     Code
MORE ->Patt# 2
  0.00740  601.0  0.00000    0.0  0.00000    0.0 1.154344  611.00   0
!
!   Background coefficients/codes  for Pattern#  2  (Fourier cosine
series, up to 18 coefficients)
    1780.798     696.990    -104.864     249.624    -232.303
209.018
      381.00      391.00      401.00      411.00      421.00
431.00
    -207.370     175.333    -161.348     158.529    -126.205
130.412
      441.00      451.00      461.00      471.00      481.00
491.00
     -80.265      76.388     -48.549      38.228     -33.340
8.957
      501.00      511.00      521.00      531.00      541.00
551.00
!--------------------------------------------------------------------
-----------
!  Data for PHASE number:   1  ==> Current R_Bragg for Pattern#  1:
1.90
!  Data for PHASE number:   1  ==> Current R_Bragg for Pattern#  2:
2.56
!--------------------------------------------------------------------
-----------
Cu1 Nd2 O3.97
!
!Nat Dis Ang Jbt Isy Str Furth        ATZ     Nvk More
   5   0   0   0   0   0   0     207257.6406   0   1
!Jvi Jdi Hel Sol Mom Ter  N_Domains
   0   3   0   0   0   0     0
!Contributions (0/1) of this phase to the  2 patterns
 1 1
!Irf Npr Jtyp  Nsp_Ref Ph_Shift for Pattern#  1
   0   7    1      0      0
! Pr1    Pr2    Pr3   Brind.   Rmua    Rmub    Rmuc     for Pattern#  1
  0.000  0.000  1.000  1.000  0.000  0.000  0.000
!Irf Npr Jtyp  Nsp_Ref Ph_Shift for Pattern#  2
   0   7    1      0      0
! Pr1    Pr2    Pr3   Brind.   Rmua    Rmub    Rmuc     for Pattern#  2
  0.000  0.000  1.000  1.000  0.000  0.000  0.000
!
! Max_dst(dist) (angles)  Bond-Valence Calc.
      3.5000    180.0000         NON
I 4/m m m                <--Space group symbol
!Atom   Typ       X         Y         Z     Biso       Occ      In Fin
N_t Spc /Codes
La1    La      0.00000  0.00000  0.35195  0.47154   2.00000   0   0
0    0
                  0.00      0.00     61.00    281.00        0.00
Cu1    Cu      0.00000  0.00000  0.00000  0.51658   1.00000   0   0
0    0
                  0.00      0.00      0.00    291.00        0.00
O1     O       0.50000  0.00000  0.00000  0.72721   2.00000   0   0
0    0
                  0.00      0.00      0.00    301.00        0.00
O2     O       0.00000  0.50000  0.25000  0.56309   1.93254   0   0
0    0
                  0.00      0.00      0.00    261.00    321.00
O3     O       0.00000  0.00000  0.13114  0.56309   0.03134   0   0
0    0
                  0.00      0.00    171.00    261.00    331.00
```

```
!-------> Profile Parameters for Pattern #  1
!  Scale        Shape1      Bov      Str1      Str2      Str3
Strain-Model
 0.26013E-01   0.00000   0.00000   0.00000   0.00000   0.00000
0
    11.00000     0.000     0.000     0.000     0.000     0.000
!       U          V          W           X          Y        GauSiz
LorSiz Size-Model
   0.064313  -0.094298   0.158341   0.000000   0.090947   0.000000
0.000000    0
    621.000    631.000    641.000      0.000    651.000      0.000
0.000
!     a          b          c        alpha      beta       gamma
#Cell Info
   4.007078   4.007078  12.532378  90.000000  90.000000  90.000000
  341.00000  341.00000  271.00000    0.00000    0.00000    0.00000
!  Pref1    Pref2      Asy1     Asy2     Asy3     Asy4      S_L
D_L
  0.00000  0.00000 -0.05311  0.00461  0.00000  0.00000  0.04000
0.02000
     0.00     0.00   181.00   191.00     0.00     0.00     0.00
0.00
!-------> Profile Parameters for Pattern #  2
!  Scale        Shape1      Bov      Str1      Str2      Str3
Strain-Model
 0.10955E-01   0.00000   0.00000   0.00000   0.00000   0.00000
0
   561.00000     0.000     0.000     0.000     0.000     0.000
!       U          V          W           X          Y        GauSiz
LorSiz Size-Model
   0.113631  -0.256318   0.257954   0.000000   0.089080   0.000000
0.000000    0
    661.000    671.000    681.000      0.000    691.000      0.000
0.000
!     a          b          c        alpha      beta       gamma
#Cell Info
   4.007078   4.007078  12.532378  90.000000  90.000000  90.000000
  341.00000  341.00000  271.00000    0.00000    0.00000    0.00000
!  Pref1    Pref2      Asy1     Asy2     Asy3     Asy4      S_L
D_L
  0.00000  0.00000 -0.03650  0.01163  0.00000  0.00000  0.04000
0.02000
     0.00     0.00   571.00   581.00     0.00     0.00     0.00
0.00
!---------------------------------------------------------------------
-----------
!  Data for PHASE number:   2  ==> Current R_Bragg for Pattern#  1:
6.54
!  Data for PHASE number:   2  ==> Current R_Bragg for Pattern#  2:
5.58
!---------------------------------------------------------------------
-----------
H3 La1 O3
!
!Nat Dis Ang Jbt Isy Str Furth        ATZ     Nvk More
   3   0   0   0   0   0   0       1468.5364   0   0
!Contributions (0/1) of this phase to the  2 patterns
 1 1
!Irf Npr Jtyp  Nsp_Ref Ph_Shift for Pattern#  1
   0   7    1      0        0
! Pr1    Pr2    Pr3   Brind.   Rmua    Rmub    Rmuc     for Pattern#  1
  0.000  0.000  1.000  1.000  0.000  0.000  0.000
!Irf Npr Jtyp  Nsp_Ref Ph_Shift for Pattern#  2
   0   7    1      0        0
! Pr1    Pr2    Pr3   Brind.   Rmua    Rmub    Rmuc     for Pattern#  2
  0.000  0.000  1.000  1.000  0.000  0.000  0.000
```

```
!
P 63/m                   <--Space group symbol
!Atom   Typ       X        Y        Z     Biso       Occ     In Fin
N_t Spc /Codes
La1    La      0.33333  0.66667  0.25000  1.00000   0.33333   0   0
0    0
                  0.00     0.00     0.00     0.00      0.00
O1     O       0.39157  0.07831  0.25000  1.00000   0.87540   0   0
0    0
                  0.00     0.00     0.00     0.00      0.00
H1     H       0.28146  0.14548  0.25000  1.00000   0.87540   0   0
0    0
                  0.00     0.00     0.00     0.00      0.00
!-------> Profile Parameters for Pattern #  1
!  Scale        Shape1      Bov      Str1      Str2      Str3
Strain-Model
 0.40185       0.00000  -0.24632   0.00000   0.00000   0.00000
0
   371.00000     0.000   101.000     0.000     0.000     0.000
!       U         V          W           X          Y        GauSiz
LorSiz Size-Model
   2.742541  -0.103117   0.167992   0.000000   0.089387   0.000000
0.000000    0
    701.000      0.000      0.000      0.000      0.000      0.000
0.000
!     a          b          c         alpha      beta       gamma
#Cell Info
   6.535812   6.535812  3.849893   90.000000  90.000000 120.000000
  361.00000  361.00000  351.00000    0.00000    0.00000  361.00000
!  Pref1    Pref2      Asy1     Asy2     Asy3     Asy4      S_L
D_L
  0.00000  0.00000  0.00499  0.01311  0.00000  0.00000  0.04000
0.02000
     0.00     0.00     0.00     0.00     0.00     0.00     0.00
0.00
!-------> Profile Parameters for Pattern #  2
!  Scale        Shape1      Bov      Str1      Str2      Str3
Strain-Model
 0.16786       0.00000  -0.24632   0.00000   0.00000   0.00000
0
   591.00000     0.000   101.000     0.000     0.000     0.000
!       U         V          W           X          Y        GauSiz
LorSiz Size-Model
   3.541487  -0.237959   0.226245   0.000000   0.078823   0.000000
0.000000    0
    711.000      0.000      0.000      0.000      0.000      0.000
0.000
!     a          b          c         alpha      beta       gamma
#Cell Info
   6.535812   6.535812  3.849893   90.000000  90.000000 120.000000
  361.00000  361.00000  351.00000    0.00000    0.00000  361.00000
!  Pref1    Pref2      Asy1     Asy2     Asy3     Asy4      S_L
D_L
  0.00000  0.00000  0.00499  0.01311  0.00000  0.00000  0.04000
0.02000
     0.00     0.00     0.00     0.00     0.00     0.00     0.00
0.00
!  2Th1/TOF1    2Th2/TOF2  Pattern # 1
       6.000     163.350       1
!  2Th1/TOF1    2Th2/TOF2  Pattern # 2
       6.000     163.350       1
```

9.2 Thermal Neutron Scattering Fullprof Refinement on T'-Pr_2CuO_4

The following is an example of a pcr code for the Fullprof software package used in the refinement of the neutron data from HRPT diffractometer, PSI.

```
0*COMM
! Current global Chi2 (Bragg contrib.) =      3.991
NPATT      2       1 1 <- Flags for patterns (1:refined, 0: excluded)
W_PAT   0.500 0.500
!Nph Dum Ias Nre Cry Opt Aut
   1   1   1   0   0   0   1
!Job Npr Nba Nex Nsc Nor Iwg Ilo Res Ste Uni Cor Anm Int
   1   5  -4   2   0   0   0   0   0   0   0   0   0   0  !-> Patt#: 1
   1   5  -4   2   0   0   0   0   0   0   0   0   0   0  !-> Patt#: 2
!File names of data(patterns) files
gwen_Pr2CuO4_RH158a_HI_1p494_T=310_K.dat
gwen_Pr2CuO4_RH158a_HI_1p1545_T=310_K.dat
!
!Mat Pcr NLI Rpa Sym Sho
   1   1   0  -1   1   0
!Ipr Ppl Ioc Ls1 Ls2 Ls3 Prf Ins Hkl Fou Ana
   1   0   1   0   4   0   3   8   0   1   1  !-> Patt#: 1
   1   0   1   0   4   0   3   8   0   1   1  !-> Patt#: 2
!
! lambda1 Lambda2    Ratio    Bkpos    Wdt    Cthm     muR   AsyLim
Rpolarz ->Patt# 1
 1.494000 0.000000  0.0000   70.000  6.0000  0.0000  0.0000   30.00
0.0000
!
! lambda1 Lambda2    Ratio    Bkpos    Wdt    Cthm     muR   AsyLim
Rpolarz ->Patt# 2
 1.154849 1.154849  0.0000   70.000  6.0000  0.0000  0.0000   30.00
0.0000
!
!NCY  Eps  R_at  R_an  R_pr  R_gl
20  0.05  0.80  0.80  0.80  0.50
!     Thmin       Step       Thmax    PSD    Sent0  -> Patt#: 1
     3.8500   0.050000   164.8000   0.000   0.000
!     Thmin       Step       Thmax    PSD    Sent0  -> Patt#: 2
     3.8500   0.050000   164.8000   0.000   0.000
!
! Excluded regions (LowT  HighT) for Pattern#  1
        0.00        6.00
      163.35      180.00
!
! Excluded regions (LowT  HighT) for Pattern#  2
        0.00        6.00
      163.35      180.00
!
!
      63    !Number of refined parameters
!
!  Zero    Code    SyCos    Code   SySin    Code  Lambda     Code MORE
->Patt# 1
 -0.04042  541.0  0.00000    0.0  0.00000    0.0 0.000000    0.00   0
!  Background coefficients/codes  for Pattern#  1
  420.92      213.46     -152.44       141.73      -136.99       127.72
      21.000       51.000       41.000       71.000       81.000       91.000
 -118.81      106.83      -91.830       88.108      -67.812       60.190
     111.000      121.000      131.000      141.000      151.000      161.000
 -46.802      36.190      -23.756       20.359      -13.747       3.2184
     221.000      231.000      241.000      251.000      211.000      201.000
!
!  Zero    Code    SyCos    Code   SySin    Code  Lambda     Code MORE
->Patt# 2
 -0.10225  551.0  0.00000    0.0  0.00000    0.0 1.154849   31.00   0
```

```
!   Background coefficients/codes  for Pattern#  2
  1032.6     -120.16      175.92     -162.86      163.58     -150.39
     381.000     391.000     401.000     411.000     421.000     431.000
  125.84     -132.74      119.33     -85.835      77.689     -62.456
     441.000     451.000     461.000     471.000     481.000     491.000
  61.128     -44.882      38.713     -25.411      8.5372     -14.008
     501.000     511.000     521.000     531.000     371.000     361.000
!------------------------------------------------------------------------
--------
!  Data for PHASE number:   1  ==> Current R_Bragg for Pattern#  1:
2.91
!  Data for PHASE number:   1  ==> Current R_Bragg for Pattern#  2:
3.23
!------------------------------------------------------------------------
--------
Cu1 Nd2 O3.97
!
!Nat Dis Ang Jbt Isy Str Furth       ATZ     Nvk More
   5   0   0   0   0   0   0     207257.6406   0   1
!Jvi Jdi Hel Sol Mom Ter  N_Domains
   0   3   0   0   0   0      0
!Contributions (0/1) of this phase to the  2 patterns
 1 1
!Irf Npr Jtyp  Nsp_Ref Ph_Shift for Pattern#  1
   0   7   1      0      0
! Pr1    Pr2    Pr3   Brind.   Rmua   Rmub   Rmuc     for Pattern#  1
  0.000  0.000  1.000  1.000  0.000  0.000  0.000
!Irf Npr Jtyp  Nsp_Ref Ph_Shift for Pattern#  2
   0   7   1      0      0
! Pr1    Pr2    Pr3   Brind.   Rmua   Rmub   Rmuc     for Pattern#  2
  0.000  0.000  1.000  1.000  0.000  0.000  0.000
!
! Max_dst(dist) (angles)  Bond-Valence Calc.
      3.5000    180.0000        NON
I 4/m m m                <--Space group symbol
!Atom   Typ       X        Y        Z     Biso       Occ     In Fin N_t
Spc /Codes
Pr1    PR      0.00000  0.00000  0.35171  0.39796   2.00000   0   0   0
0
                  0.00     0.00    61.00   281.00      0.00
Cu1    Cu      0.00000  0.00000  0.00000  0.38591   1.00000   0   0   0
0
                  0.00     0.00     0.00   291.00      0.00
O1     O       0.50000  0.00000  0.00000  0.63052   2.00000   0   0   0
0
                  0.00     0.00     0.00   301.00      0.00
O2     O       0.00000  0.50000  0.25000  0.52457   2.01429   0   0   0
0
                  0.00     0.00     0.00   261.00    631.00
O3     O       0.00000  0.00000  0.20586  0.52457   0.00703   0   0   0
0
                  0.00     0.00   171.00   261.00    331.00
!-------> Profile Parameters for Pattern #  1
!  Scale        Shape1      Bov      Str1      Str2      Str3   Strain-
Model
 0.23193E-01   0.00000   0.00000   0.00000   0.00000   0.00000       0
    11.00000     0.000     0.000     0.000     0.000     0.000
!       U          V          W           X          Y        GauSiz
LorSiz Size-Model
   0.053748  -0.120651   0.156943   0.000000   0.063764   0.000000
0.000000    0
```

```
    561.000    591.000    601.000      0.000    571.000      0.000
0.000
!     a          b          c        alpha      beta       gamma
#Cell Info
   3.960164   3.960164  12.243764  90.000000  90.000000  90.000000
  341.00000  341.00000  271.00000    0.00000    0.00000    0.00000
!  Pref1    Pref2      Asy1      Asy2      Asy3      Asy4      S_L      D_L
  0.00000  0.00000 -0.04924  0.00799  0.00000  0.00000  0.04000  0.02000
     0.00     0.00   181.00   191.00     0.00     0.00     0.00     0.00
!-------> Profile Parameters for Pattern #  2
!  Scale        Shape1      Bov      Str1      Str2      Str3   Strain-
Model
 0.18397E-01   0.00000   0.00000   0.00000   0.00000   0.00000       0
   351.00000     0.000     0.000     0.000     0.000     0.000
!       U          V          W          X          Y        GauSiz
LorSiz Size-Model
   0.105024  -0.276815   0.250480   0.000000   0.066512   0.000000
0.000000    0
    581.000    611.000    621.000      0.000    321.000      0.000
0.000
!     a          b          c        alpha      beta       gamma
#Cell Info
   3.960164   3.960164  12.243764  90.000000  90.000000  90.000000
  341.00000  341.00000  271.00000    0.00000    0.00000    0.00000
!  Pref1    Pref2      Asy1      Asy2      Asy3      Asy4      S_L      D_L
  0.00000  0.00000 -0.01903  0.01489  0.00000  0.00000  0.04000  0.02000
     0.00     0.00   311.00   101.00     0.00     0.00     0.00     0.00
!  2Th1/TOF1    2Th2/TOF2  Pattern # 1
      6.000     163.350       1
!  2Th1/TOF1    2Th2/TOF2  Pattern # 2
      6.000     163.350       1
```

9.3 Cold Neutron Scattering Fullprof Refinement on T'-$\mathrm{Pr_2CuO_4}$

The following is an example of a pcr code for the Fullprof software package used in the refinement of the neutron data from DMC diffractometer, PSI.

```
COMMPr2CuO4 2 DMC
! Current global Chi2 (Bragg contrib.) =      27.58
! Files => DAT-file: 1p6K-2,  PCR-file: pco2
!Job Npr Nph Nba Nex Nsc Nor Dum Iwg Ilo Ias Res Ste Nre Cry Uni Cor Opt
Aut
   1   4   2  57   1   0   0   1   0   0   1   0   0   0   0   0   0   0
0
!
!Ipr Ppl Ioc Mat Pcr Ls1 Ls2 Ls3 NLI Prf Ins Rpa Sym Hkl Fou Sho Ana
   1   0   1   1   2   0   4   0   0   3   8   1   1   0   1   0   1
!
! lambda1 Lambda2    Ratio    Bkpos    Wdt    Cthm     muR   AsyLim
Rpolarz ->Patt# 1
 4.207000 4.207000  1.0000   70.000  3.0000  0.0000  0.0000   50.00
0.0000
!
!NCY  Eps  R_at  R_an  R_pr  R_gl     Thmin       Step       Thmax
PSD    Sent0
 40  0.05  0.80  0.80  0.80  0.80      5.0000    0.100000   125.7000
0.000   0.000
!
!2Theta/TOF/E(Kev)   Background  for Pattern#  1
        5.090    25662.340        0.000
        5.984    22209.791        0.000
        7.267    17222.779        0.000
        8.768    13194.807        0.000
       10.000    10125.875        0.000
       11.046     7824.176        0.000
       12.598     5426.574        0.000
       14.396     3502.499        0.000
       16.049     2255.745        0.000
       17.667     1488.513        0.000
       19.776      961.040        0.000
       22.695      721.280        0.000
       24.903      577.424        0.000
       26.861      577.424        0.000
       29.375      577.424        0.000
       31.773      625.375        91.000
       34.422      529.471        101.000
       37.307      577.424        111.000
       39.591      625.375        121.000
       40.991      673.328        131.000
       42.189      529.471        141.000
       43.741      577.424        151.000
       46.359      577.424        161.000
       48.282      529.471        171.000
       49.750      529.471        181.000
       51.049      529.471        0.000
       52.587      529.471        0.000
       54.325      529.471        191.000
       56.400      529.471        201.000
       59.016      529.471        211.000
       60.751      529.471        221.000
       62.979      577.424        231.000
       65.240      625.375        241.000
       67.197      625.375        251.000
       69.233      577.424        261.000
       71.106      577.424        271.000
       73.519      529.471        281.000
       75.729      529.471        291.000
       77.495      577.424        301.000
```

```
       80.178      529.471        311.000
       83.164      577.424        321.000
       85.763      769.231        331.000
       88.773      961.040        341.000
       90.561      721.280        351.000
       92.282      721.280        361.000
       94.290     1248.753        371.000
       99.017      913.088        381.000
      100.856      577.424        391.000
      102.999      625.375        401.000
      105.549      481.519        411.000
      108.654      529.471        421.000
      110.341      625.375        431.000
      113.569      721.280        441.000
      115.847      481.519        451.000
      118.751      577.424        461.000
      122.161      529.471        471.000
      125.520      433.568        481.000
!
! Excluded regions (LowT  HighT) for Pattern#  1
        0.00       30.00
!
!
       48    !Number of refined parameters
!
!  Zero    Code    SyCos    Code   SySin    Code  Lambda     Code MORE
->Patt# 1
 -0.00688   21.0  0.00000    0.0  0.00000    0.0 4.207000    0.00   0
!-----------------------------------------------------------------------
--------
!  Data for PHASE number:   1  ==> Current R_Bragg for Pattern#  1:
4.43
!-----------------------------------------------------------------------
--------
Pr2CuO4
!
!Nat Dis Ang Pr1 Pr2 Pr3 Jbt Irf Isy Str Furth       ATZ    Nvk Npr More
   5   0   0 0.0 0.0 1.0   0   0   0   0   0       1944.600   0   4   0
!
I 4/M M M                <--Space group symbol
!Atom   Typ       X        Y        Z     Biso       Occ     In Fin N_t
Spc /Codes
Pr1    Pr      0.00000  0.00000  0.35171  0.39800   0.12500   0   0   0
0
                  0.00     0.00     0.00     0.00      0.00
Cu1    Cu      0.00000  0.00000  0.00000  0.38600   0.06250   0   0   0
0
                  0.00     0.00     0.00     0.00      0.00
O1     O       0.50000  0.00000  0.00000  0.63100   0.12500   0   0   0
0
                  0.00     0.00     0.00     0.00      0.00
O2     O       0.00000  0.50000  0.25000  0.52500   0.12500   0   0   0
0
                  0.00     0.00     0.00     0.00      0.00
O3     O       0.00000  0.00000  0.20586  0.52500   0.00044   0   0   0
0
                  0.00     0.00     0.00     0.00      0.00
!-------> Profile Parameters for Pattern #  1
!  Scale        Shape1      Bov       Str1      Str2      Str3   Strain-
Model
  635.76       0.00000  0.00000  0.00000  0.00000  0.00000        0
```

```
    11.00000     0.000     0.000     0.000     0.000     0.000
!       U         V          W           X          Y        GauSiz
LorSiz Size-Model
   0.481030  -0.389177   0.265897   0.438100   0.409200   0.000000
0.000000    0
     61.000     71.000     81.000      0.000      0.000      0.000
0.000
!     a          b          c        alpha      beta       gamma
#Cell Info
   3.953548   3.953548  12.199910  90.000000  90.000000  90.000000
   41.00000   41.00000   51.00000    0.00000    0.00000    0.00000
!  Pref1    Pref2      Asy1     Asy2     Asy3     Asy4
  0.00000  0.00000  0.00000  0.00000  0.00000  0.00000
     0.00     0.00     0.00     0.00     0.00     0.00
!Additional shape parameters
   0.00457    0.00   0.00000    0.00          Shape: Shp1 CShp1 & Shp2
CShp2
!-------------------------------------------------------------------
--------
!  Data for PHASE number:   2  ==> Current R_Bragg for Pattern#  1:
32.13
!-------------------------------------------------------------------
--------
phase 2: magnetic comm
!
!Nat Dis Mom Pr1 Pr2 Pr3 Jbt Irf Isy Str Furth       ATZ    Nvk Npr More
   2   0   0 0.0 0.0 1.0   1  -1  -1   0   0       598.070   1   4   0
!
P -1                     <--Space group symbol for hkl generation
!Nsym Cen Laue MagMat
   1   1   1   1
!
SYMM x,y,z
MSYM  U,V,W, 0.0
!
!Atom   Typ  Mag Vek    X      Y      Z       Biso    Occ       Rx
Ry       Rz
!     Ix      Iy      Iz    beta11  beta22  beta33    MagPh
Cu1    MCU2  1  0  0.00000 0.00000 0.00000 0.00000  1.00000   0.362
0.362   0.000
                      0.00    0.00    0.00    0.00     0.00   31.00
31.00    0.00
     0.000   0.000   0.000   0.000   0.000   0.000  0.00000
      0.00    0.00    0.00    0.00    0.00    0.00     0.00
Cu2    MCU2  1  0  0.50000 0.50000 0.50000 0.00000  1.00000  -0.362  -
0.362   0.000
                      0.00    0.00    0.00    0.00     0.00  -31.00  -
31.00    0.00
     0.000   0.000   0.000   0.000   0.000   0.000  0.00000
      0.00    0.00    0.00    0.00    0.00    0.00     0.00
!-------> Profile Parameters for Pattern #  1
!  Scale        Shape1      Bov       Str1      Str2      Str3   Strain-
Model
  635.76       0.00000   0.00000   0.00000   0.00000   0.00000       0
    11.00000     0.000     0.000     0.000     0.000     0.000
!       U         V          W           X          Y        GauSiz
LorSiz Size-Model
   0.481030  -0.389177   0.265897   0.438100   0.409200   0.000000
0.000000    0
     61.000     71.000     81.000      0.000      0.000      0.000
0.000
```

```
!     a          b          c        alpha      beta       gamma
#Cell Info
   3.953548   3.953548  12.199910  90.000000  90.000000  90.000000
   41.00000   41.00000   51.00000    0.00000    0.00000    0.00000
!  Pref1    Pref2      Asy1     Asy2     Asy3     Asy4
  0.00000  0.00000  0.00000  0.00000  0.00000  0.00000
     0.00     0.00     0.00     0.00     0.00     0.00
!Additional shape parameters
   0.00457    0.00   0.00000    0.00           Shape: Shp1 CShp1 & Shp2
CShp2
! Propagation vectors:
   0.5000000   0.5000000   1.0000000          Propagation Vector  1
    0.000000    0.000000    0.000000
!  2Th1/TOF1    2Th2/TOF2  Pattern # 1
      30.000     125.700       1
```

9.4 Additional Neutron Scattering Results on T'-Pr_2CuO_4

9.4.1 As-grown A T'-Pr_2CuO_4

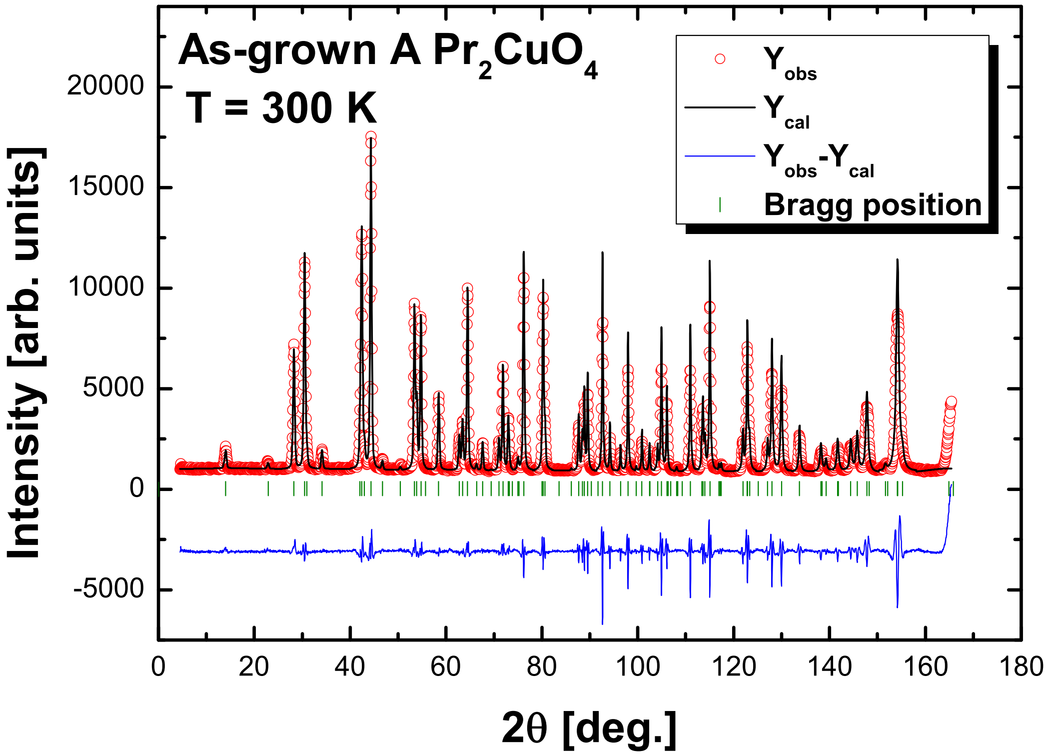

Figure 9.1: Diffraction pattern for sample As-grown A at $T = 300$ K.

Table 9.1: As-grown A: Lattice Constants

a	b	c
3.96005(2)	3.96005(2)	12.23728(10)

Table 9.2: As-grown A: Positional parameters and occupation sites

Name	x	sx	y	sy	z	sz	B	sB	occ.	socc
Pr1	0.00000	(0)	0.00000	(0)	0.35168	(23)	0.435	(45)	2.000	(0)
Cu1	0.00000	(0)	0.00000	(0)	0.00000	(0)	0.237	(36)	1.000	(0)
O1	0.50000	(0)	0.00000	(0)	0.00000	(0)	0.481	(27)	2.000	(0)
O2	0.00000	(0)	0.50000	(0)	0.25000	(0)	0.517	(34)	2.048	(19)
O3	0.00000	(0)	0.00000	(0)	0.59970	(1358)	0.517	(34)	0.029	(12)

9.4.2 Reduced A_{900-Ar} T'-Pr_2CuO_4

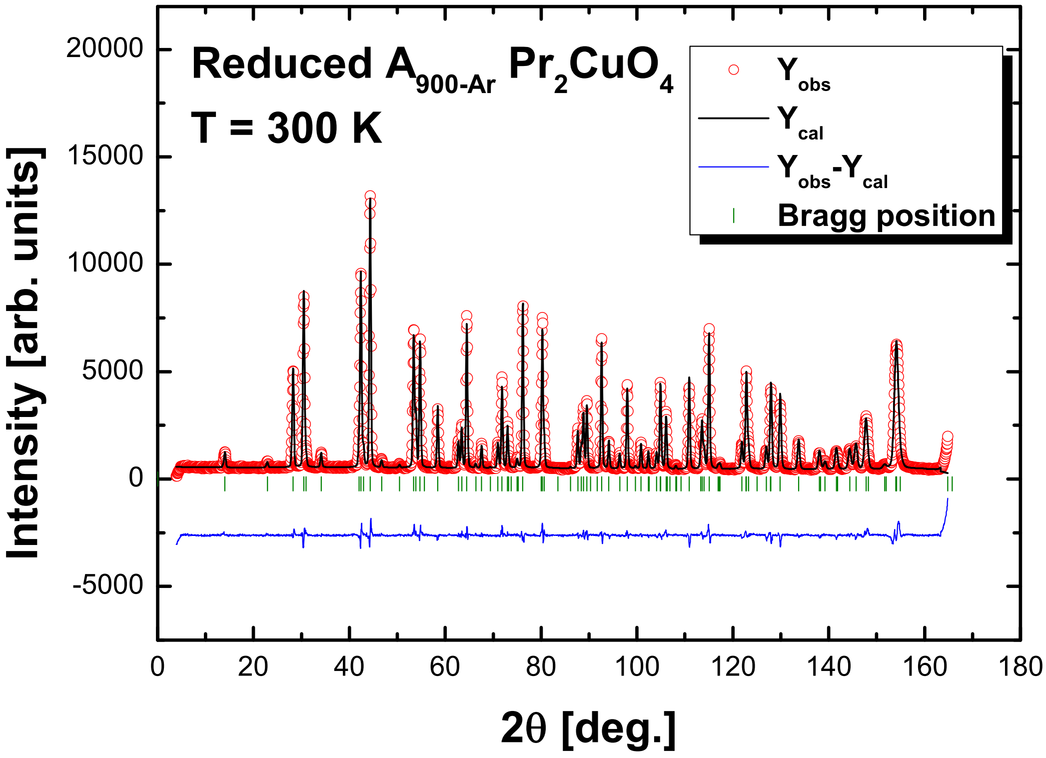

Figure 9.2: Diffraction pattern for sample Reduced A_{900-Ar} at $T = 300$ K.

Table 9.3: Reduced A_{900-Ar}: Lattice Constants

a	b	c
3.96016(1)	3.96016(1)	12.24376(6)

Table 9.4: Reduced A_{900-Ar}: Positional parameters and occupation sites

Name	x	sx	y	sy	z	sz	B	sB	occ.	socc
Pr1	0.00000	(0)	0.00000	(0)	0.35171	(6)	0.398	(14)	2.000	(0)
Cu1	0.00000	(0)	0.00000	(0)	0.00000	(0)	0.386	(10)	1.000	(0)
O1	0.50000	(0)	0.00000	(0)	0.00000	(0)	0.631	(11)	2.000	(0)
O2	0.00000	(0)	0.50000	(0)	0.25000	(0)	0.525	(12)	2.014	(8)
O3	0.00000	(0)	0.00000	(0)	0.20586	(1586)	0.525	(12)	0.007	(4)

9.4.3 Reduced $B_{800-Vac}$ T'-Pr_2CuO_4

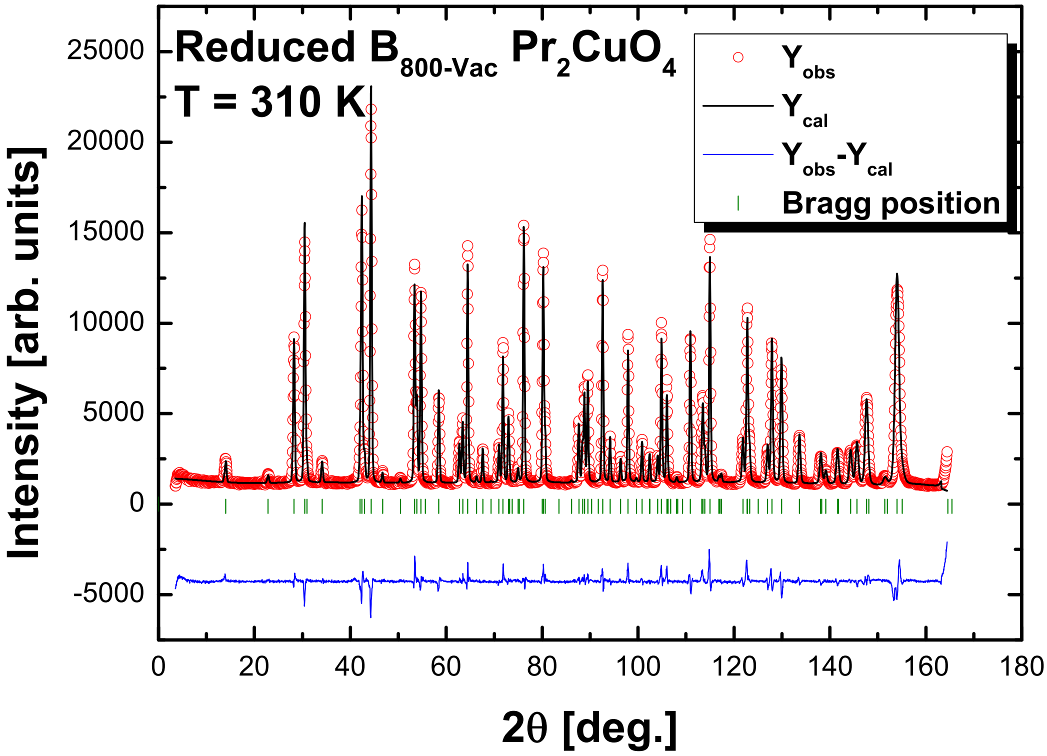

Figure 9.3: Diffraction pattern for sample Reduced $B_{800-Vac}$ at $T = 310$ K.

Table 9.5: Reduced $A_{800-Vac}$: Lattice Constants

a	b	c
3.96157(1)	3.96157(1)	12.24099(6)

Table 9.6: Reduced $B_{800-Vac}$: Positional parameters and occupation sites

Name	x	sx	y	sy	z	sz	B	sB	occ.	socc
Pr1	0.00000	(0)	0.00000	(0)	0.35157	(6)	0.250	(16)	2.000	(0)
Cu1	0.00000	(0)	0.00000	(0)	0.00000	(0)	0.203	(13)	1.000	(0)
O1	0.50000	(0)	0.00000	(0)	0.00000	(0)	0.489	(12)	2.000	(0)
O2	0.00000	(0)	0.50000	(0)	0.25000	(0)	0.346	(13)	2.018	(9)
O3	0.00000	(0)	0.00000	(0)	0.29192	(1487)	0.346	(13)	0.009	(5)

9.4.4 Reduced B_{900-Ar} T'-Pr_2CuO_4

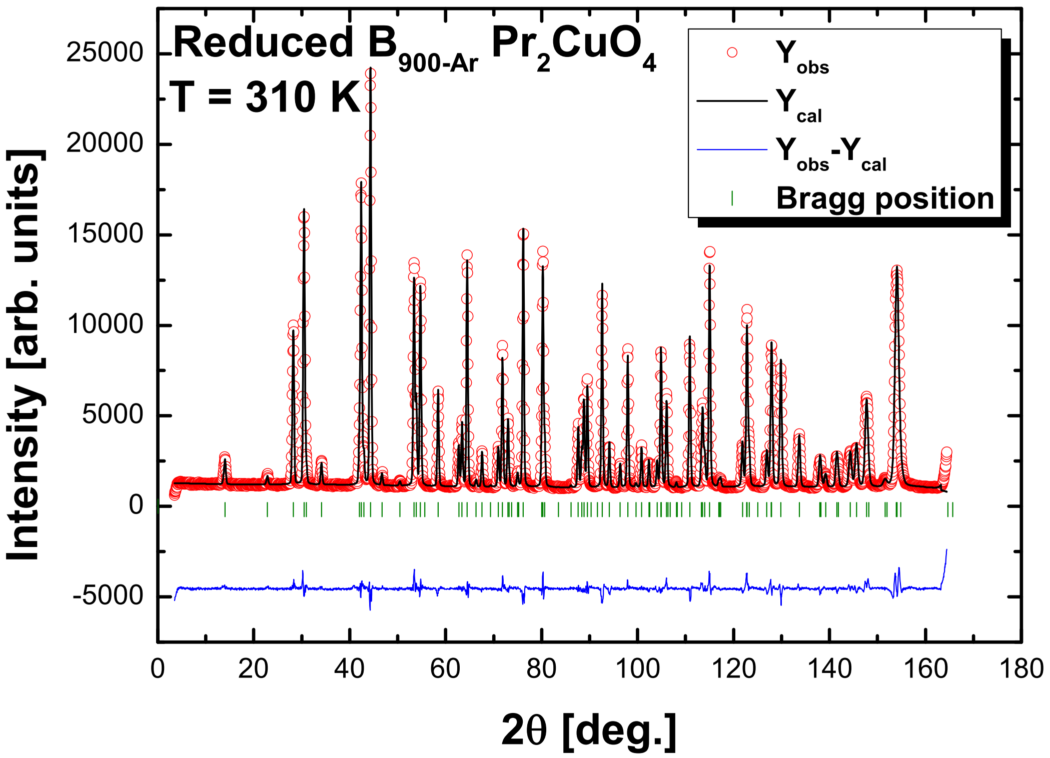

Figure 9.4: Diffraction pattern for sample Reduced B_{900-Ar} at $T = 310$ K.

Table 9.7: Reduced B_{900-Ar}: Lattice Constants

a	b	c
3.96070(1)	3.96070(1)	12.24528(6)

Table 9.8: Reduced B_{900-Ar}: Positional parameters and occupation sites

Name	x	sx	y	sy	z	sz	B	sB	occ.	socc
Pr1	0.00000	(0)	0.00000	(0)	0.35157	(5)	0.321	(14)	2.000	(0)
Cu1	0.00000	(0)	0.00000	(0)	0.00000	(0)	0.283	(10)	1.000	(0)
O1	0.50000	(0)	0.00000	(0)	0.00000	(0)	0.532	(10)	2.000	(0)
O2	0.00000	(0)	0.50000	(0)	0.25000	(0)	0.419	(12)	1.993	(8)
O3	0.00000	(0)	0.00000	(0)	0.20173	(2201)	0.419	(12)	0.004	(4)

Bibliography

[1] A.P. Guimaraes. *From Lodestone to Supermagnets*. Wiley-VCH Verlag GmbH and Co., 2005.

[2] S. Blundell. *Magnetism in Condensed Matter*. Oxford Master Series in Condensed Matter Physics, 2007.

[3] N. Spaldin. *Magnetic Materials Fundamentals and Applications*. Cambridge University Press, Cambridge, United Kingdom, 2011.

[4] H. Kamerlingh Onnes. Further experiments with liquid helium d - on the change of the electrical resistance of pure metals at very low temperatures, etc. the disappearance of the resistance of mercury. *Proc. K. Akad. Amsterdam*, 14:113, 1911.

[5] H. Kamerlingh Onnes. The resistance of pure mercury at helium temperatures. *Comm. Phys. Lab Leiden*, page 120b, 1911.

[6] H. Kamerlingh Onnes. The disappearance of the resistance of mercury. *Comm. Phys. Lab Leiden*, page 122b, 1911.

[7] H. Kamerlingh Onnes. On the sudden change in the rate at which the resistance of mercury disappears. *Comm. Phys. Lab Leiden*, page 124c, 1911.

[8] W. Meissner and R. Ochsenfeld. Short initial announcements. *Naturwissenschaften*, 21:787, 1933.

[9] F. London and H. London. The electromagnetic equations of the supraconductor. *Proc. R. Soc. A*, 149:71, 1935.

[10] V. L. Ginzburg and L. D. Landau. On the theory of superconductivity. *Zh. Eksp. Theor. Fiz.*, 20:1064, 1950.

[11] E. Maxwell. Isotope effect on the superconductivity of mercury. *Phys. Rev.*, 78:477, 1950.

[12] C. A. Reynolds, B. Serin, W. H. Wright, and L. B. Nesbitt. Superconductivity of isotopes of mercury. *Phys. Rev.*, 78:487, 1950.

[13] Leon N. Cooper. Bound electron pairs in a degenerate fermi gas. *Phys. Rev.*, 104:1189–1190, 1956.

[14] J. Bardeen, L. N. Cooper, and J. R. Schrieffer. Microscopic theory of superconductivity. *Phys. Rev.*, 106:162–164, 1957.

[15] J. Bardeen, L. N. Cooper, and J. R. Schrieffer. Theory of superconductivity. *Phys. Rev.*, 108:1175–1204, 1957.

[16] J. G. Bednorz and K.A. Müller. *Z. Phys. B*, 64:189, 1986.

[17] A. Schilling, M. Cantoni, J. D. Guo, and H. R. Ott. *Nature*, 363:56–58, 1993.

[18] A. Schilling, M. Cantoni, J. D. Guo, and H. R. Ott. *Physica C*, 178:183, 1993.

[19] L. Gao, Z. J. Huang, R. L. Meng, J. G. Lin, F. Chen, L. Beauvais, Y. Y. Sun, Y.Y. Xue, and C. W. Chu. *Physica C*, 213:261, 1993.

[20] L. Gao, Y.Y. Xue, F. Chen, Q. Xiong, R. L. Meng, D. Ramirez, C. W. Chu, J. H. Eggert, and H. K. Mao. *Phys. Rev. B*, 50:4260, 1994.

[21] Y. Kamihara, T. Watanabe, M. Hirano, and H. Hosono. *J. Am. Chem. Soc.*, 130:3296, 2008.

[22] W. Malaeb. *Iron-Pnictide and Cuprate High-temperature Superconductors Investigated by Photoemission Spectroscopy*. PhD thesis, University of Tokyo, 2009.

[23] H. Keller, A. Bussmann-Holder, and K. A. Müller. *Mater. Today*, 11:38, 2008.

[24] A. Bussmann-Holder and H. Keller. *Eur. Phys. J. B*, 44:487, 2005.

[25] A. Bussmann-Holder, H. Keller, A. R. Bishop, A. Simon, R. Micnas, and K. A. Müller. *Europhys. Lett.*, 72:423, 2005.

[26] M. A. Kastner, R. J. Birgeneau, G. Shirane, and Y. Endoh. *Rev. Mod. Phys.*, 70:897–928, 1998.

[27] P. K. Mang, O. P. Vajk, A. Arvanitaki, J. W. Lynn, and M. Greven. *Phys. Rev. Lett.*, 93:027002, 2004.

[28] H. Takagi, S. Uchida, and Y. Tokura. *Phys. Rev. Lett.*, 62:1197–1200, 1989.

[29] G. M. Luke, L. P. Le, B. J. Sternlieb, Y. J. Uemura, J. H. Brewer, R. Kadono, R. F. Kiefl, S. R. Kreitzman, T. M. Riseman, M. N. Maple, C. L. Seaman, K. Kakurai, S. Uchida, H. Takagi, Y. Tokura, Y. Hidaka, T. Murakami, J. Gopalakrishnan, A. W. Sleight, and M. A. Subramanian. *Physica C*, 162-164:825, 1989.

[30] G. M. Luke, B. J. Sternlieb, Y. J. Uemura, J. H. Brewer, R. Kadono, R. F. Kiefl, S. R. Kreitzman, T. M. Riseman, J. Gopalakrishnan, A. W. Sleight, M. A. Subramanian, S. Uchida, H. Takagi, and Y. Tokura. *Nature*, 338:49–51, 1989.

[31] G. M. Luke, L. P. Le, B. J. Sternlieb, Y. J. Uemura, J. H. Brewer, R. Kadono, R. F. Kiefl, S. R. Kreitzman, T. M. Riseman, C. E. Stronach, M. R. Davis, S. Uchida, H. Takagi, Y. Tokura, Y. Hidaka, T. Murakami, J. Gopalakrishnan, A. W. Sleight, M. A. Subramanian, E. A. Early, J. T. Markert, M. B. Maple, and C. L. Seaman. *Phys. Rev. B*, 42:7981, 1990.

[32] Y. Dalichaouch, M. C. de Andrade, and M. B. Maple. *Physica C*, 218:309–315, 1993.

[33] I.W. Sumarlin, J.W. Lynn, T. Chattopadhyay, S.N. Barilo, D.I. Zhigunov, and J.L. Peng. *Phys. Rev. B*, 51:5824, 1995.

[34] A. Tsukada, Y. Krockenberger, M. Noda, H. Yamamoto, D. Manske, L. Alff, and M. Naito. *Solid State Commun.*, 133:427–431, 2005.

[35] Y. Tokura, H. Takagi, and S. Uchida. *Nature*, 337:345–347, 1989.

[36] B. Grande, Hk. Müller-Buschbaum, and M. Schweizer. *Z. Anorg. Allg. Chem.*, 428:120, 1977.

[37] Hk. Müller-Buschbaum. *J. Alloys Comp.*, 349:49, 2003.

[38] H. Sawa, S. Suzuki, M. Watanabe, J. Akimitsu, H. Matsubara, H. Watabe, S. Uchida, K. Kokusho, H. Asano, F. Izumi, and E. Takayama-Muromachi. *Nature*, 337:347–348, 1989.

[39] L. Le Dréau. *Phase transitions and oxygen ordering in* $La_2CoO_{4+\delta}$ *and (T,T')-*La_2CuO_4*: single crystal growth and structural studies using synchrotron and neutron diffraction methods*. PhD thesis, Université de Rennes 1, 2011.

[40] H. Müller-Buschbaum and W. Wollsglager. *Z. Anorg. Allg. Chm.*, 414:76–80, 1975.

[41] J. F. Bringley, S. S. Trail, and B. A. Scott. *J. Solid State Chem.*, 86:310–322, 1990.

[42] A. Manthiram and Goodenough J. B. *J. Solid State Chem.*, 87:402–407, 1990.

[43] M. Braden, W. Paulus, A. Cousson, P. Vigoureux, G. Heger, A. Goukassov, P. Bourges, and D. Petitgrand. *Europhys. Lett.*, 25:625, 1994.

[44] R. Hord, H. Luetkens, G. Pascua, A. Buckow, K. Hofmann, Y. Krockenberger, J. Kurian, H. Maeter, H.-H. Klauss, V. Pomjakushin, A. Suter, B. Albert, and L. Alff. *Phys. Rev. B*, 82:180508, 2010.

[45] J.L Luce and A.M. Stacy. *Chem. Mater.*, 9:1508–1515, 1997.

[46] Y. Imai, M. Kato, Y. Takarabe, T. Noji, T. Adachi, and Y. Koike. *Physica C*, 460-462:395–396, 2007.

[47] M. Kato, Y. Imai, T. Kajita, Y. Takarabe, T. Minakawa, K. Nemoto, H. Tezuka, T. Noji, and Y. Koike. *Mater. Sci. Eng. B*, 148:53–57, 2008.

[48] Y. Imai, M. Kato, Y. Takarabe, T. Noji, and Y. Koike. *Chem. Mater.*, 19:3584–3585, 2007.

[49] N. F. Mott. *Rev. Mod. Phys.*, 40:677–683, 1968.

[50] L. F. Mattheiss. *Phys. Rev. Lett.*, 58:1028–1030, 1987.

[51] Eugene Makalu Davenport Motoyama. *Neutron scattering studies of the electron-doped high-temperature superconductor neodymium cerium copper oxide*. PhD thesis, Stanford University, 2009.

[52] Elbio Dagotto. *Rev. Mod. Phys.*, 66:763, 1994.

[53] N. P. Armitage, P. Fournier, and R. L. Greene. *Rev. Mod. Phys.*, 82:2421, 2010.

[54] Tineke Thio, T. R. Thurston, N. W. Preyer, P. J. Picone, M. A. Kastner, H. P. Jenssen, D. R. Gabbe, C. Y. Chen, R. J. Birgeneau, and Amnon Aharony. *Phys. Rev. B*, 38:905, 1988.

[55] M. Greven, J. Birgeneau, Y. Endoh, M.A. Kastner, B. Keimer, M. Matsuda, G. Shirane, and T.R. Thurston. *Phys. Rev. Lett.*, 72:1096, 1994.

[56] Y. Endoh, K. Yamada, R. J. Birgeneau, D. R. Gabbe, H. P. Jenssen, M. A. Kastner, C. J. Peters, P. J. Picone, T. R. Thurston, J. M. Tranquada, G. Shirane, Y. Hidaka, M. Oda, Y. Enomoto, M. Suzuki, and T. Murakami. *Phys. Rev. B*, 37:7443, 1988.

[57] K. Yamada, K. Kakurai, Y. Endoh, T. R. Thurston, M. A. Kastner, R. J. Birgeneau, G. Shirane, Y. Hidaka, and T. Murakami. *Phys. Rev. B*, 40:4557, 1989.

[58] B. Keimer, N. Belk, R. J. Birgeneau, A. Cassanho, C. Y. Chen, M. Greven, M. A. Kastner, A. Aharony, Y. Endoh, R. W. Erwin, and G. Shirane. *Phys. Rev. B*, 46:14034, 1992.

[59] M. Matsuda, K. Yamada, K. Kakurai, H. Kadowaki, T.R. Thurston, Y. Endoh, Y. Hidaka, R. J. Birgeneau, M. A. Kastner, P. M. Gehring, A. H. Moudden, and G. Shirane. *Phys. Rev. B*, 42:10098, 1990.

[60] Ravi Sachidanandam, T. Yildirim, A. B. Harris, Amnon Aharony, and O. Entin-Wohlman. *Phys. Rev. B*, 56:260, 1997.

[61] Sudip Chakravarty, Bertrand I. Halperin, and David R. Nelson. *Phys. Rev. Lett.*, 60:1057, 1988.

[62] Sudip Chakravarty, Bertrand I. Halperin, and David R. Nelson. *Phys. Rev. Lett.*, 39:2344, 1989.

[63] P.C. Hohenberg. *Phys. Rev.*, 158:383, 1967.

[64] N.D. Mermin and H. Wagner. *Phys. Rev. Lett.*, 17:1133, 1966.

[65] T. Einarsson and H. J. Schulz. *Phys. Rev. B*, 51:6151–6154, 1995.

[66] Rajiv R. P. Singh and David A. Huse. *Phys. Rev. B*, 40:7247–7251, 1989.

[67] E.F. Shender and P.C.W. Holdsworth. *Fluctuations and Order: The New Synthesis*. edited by M. Milonas, Springer-Verlag, Berlin, 1995.

[68] J. Villain, R. Bidaux, J.P Carton, and R. Conte. *J.Phys. (Paris)*, 41:1263–1272, 1980.

[69] N.D. MacKenzie and A.P. Young. *J. Phys. C*, 14:3927, 1981.

[70] J.L. Lebowitz, M.K. Phani, and D.F. Styer. *J. Stat. Phys.*, 41:413, 1985.

[71] T. Yildirim, A.B. Harris, O. Entin-Wohlman, and A. Aharony. *Phys. Rev. Lett.*, 72:3710, 1994.

[72] T. Yildirim. *Tr. J. of Physics*, 23:47–76, 1999.

[73] C. L. Henley. *J. Appl. Phys.*, 61:3962, 1987.

[74] C. L. Henley. *Phys. Rev. Lett.*, 62:2056, 1989.

[75] J. M. Kosterlitz and D. J. Thouless. *J. Phys. C*, 6:1181–1203, 1973.

[76] H.-Q. Ding. *Phys. Rev. Lett.*, 68:1927–1930, 1992.

[77] D. Vaknin, S.K. Sinha, C. Stassis, L.L. Miller, and D.C. Johnston. *Phys. Rev. B*, 41:1926, 1990.

[78] B. Grande and Hk. Müller-Buschbaum. *Z. Anorg. Allg. Chem.*, 417:68, 1975.

[79] L.L. Miller, X.L. Wang, S.X. Wang, C. Stassis, and D.C. Johnston. *Phys. Rev. B*, 41:1921, 1990.

[80] M. Corti, F. Borsa, L.L. Miller, and A. Rigamonti. *J. Appl. Phys.*, 75:7146, 1994.

[81] R.J. Birgeneau and G. Shirane. *Physical Properties of High Temperature Superconductors I.* edited by D.M. Ginsberg, World-Scientific, Singapore, 1989.

[82] M. Greven, R.J. Birgeneau, Y. Endoh, M.A. Kastner, M. Matsuda, and G. Shirane. *Z.Phys.B*, 96:465–477, 1995.

[83] D. Petitgrand, S. V. Maleyev, Ph. Bourges, and A. S. Ivanov. *Phys. Rev. B*, 59:1079–1104, 1999.

[84] S. Skanthakumar, J. W. Lynn, J. L. Peng, and Z. Y. Li. *Phys. Rev. B*, 47:6173, 1993.

[85] S. Ghamaty, B. W. Lee, J.T. Markert, E.A. Early, T. Bjørnholm, C.L. Seaman, and M.B. Maple. *Physica C*, 160:217–222, 1989.

[86] P. Vigoureux. PhD thesis, Université Paris XI, 1995.

[87] J. Lynn and S. Skanthakumar. *Handbook on the Physics and Chemistry of Rare Earths*, volume 31. edited by L. E. K. A. Gschneidner, Jr. and M. Maple Elsevier, New York, 2001.

[88] H. Kramers. *Proc. R. Acad. Sci. Amsterdam*, 33:959, 1930.

[89] J. W. Lynn, I. W. Sumarlin, S. Skanthakumar, W-H. Li, R. N. Shelton, J. L. Peng, Z. Fisk, and S-W. Cheong. *Phys. Rev. B*, 41:2569–2572, 1990.

[90] A. S. Cherny, E. N. Khats'ko, G. Chouteau, J. M. Louis, A. A. Stepanov, P. Wyder, S. N. Barilo, and D. I. Zhigunov. *Phys. Rev. B*, 45:12600–12603(R), 1992.

[91] Y. Endoh, M. Matsuda, K. Yamada, K. Kakurai, Y. Hidaka, G. Shirane, and R. J. Birgeneau. *Phys. Rev. B*, 40:7023, 1989.

[92] J. Akimitsu, H. Sawa, T. Kobayashi, H. Fujiki, and Y. Yamada. *J. Phys. Soc. Jpn.*, 58:2646, 1989.

[93] S. Skanthakumar, H. Zhang, T.W. Clinton, W.H. Li, J.W. Lynn, Z. Fisk, and S.-W. Cheong. *Physica C*, 160:124, 1989.

[94] I.A. Zobkalo, A.G. Gukasov, S.Yu. Kokovin, S.N. Barilo, and D.I. Zhigunov. *Solid State Commun.*, 80:921–924, 1991.

[95] M. Matsuura, Pengcheng Dai, H. J. Kang, J. W. Lynn, D. N. Argyriou, K. Prokes, Y. Onose, and Y. Tokura. *Phys. Rev. B*, 68:144503, 2003.

[96] S. Jandl, P. Richard, V. Nekvasil, D. I. Zhigunov, S. N. Barilo, and S. V. Shiryaev. *Physica C*, 314:189, 1999.

[97] P. Richard, M. Poirier, and S. Jandl. *Phys. Rev. B*, 71:144425, 2005.

[98] D.A. Yablonsky. *Physica C*, 182:105, 1991.

[99] S. Katano, R.M. Nicklow, S. Funahashi, N. Môri, T. Kobayashi, and J. Akimitsu. *Physica C*, 215:92–96, 1993.

[100] Jun Akimitsu, Jiro Amano, Yoshinari Masaki, Michio Kokubun, Tatsuya Iwasaki, Satoshi Okuma, Nobuhiko Nishida, Kusuo Nishiyama, and Nobuo Mori. *Hyperfine Interact.*, 85:187–192, 1994.

[101] A. N. Lavrov, H. J. Kang, Y. Kurita, T. Suzuki, Seiki Komiya, J. W. Lynn, S.-H. Lee, Pengcheng Dai, and Yoichi Ando. *Phys. Rev. Lett.*, 92:227003, 2004.

[102] T. Chattopadhyay, J.W. Lynn, N. Rosov, T.E. Grigereit, S.N. Barilo, and D.I. Zhigunov. *Phys. Rev. B*, 49:9944, 1994.

[103] O.V. Kovalev. *Representations of the Crystallographic Space Groups: Irreducible representations, Induced representations and Corepresentations (2nd Ed.)*. Gordon and Breach Science Publishers, London, 1993.

[104] Yoichi Ando, Kouji Segawa, Seiki Komiya, and A. N. Lavrov. *Phys. Rev. Lett.*, 88:137005, 2002.

[105] A.I. Ponomarev, L.D. Sabirzyanova, A.A. Ivanov, A.S. Moskvin, and Yu. D. Panov. *JETP Letters*, 81:394, 2005.

[106] Yu. A. Izyumov, V. E. Naish, and R.P. Ozerov. *Neutron Diffraction of Magnetic Materials*. Plenum Publishing Corporation, New York, 1991.

[107] M. Naito and M. Hepp. *Jpn. J. Appl. Phys.*, 39:L485, 2000.

[108] M. Sawa, A. Kawasaki, H. Takagi, and Y. Tokura. *Phys. Rev. B*, 66:014531, 2002.

[109] M. Fujita, T. Kubo, S. Kuroshima, T. Uefuji, K. Kawashima, K. Yamada, I. Watanabe, and K. Nagamine. *Phys. Rev. B*, 67:014514, 2003.

[110] Matthias Brinkmann, Thomas Rex, Heinrich Bach, and Kurt Westerholt. *Phys. Rev. Lett.*, 74:4927, 1995.

[111] D. Petitgrand, S. V. Maleyev, Ph. Bourges, and A. S. Ivanov. *Science*, 265:73–74, 1994.

[112] G. Riou, P. Richard, S. Jandl, M. Poirier, P. Fournier, V. Nekvasil, S. N. Barilo, and L. A. Kurnevich. *Phys. Rev. B*, 69:024511, 2004.

[113] P. Richard, G. Riou, I. Hetel, S. Jandl, M. Poirier, and P. Fournier. *Phys. Rev. B*, 70:064513, 2004.

[114] A. J. Schultz, J. D. Jorgensen, J. L. Peng, and R. L. Greene. *Phys. Rev. B*, 53:5157–5159, 1996.

[115] P. G. Radaelli, J. D. Jorgensen, A. J. Schultz, J. L. Peng, and R. L. Greene. *Phys. Rev. B*, 49:15322–15326, 1994.

[116] P. Ghigna, G. Spinolo, E. Santacroce, S. Colonna, S. Mobilio, M. Scavini, and R. Bianchi. *Eur. Phys. J. B*, 41:31–42, 2004.

[117] Y. Tanaka, M. Karppinen, T. Kobayashi, T. S. Chan, R. S. Liu, J. M. Chen, and H. Yamauchi. *Chem. Mater.*, 20:5414–5420, 2008.

[118] Tsuyoshi Sekitani, Michio Naito, and Noboru Miura. *Phys. Rev. B*, 67:174503, 2003.

[119] Shiliang Li, Songxue Chi, Jun Zhao, H.-H. Wen, M. B. Stone, J. W. Lynn, and Pengcheng Dai. *Phys. Rev. B*, 78:014520, 2008.

[120] O. Matsumoto, A. Utsuki, A. Tsukada, H. Yamamoto, T. Manabe, and M. Naito. *Physica C*, 469:924–927, 2009.

[121] H.J. Kang, P. Dai, B.J. Campbell, P.J. Chupas, S. Rosenkranz, P.L. Lee, Q. Huang, S. Li, S. Komiya, and Y. Ando. *Nature Materials*, 6:224–229, 2007.

[122] G. Yu I. M. Vishik O. P. Vajk P. K. Mang Motoyama, E. M. and M. Greven. *Nature*, 445:186, 2007.

[123] O. Matsumoto, A. Utsuki, A. Tsukada, H. Yamamoto, T. Manabe, and M. Naito. *Physica C*, 468:1148–1151, 2008.

[124] O. Matsumoto, A. Utsuki, A. Tsukada, H. Yamamoto, T. Manabe, and M. Naito. *Phys. Rev. B*, 79:100508(R), 2009.

[125] Y. Krockenberger, H. Irie, O. Matsumoto, K. Yamagami, M. Mitsuhashi, A. Tsukada, M. Naito, and H. Yamamoto. *Scientific Reports*, 3:2235, 2013.

[126] D. M. King, Z.-X. Shen, D. S. Dessau, B. O. Wells, W. E. Spicer, A. J. Arko, D. S. Marshall, J. DiCarlo, A. G. Loeser, C. H. Park, E. R. Ratner, J. L. Peng, Z. Y. Li, and R. L. Greene. *Phys. Rev. Lett.*, 70:3159–3162, 1993.

[127] A. Schenk. *Muon Spin Rotation Spectroscopy: Principles and Applications in Solid State Physics*. Adam Hilger, Bristol, England, 1985.

[128] A. Schatz and A. Weidinger. *Nuclear Condensed Matter Physics*. Wiley, New York, 1996.

[129] K. Nagamine. *Introductory Muon Science*. Cambridge University Press, 2003.

[130] A. Yaouanc and P. Dalmas de Réotier. *Muon Spin Rotation, Relaxation, and Resonance*. Oxford University Press, Inc., New York, 2011.

[131] A. Seeger and L. Schimmele. *μSR in Magnetically Ordered Metals, Perspectives of Meson Science*. edited by T. Yamazaki, K. Nakai, and K. Nagamine (North Holland, Amsterdam), 1992.

[132] J. H. Brewer. *in Muon Spin Rotation / Relaxation /Resonance*, Vol. 11 of Encyclopedia of Applied Physics (VCH Publishers, New York):2353, 1994.

[133] A. Schenk and F. N. Gygax. *Magnetic Materials studied by Muon Spin Rotation Spectroscopy*. Vol. 9 of Handbook of Magnetic Materials, edited by K.H.J. Buschow (Elsevier Science B.V. Amsterdam), 1995.

[134] P. Dalmas de Réotier and A. Yaouanc. *J. Phys.:Cond. Matt.*, 9:9113, 1997.

[135] K. Hagiwara and *et al. Phys. Rev. D*, 66:010001, 2002.

[136] T. D. Lee and C. N. Yang. *Phys. Rev.*, 104:254–258, 1956.

[137] C. S. Wu, E. Ambler, R. W. Hayward, D. D. Hoppes, and R. P. Hudson. *Phys. Rev.*, 105:1413–1415, 1957.

[138] R. L. Garwin, L. M. Lederman, and M. Weinrich. *Phys. Rev.*, 105:1415–1417, 1957.

[139] Michael I. Larkin. *Evolution of the Ground State in Two Leg Spin Ladder System* $SrCu_2O_3$ *upon (Cu,Zn) Substitution*. PhD thesis, Columbia University, 1999.

[140] R. Kubo and T. Toyabe. *Magnetic Resonance and Relaxation*. North-Holland, Amsterdam, 1967.

[141] Y. J. Uemura. *μSR Relaxation Functions in Magnetic Materials*. Institute of Physics Publishing, 1999.

[142] R. S. Hayano, Y. J. Uemura, J. Imazato, N. Nishida, T. Yamazaki, and R. Kubo. *Phys. Rev. B*, 20:850–859, 1979.

[143] L. P. Le, A. Keren, G. M. Luke, B. J. Sternlieb, W. D. Wu, Y. J. Uemura, J. H. Brewer, T. M. Riseman, R. V. Upasani, L. Y. Chiang, W. Kang, P. M. Chaikin, T. Csiba, and G. Grüner. *Phys. Rev. B*, 48:7284–7296, 1993.

[144] Roland Hord, Gerhard Cordier, Kathrin Hofmann, Alexander Buckow, Gwendolyne Pascua, Hubertus Luetkens, Lambert Alff, and Barbara Albert. *Z. Anorg. Allg. Chem.*, 637:1114, 2011.

[145] I. P. Makarova, V. I. Simonov, M. K. Blomberg, and M. J. Merisalo. *Acta Cryst.*, B52:93–99, 1996.

[146] W. H. Zachariasen. *Acta Cryst.*, 1:265, 1948.

[147] R. Hord, G. Pascua, K. Hofmann, G. Cordier, J. Kurian, H. Luetkens, V. Pomjakushin, M. Reehuis, B. Albert, and L. Alff. *Supercond. Sci. Technol.*, 26:105026, 2013.

[148] A. Suter and B. M. Wojek. *Physics Procedia*, 30:69–73, 2012.

[149] H.U. Suter, E.P. Stoll, and P.F. Meier. *Physica B*, 326:329–332, 2003.

[150] Chappert J. and Grynszpan R.I. *Muons and pions in materials research.* North-Holland, 1984.

[151] F. Bernardini, P. Bonfà, S. Massidda, and R. De Renzi. *Phys. Rev. B*, 87:115148, 2013.

[152] John P. Perdew, Kieron Burke, and Matthias Ernzerhof. *Phys. Rev. Lett.*, 77:3865–3868, 1996.

[153] S-W. Cheong, A. S. Cooper, L. W. Rupp, B. Batlogg, J. D. Thompson, and Z. Fisk. *Phys. Rev. B*, pages 9739–9742.

[154] B. Keimer, A. Aharony, A. Auerbach, R. J. Birgeneau, A. Cassanho, Y. Endoh, R. W. Erwin, M. A. Kastner, and G. Shirane. *Phys. Rev. B*, 45:7430–7435, 1992.

[155] R. Hord, G. Cordier, K Hofmann, A. Buckow, G. Pascua, H. Luetkens, L. Alff, and B. Albert. *Z. Anorg. Allg. Chem.*, 637:1114–1117, 2011.

[156] P. E. Sulewski, P. A. Fleury, K. B. Lyons, S-W. Cheong, and Z. Fisk. *Phys. Rev. B*, 41:225–230, 1990.

[157] S. L. Cooper, G. A. Thomas, A. J. Millis, P. E. Sulewski, J. Orenstein, D. H. Rapkine, S-W. Cheong, and P. L. Trevor. *Phys. Rev. B*, 42:10785–10788, 1990.

[158] T. Yildirim, A. B. Harris, Amnon Aharony, and O. Entin-Wohlman. *Phys. Rev. B*, 52:10239–10267, 1995.

[159] T. Kubo, T. Uefuji, M. Fujita, K Yamada, I. Watanabe, and K. Nagamine. *Physica C*, 378-381:354, 2002.

[160] A. J. Steele, T. Lancaster, S. J. Blundell, P. J. Baker, F. L. Pratt, C. Baines, M. M. Conner, H. I. Southerland, J. L. Manson, and J. A. Schlueter. *Phys. Rev. B*, 84:064412, 2011.

[161] E. Takayama-Muromachi, F. Izumi, Y. Uchida, K. Kato, and H. Asano. *Physica C*, 159:634–638, 1989.

[162] Wu Jiang, J. L. Peng, Z. Y. Li, and R. L. Greene. *Phys. Rev. B*, 47:8151–8155, 1993.

[163] X. Q. Xu, S. N. Mao, Wu Jiang, J. L. Peng, and R. L. Greene. *Phys. Rev. B*, 53:871–875, 1996.

[164] Brian H. Toby. *Powder Diffr.*, 21:67–70, 2006.

[165] R. E. Dinnebier and S. J. L. Billinge. *Powder Diffraction: Theory and Practice*. The Royal Society of Chemistry, Cambridge, United Kingdom, 2008.

[166] S. Asai, S. Ueda, and M. Naito. *Physica C*, 471:682, 2011.

[167] A. Seffar, J. Fontcuberta, S. Piñol, X. Obradors, G. Peraudeau, and R. Berjoan. *Physica C*, 259:75–82, 1996.

[168] F. Prado, J. Briático, A. Caneiro, M. Tovar, and M.T. Causa. *Solid State Commun.*, 90:695–699, 1994.

[169] H. J. Kang, Pengcheng Dai, H. A. Mook, D. N. Argyriou, V. Sikolenko, J. W. Lynn, Y. Kurita, Seiki Komiya, and Yoichi Ando. *Phys. Rev. B*, 71:214512, 2005.

[170] D. Petitgrand, A. H. Moudden, P. Galez, and P. Boutrouille. *J. Less-Common Met.*, 164-165:768, 1990.

[171] S. Skanthakumar, J. W. Lynn, J. L. Peng, and Z. Y. Li. *J. Appl. Phys.*, 73:6326, 1993.

[172] S. Skanthakumar, J. W. Lynn, J. L. Peng, and Z.Y. Li. *J. Appl. Phys.*, 69:4866, 1991.

[173] I.W. Sumarlin and J. W. Skanthakumar, S.and Lynn. *Phys. Rev. Lett.*, 68:2228, 1992.

[174] D. E. Cox, A. I. Goldman, M. A. Subramanian, J. Gopalakrishnan, and A. W. Sleight. *Phys. Rev. B*, 40:6998–7004, 1989.

[175] V. P. Plakhty, S. V. Maleyev, P. Burlet, S. V. Gavrilov, and O. P. Smirnov. *Phys. Lett. A*, 250:201–204, 1998.

Acknowledgements

During my research, PSI and UZH were my mentoring institutions that supported my development through collective interactions and cooperation. This thesis is the outcome of the relationships that I have cultivated with the wonderful individuals that have supported and motivated me through the whole process.

I am deeply grateful for the excellent mentorship with my professors Elvezio Morenzoni in PSI and Hugo Keller in the UZH, whose respective expertise and leadership continue to inspire me. Also, their proofreading of my thesis has been invaluable for its improvement.

I can not find words to express enough thanks to my supervisor and mentor Hubertus Luetkens, whose unparalleled guidance were sometimes all that kept me going to withstand the challenges of PhD life. I owe him an enormous debt of gratitude for his dedication to both my academic and personal development. His thorough scrutinies to my thesis and insights have been truly important.

To all my colleagues, the members of the Laboratory for Muon Spin Spectroscopy, thank you very much for the amicable and stimulating atmosphere. Special thanks to my constant lunch-mates, Alex Amato, Andreas Suter, Andrea Raselli, Matthias Elender, Robert Scheuermann, Hubertus Luetkens, and Elvezio Morenzoni, for the interesting conversations and for patiently waiting for me to finish my meal.

Working in a large-scale facility provided me a huge number of opportunities that allowed me to collaborate with other researchers from different backgrounds of expertise, both locally and globally. I am enormously grateful to all my collaborators for their willingness to share their expertise and knowledge and for their contributions to my work. They are the following:

I am deeply grateful to Marco Günther for the NMR measurements and analysis and for helping us with the dipole field calculations. I appreciate his organizational skills and for being always dependable to respond to our requests. I also immensely thank Hans-Henning Klauss for the useful discussions and inputs, and all the TU Dresden friends especially to Til Goltz and Johannes Spehling, for the good company during beamtimes.

To my collaborators from TU Darmstadt, I am grateful to Roland Hord and Barbara Albert for my cuprate samples and to Lambert Alff, for helping shape and guide the direction of our project.

My data analysis and interpretations were made more complete with the determination of the muon site from the theoretical contributions from Pietro Bonfa, Roberto de Renzi, and Yurii Pashkevich, all of whom I delightedly thank.

To our neutron experts, Lukas Keller, Vladimir Pomjakushin, and Matthias Frontzek, I am truly thankful for helping me carry out the experiments and Fullprof refinements. To Maria Luisa Medarde Barragan, thank you for patiently answering my Fullprof-related queries. Also to Ekaterina Pomjakushina, for helping me with the reduction annealing procedures in the Chemistry lab.

To Erwin Wiesenmayer and Dirk Johrendt, I am grateful for giving me the opportunity to extend my research to iron-based superconductors by providing us with good samples.

I would like to thank my colleagues from my group in the university, Saskia Bosma, Zurab Guguchia, Evelyn Stilp, and Ludovic Howald, for the friendly atmosphere and discussions. Special thanks to Saskia and Zurab for their help with university-related administrative matters involving thesis submissions.

And to my support group, my friends both near and far, their way of extending their moral support and encouragements is beyond borders of time difference or distance that I appreciate, notably to Rem and Gab Belen, Shuang Wang, Peter Babkevich, Simon Ward, Nikola Anna Egetenmeyer, Diana Lucia Quintero Castro, Shravani Chillal, Hu Yi, Margie Olbinado, Mariel Dimamay, Geraldine Dumlao, Matthias Thede, Mahsa Silatani, Omar Pecho, Zurab Shermadini, Pabitra Biswas, Mickaël Morin, Romain Sibille, Nicolas Gauthier, Aurelien Rizk, Hassan Saadaoui, and Jose Rodriguez.

As always, my family both in the Philippines and my new family in France both served as my inspirations and to them, I am dedicating this milestone. Special thanks to my mother, Paulita Banasan Pascua, for her enormous support and love, and for her presence during my thesis-writing that made me worry-free and calm. To my Lolo William and Lola Catalina, for the great foundations they instilled in me. To my parents-in-law, Michel and Michèle Demoulin, I am earnestly grateful for the very warm support and encouragements, and for making a superb celebration after my defense.

Last but certainly not the least, I am wholeheartedly grateful to my significant other Thibault Demoulin, who gave me steadfast love, support, and inspiration all throughout my PhD and even during our Masters. Needless to mention, his numerous contributions to this achievement are remarkable, ranging from helping me with my figures, driving me in the wee hours of the night during my experiment beamtimes and bringing nourishments, patiently listening to my ideas and even to my angst when I have to vent out my pressures, and

for all those heartwarming and selfless gestures that always keep me strong, grounded and motivated.

Curriculum Vitae

Personal Data

Name	Gwendolyne Banasan Pascua
Date of birth	5 June 1982
Place of birth	Kalinga, Philippines
Nationality	Filipino

Education and Academic Degrees

1994–1998	*Tabuk National High School- Special Science Class* High School Diploma, Salutatorian
1999–2005	University of the Philippines- Diliman Bachelor of Science in Applied Physics Subject of Bachelor thesis: *Synthesis and characterization of c-axis oriented $YBa_2Cu_3O_{7-\delta}$ thin films on $SrTiO_3$ via liquid-assisted deposition method and growth by partial melting and annealing techniques*
2005–2008	University of the Philippines- Diliman Master of Science in Physics student
2008–2009	Universite de Rennes I Ludwig-Maximilians-Universität München Master in Material Science Exploiting Large-scale Facilities Subject of Master thesis: *3D-Layered Materials for Spintronics $Pb_3Mn_7O_{15}$*

2009–2014	Doctoral Researcher Paul Scherrer Institut Universität Zürich Supervisor: Dr. Hubertus Luetkens Thesis subject: *Structural and Magnetic Properties of the Insulating T'-RE_2CuO_4 Parent Compounds of Electron-Doped Superconductors*

Publication list (work performed in the framework of this PhD thesis)

- *Oxygen stoichiometry of low-temperature synthesized metastable T'-La_2CuO_4*
  Hord, R., **Pascua, G.**, Hofmann, K, Cordier, G., Kurian, J., Luetkens, H., Pomjakushin, V., Reehuis, M., Albert, B., and Alff, L.
  Supercond. Sci. Technol **26**, 105026 (2013).

- *Low temperature ballistic spin transport in the S=1/2 antiferromagnetic Heisenberg chain compound $SrCuO_2$*
  Maeter, H., Zvyagin, A. A., Luetkens, H., **Pascua, G.**, Shermadini, Z., Saint-Martin, R., Revcolevschi, A., Hess, C., Buechner, B., and Klauss, H.-H.
  J. Phys.: Condens. Matter **25**, 365601 (2013).

- *Short-range magnetic order and effective suppression of superconductivity by manganese doping in $LaFe_{1-x}Mn_xAsO_{1-y}F_y$*
  Frankovsky, R., Luetkens, H., Tambornino, F., Marchuk, A., **Pascua, G.**, Amato, A., Klauss, H.-H., and Johrendt, D.
  Phys. Rev. B **87**, 174515 (2013).

- *Evidence for superconductivity with broken time-reversal symmetry in locally noncentrosymmetric SrPtAs*
  Biswas, P. K., Luetkens, H., Neupert, T., Stuerzer, T., Baines, C., **Pascua, G.**, Schnyder, A. P., Fischer, M. H., Goryo, J., Lees, M.R., Maeter, H., Brueckner, F., Klauss, H.-H., Nicklas, M., Baker, P. J., Hillier, A. D., Sigrist, M., Amato, A., and Johrendt, D.
  Phys. Rev. B **87**, 180503 (2013).

- *Microscopic Coexistence of Superconductivity and Magnetism in $Ba_{1-x}K_xFe_2As_2$*
  Wiesenmayer, E., Luetkens, H., **Pascua, G.**, Khasanov, R., Amato, A., Potts, H., Banusch, B., Klauss, H.-H., and Johrendt, D.
  Phys. Rev. Lett. **107**, 237001(2011).

- *Transitions Between Lanthanum Cuprates: Crystal Structures of T', Orthorhombic, and K_2NiF_4-type La_2CuO_4*
  Hord, R., Cordier, G., Hofmann, K., Buckow, A., **Pascua, G.**, Luetkens, H., Alff, L., and Albert, B.
  Z. Anor. Allg. Chem. **637**, 1114-1117 (2011).

- *Enhanced two-dimensional behavior of metastable T'-La_2CuO_4, the parent compound of electron-doped cuprate superconductors*
  Hord, R., Luetkens, H., **Pascua, G.**, Buckow, A., Hofmann, K., Krockenberger, Y., Kurian, J., Maeter, H., Klauss, H.-H., Pomjakushin, V., Suter, A., Albert, B., and Alff, L.
  Phys. Rev. B **82**, 180508 (2010).

- *Microscopic study of the superconducting state of the iron pnictide $RbFe_2As_2$ via muon spin rotation*
  Shermadini, Z., Kanter, J., Baines, C., Bendele, M., Bukowski, Z., Khasanov, R., Klauss, H. -H., Letkens, H., Maeter, H., **Pascua, G.**, Batlogg, B. and Amato, A.
  Phys. Rev. B **82**, 144527 (2010).